MONTAN
UNIVERSITÄT
LEOBEN

Chair of Functional Materials and Materials Systems

Doctoral Thesis

Cross-sectional and High-Temperature Structure-Property Relationships in Nanocrystalline Thin Films

Dipl.-Ing. Michael Meindlhumer, BSc

October 2020

Affidavit

MONTANUNIVERSITÄT LEOBEN
www.unileoben.ac.at

EIDESSTATTLICHE ERKLÄRUNG

I declare on oath that I wrote this thesis independently, did not use other than the specified sources and aids, and did not otherwise use any unauthorized aids.

I declare that I have read, understood, and complied with the guidelines of the senate of the Montanuniversität Leoben for "Good Scientific Practice".

Furthermore, I declare that the electronic and printed version of the submitted thesis are identical, both, formally and with regard to content.

Datum 12.10.2020

Signature Author
Michael, Meindlhumer

Acknowledgments

I wish to express my deepest thanks and gratitude to all the people who have helped me forming this thesis in the past 4 years, either professionally or personally.

First and foremost I want to thank my advisors, Prof. Jozef Keckes and Prof. Christian Mitterer. Their continuous support and their constructive feedback on numerous scientific topics are a great source of improvement for my work, as well as for myself. Furthermore, I want to thank Assoz. Prof. Rostislav Daniel for the possibility to perform this thesis within the framework of the Christian Doppler Laboratory for the Advanced Synthesis of Novel Multifunctional Coatings. His support and critical review of the scientific work and during writing of the publications are also greatly acknowledged.

A special thank-you is directed towards Jozef Keckes, who employed me during my bachelor and master studies from 2013 to 2016, and who always gave ear to my questions, and was always enthusiastic about my results and queries. His mentoring also encouraged me to pursue my scientific ideas, some which were even incorporated into this thesis.

Significant parts of this work were carried out at the ID13 beamline of the European Synchrotron (ESRF, Grenoble) and the P07 beamline of the PETRA III lightsource at DESY in Hamburg, Germany. I want to thank the responsible beamline scientists, Manfred Burghammer and Martin Rosenthal from the ESRF and Andreas Stark from the P07 at DESY for their excellent support during the measurements and the numerous discussions about topics related to materials science and various other fields of science, life or fiction.

A great number of samples for synchrotron beamtimes and micromechanical testing was prepared by Gabriele Felber, Herwig Felber and Daniela Keckesova in our department's TEM preparation laboratory. Their efforts and skill were essential for the success of this work.

Among my former and present colleagues I would like to thank especially Sabine Bodner, David Gruber, Julius Keckes, Kevin Kutlesa, Michael Reisinger, Juraj Todt Jakub Zalesak, Tobias Ziegelwanger, and all the others, I might have missed here, for the (sometimes) thriving office discussions, partly even related to materials science, their support and generally all the other little distractions.

I want to express my thanks to all my friends here in Leoben, especially Markus, Andrea, Severin and Julia for all the time spent having fun together. Additionally, I very much appreciate the time spent with my co-musicians from my chamber music

ensemble Música Atmósfera. Thank you for leading me astray from materials science sometimes.

Furthermore, I want to thank my brothers Martin and Andreas, as well as their fiancées, Martina and Anna. Especially, I want to thank my parents Gabriele and Erwin, without their support in every issue, this thesis would not have been written.

Last but most importantly, I want to thank my girlfriend Julia, for her unconditional love, her constant support and all the joy she brings to my life, including also (a little more) chaos.

This work was carried out within the framework of the Christian Doppler Laboratory for the Advanced Synthesis of Novel Multifunctional Coatings and has been financially supported by Christian Doppler Research Association. The financial support by the Austrian Federal Ministry of Science, Research and Economy and the National Foundation for Research, Technology and Development is also gratefully acknowledged.

Abstract

Microstructure, mechanical and functional properties of thin films often exhibit gradients at the nanoscale, which originate either from the nonuniform vapour deposition processes or were introduced in the film via external loads. Independent of their origin, resolving thin films gradients of interest, needs characterisation tools operating with a spatial resolution at the nanoscale. These gradients of microstructure, residual and applied strains in hard protective thin films are the focus of this work, since they are critical to the performance of coated structures, such as coated tools used in the machining industry.

Three model problems within thin film research were approached within this thesis, including (i) the nanoscale microstructure and residual stress gradients emerging from the deposition process in a thin film coated onto a cutting edge area, (ii) the nanoscale mechanical response against scratching and (iii) the in situ evaluation of the fracture response of thin films. Moreover, (iv) the thorough investigation of decomposition of thin films during annealing up to 1100°C, and finally (v) a self-assembled hierarchical thin film with a superior combination of mechanical and thermal properties is presented. In detail, the following characterisations on various thin films were performed:

- Cross-sectional X-ray nanodiffraction was applied to access the nanoscale microstructure and stress gradients originating from the physical vapour deposition process in a TiN coating on a WC-Co cutting edge. While gradual and constant residual stress distributions with magnitudes between -1.4 and $-2.4\,\text{GPa}$ were found at the flank and rake faces, respectively, directly at the cutting edge a pronounced lateral and cross-sectional gradient ranging from 0 to $-3\,\text{GPa}$ was evaluated from the X-ray data.

- 50 nm X-ray nanodiffraction and alectron microscopy were applied to characterize the nanoscale stress gradients and microstructural changes across the scratch track area of a brittle-ductile Cr/CrN thin film on a high speed steel substrate. After scratching, the formation of severe nanoscopic gradients of in-plane, out-of-plane and shear stress distributions were revealed in Cr and CrN, ranging from -6 to $1.5\,\text{GPa}$. These stress gradients were accompanied by and correlated to irreversible microstructural changes, such as either intergranular crack formation and transgranular defects, or crystallite bending and uniaxial gliding in CrN and Cr, respectively.

- The fracture response of a notched clamped cantilever composed of four alternating Cr and CrN layers on high speed steel was evaluated by in situ cross-sectional X-ray nanodiffraction. The residual stress distributions in the notched Cr layer result in an effective stress intensity factor of $-5.9 \pm 0.4\mathrm{MPa\,m}^{1/2}$ and a pronounced stress concentration and a plastic zone around the notch. At a critical stress intensity of $2.8 \pm 0.5\mathrm{MPa\,m}^{1/2}$, crack growth occurred up to the adjacent CrN-Cr interface, where the crack was arrested.

- The stress-controlled decomposition routes of three AlCrN thin films have been assessed by the newly developed in situ high-temperature high-energy grazing-incidence-transmission X-ray diffraction method. Whereas the decomposition temperatures of the metastable cubic $\mathrm{Al}_{0.7}\mathrm{Cr}_{0.3}\mathrm{N}$ phase ranged from 698-914°C, the residual stress level of $\sim -4.3\,\mathrm{GPa}$ was similar for all three investigated thin films.

- A TiAlN thin film composed of 6 hierarchical levels and mimicking biological materials, such as nacre or enamel, was synthesized by chemical vapour deposition, by alternating two variants of chemical precursors. In such a way, an irregular multilayer stack was formed by bottom-up self-assembly, consisting of hard herringbone stacks separated by interlayers of spherical nanograins. It exhibits superior functional properties and represents a milestone in the field of synthesis of protective wear resistant thin films.

Kurzfassung

Die Mikrostruktur, die mechanischen und funktionellen Eigenschaften von dünnen Schichten haben oft nanoskalige Gradienten, welche entweder im inhomogenen Gasphasen-Abscheideprozess oder durch externe Belastung entstehen. Unabhängig ihrer Herkunft benötigt das Erfassen dieser Gradienten Untersuchungsmethoden mit einer nanoskopischen räumlichen Auflösung. Die Gradienten von Mikrostruktur, Eigen- und angelegter Spannungen in harten, dünnen Schutzschichten sind der Fokus dieser Arbeit, denn diese sind kritisch für die Leistungsfähigkeit von beschichteten Strukturen, wie z.B. beschichtete Werkzeuge in der spanenden Bearbeitung.

Drei Modellprobleme in der Dünnschichtforschung wurden in dieser Arbeit untersucht, einschließlich (i) der nanoskaligen Mikrostruktur- und Eigenspannungsgradienten, welche im Bereich einer Schneidkante durch den Beschichtungsprozess auftreten, (ii) der nanoskaligen mechanischen Antwort auf den Ritzversuch und (iii) der in situ Auswertung der Bruchantwort von Dünnschichten. Zudem wurde (iv) die Analyse der Zersetzung von Dünnschichten bis 1100°C durchgeführt und abschließend (v) wird eine selbstorganisierte, hierarchisch aufgebaute Dünnschicht mit einer überragenden Kombination von mechanischen und thermischen Eigenschaften präsentiert. Folgende Charakterisierungen wurden an Dünnschichten durchgeführt:

- Röntgen-Nanobeugung wurde angewandt um die nanoskopischen Mikrostruktur- und Eigenspannungsgradienten in einer TiN Beschichtung auf einer WC-Co Schneidkante, entstanden durch den Abscheidungsprozess, zu charakterisieren . Während graduelle und konstante Eigenspannungsverteilungen mit einer Größe zwischen -1.4 und -2.4 GPa an der Frei- bzw. Spanfläche gemessen wurden, wurden direkt an der Kante ausgeprägte laterale und Querschnittsgradienten in einem Bereich von 0 bis -3 GPa aus den Röntgendaten ausgewertet.

- Röntgen-Nanobeugung und Elektronenmikroskopie wurden eingesetzt um die nanoskopischen Eigenspannungs- und Mikrostrukturänderungen in der Umgebung einer Ritzspur in einer Dünnschicht bestehend aus spröd-duktilem Cr/CrN auf Schnellarbeitsstahl zu charakterisieren. Nach dem Ritztest wurden ausgeprägte Spannungsgradienten in CrN und Cr festgestellt, welche in einem Bereich zwischen -6 und 1.5 GPa liegen. Diese wurden irreversiblen Mikrostrukturänderungen, wie interkristalliner Rissbildung und transkristalliner Defektansammlung, sowie Kristallitbiegung und gerichtetem Abgleiten in

CrN bzw. Cr zugeordnet.

- Die Bruchantwort eines gekerbten, beidseitig eingespannten Biegebalkens aus vier abwechselnden Cr- und CrN-Lagen auf Schnellarbeitsstahl wurde mittels in situ Röntgen-Nanobeugung ausgewertet. Die Eigenspannungen in der gekerbten Cr-Schicht ergaben eine effektive Spannungsintensität von $-5.9 \pm 0.4\mathrm{MPa\,m}^{1/2}$, begleitet von einer plastischen Zone rund um die Kerbe. Eine kritische Spannungsintensität von $2.8 \pm 0.5\mathrm{MPa\,m}^{1/2}$ führte zu Rissausbreitung an die anliegenden CrN-Cr Grenzfläche, wo diese gestoppt wurde.
- Die spannungskontrollierten Zersetzungsrouten in drei AlCrN Dünnschichten wurden mittels der neu entwickelten in situ Hochtemperatur-Hochenergie-Durchstrahlungs-Röntgenbeugung festgestellt. Obwohl die Zersetzungstemperaturen des metastabilen kubischen $Al_{0.7}Cr_{0.3}N$ zwischen 698 und 914°C variieren, ist die Eigenspannung zu Beginn der Zersetzung mit $\sim -4.3\,\mathrm{GPa}$ für alle drei untersuchten Dünnschichten gleich.
- Eine TiAlN Dünnschicht mit 6 hierarchischen Ebenen, welche Biomaterialien imitiert, wurde mittels chemischer Gasphasenabscheidung durch Abwechslung zweier verschiedener Ausgangsstoffvarianten hergestellt. So wurde ein irregulärer Multilagenaufbau durch Selbstorganisation hergestellt, bestehend aus harten fischgrätenartig aufgebauten Lagen, welche durch Zwischenlagen sphärischer Nanokörner getrennt werden. Diese Beschichtung zeigt überragende funktionale Eigenschaften und repräsentiert einen Meilenstein im Bereich der Herstellung harter, verschleißfester Schutzschichten.

Contents

1

Introduction

Nowadays, thin films are essential in many state-of-the art technologies, such as functional layers in electronic devices or wear-protective coatings for high-speed cutting tools. Especially, in the case of hard protective thin films deposited on cutting tools, research and development have been stimulated by demands from machining industry over the recent years [1–5]. The films protecting cutting tools have to withstand severe conditions during operation, which are mainly high mechanical loads such as friction-induced stress [6, 7] and temperatures up to 1000°C [8] directly at the cutting edge. These films must exhibit outstanding mechanical properties, which allow them resisting the thermal, abrasive and mechanical loading conditions during operation, as summarized above. Required film properties include mainly high hardness, Young's modulus, fracture toughness, as well as wear and oxidation resistance [9, 10]. Additionally, growth defects originating from the deposition process [11], such as droplets, can act as stress concentrators during loading, which can initiate premature failure of the thin film [12].

Multiple gas phase techniques have been developed to deposit thin films, which can be roughly separated into two categories, physical (PVD) and chemical vapour deposition (CVD).

Typical PVD techniques are cathodic arc evaporation (CAE) and magnetron sputter deposition (MSD). Both CAE and MSD are plasma-assisted deposition techniques operating far from the thermodynamic equilibrium, which allows deposition of mixtures of immiscible elements [13–15].

In detail, CAE utilizes arc discharges to vaporize material from the surface of an electrode (the cathode) [15, 16]. Using CAE has some advantages, like high deposition rates and generally a good adhesion of the film to the substrate [15]. However, the main drawback is the frequent formation of macroparticles, known as droplets, which are generally detrimental to the film's quality and properties [11, 12].

The main advantages of MSD are that no macroparticles are formed during deposition and that the surface and interface roughnesses are significantly lower compared to CAE and CVD [13, 14]. However, deposition rates are rather low compared to CAE or CVD.

On the other hand, during CVD [17], gaseous precursors form a solid film on the substrate surface via chemical gas phase reactions, condensation from the vapour phase and further surface reactions. The advantages of CVD are the high deposition rates and that it is possible to form films even on geometrically complex structures, however the main drawback is that high deposition temperatures of ∼700-1100°C are necessary [17, 18].

Thin films synthesized by PVD or CVD normally exhibit complex cross-sectional and lateral nanoscale gradients of microstructure and physical properties, as a consequence of the non-equilibrium preparation process [19–21]. These gradients are a result of the gradual development of crystalline and amorphous phases, the crystallite's size and shape, crystallographic texture and strains of 1^{st}, 2^{nd} and 3^{rd} order developed during deposition of the thin film. In order to guide the functional properties of thin films, it is necessary to understand the specific local structure-property relationships induced by the non-equilibrium deposition processes. All of the properties necessary for hard protective thin films stated above, are decisively influenced by the gradients of microstructure and residual stress predefined by the deposition process, which in turn can be altered deliberately by tuning particular process parameters [20–22].

In the following, the state-of-the art in the analysis of (i) deposition-induced gradients of microstructure and residual stress and (ii) the nanoscale stress gradients originating in the thin films from external loads are briefly addressed and (iii) the aim of this thesis is outlined.

1.1. Deposition-induced gradients of microstructure and residual stress along the cutting edge

As already mentioned above, especially the cutting edge area, which is in direct contact with the workpiece, undergoes heavy mechanical and thermal loads during operation [6, 7, 23]. Consequently, design strategies of thin films controlling chemical composition, microstructure, residual stress, thermal stability and mechanical properties should be focused exactly on this area. However, up to now, optimisation of the deposition process in terms of the loop of design, synthesis and property characterisation is almost exclusively performed on flat surfaces. This systematic inconsistency completely neglects the nanoscale gradients of chemical composition, microstructure, thickness and morphology evaluated by previous studies for PVD thin films at the cutting edges [24–27], which differ significantly from the ones observed on flat surfaces. In detail, a thickness increase of up to 26% and a decrease of the Al/Ti ratio up to 14% was evaluated for a TiAlCrYN coating on sharp WC-Co edges with varying opening angles by Macak *et al.* [25]. On a milling tool coated with TiAlN, stress relaxation from -5.5 to $-2.5\,\mathrm{GPa}$ was observed from the centre to the edge by laboratory X-ray diffraction (XRD) [28].

Generally, these findings were related to the evolution of a spatially non-homogeneous process plasma around the substrate edges and a locally enhanced deposition temperature [24–26, 29]. Given the observed change in microstructure, chemical composition and morphology revealed by Refs. [24–26, 29], tremendous nanoscale lateral and cross-sectional changes of microstructure and residual stress are to be expected in coatings in cutting edge areas, after deposition. The nanoscale evaluation of these gradients, whose origin lies in the deposition process itself, could lead to further coating optimization, detect the origins of premature film failure and eventually prolong the lifetime of coated cutting tools.

1.2. Gradients of microstructure and stresses induced by external loads

Alongside nanoscale elemental, microstructural and mechanical/stress gradients originating from the deposition process, additional microstructural and stress gradients are introduced in a coating during service, which are mostly related to either thermal, mechanical or abrasive loads applied to the coating. Generally, abrasive loads can be simulated by tribological tests, such as the ball-on-disk test using a sphere of an abrasive material, which slides over the coating surface [30], or the scratch test, where an indenter tip is moved uniaxially over the coating's surface [31, 32]. The scratch test itself was initially developed to qualitatively assess the adhesion of hard ceramic thin films on various types of substrates. Subsequently it was revealed, that by changing a variety of sample (intrinsic) and method (extrinsic) related parameters, the testing mode can be altered in such way, that not the adhesion of a film is decisive, but where deformation/cohesive strength of the film itself is crucial [33–35]. The latter is a model case for the single-asperity contact, *e.g.* for a metal chip sliding over the flank face of a coated cutting tool. However, the state-of-the art for assessing structural changes in thin films, induced by scratch testing, is a combination of acoustic emission spectroscopy, analysis of the load-indentation depth curve over the scratched distance and optical and electron microscopy of the scratched surface, to identify critical loads at specific damage levels to the film [36]. Up to now, strains/stresses induced by scratch testing have been primarily assessed by finite element modelling [37–39]. However, currently, there is only limited understanding about the microstructural changes and deformation-induced stresses in thin films after application of abrasive loads.

Additionally, externally applied loads during operation in the vicinity of pre-existing defects in hard protective thin films can induce fracture of the coating and subsequently lead to tool failure. Consequently, a sufficiently high fracture toughness is necessary to suppress overcritical brittle fracture, since the fracture toughness itself is a value for the resistance of a material against critical crack growth [40, 41]. Since nanoceramic protective thin films are inherently brittle, they naturally lack fracture toughness, despite their beneficial high hardness and Young's modulus. Additionally, fracture in thin films progresses along columnar grain boundaries of low cohesive energy, which results in even further decreased fracture resistance [42]. Several approaches have been reported in literature to increase the fracture toughness of thin films, such as multi-layered thin films with constituents exhibiting pronounced spatial heterogeneity [42–44], alloying with B and C, as well as microstructural design of CVD TiN [45–47], tilting of columnar grain boundaries [2, 48, 49], formation of superlattice thin films [50, 51] and by enhancing plasticity via vacancy formation on the non-metal sublattice [52]. Alternating stiff and compliant sublayers is an effective measure to increase the fracture toughness of thin films without major influences on stiffness and hardness, which has its role-models in natural materials, such as nacre, bone or enamel [53–56].

In order to assess the fracture toughness of thin films, bending of focused ion beam (FIB) fabricated single-clamped micro-cantilevers has evolved into the state-of-the art methodology for testing of hard protective thin films [2, 42, 43, 45–49, 57]. However, in recent years, also the testing of double-clamped cantilevers, manufactured by FIB has drawn significant attention [58–60]. In single-edged cantilevers the mechanical equilibrium condition has to be fulfilled at the freestanding end, which relieves nearly all residual stress contributions from the film. On the contrary, in the double-clamped cantilever geometry, the residual strain from deposition is nearly fully preserved, since the cantilever has no freestanding end. This makes the double-clamped cantilever geometry a suitable and interesting candidate to investigate the influence of residual stresses on the fracture response of thin films.

In summary, despite significant progress in the development of thin films over the recent years, it is still necessary to evaluate and understand the formation of local mechanical and microstructural gradients of thin films at the nanoscale, either introduced by the deposition process or by externally applied loads.

1.3. Aim of the thesis

The aim of the present thesis is focussed on examining and evaluating structure-property relationships of hard protective thin films at the nanoscale and at elevated temperatures. In detail, the five enclosed publications deal with the characterization of nanoscale stress and microstructure gradients in thin films (i) deposited onto industrially manufactured cutting-edge WC-Co substrates, (ii) after scratch testing, which is a model of the single-asperity contact, and (iii) during *in situ* micromechanical loading. Moreover, (iv) a new methodology evaluating the crucial influence of residual stress on the decomposition of metastable AlCrN thin films and a (v) novel six-level hierarchical thin film with superior fracture resistance are presented. In detail, within this thesis, several aspects of the structure-property relationships of thin films have been investigated, such as:

1. The nanoscale microstructural and residual stress gradients of hard protective thin films are of high scientific and industrial interest. In Paper A, cross-sectional X-ray nanodiffraction with a beam size of $35 \times 25\,\mathrm{nm}^2$ was used to retrieve structural and mechanical gradients in the cutting edge area of a $\sim 2\,\mu\mathrm{m}$ thick TiN thin film on WC-Co substrate. Within this work, scanning small-angle X-ray scattering microscopy (SAXSM) was presented and utilized for the first time to investigate the nanoscale defect density variations in the cutting edge area. At the cutting edge, interface-like planar domains of high scattered intensity were found, while a gradual increase of the SAXS intensity at the rake face was correlated with pores found by scanning electron microscopy. Furthermore, the coating's $\langle 111 \rangle$ fibre texture orientation correlates with the surface normal of the substrate, with abrupt orientation changes across the aforementioned interface-like structures. The planar regions next to the edge exhibit gradual and constant stress profiles on the flank and rake faces, respectively, with anisotropic defect build-ups. Directly at the edge, nonlinear lateral and cross-sectional compressive residual stress gradients ranging from ~ 0 to $-3\,\mathrm{GPa}$ were observed, which, together with the interface-like planar domains, may represent a reliability issue during operation.

2. A bilayer Cr-CrN thin film was subjected to scratch testing to simulate a single-asperity contact and evaluate the stresses induced by elasto-plastic de-

formation accompanying the contact. The experimental results presented in Paper B revealed a complex alternation of the columnar grain microstructure and the formation of pronounced lateral and through-thickness stress gradients, which are interpreted by a finite element model. After scratching, the in-plane stresses within the CrN toplayer relax from ~ -3.5 to ~ 0 GPa at the surface along the scratch track, while they increase up to -6 GPa at a distance of about 6 µm away from the imprint centre. Within the ductile Cr interlayer, compressive and tensile stresses of up to -1.5 and 1.5 GPa formed at the imprint centre and in the surrounding pile-ups, respectively. Also, the evaluated out-of-plane and shear stress distributions exhibit steep gradients, which are correlated with the nanoscopic microstructural changes observed by transmission electron microscopy, transmission Kikuchi diffraction, SAXSM and peak width analysis. Within the brittle CrN, the scratch test results in grain sliding and the formation of nanoscopic intragranular defects. The Cr interlayer's thickness reduction and pile-up formation are accompanied by a bending of columnar crystallites and localized plastic deformation. In summary, the quantitative stress data elucidate the stabilizing role of the ductile Cr sublayer, which suppresses catastrophic cross-sectional fracture during scratch tests.

3. In order to understand better the nanoscale fracture response of thin films and their effect on functional properties, new high-resolution *in situ* investigation tools need to be developed. In Paper C, a clamped cantilever with dimensions of 200 µm × 23.6 µm × 40 µm was cut by focused ion beam milling from a thin film composed of, in total four, alternating CrN and Cr sublayers on high strength steel. The clamped cantilever was loaded in two steps to 460 mN and four two-dimensional strain maps were obtained by *in situ* cross-sectional X-ray nanodiffraction. Preliminary *ex situ* characterisation revealed the depth variation of fibre texture within CrN and Cr, respectively, allowing also the depth-dependent alteration of stiffness to be evaluated, as well as residual stress gradients within the individual layers. The *in situ* diffraction experiment revealed (i) a strong influence of the residual stresses on the deformation behaviour, (ii) the crack arrest capability of the CrN-Cr interface, and (iii) a crack tip blunting effect. In detail, effective stress intensity of $-5.9 \pm 0.4\mathrm{MPa\,m}^{1/2}$ arose in the notched Cr layer, as a consequence of the pre-existing residual stress state. Crack growth within the Cr sublayer occurred at a critical stress intensity of $2.8 \pm 0.5\mathrm{MPa\,m}^{1/2}$. At 460 mN, after crack growth

to the adjacent CrN-Cr interface, the stress fields of the crack vanished. The results were furthermore complemented by two-dimensional numerical simulation using the eigenstrain reconstruction method, to gain further insight into the stress evolution during loading. Finally, the results represent an important step towards the understanding of the fracture behaviour of thin films composed of alternating brittle and ductile materials.

4. In order to address the aspect of thermal stability and of temperature-dependent changes in hard protective thin films, the decomposition routes of metastable c-AlCrN were assessed in the temperature range of 25 to 1100°C, using the newly developed multi-parameter *in situ* high-energy high-temperature grazing incidence transmission X-ray diffraction (HE-HT-GIT-XRD) method. The onset temperature of decomposition of c-AlCrN into w-Al(Cr)N and c-Cr(Al)N was indirectly proportional to the as-deposited residual stress magnitude, whereas the onset stress of decomposition was found to be independent of the thermo-mechanical history of the investigated thin films. The methodology and results were published in Paper D. The newly developed HE-HT-GIT-XRD method was also employed to investigate the thermal stability of microstructure and phases of a biomimetic self-assembled hard and tough CVD TiAlN thin film investigated in Paper E.

5. In Paper E, the mechanical and thermal properties of a biomimetic self-assembled hard and tough TiAlN thin film consisting of six hierarchical levels have been investigated extensively. The 2.7 µm thick film was formed by chemical vapour deposition by a variation of two different gaseous precursors and through bottom-up self-assembly in only $\sim$ 15 mins of deposition time, which resulted in an irregularly arranged hard and tough multilayer stack. The hard sublayers consisted of herringbone-shaped micrograins, while tough interlayers were composed of spherical nanograins, forming a stack of lamellar nanostructures of alternating coherent/incoherent, hard/tough, single-/poly-crystalline platelets. Thermal stability was studied by the HT-HE-GIT-XRD method presented in Paper D and revealed microstructural and phase stability up to 900 and 950°C, respectively. Intrinsic toughening mechanisms mediated by five different types of interfaces resulting in inter- and transgranular fracture modes with zigzag-like crack patterns at multiple length-scales were revealed by micro- and nanomechanical testing, performed *in situ* in scanning and transmission electron microscopes. Hardness, fracture stress and toughness of 31 GPa, 7.9 GPa and 4.7 MPa $\mathrm{m}^{1/2}$ were evaluated. The film's thermal, mi-

> crostructural and mechanical characteristics represent a breakthrough in the production of hard protective, wear-resistant thin films.

In the following chapters, the characteristics of the investigated thin films and the analytical techniques employed in the appended publications are introduced and briefly discussed.

2

Hard protective thin films

The demands on properties of hard protective thin films are set by the metal cutting industry and films therefore have to be continuously improved to meet their growing requirements. High hardness, together with sufficient toughness, is necessary for wear resistant thin films [61]. Hard protective thin films composed of transition metal nitrides are characterized by their mixed bonding state (*cf.* Fig. 2.1), which is tuneable by alloying between metallic, covalent and ionic bonding [62].

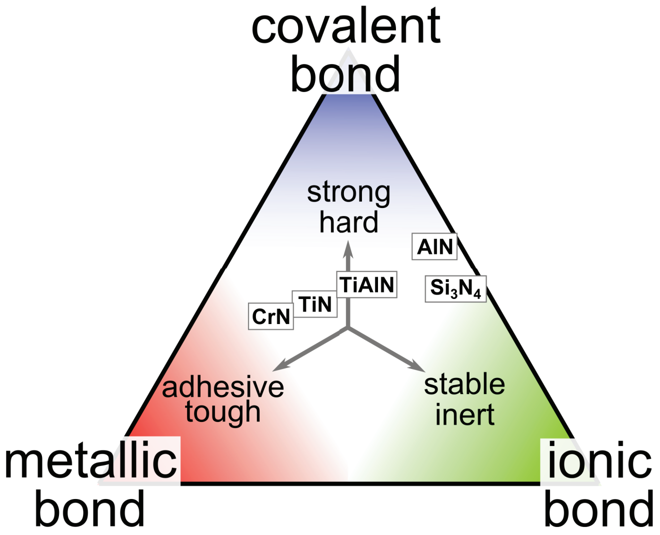

Figure 2.1.: Schematic sketch of possible bonding types and properties associated with them, along with the approximate placement of selected nitride ceramics within this context. Reproduced from Ref. [62].

In this section, the main characteristics of the hard protective nitride thin films investigated in this thesis are outlined.

2.1. TiN

TiN has been introduced nearly half a century ago as a material for hard protective thin films and is still relevant in thin film research and industry. Nowadays it is mostly used as adhesion layer, diffusion barrier and as marker for wear, the latter due to its bright golden colour [63]. The oxidation resistance of TiN is limited, and oxidation starts already at $\sim$ 550°C, when the poorly-adherent porous rutile TiO_2 phase is formed [64–67]. Additionally, mechanical properties are quite moderate, as reported values for hardness lie in the range of $\sim$ 18-25 GPa [2,61] and those for fracture toughness in the range of 2-3 $\mathrm{MPa\,m^{1/2}}$ [44, 68].

However, for the analysis of deposition-process-induced nanoscale stress and microstructure gradients, it is perfectly suitable, due to the facts, that it crystallizes in the B1 NaCl structure over a relatively wide Ti/N ratio [69] and its elastic properties are quite isotropic [70]. Additionally, during deposition using CAE moderate compressive stresses are introduced in the coating, which is in contrast to Al-alloyed thin films (see for example the as-deposited stress magnitudes of c-AlCrN (Paper D) and TiN (Paper A) of -4.3 and -1.7 GPa, respectively, on flat surfaces when applying the same deposition conditions).

2.2. Cr/CrN multilayer thin films

Significant scientific interest was drawn during recent years on CrN-based thin films. The mechanical and structural properties of CrN are quite similar to the ones observed for TiN, which is a hardness of 18-29 GPa and that it crystallizes in the cubic B1 NaCl structure [71–74]. During annealing in vacuum, N diffuses out of the lattice and in a two-step process hexagonal Cr_2N and finally metallic Cr are formed at temperatures above $\sim$ 930°C and 1100°C, respectively [75]. However, the oxidation resistance of CrN is higher compared to TiN, which can be related to the formation of dense and passivating Cr_2O_3 instead of porous rutile [9, 65]. In contrast to TiN, the elastic modulus of CrN is highly anisotropic, ranging from $\sim$ 230 GPa along the $\langle 111 \rangle$ orientation to $\sim$ 230 GPa along the $\langle 100 \rangle$ orientation [70]. The compressive residual stress magnitude, the grain size, the texture and the thermal expansion coefficient of MSD CrN films can be varied in a broad range, depending on the applied deposition conditions [76, 77].

The formation of a $\langle 100 \rangle$ fibre texture and accompanying increase of stiffness can be triggered by the incorporation of ductile Cr interlayers and results in a pseudo-epitaxial relationship, which can be expressed as $\{100\}_{\mathrm{CrN}} \parallel \{100\}_{\mathrm{Cr}}$ [78]. Using this, a bilayer film, consisting of 1 µm CrN and 2 µm Cr on high-speed steel was designed, for which a wear rate reduced by an order of magnitude compared to a 3 µm thick CrN thin film was revealed, despite the fact, that the thickness of the wear resistant nanoceramic CrN layer was reduced accordingly [79]. Furthermore, alternating Cr and CrN have been proven (i) to prevent catastrophic failure of the film during indentation, by dissipating cracks at the Cr/CrN interfaces [80] and (ii) to simultaneously increase the stiffness, fracture stress and fracture toughness of Cr/CrN multilayer thin films tremendously [43, 44].

Clarifying the influence of interfaces separating sublayers of distinctly different properties (brittle/hard nanoceramic CrN and ductile/soft nanocrystalline Cr) on the scratch and fracture resistance of a hard protective thin film, and resolving the accompanying nanoscale microstructure and stress gradients were the main focus of Paper B and Paper C.

2.3. AlCrN

The replacement of Cr with Al in $\mathrm{Al}_x\mathrm{Cr}_{1-x}\mathrm{N}$ over a wide compositional range is generally beneficial, since it leads to the formation of a metastable solid solution with increased hardness, oxidation and wear resistance [81, 82]. However, when the solubility limit ($x \lesssim 0.7$) for Al in the cubic (c) B1 lattice is exceeded or when the metastable solid solution is heated above 800-900°C, wurtzite (w) B4 AlCrN is formed, which is generally detrimental to the mechanical properties and oxidation resistance [83–85]. Upon annealing in vacuum, the decomposition path of metastable c-AlCrN thin films is well-known [86–89] and can be expressed as follows

$$
\begin{gathered}
\mathrm{c{-}AlCrN} \xrightarrow{700-900°C} \mathrm{c-Cr(Al)N + w-Al(Cr)N} \\
\xrightarrow{900-1000°C} \mathrm{c-Cr(Al)N + w-Al(CrN)} \xrightarrow{1000-1200°\mathrm{C}} \mathrm{c-Cr(Al)N} \\
\mathrm{+w-Al(Cr)N + h-Cr_2N + N_2} \xrightarrow{1000-1200°\mathrm{C}} \mathrm{+w-Al(Cr)N + Cr + N_2}.
\end{gathered}
$$

However, these data were obtained from AlCrN powders by a combination of *in situ* differential scanning calorimetry and thermo-gravimetral analysis in vacuum, combined with *ex situ* microstructure and phase analysis by transmission electron microscopy and laboratory XRD [86–89], respectively. Therefore, they are inherently not able to explore the influence of microstructure and residual stress on the decomposition process, since residual stress is released and diffusion paths are shortened in powdered thin films. Exceptionally, powders of other thin film materials, such as

TiAlN [90], ZrAlN [91] and TiCrAlN [92], as well as thin lamellas of TiAlN [93] and TiZrAlN [94] have been investigated by means of *in situ* synchrotron XRD, to study several temperature-dependent phenomena, such as evolution of phases, lattice parameters and/or in-plane strains. However, these experiments were mainly focussed on the investigation of complex decomposition routes and the related lattice parameter changes. In total, the complex interplay between microstructure/residual strains originating from the deposition process and the temperature-dependent multi-stage decomposition process of transition metal nitrides is still unexplored, which was the main motivation behind Paper D.

2.4. AlTiN

$Al_xTi_{1-x}N$ was proposed as an alternative to TiN approximately 35 years ago [65]. The suggestion is that Ti is replaced in the cubic B1 NaCl lattice by Al, forming a metastable solid solution with a solubility limit of $x \lesssim 0.67$ [69] or $\lesssim 0.8$-0.9 [95] when synthesized using PVD or CVD, respectively. Generally, also for TiN, the replacement of Ti with Al leads to a pronounced increase of hardness, up to $\sim 35\,\text{GPa}$ [96], while exceeding the solubility limit promotes the formation of w-Al(Ti)N, which is detrimental to mechanical properties [97–101]. To increase the oxidation resistance, however, high Al contents are necessary and prevent the formation of porous and poorly adherent TiO_2, but again, formation of w-Al(Ti)N is also considered unfavourable [102, 103]. Furthermore, during annealing to temperatures above ~ 850-900°C, the metastable cubic solid solution decomposes via a spinodal decomposition into c-TiN and c-AlN, which leads to a nanoscale structuring and a further increase of hardness [96, 98] and also fracture toughness [104]. However, when annealing to even higher temperatures, w-Al(Ti)N is formed, which again leads to a deterioration of mechanical properties [96, 98, 104].

Here, the further attention was focussed on recent research progress concerning $Al_xTi_{1-x}N$ synthesized by low-pressure CVD [3, 105–107], which forms self-organized nanolamellar structures of different shapes and sizes depending on the Al-content. When synthesized with an Al-content of $x = 0.95$, the particular growth conditions resulted in randomly oriented cubes of the self-organized nanolamellar structure with a size of ~ 100 nm embedded in a c-TiAlN matrix [106], where the lamellae consisted of alternating incoherent 2 and 11 nm thick layers of w-Al(Ti)N and c-Ti(Al)N, respectively. The film formed with such a microstructure exhibited a moderate hardness of 27 GPa, but superior oxidation resistance up to 1100°C. By slightly reducing the Al-content to $x = 0.8$, a different film is grown, consisting of irregularly formed stacks of herringbone crystallites extending over the whole coating thickness without interruption of nanocrystalline matrix regions [3, 107]. The herringbone crystallites are composed of coherent lamellae consisting of 1.5 and 11 nm thick c-TiN and c-AlN layers, respectively, resulting in outstanding mechanical properties with a peak hardness of 37 GPa and slightly reduced oxidation resistance. These two unique microstructures, differing significantly in mechanical properties, can then be formed alternatingly, by a simple alternation of the precursor compositions in the CVD process [106, 107]. The multi-layered hierarchically structured thin film system produced thus opens up huge potential for the advancement of hard protective thin films, which was the main encouragement for the work carried out in Paper E.

3

Selected advanced characterization techniques

3.1. X-ray diffraction

X-ray diffraction is a versatile and capable tool for the structural characterization of materials and therefore widely used in materials science [108–112]. It can be used to identify individual crystal structures within the investigated volume and thus also (i) the *phase composition*, (ii) the phase-specific crystallite orientation distribution (so-called *texture*), (iii) the orientation-dependent shape and size of coherently diffracting domains, defect density and strains of 2^{nd} and 3^{rd} order, qualitatively assessed by the full width at half maximum ($FWHM$) of diffraction peaks and (iv) to perform a quantitative analysis of *residual strains* of 1^{st} order. Generally, XRD is limited to crystalline materials, which however includes most ceramic and metallic thin films.

Interference of coherent waves scattered by a periodic structure, *e.g.* a crystal, is called diffraction [108–112]. Independent of the X-ray source and measurement geometry, the basic principle for investigations using XRD is Bragg's law. Fig. 3.1 presents a geometric representation of Bragg's law, where the elastic scattering of two parallel waves of an X-ray beam on two parallel planes of a crystal lattice and subsequent constructive interference of the scattered waves at an angle 2θ with respect to the incident wave vector can be observed. Bragg's law is defined as follows

$$2\,d\,\sin\theta = n\lambda, \tag{3.1}$$

where d is the lattice parameter, θ is Bragg's angle, λ is the X-ray wavelength and n is an integer giving the order of the diffraction peak. Constructive interference of the two scattered waves, *i.e.* diffraction, is observed, when the phase shift between the waves is a multiple of the X-ray wavelength λ.

A set of observed peaks corresponding to a set of Bragg angles (and hence also

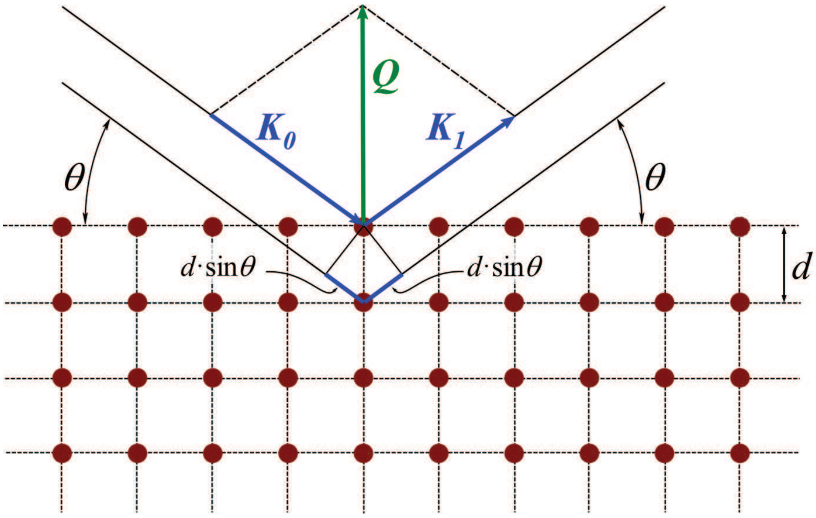

Figure 3.1.: Schematic representation of the Bragg condition for a primitive square lattice. The incident X-rays described by a wave vector K_0 are scattered by atoms, which results in a phase shift of $2\,d\,\sin\theta$ for waves scattered at adjacent planes. Maximal intensity is only observed, when the phase shift is a multiple of the wavelength λ, resulting in a diffracted wave with wave vector K_1. Reproduced from [111, 112].

lattice parameters) is usually distinct for every crystalline phase within *e.g.* a polycrystalline multi-phase material [108–112]. However, there are materials with similar crystal structures, which differ only slightly in their lattice constants, *e.g.* Fe and Cr [113] or Al_2O_3 and Cr_2O_3 [114].

Given that the material is (i) polycrystalline with individual crystallites oriented randomly and that (ii) the incident X-ray beam is monochromatic, the sequence of lattice planes results in a sequence of (powder) diffraction cones.

These diffraction cones are often assessed by a symmetric ($\theta - 2\theta$) scan using a laboratory XRD instrument, resulting in a plot of diffraction intensity I vs. diffraction angle 2θ. However, when employing this reflection geometry [111, 115], several restrictions are imposed by it. First and foremost, it is very challenging and usually not unambiguously possible, to deconvolute signal contributions from different penetration depths of the X-ray (dependent on the incidence and exit angles), which is an intrinsic problem of the reflection geometry. Second, the brilliance, a product of several parameters describing the radiation source, including photon flux density, monochromaticity and beam parallelity, of laboratory X-ray sources is limited. A high brilliance of the X-ray source is however necessary in order to (i) provide beam diameters below the micrometre-regime at a sufficient flux, since beam intensity and focussing are mutually exclusive parameters, due to low efficiency of X-ray optics

[1, 115–117] and to (ii) provide short exposure times for *in situ* experiments, for instance when high temperature (time) resolution is necessary, during annealing of thin films [118].

Hence, to perform XRD measurements with small X-ray beams, it is necessary to use synchrotron light sources producing X-ray beams with brilliances orders of magnitude higher compared to the ones available in the laboratory. Furthermore, with such high brilliance, it is also possible to employ transmission geometries for the measurements, which is a key feature for the technique of cross-sectional X-ray nanodiffraction presented hereafter.

3.1.1. Cross-sectional X-ray nanodiffraction

In order to assess nanoscale gradients in thin films originating from the deposition process or through externally applied loads, high resolution characterization tools are necessary. Since 2012, cross-sectional X-ray nanodiffraction (CSnanoXRD) has been developed and advanced, resulting in a minimum achievable size of the incident X-ray beam of even below 30 nm [1, 116]. In prior studies, CSnanoXRD has been proven to be successful at revealing gradients of phases, crystallite size and shape, texture and strains in thin films in as-deposited state [4, 117, 119], after annealing [120], after oxidation [121] or after *ex situ* indentation [80]. Furthermore, CSnanoXRD using a spatial resolution down to 200 nm coupled with an *in situ* indentation device has been developed and successfully utilized to probe the stress fields emanating from indentation of TiN and CrN thin film featuring sublayers of alternated deposition conditions resulting in monophasic/microstructural interfaces [57, 122]. Given the available literature, CSnanoXRD shows great potential in resolving the problems regarding above mentioned nanoscale gradients and give novel insights into the structure-property relationships of thin films. In the following section, the methodology of CSnanoXRD, which was used in Papers A, B, C and E, is briefly discussed.

3.1.1.1 Phase analysis

One of the basic tasks of the analysis of structure-property relationships in thin films is the characterization of phases present in the thin film. Since the set of diffraction angles is distinct for every phase, the phase analysis can be performed by a comparison of the experimentally assessed $I - 2\theta$ plot with a model diffractogram composed of diffraction lines from the Powder Diffraction Files (PDF) database from the International Centre for Diffraction Data (ICDD, formerly JCPDS) [123, 124].

The differences between the experimentally assessed and the modeled diffractogram give then important information about the microstructure and morphology of the thin films, which will be discussed later.

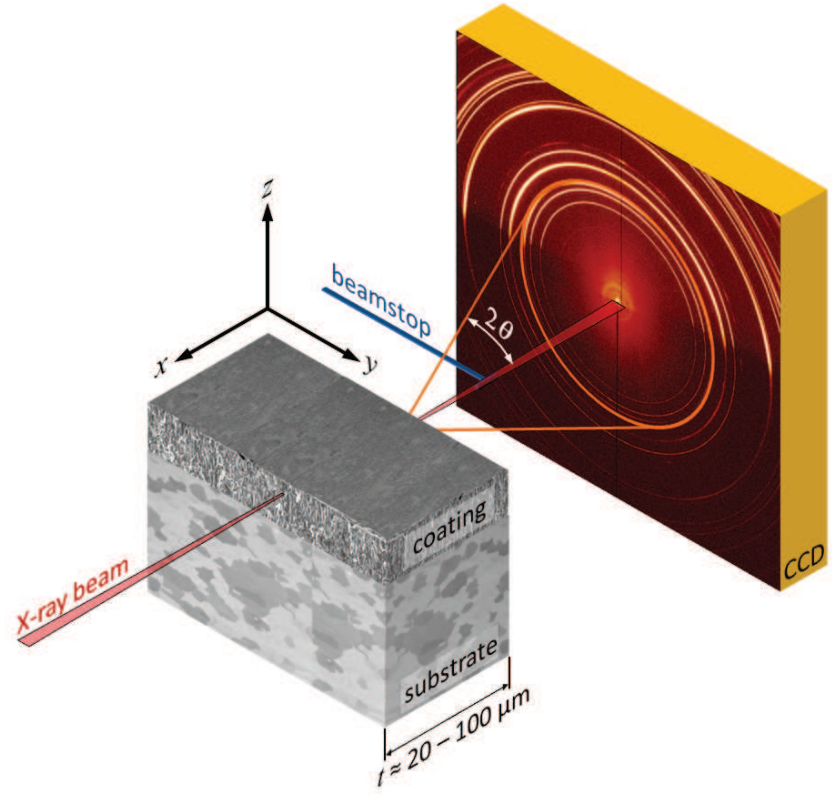

Figure 3.2.: Schematics of a typical CSnanoXRD experiment. A monochromatic X-ray beam, for instance focused using multi-layer Laue lenses [1, 125], with a diameter in the range 30-50 nm irradiates the sample, which is placed in the beam's focal spot (*i.e.* where the beam dimensions are minimal). The 2D detector, a charged coupled device (CCD), intersects the diffraction cones emanating from the sample resulting in a diffraction pattern composed of Debye-Scherrer rings. The sample is scanned perpendicular to the beam resulting in either one- (z-scan) or two-dimensional (y-z-scan) maps of diffraction patterns recorded and subsequently evaluated. (own unpublished work)

A typical CSnanoXRD experiment is performed either as one-dimensional (i.e. cross-sectional) scan along the z-axis or as a two-dimensional (2D) mesh scan by moving the sample along the y- and z-axis with a defined step size(s). The 2D detector intersects the diffraction cones (*cf.* Fig. 3.2), which results in a 2D diffraction pattern composed of Debye-Scherrer rings emanating from the individual phases within the thin film at every measurement point during the experiment. When a

4 µm thick thin film is investigated with a step size of 50 nm in a cross-sectional manner, 80 diffractograms are recorded. The collected data needs to be integrated azimuthally in order to perform phase analysis. Dedicated programs, which are widely used in the synchrotron X-ray community, are Fit2D [126] and PyFAI [127, 128].

A prerequisite for correct azimuthal integration is determination of the precise position and orientation of the 2D detector with respect to the beam and the sample. The (i) sample-to-detector distance, (ii) the beam centre on the detector, (iii) the rotational misalignment and (iv) the detector tilt are obtained by measuring a samples, which yields near-ideal and well-known diffraction patterns, a so-called calibration standard. Calibration standards are, for instance, Al_2O_3 or LaB_6 powders prepared by the National Institute for Standards and Technology (NIST). The software used for azimuthal integration provides procedures that extract these detector geometry parameters from such calibration measurements and subsequently accounts for them during further processing.

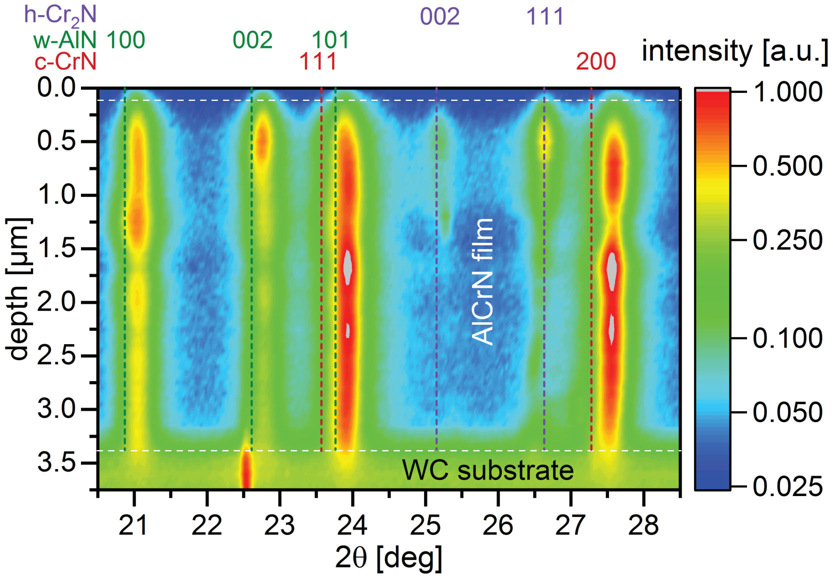

Figure 3.3.: Exemplary phase plot obtained from CSnanoXRD performed on an ∼ 3.2 µm thick AlCrN film deposited by CAE on a cemented carbide substrate and annealed in vacuum at 1000°C for 1 h. 2θ is the diffraction angle and the diffraction intensities are colour-coded. Peaks of specific phases are marked with Miller indices of the corresponding lattice plane families. (own unpublished work)

After azimuthal integration, $I - 2\theta$ datasets are obtained for every measurement point of the scan, are collated and finally plotted against the scanned coordinate, which results in phase plots, where the diffracted intensities are colour-coded (*cf.* Fig. 3.3). The individual diffraction peaks obtained at different scan positions can then be related to the phases present in the film at the respective film thickness. In the example given in Fig. 3.3, an AlCrN film annealed in vacuum at 1000°C for 1 h is presented, along with the tabulated reflections for c-CrN, w-AlN and hexagonal (h) Cr_2N from the PDF database [129]. During an annealing experiment at 1000°C, the metastable c-CrAlN phase decomposes into c-CrN, w-AlN and h-Cr_2N and N_2, which is reflected by the increasing intensity of w-AlN and h-Cr_2N peaks towards the film surface. Furthermore, it can be seen, that the w-AlN and c-CrN reflections are not exactly at their indexed positions, which indicates, that the wurtzite and cubic phases are not stoichiometric.

3.1.1.2 Small-angle X-ray scattering microscopy

Unlike diffraction, which originates from the lattice periodicity of a material, diffuse scattering at small diffraction angles ($\theta \sim 0.1$-$10\,\mathrm{deg}$, depending on the X-ray wavelength) is sensitive to significantly longer-range variations of electron density within the X-ray gauge volume, such as nanoscale alternation of phases, grain boundaries, interfaces, cracks, pores, etc. The observable nanoscopic structural heterogeneities are of the size of $\sim \lambda/\theta$ [130]. Especially in deformed sample regions or in nonuniform sample environments, changes of this small-angle signal are to be expected, as they are correlated with structural and mechanical gradients. A qualitative value is obtained for every point within a measurement area, by azimuthal (δ) and radial (θ) integration of the scattered intensity $I(\theta, \delta)$, as follows

$$I = \iint_{\delta=0^\circ,\theta_0}^{\delta=360^\circ,\theta_1} I(\theta, \delta) d\theta d\delta \tag{3.2}$$

The resulting integrated small-angle X-ray scattering (SAXS) intensity is then a measure for the amount of structural heterogeneities within the X-ray gauge volume. By scanning/mapping a sample region, SAXS microscopy (SAXSM) can thus be performed.

An exemplary scan and map are presented in Figs. 3.4 and 3.5, respectively. In Fig. 3.4, the integrated SAXS intensity obtained from the same AlCrN coating as in Fig. 3.3 is presented. The highest scattered intensity is found close to the coating-substrate interface, with a strong decay with increasing film thickness. This can be related to the small grain size and high interface density within the nucleation zone close to the substrate. In Fig. 3.5, the SAXS micrograph obtained from the cutting edge area of a TiN coating on a cemented carbide substrate is presented [131]. Here,

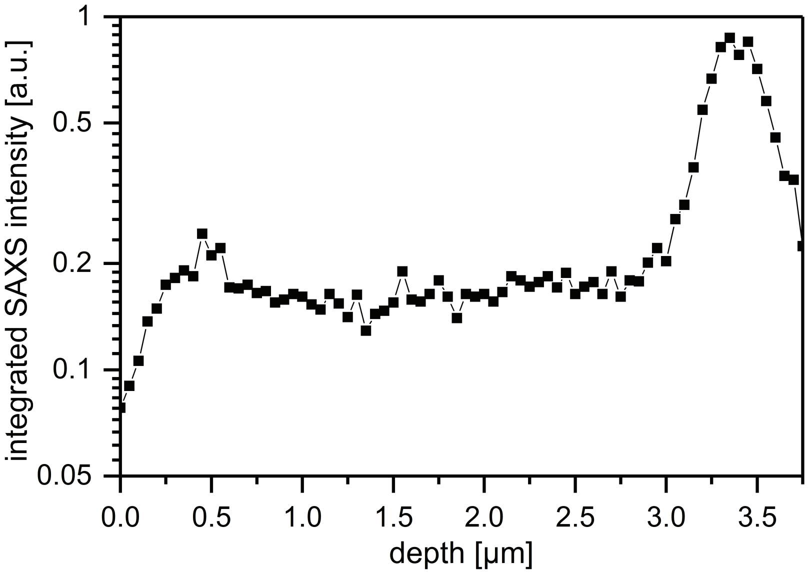

Figure 3.4.: Integrated SAXS signal obtained from the ∼ 3.2 µm thick AlCrN film presented in Fig. 3.3. A local rise of scattered intensity can be seen at depths of 0.5 and 3.3 µm corresponding approximately to the surface and the substrate coating interface, respectively. A minimum of scattered signal was found at a depth of ∼ 1.25 µm. The increase in scattered intensity can be correlated to the higher diffracted intensity of Cr_2N, which corresponds to a higher interface density (smaller crystallites). (own unpublished work)

a gradually increasing SAXS intensity towards the rake face can be correlated to the promoted formation of pores at the rake face and the lines of increased intensity directly at the edge are related to planar domains in the coating, separated by interface-like under-dense structures [131]. Especially in the latter case, SAXSM has been proven to be useful to obtain data about the coating's microstructure, which are furthermore directly correlated to gradients of texture and residual stress [131].

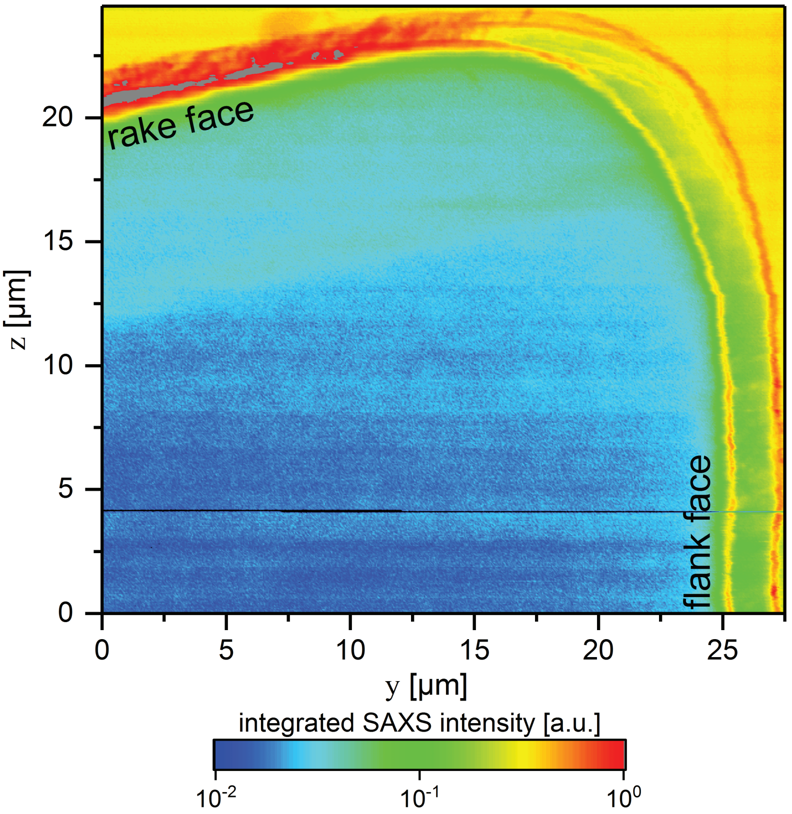

Figure 3.5.: Integrated SAXS signal obtained from a TiN hard coating deposited onto cemented carbide cutting edge. The substrate-coating interface and the surface can be clearly detected due to their comparatively higher scattering intensity. Additionally, a gradual intensity increase from the flank to the rake face was detected, corresponding to an increase of structural defects along the rake face. Furthermore, the lines of increased scattered intensity, visible within the edge region, could be related to planar domains within the coating, separated by an interface like morphological feature. Reproduced from [131].

3.1.1.3 Texture analysis

Only in rare cases, the distribution of the crystallite orientations in a polycrystalline thin film is random. Texture of materials can span over the whole range of ordering, from solids where crystallites have nearly the same alignment (high mosaicity, sharp texture) to materials where it is nearly impossible to distinguish the diffraction pattern of the solid from that of a powder [111, 112].

Furthermore, many important mechanical and functional properties of materials are also anisotropic, *i.e.* dependent on crystal orientation. A sound example is the anisotropic Young's modulus of CrN, which varies between ~ 230 and 450 GPa, when considering the ⟨111⟩ or ⟨100⟩ orientations [70], respectively.

In laboratory XRD, crystallographic texture is investigated by considering the variation of diffraction intensities with respect to the orientation of the investigated sample. During the measurement, the diffraction angle 2θ of a certain reflection is fixed, while the sample is rotated around two axes [108, 109, 111, 112]. The recorded intensity distribution of the investigated reflection is then proportional to the orientation frequency of the chosen lattice plane family with respect to the sample coordinate system. The common representation for this orientation distribution is the pole figure, which is a stereographic projection of the lattice plane normal vectors onto a plane. The orientation-dependent diffraction intensities are then plotted in a colour-coded fashion.

It can be seen in Fig. 3.6 that during a CSnanoXRD experiment performed in transmission geometry the orientation information contained in a Debye-Scherrer ring is rather limited. The intensity distribution along the ring represents a cut

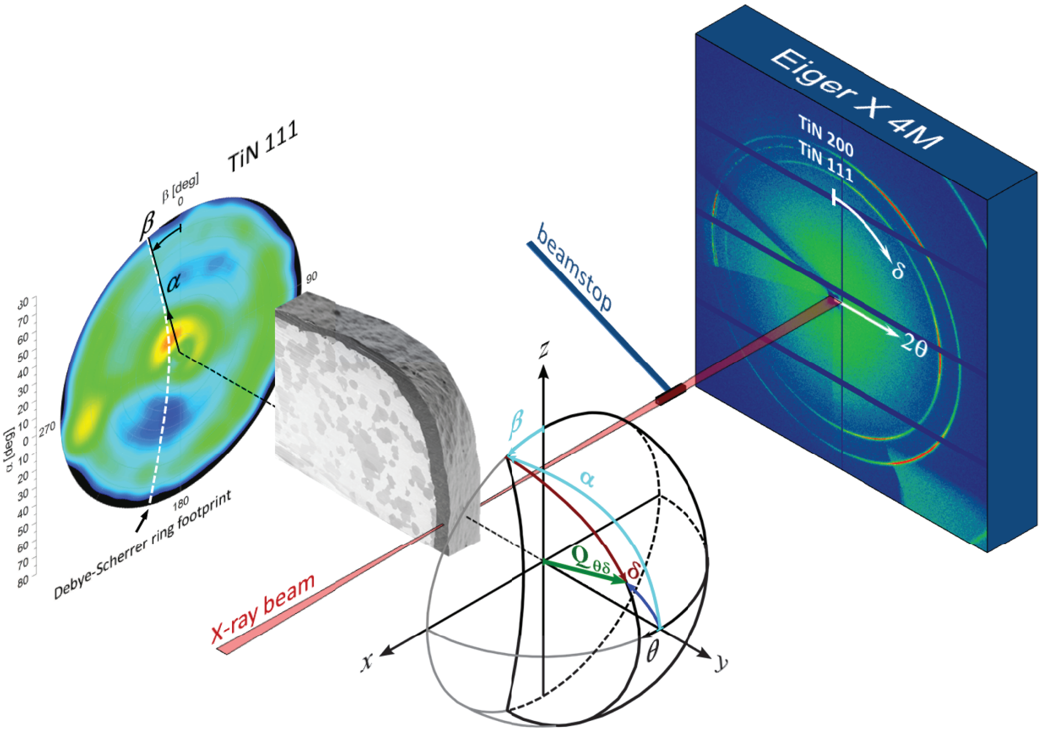

Figure 3.6.: Schematic representation of the orientation relationship between the out-of-plane centred pole figure and the diffraction intensity distribution $I(\theta, \delta)$ recored along a Debye-Scherrer ring on a 2D detector in transmission geometry. Pole figure and detector image are taken from an experiment performed on a TiN coating deposited on a cemented carbide cutting edge reproduced form [131].

through the corresponding pole figure (*cf.* Fig. 3.6). Without further assumptions, the texture of a thin film material thus cannot be evaluated unambiguously.

However, with regards to thin films, two types of texture are dominant, the so-called biaxial texture and the fibre texture, where the latter is observed in most hard protective thin films. When a thin film develops a fibre texture, all crystallites have a fixed orientation in the direction of the fibre axis and one remaining orientational degree of freedom, allowing for a rotation around the fibre axis. In nearly all cases of thin films studied, the fibre axis is parallel to the surface normal, except, when the deposition flux is strongly inclined, as in glancing-angle deposition (*cf.* [2, 48, 49]).

Since most thin films develop the above-mentioned fibre texture during growth, the pole figure can be reconstructed for the thin film material of interest, supposing rotational symmetry around the out-of-plane sample axis. The reconstruction is performed by considering the geometrical relationship between the coordinates of a point on the 2D detector and the coordinates of the same point on the corresponding out-of-plane pole figure (*cf.* Fig. 3.6). This geometrical relationship is expressed as follows

$$\sin\alpha = \sin\delta\cos\theta \tag{3.3}$$

and

$$\begin{aligned}\cos\beta = &+\sqrt{\frac{\cos^2\delta\cos^2\theta}{1-\sin^2\delta\cos^2\theta}} \mid -90^\circ < \delta < 90^\circ, \\ &-\sqrt{\frac{\cos^2\delta\cos^2\theta}{1-\sin^2\delta\cos^2\theta}} \mid 90^\circ < \delta < 270^\circ,\end{aligned} \tag{3.4}$$

where δ and 2θ are the azimuthal and radial (diffraction) angle on the 2D detector, respectively, while α and β represent the radial and azimuthal coordinates of the pole figure, respectively (*cf.* Fig. 3.6) [132]. An example for an out-of-plane pole figure and the corresponding reconstruction from a synchrotron detector image of a TiN film deposited on a WC-Co cutting edge can be seen in Fig. 3.7a and 3.7b, respectively.

Having confirmed the fibre nature of the thin films texture, the preferred orientation of the thin film along the cutting edge can be evaluated by simply considering the orientation δ_p^{111} of the maximum intensity of the Debye-Scherrer ring for every dataset obtained during the experiment (*cf.* Fig. 3.8).

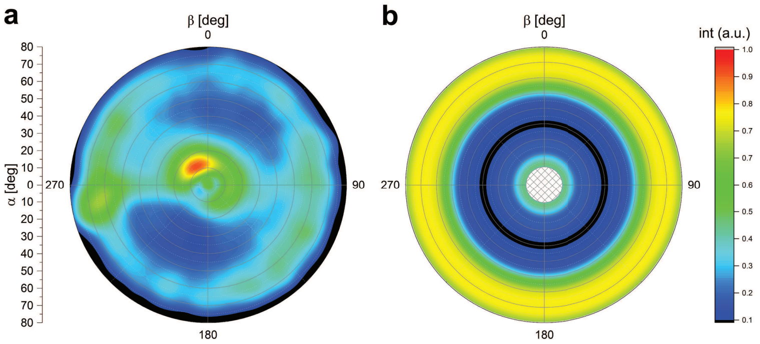

Figure 3.7.: Pole figures evaluated from the 111 reflection of a TiN thin film. A pole figure obtained by a laboratory measurement (a) and a pole figure reconstructed from 2D data obtained during the corresponding synchrotron measurement in transmission geometry (b) are presented. Reproduced from [131].

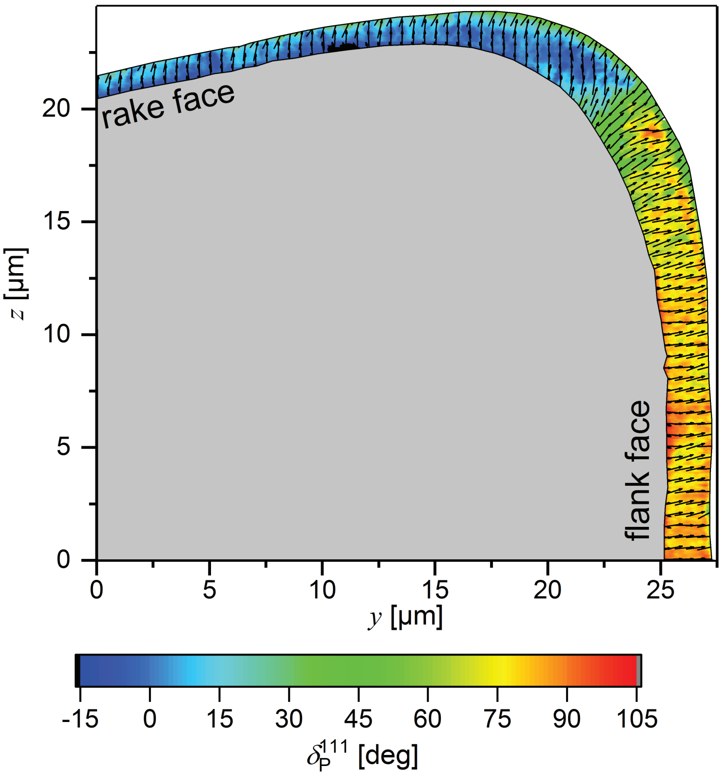

Figure 3.8.: 2D contour plot of the orientation $\delta_{\mathrm{p}}^{111}$ of the $\langle 111\rangle$ fibre texture. Reproduced from [131].

3.1.1.4 FWHM analysis

When an ideally parallel and monochromatic X-ray beam interacts with a single coherently diffracting domain of a hypothetical ideal material having infinite dimension, which is furthermore free of any kind of lattice defects, a perfectly sharp diffraction peak with negligible width would emerge. Any kind of deviation from these idealisations will lead to an increase of the peak width. The measure to describe the peak width is the full width at half maximum (FWHM) β. Contributions to the FWHM are the size of coherently diffracting domains, gradients of strains of $1^{\mathbf{st}}$ order (macrostrains) and strains of $2^{\mathbf{nd}}$ and $3^{\mathbf{rd}}$ order, which are, in general, lattice defects, such as dislocations and lattice distortions.

In order to quantify the FWHM of Debye-Scherrer rings, it is necessary to fit the diffraction peaks to analytical functions. Therefore, the 2D diffraction patterns collected during the CSnanoXRD experiment are integrated azimuthally, similar to the procedure described for phase analysis (*cf.* Sec. 3.1.1.1). However, the main difference is that the integration is performed in n circular sections of a predefined azimuthal width $w = \frac{360}{n}$ deg, so-called cakes. The result is a set of $I(2\theta, \delta_i)$ profiles, where $\delta_i = iw$ is the azimuthal orientation of the centre of the i-th cake and which can be used for orientation-dependent peak fitting.

Typical functions which are used for peak fitting are the Lorentzian or Gaussian functions. Generally, the use of the pseudo-Voigt function, which is a linear combination of the former two, is beneficial. The pseudo-Voigt function, modified to diffraction-related quantities, reads as follows, for every azimuthal section,

$$I(2\theta, \delta_i) = \mu \frac{I_0}{1 + \left(\frac{2\theta - 2\theta_0(\delta_i)}{\frac{1}{2}\beta(\delta_i)} \right)^2} + (1-\mu) I_0 e^{\left[-\ln 2 \left(\frac{2\theta - 2\theta_0(\delta_i)}{\frac{1}{2}\beta(\delta_i)} \right)^2 \right]}, \tag{3.5}$$

where $I(2\theta, \delta_i)$ is the observed diffraction angle-dependent intensity at the azimuthal orientation δ_i, $2\theta_0(\delta_i)$ is the peak's centre position, I_0 is the maximum intensity of the peak at $2\theta_0$, $\beta(\delta_i)$ is the orientation dependent FWHM of the peak and μ is the ratio of the Lorentzian over Gaussian distributions contributing to the peak function.

The Scherrer equation [108, 109, 111, 112] describes the inverse relationship between the width of a diffraction peak (or the corresponding Debye-Scherrer ring) and the average size of coherently diffracting domains, which is roughly similar to the grain size of a polycrystalline material. The Scherrer equation is expressed as follows,

$$D = \frac{K\lambda}{\beta \cos\theta}, \tag{3.6}$$

wwhere D is the size of coherently diffracting domains, λ is the X-ray wavelength, β is the FWHM, and θ is the diffraction angle. The parameter K is a dimensionless factor, which takes into account different grain shapes. Values of K are close to unity and differ only slightly between equiaxed and elongated grains. However, since there are also other contributions to the FWHM (see above), no absolute values regarding the size of coherently diffracting domains can be obtained from the diffraction data using only the Scherrer equation. However, it is still possible to get useful information about the material's defect density and microstructure. First, the shape of the thin film's grains can be resolved by evaluating the orientation-dependent FWHM of the Debye-Scherrer rings, which is approximately inversely proportional to the orientation-dependent size of coherently diffracting domains. Therefore, an increase of FWHM from out-of-plane ($\delta = 0\,\mathrm{deg}$) to in-plane ($\delta = 90\,\mathrm{deg}$) orientation (*cf.* Fig. 3.2) corresponds to a reduction of the size of coherently diffracting domains in the same orientation change and would indicate a columnar-grained microstructure (*cf.* Ref. [116, 133]).

In order to perform a comprehensive analysis of nanoscale microstructural changes, the analysis should not only rely on the peak width, but be performed together with SAXSM and electron microscopy in order to strengthen the interpretation of the data. An example for the benefits of combining electron microscopy and CSnanoXRD data for microstructural analysis is presented in Figs. B.2, B.3, B.4, B.5, B.6 and B.7 of Paper B.

3.1.1.5 Stress analysis

Mechanical stresses in thin films are either introduced by the deposition process, as a result from ion bombardment and as a consequence of the mismatch of thermal expansion coefficients during cooling from the deposition temperature to room temperature, or by external loading. In most cases, the stresses are measured after their introduction in the material and therefore represent residual stresses.

XRD can be employed to quantify strains and stresses of $1^{\mathbf{st}}$ order present in a crystalline material. Strains of $1^{\mathbf{st}}$ order span over many grains and therefore represent macro-strains. The strain measurement is performed by the investigation of the elastic shrinkage and expansion of the crystallites, which leads to changes of their lattice plane spacings. Since the strains quantified by XRD are of elastic nature, they can be converted directly to stresses, if the elastic properties of the material are known [111, 112, 134]. For an isotropic material, the relationship between stress σ_{ij} and strain ε_{ij} is defined as follows

$$\varepsilon_{ij} = \frac{1+\upsilon}{E}\sigma_{ij} - \delta_{ij}\frac{\upsilon}{E}\sum_{k=1}^{3}\sigma_{kk}, \tag{3.7}$$

where ν is the Poisson's ratio, E is the Young's modulus and δ_{ij} is the Kronecker's delta. Since most materials have anisotropic elastic properties, the strain measured during an X-ray experiment is also dependent on the lattice plane family *hkl* from which it was evaluated and the factors $\frac{1+\upsilon}{E}$ and $-\frac{\upsilon}{E}$ are replaced by the *hkl*-dependent X-ray elastic constants (XEC) $\frac{1}{2}S_2^{hkl}$ and S_1^{hkl}, respectively. These XECs are determined from the single-crystalline stiffness tensor by employing grain interaction models. Basic grain interaction models are the Voigt and the Reuss model, as well as the Hill model, which is a linear combination of the former two [111, 112, 134]. The relationship between stress σ_{ij} and *hkl*-dependent strain ε_{ij}^{hkl} is then defined as follows

$$\varepsilon_{ij}^{hkl} = \frac{1}{2}S_2^{hkl}\sigma_{ij} + \delta_{ij}S_1^{hkl}\sum_{k=1}^{3}\sigma_{kk}. \tag{3.8}$$

Generally, the strain $\varepsilon'(\xi,\varsigma)$ in an XRD experiment is determined along two rotational coordinates ξ and ς as follows

$$\varepsilon'(\xi,\varsigma) = \frac{d(\xi,\varsigma) - d_0}{d_0}, \tag{3.9}$$

where $d(\xi,\varsigma)$ is the orientation-dependent lattice parameter and d_0 is the strain-free lattice parameter of the material of interest. The knowledge of d_0 is a prerequisite for the stress analysis by means of XRD. In a synchrotron CSnanoXRD experiment, the coordinates used for the determination of the orientation dependent lattice strain are the diffraction angle θ and the azimuthal angle of the Debye-Scherrer ring δ. The orientation-dependent lattice strain $\varepsilon_{\delta\theta}^{m,hkl}(y,z)$ at every position (y,z) in the investigated sample for each phase m and DS ring *hkl* can be determined as follows

$$\varepsilon_{\delta\theta}^{m,hkl}(y,z) = \frac{d_{\delta\theta}^{m,hkl}(y,z) - d_0^{m,hkl}}{d_0^{m,hkl}}, \tag{3.10}$$

where $d_{\delta\theta}^{m,hkl}(y,z)$ is the measured lattice spacing and $d_0^{m,hkl}$ is the strain-free lattice spacing for a particular *hkl* reflection.

In the coordinate system of the CSnanoXRD experiment (*cf.* Fig. 3.2), the orientation-dependent lattice strain $\varepsilon_{\delta\theta}^{m,hkl}(y,z)$ measured in the direction of the diffraction vector is a function of triaxial strain components $\varepsilon_{ij}^{m,hkl}(y,z)$ defined by the *fundamental equation of X-ray strain determination* [80, 134] as follows:

$$
\begin{aligned}
\varepsilon_{\delta\theta}^{m,hkl}(y,z) = \sin^2\theta\varepsilon_{11}^{m,hkl}(y,z) + \cos^2\theta\sin^2\delta\varepsilon_{22}^{m,hkl}(y,z) + \cos^2\theta\cos^2\delta\varepsilon_{33}^{m,hkl}(y,z) \\
- \sin 2\theta\cos\delta\varepsilon_{13}^{m,hkl}(y,z) + \cos^2\theta\sin 2\delta\varepsilon_{23}^{m,hkl}(y,z) - \sin 2\theta\sin\delta\varepsilon_{12}^{m,hkl},
\end{aligned}
\tag{3.11}
$$

where *i, j* = 1, 2 and 3 correspond to the experimental axes x, y and z in Fig. 3.2, respectively.

The components of the stress tensor $\sigma_{ij}^{m}(y,z)$ can be determined by substituting $\varepsilon_{ij}^{m,hkl}(y,z)$ using Eq. 3.5 and are defined in the sample coordinate system as follows

$$
\begin{aligned}
\varepsilon_{\delta\theta}^{m,hkl}(y,z) = S_1^{m,hkl}\left[\sigma_{11}^{m}(y,z) + \sigma_{22}^{m}(y,z) + \sigma_{33}^{m}(y,z)\right] \\
+\tfrac{1}{2}S_2^{m,hkl}\Big[\sin^2\theta\sigma_{11}^{m,hkl}(y,z) + \cos^2\theta\sin^2\delta\sigma_{22}^{m,hkl}(y,z) + \cos^2\theta\cos^2\delta\sigma_{33}^{m,hkl}(y,z) \\
- \sin 2\theta\cos\delta\sigma_{13}^{m,hkl}(y,z) + \cos^2\theta\sin 2\delta\sigma_{23}^{m,hkl}(y,z) - \sin 2\theta\sin\delta\sigma_{12}^{m,hkl}\,\Big].
\end{aligned}
\tag{3.12}
$$

During stress analysis of thin films, it is often sufficient to characterize the equibiaxial stress state originating from the deposition process, where the shear components $\sigma_{ij}^{m}(y,z)$ with $i \neq j$ and the out-of-plane normal stress component $\sigma_{33}^{m}(y,z)$ along the z-axis are considered to be zero and the non-zero in-plane normal stress components $\sigma_{11}^{m}(y,z) = \sigma_{22}^{m}(y,z)$ are equal [111, 134]. The simplified equation for the evaluation of the residual stress can then be expressed as follows

$$
\varepsilon_{\delta\theta}^{m,hkl}(y,z) = \sigma_{22}^{m}(y,z)\,2S_1^{m,hkl} + \sigma_{22}^{m,hkl}(y,z)\,\frac{1}{2}S_2^{m,hkl}\left[\sin^2\theta + \cos^2\theta\sin^2\delta\right]. \tag{3.13}
$$

In this way, in-plane residual stress gradients $\sigma_{22}^{m}(y,z)$ within all crystalline phases present in the investigated sample volume can be determined.

In order to evaluate the stress, the peaks have to be fitted along azimuthal sections, similar to the analysis of the FWHM above, which allows to retrieve the lattice spacing $d_{\delta\theta}^{m,hkl}(y,z)$ from the fitted peak positions in every azimuthal section. The stress is then evaluated by a two-step process: first, the orientation-dependent lattice strain is $\varepsilon_{\delta\theta}^{m,hkl}(y,z)$ calculated according to Eq. 3.10. Second, a linear regression of the lattice spacing $\varepsilon_{ij}^{m,hkl}(y,z)$ evaluated at different azimuthal positions δ (*cf.* Eq. 3.10) versus $\sin^2\delta$ is performed to obtain in-plane stress values from Eq. 3.13. This procedure is performed for every diffraction pattern measured during the CSnanoXRD experiment.

In Fig. 3.9, the stresses evaluated from the c-Cr(Al)N, w-Al(Cr)N and h-(Cr, Al)$_2$N phases in a multi-phase AlCrN hard protective thin film are shown. The applied X-ray elastic constants are similar to those used for the evaluation of stresses in Paper D.

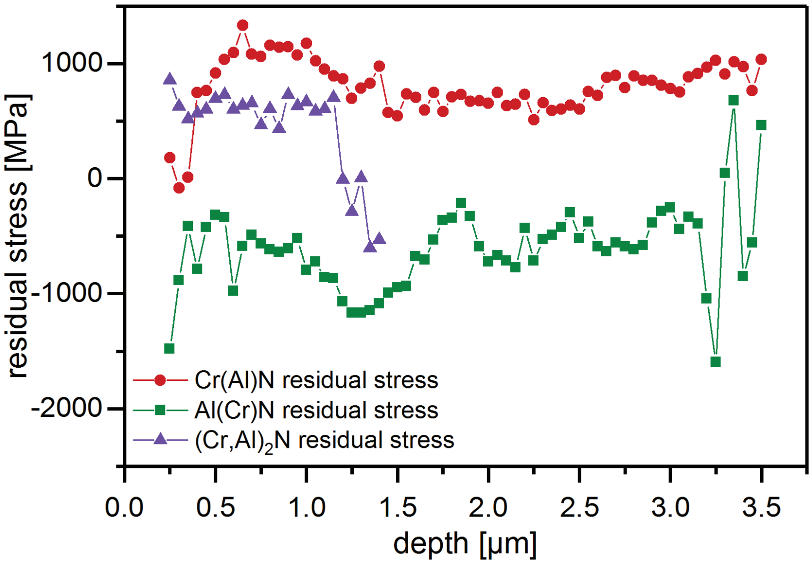

Figure 3.9.: In-plane stresses evaluated for an exemplary ~ 3.2 µm AlCrN thin film annealed at 1000°C, whose phase diagram is presented in Fig. 3.3. (own unpublished work)

In order to evaluate the stress distributions $\sigma_{ij}^{m}(y,z)$ within deformed areas, the generally expected three-axial stress state in the material has to be taken into account. Therefore, Eq. 3.12 is the appropriate choice to evaluate stress distributions within the investigated sample volume. However, it is still possible to use simplifications during the evaluation.

First, it is generally beneficial to retrieve stresses also from an undeformed sample area according to Eq. 3.13. Since coefficients of the in-plane stress component $\sigma_{11}^{m}(y,z)$ along the x-axis in Eq. 3.12 are independent of the azimuthal angle δ, the presence of this stress component leads to a shift of the diffraction angle 2θ of the respective Debye-Scherrer ring, similar to a change of the unstrained lattice parameter $d_0^{m,hkl}$. Therefore, it is necessary, to set a boundary condition for $\sigma_{11}^{m}(y,z)$, for example, the assumption that the in-plane stress component $\sigma_{11}^{m}(y,z)$ along the x-axis does not change significantly during the experiment, or that $\sigma_{11}^{m}(y,z)$ can be approximated by the $\sigma_{22}^{m}(z)$ evaluated using Eq. 3.13 from an undeformed sample region. Especially, when considering only Debye-Scherrer rings with low diffraction angles 2θ, the coefficient $\left(S_1^{m,hkl} + \frac{1}{2}S_2^{m,hkl}\sin^2\theta\right)$ becomes very small (*cf.* Eq. 3.12) and small variations of $d_0^{m,hkl}$ in the investigated volume would compromise the evaluation and lead to unrealistic $\sigma_{11}^m(y,z)$ values.

Additionally, the shear stress components $\sigma_{12}^m(y,z)$ and $\sigma_{13}^m(y,z)$ would lead to a distortion of the Debye-Scherrer ring similar to a miscalculated beam centre. However, even when no shear stresses along the beam direction are expected, it is beneficial to evaluate $\sigma_{12}^m(y,z)$ and $\sigma_{13}^m(y,z)$. When there are rather constant $\sigma_{12}^m(y,z)$ and $\sigma_{13}^m(y,z)$ values extracted from the investigated sample volume, this is an indication for a miscalculated beam centre and leads to an better refinement of the stress components $\sigma_{22}^m(y,z)$, $\sigma_{33}^m(y,z)$ and $\sigma_{23}^m(y,z)$ perpendicular to the incident X-ray beam [132, 135–137]. For further details regarding to how the individual stress components influence the Debye-Scherrer ring's shape evaluated on the detector, the readers are referred to Ref. [132].

For every sample measurement point, a system of n linear equations based on Eq. 3.13 has to be solved for the unknown stress components numerically, *e.g.* by least-squares refinement and with the assumptions valid for the actual stress tensor in the investigated thin film volume. This method to analyse stresses from XRD patterns obtained during a CSnanoXRD experiment was utilized in Papers A, B, and C.

3.1.2. *In situ* high-energy high-temperature grazing incidence transmission X-ray diffraction

In order to investigate the thermal stability of metastable thin films, a new diffraction-based multi-parameter method called *in situ high-temperature high-energy grazing incidence transmission X-ray diffraction* (HT-HE-GIT-XRD) was developed and carried out at the P07B beamline of the PETRA III synchrotron source in Hamburg (Germany). Experimental results obtained from arc-evaporated AlCrN thin films and the methodology itself have been published in Paper D, while experimental results obtained from CVD TiAlN thin films have been published in Paper E. While the methodology of data evaluation is given in full detail in Paper D, a more detailed description of the experimental setup and parameters is given hereafter, which was omitted in the article, for the sake of brevity.

In order to carry out the *in situ* experiments, a type S thermocouple (temperature resolution $\lesssim$ 0.5°C) was welded centrally onto the sample's surface, opposite of the coated surface of interest. The coated sample was then mounted in a DIL 805 dilatometer (TA Instruments) equipped with two X-ray-transparent Kapton$^{\mathrm{TM}}$

windows to ensure transmission of the X-ray beam. The surface of the sample is aligned with respect to the primary beam at an incidence angle β, as shown in Fig. 3.10. The incidence angle has to be set to achieve maximum intensity of the film signal, while still keeping the substrate signal as low as possible, which is dependent on the actual sample geometry and needs individual adjustment for each sample.

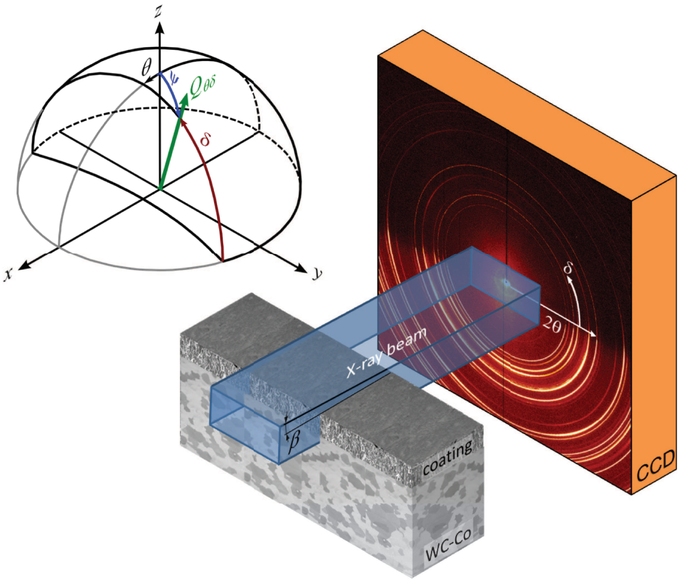

Figure 3.10.: A schematic of the *in situ* HE-HT-GIT XRD experimental setup. Reproduced from [118].

Heating and cooling rates, as well as holding times can be adjusted individually using the dilatometer software. In Paper D, a constant heating rate of 1 K/s from RT to 1100°C was followed by holding for 300 s at 1100°C. Subsequent cooling at a rate of −1 K/s was achieved through constant Ar flow of $0.005\,\mathrm{m}^3/s$. However, technically the dilatometer can be heated to temperatures up to 1400°C and much higher heating and cooling rates can be reached by adjusting the heating power and the Ar flow, respectively. During the temperature cycle, the sample was illuminated with a pencil X-ray beam of $y \times z = 100 \times 400\,\mu\mathrm{m}^2$ at an energy of 87.1 keV and diffraction patterns were recorded continuously using a Perkin-Elmer detector with a pixel size of $200 \times 200\,\mu\mathrm{m}^2$, using an exposure time of 1 s, each followed by a dark image of also 1 s exposure time for image correction purposes. Depending on the incidence angle β and the sample geometry, 10-25 exposures were summed up into one 2D diffraction pattern to increase diffraction statistics, which results in a temperature resolution of 20-50°C.

Prior to the diffraction experiments, detector calibration has to be carried out using a NIST LaB_6 powder to evaluate the sample-to-detector distance, detector tilt and rotation of the tilt plane, similar as described in Sec. 3.1.1.1. While in this experiment detector calibration was evaluated using the FIT2D software package [126], evaluation of the 2D diffraction patterns recorded in the *in situ* experiment was carried out using the PyFAI software package [127, 128].

3.2. Micromechanical testing

In order to obtain information about structure-property relationship of thin films, advanced mechanical testing taking into account the reduced thickness dimension of the film is necessary. Besides nanoindentation [138], which represents a common technique for obtaining local mechanical properties of thin films, in detail hardness and reduced modulus, micromechanical cantilever bending tests [2, 42–47, 119, 121] have been established as state-of-the-art in terms of mechanical testing of thin films.

3.2.1. Nanoindentation

Nanoindentation is nowadays extensively used to obtain basic mechanical properties of thin films, in detail hardness and indentation modulus, which are easily obtained without high sample preparation effort. During nanoindentation, the indentation load and indenter displacement are recorded continuously, which makes it an instrumented technique, in contrast to most other indentation techniques, which calculate hardness from the applied load and the cross-section of the remaining imprint, *cf.* for example [139]. The resulting load-displacement curves are evaluated by the methodology developed by Oliver and Pharr [138], which allows to obtain hardness H and indentation modulus E_r.

The hardness is defined as maximum contact pressure supported by the tested material, which is calculated dividing the maximum applied indentation load $P_{\max}$ and the projected contact area A_c (*cf.* Fig. 3.11),

$$H = \frac{P_{\max}}{A_c}. \tag{3.14}$$

Since the applied indenter loads are usually in the range of milli-Newtons, the resulting penetration depths of the indenter range from several tens of nanometers to $\sim 1\,\mu\text{m}$, depending on the hardness of the tested material. It is therefore convenient to calculate the contact area by a so-called area function, which depends on the contact depth h_c and the shape of the indenter tip. The area function was determined

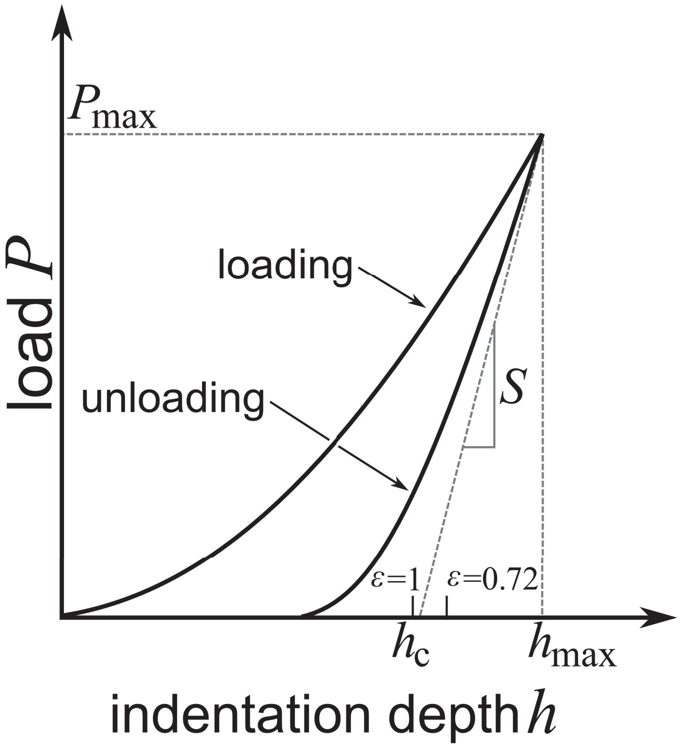

Figure 3.11.: A schematic sketch of the load-indentation depth curve recorded during a nanoindentation experiment. P_{max} is the maximum applied load, h_{max} the maximum indentation depth, S is the contact stiffness and h_c is the contact depth, depending on the tip geometry parameter ε. Reproduced from [138].

analytically by Sneddon [140] for flat punches, spherical, conical and pyramidal tips as a power law function as follows

$$A_c = \alpha\, h_c^m \tag{3.15}$$

where α is a dimensionless parameter and m is the exponent depending on the actual shape of the tip. The power law exponent m was determined by Sneddon as 1, 1.5 and 2 for the flat punch, spherical and conical or pyramidal indenter shapes, respectively. However, since real indenter tips always deviate from the ideal shape, it is convenient to approximate the area function in a polynomial form

$$A_c = A(h_c) = \sum_{n=0}^{8} C_n h_c^{2\left(\frac{1}{2}\right)^n}, \tag{3.16}$$

where C_n are fitted constants. The contact depth itself is calculated from the load-displacement curve (*cf.* Fig. 3.11) using the initial slope, *i.e.* the contact stiffness

S of the unloading curve (at $P_{\max}$) and the maximum penetration depth $h_{\max}$ as follows ,

$$h_c = h_{max} - \varepsilon \frac{P_{\max}}{S}, \tag{3.17}$$

where ε is a parameter ranging between 0.72 and 1 depending on the shape of the indenter tip. $\varepsilon = 0.72$ was analytically derived for conical and pyramidal tips, while $\varepsilon = 1$ corresponds to a flat punch. But, similar to the contact area, the real tip shape deviates from model shapes and it is convenient to use a value of 0.75, which corresponds to a paraboloid of revolution. The contact stiffness S is extracted from the unloading curve of the indentation experiment by fitting a power law function to the former and then calculating analytically the first derivative of the fitted function and evaluating it at $P_{\max}$.

Finally, the compliance of the indentation device C_{f} has to be determined, since it can have a significant influence on the measured penetration depth. The calibration of C_{f} is performed together with the area function by various procedures. Oliver and Pharr assumed, that the elastic modulus of the tested material is independent of the indentation depth. Thus, by varying the indentation depth, C_{f} can be calculated by using the area function of an ideally shaped tip as a starting point. Following, the approximated function given in Eq. 3.16 and C_{f} are refined iteratively until C_{n} and C_{f} converge. Nowadays, the machine calibration is performed by a series of indents in a material with well-known hardness and elastic modulus. The material of choice is fused silica, since it has a high hardness and a well-known elastic modulus, is isotropic and shows no recognizable size effect or creep [141, 142].

Following, the reduced modulus E_r of the whole system can then be determined as

$$E_r = \frac{\sqrt{\pi}}{2} \frac{S}{\sqrt{A_c}}, \tag{3.18}$$

and

$$\frac{1}{E_r} = \frac{1 - \nu_f^2}{E_f} + \frac{1 - \nu_i^2}{E_i}, \tag{3.19}$$

where ν_f and E_f are the Poisson's ratio and Young's modulus of the film, respectively and ν_i and E_i are the Poisson's ratio and Young's modulus of the indenter tip, respectively. However, for the exact evaluation of E_f, the Poisson's ratio of the film has to be known, otherwise, the indentation modulus can only be quantified approximately. The standard indenter material is diamond, which has elastic properties of $E_i = 1141\,\mathrm{GPa}$ and $\nu_i = 0.07$ [143].

Practically, the Berkovich indenter tip, which is a three-sided pyramid with a shape function similar to the Vickers indenter, is often used for nanoindentation, since in such way, the results are comparable to macrohardness tests [144]. Additionally, a maximum indentation depth of $\frac{1}{10}$ of the film's thickness and a lateral distance of 4-5 times the indent's width have been established as guidelines for testing thin films. Finally, the analysis of nanoindentation data is routinely performed by incorporated software package of commercially available nanoindenters.

Due to its easy feasibility, nanoindentation is the starting point of mechanical characterisation of thin films giving the first insight into mechanical properties of thin films of interest. Miniaturised nanoindenters fitting in a scanning or transmission electron microscope are nowadays commercially available and regularly used for *in situ* micromechanical testing of thin films, as discussed hereafter.

3.2.2. *In situ* micromechanical cantilever bending experiments

In following, the preparation by focused ion beam milling and *in situ* testing of micro-sized cantilever specimens in the SEM is depicted. This methodology was used in Paper E. Cantilever bending tests can be performed *ex situ* using a stand-alone nanoindenter (*cf.* [42, 43, 45–47]) or *in situ* by using an indentation device which is introduced either in a scanning [2, 44, 48, 49, 119, 121] or transmission electron microscope [145]. For brevity, this section is restricted to *in situ* micromechanical cantilever bending tests carried out in a SEM.

Cantilevers for micromechanical bending test are fabricated by means of focused ion beam (FIB) milling. In the beginning, a freestanding cantilever with rather undefined geometry is formed by using high Ga^+-ion currents in the range of 2-20 nA. Afterwards, the actual shape of cantilevers is defined by continuously lowering the milling currents down to $\sim$ 100 pA, depending on the cantilevers material. Additionally, by using low milling currents in the final preparation steps, damage of the material of interest by Ga^+-ions is avoided. In order to measure fracture toughness of the cantilevers, on at least 4 specimens a notch has to be milled, which is performed by currents in the range of 5-20 pA. Finally, before the experiment, the dimensions of the cantilever have to be measured. A more detailed description of the fabrication of cantilever specimens is given for example in Refs. [42, 146–148].

In situ micromechanical bending tests performed during this thesis were carried out in a ZEISS LEO 982 SEM using a Hysitron PI85 nanoindenter equipped with a sphero-conical tip of 700 nm radius provided by Synton MDP AG. The sphero-conical indenter tip is chosen to minimize the influence of the plastic deformation at the loading point due to the imprint of indenter tip (*cf.* Sec. 3.2.1). The indentation device consists of a transducer controlling the indenter tip with a range of 5 µm and a three-axis piezo stage for positioning the sample. For testing, the samples are mounted on the three-axis piezo stage of the nanoindenter and the rotational adjustment is performed using a stereo microscope. The indentation setup is then mounted in the SEM and the image is centred at the indenter tip. The sample is moved by the piezo stage towards the tip and precisely aligned for testing. A schematic representation of the geometry of *in situ* experiment is shown in Fig. 3.12.

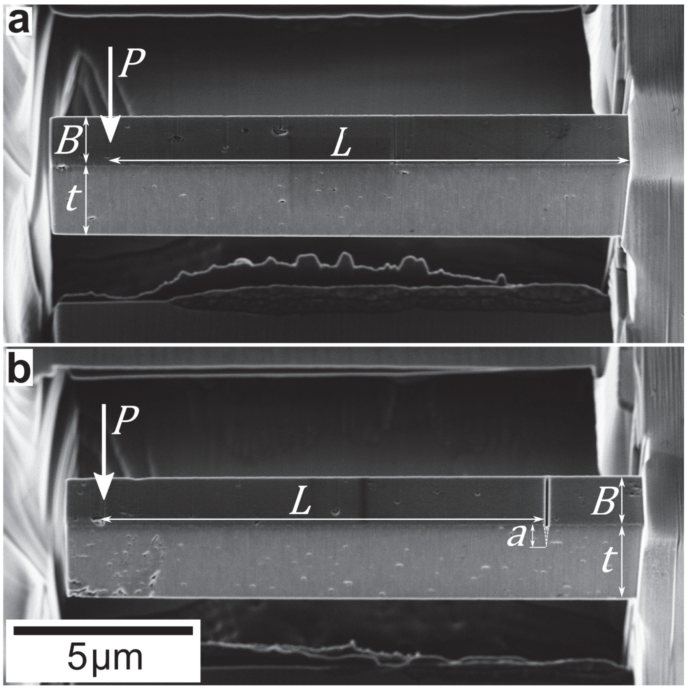

Figure 3.12.: Schematic geometric representation of the micromechanical cantilever bending tests of unnotched (a) and notched (b) freestanding cantilevers prepared from an AlCrN thin film, where L, B and t are the length, width and thickness of the cantilevers, respectively, whereas P denotes the applied load. The dashed lines in (b) represent the notch, and a is the notch depth evaluated *ex situ* (cf. Fig. 3.14) from the fracture surfaces after the *in situ* experiment. (own unpublished work)

Testing itself is performed in a displacement-controlled mode with a predefined loading rate. Typically, for a cantilever with a geometry of $L \times B \times t = 10 \times 2 \times 2\,\mu\mathrm{m}^3$ a loading rate of 20 nm is applied [2, 44, 48, 49, 119, 121]. The loading is performed monotonically until fracture occurs and during loading, load (P) and displacement (d) are continuously recorded. Exemplary load-displacement curves obtained from unnotched and notched cantilever specimens prepared from an AlCrN thin film are shown in Fig. 3.13. The recorded load-displacement curves are then utilized for the evaluation of mechanical properties, such as elastic modulus, fracture stress and fracture toughness.

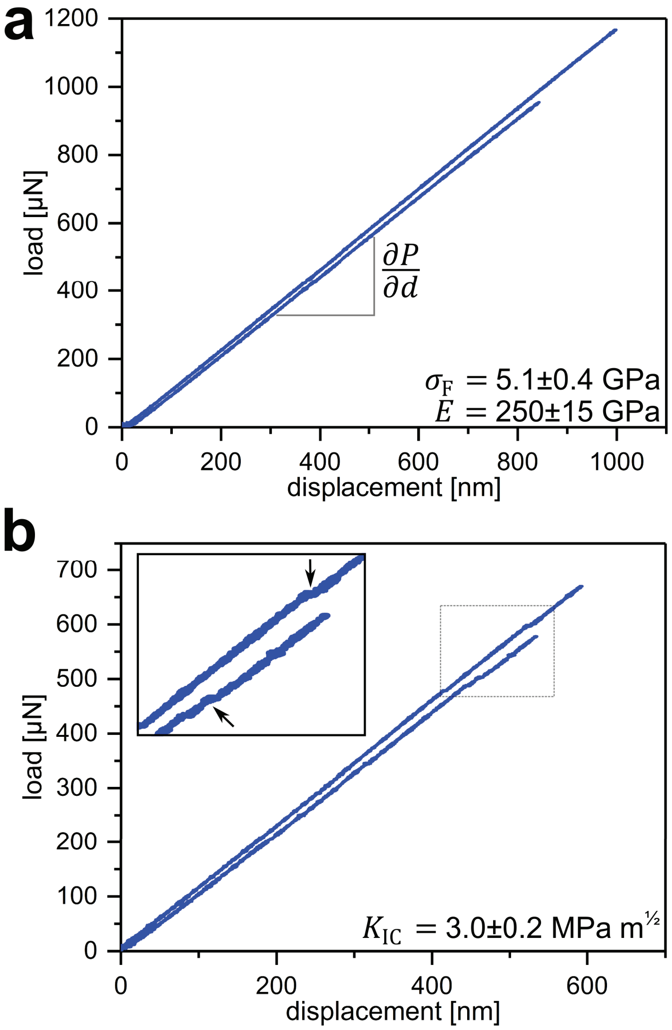

Figure 3.13.: Exemplary load-displacement curves recorded during the *in situ* micromechanical bending experiments for unnotched (a) and notched (b) AlCrN cantilevers, as depicted in Fig. 3.12a and 3.12b, respectively. $\frac{\partial P}{\partial d}$ in (a) represents the slope of the load-displacement curve, while in the inset in (b), the arrows mark the load drop associated with the fracture of the bridges at the sides of the FIB-fabricated notch as shown in Fig. 3.14b. (own unpublished work)

In case of hard protective thin films, the absence of significant plastic deformation allows for Euler-Bernoulli theory of bending [149] and linear elastic fracture mechanics [40, 150] to be applied for calculation of elastic modulus E, fracture stress σ_F

and fracture toughness K_{IC}, respectively. According to Euler-Bernoulli theory of bending [149], the elastic modulus E of a freestanding cantilever is determined from the slope of the load-displacement curve $\frac{\partial P}{\partial d}$ as follows

$$E = \frac{\partial P}{\partial d}\frac{4}{B}\left(\frac{L}{t}\right)^3, \tag{3.20}$$

where L, B and t are the length, width and thickness of the tested cantilever. Ideally, for an elastic material, the slope $\frac{\partial P}{\partial d}$ of the load-displacement curve should not change during loading. However, in order to minimize errors originating from the inelastic imprint of the indenter tip, the slope should be evaluated from a segment of the load-displacement curve where sufficient contact of the indenter tip is applied, but inelastic deformation of the edge of the cantilever and the loading point can be excluded or minimized. In the presented exemplary load-displacement curves, a load range of 100-250 µN has been proven beneficial for the evaluation of Young's modulus.

From the maximum load $P_{\max}$ at fracture, fracture stress σ_{F} is calculated as follows

$$\sigma_{\mathrm{F}} = \frac{6\,P_{\max}\,L}{B\,t^2} \tag{3.21}$$

Fracture stress and elastic modulus are evaluated from multiple specimens; based on own experience, at least 4-5 cantilevers should be fractured. After the experiment, the fracture surfaces are investigated for microstructural features, which can be associated to certain effects found in the load-displacement curves. An exemplary fracture surface of an unnotched cantilever is shown in Fig. 3.14a, where the relatively coarse columnar-grained microstructure of the AlCrN film is clearly visible. However, due to the absence of abnormal events in the presented load-displacement curves (Fig. 3.13a) and the absence of morphological irregularities (Fig. 3.14a), the experimental results obtained from these cantilevers are validated.

Fracture toughness K_{IC} is assessed by loading and fracturing of notched cantilevers (*cf.* Fig. 3.12b) as follows

$$K_{\mathrm{IC}} = \sigma\sqrt{\pi a}\,Y\left(\frac{a}{t}\right) \tag{3.22}$$

where σ is the applied stress on the notched cantilever at fracture (*cf.* Eq. 3.21), a is the notch depth and $Y\left(\frac{a}{t}\right)$ is the geometry factor taking into account the actual dimensions of the cantilever. The geometry factor $Y\left(\frac{a}{t}\right)$ has to be accounted for independent of the measurement geometry and is either calculated by finite element

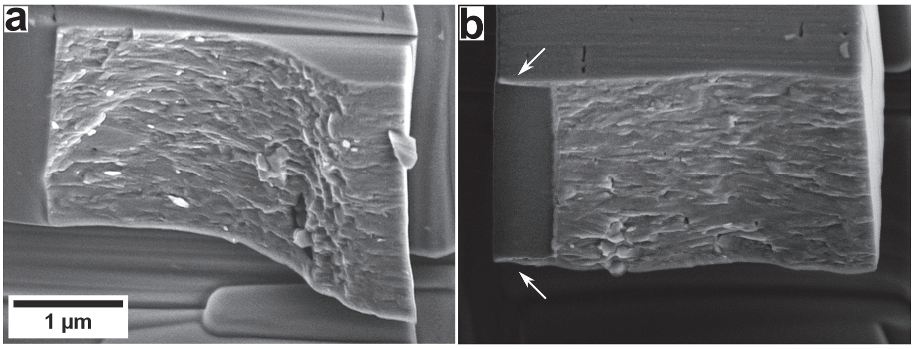

Figure 3.14.: Exemplary fracture surfaces of unnotched (a) and notched (b) AlCrN cantilevers, each corresponding to a cantilever of one load-displacement curve shown in Fig. 3.13a and 3.13b, respectively. The arrows in (b) indicate the materials bridges remaining at the sides of the notch. (own unpublished work)

modelling or tabulated in a handbook. For the freestanding cantilever, $Y\left(\frac{a}{t}\right)$ was calculated in the range of $\frac{a}{t} = [0, 1]$ by Tada *et al.* [151] as follows

$$Y\left(\frac{a}{t}\right) = \sqrt{\frac{2t}{\pi a}} \tan\left(\frac{\pi a}{2t}\right) \frac{0.923 + 0.199\left(1 - \sin\left(\frac{\pi a}{2t}\right)\right)^4}{\cos\left(\frac{\pi a}{2t}\right)} \tag{3.23}$$

During loading of a notched cantilever, load drops, as shown in the inset of Fig. 3.13b, should occur before fracture of the cantilever. These load drops suggest, that the material bridges at the sides of the notch (indicated by an arrow in Fig. 3.14b) fractured before the fracture of the entire cantilever. According to Refs. [42, 146, 147], the fractured bridges act as a sharp crack and in such way that the fracture toughness of the experiment is not overestimated. For any case, where the load drops presented in the inset of Fig. 3.13b are not seen, in Ref. [152] the discrepancy between the apparent fracture toughness evaluated from the experiment and the actual fracture toughness were modelled by extensive numerical calculations.

Finally, the notch depth a, critical for the evaluation of the fracture toughness K_{IC}, is assessed *ex situ* after the fracture experiment in the SEM. Similar to the scenario of unnotched cantilevers, the fracture surfaces are imaged and examined for morphological and microstructural irregularities, which could inflict the evaluation of fracture toughness for the thin film material. In Fig. 3.14b, a fracture surface of a notched cantilever corresponding to a load-displacement curve in Fig. 3.13b is shown. Again, the absence of morphological and microstructural features, together with the linear behaviour of the load-displacement curve obtained from the experiment, indicates, that the fracture experiment was conducted properly.

When conducted properly, micromechanical cantilever bending experiments allow for the direct evaluation of elastic modulus, fracture stress and fracture toughness. The knowledge obtained from micro-cantilever experiments can be used to quantify the improvement by the previously undergone thin film development and can be used subsequently for the further advancement of hard protective thin films.

4

Conclusions and Outlook

Within this thesis, several aspects of the nanoscale gradients emerging in hard protective thin films from the deposition process or external loads have been investigated. Moreover, novel characterization approaches were introduced:

- In a pioneering cross-sectional X-ray nanodiffraction experiment, nanoscale microstructure and residual stress gradients across a TiN thin film deposited on a WC-Co cutting edge were evaluated for the first time. The results uncovered pronounced gradients directly at the cutting edge, which can represent a reliability issue during tool service. The unique results open up new possibilities for further thin film design of cutting edges.

- The nanoscale residual stress and microstructure gradients across scratch track cross-sections in a Cr/CrN bilayer were assessed for the first time. In this way, scratching-induced deformation mechanisms within a brittle-ductile thin film could be elucidated. A significant portion of the damage was absorbed by the ductile Cr sublayer, suppressing overall bilayer as well as hard CrN toplayer failures.

- The multi-axial stress distributions emerging in a notched clamped cantilever upon loading were evaluated using cross-sectional X-ray nanodiffraction. For the first time, it was possible to evaluate the stress distributions around a notch in presence of a heterogeneous Cr-CrN interface and the influence of the latter to the former. As a consequence of the as-deposited residual stress state in the notched Cr layer, fracture was retarded by a factor of 3, thus proving again the potential of microstructural design in microstructurally heterogeneous thin films.

The results obtained in this thesis advance the understanding of nanoscale gradients across thin films. The collected data and developed methods can be further utilized to understand and tailor the mechanical properties of thin films by establishing design guidelines for particular applications. Furthermore, the results published in

Papers A, B and C show the current possibilities of cross-sectional X-ray nanodiffraction with a spatial resolution down to 50 nm and also include the newly developed small-angle X-ray scattering microscopy.

In an accompanying work, the crucial influence of residual stress on the decomposition temperature of metastable AlCrN thin films was assessed by a newly developed *in situ* high-temperature high-energy grazing incidence transmission X-ray diffraction method (Paper D). For the first time, it was also possible to assess the experimental thermal and intrinsic stress components of the residual stress during annealing. The newly developed approach improves the understanding of microstructural and phase changes of thin films at elevated temperatures and can be used for further thin film design.

Finally, in Paper E a six-level hierarchical thin film mimicking biological hard and tough structures, such as nacre or bone was extensively studied. It shows excellent mechanical properties, as well as high thermal stability of microstructure and phases. The self-assembly reaction of the CVD process holds much potential for the incorporation of biomimetical design in the field of hard protective thin films.

With ongoing development of X-ray optics and the upgrade of the European Synchrotron (ESRF), in the next years X-ray beams with dimensions below 20 nm will be achievable, which can be utilized for further thin film development. Especially the influence of heterogeneous interfaces on the stress fields during stable growth of cracks towards the interface is of high scientific interest.

For future work, attention will be drawn to the investigation of nanoscale deposition-induced gradients of phase composition, microstructure and residual stress of compositionally more complex metastable thin films deposited on a cutting edge. Additionally, the influence of heterogeneous interfaces in materials combinations with higher ductility will be of future interest.

Finally, the current development of an *in situ* heating device at the ID13 nanofocus beamline of the ESRF allows for *depth-* and *temperature-dependent resolution* of the interdependence between nanoscale structural and stress gradients of thin films originating in the deposition process and the microstructural and phase changes at elevated temperatures. Thus, it will represent a combination of cross-sectional X-ray nanodiffraction with the newly developed *in situ* high-temperature high-energy grazing incidence transmission X-ray diffraction approach.

Bibliography

[1] J. Keckes, R. Daniel, J. Todt, J. Zalesak, B. Sartory, S. Braun et al., *Acta Materialia*, 2018, **144**, 862–873, DOI: `10.1016/j.actamat.2017.11.049`.

[2] R. Daniel, M. Meindlhumer, W. Baumegger, J. Zalesak, B. Sartory, M. Burghammer et al., *Acta Materialia*, 2017, **122**, 130–137, DOI: `10.1016/j.actamat.2016.09.027`.

[3] J. Zalesak, D. Holec, I. Matko, M. Petrenec, B. Sartory, N. Koutná et al., *Acta Materialia*, 2017, **131**, 391–399, DOI: `10.1016/j.actamat.2017.04.009`.

[4] S. Klima, N. Jäger, H. Hruby, C. Mitterer, J. Keckes, M. Burghammer et al., *Materials & Design*, 2019, **170**, 107702, DOI: `10.1016/j.matdes.2019.107702`.

[5] N. Jäger, M. Meindlhumer, S. Spor, H. Hruby, J. Julin, A. Stark et al., *Acta Materialia*, 2020, **186**, 545–554, DOI: `10.1016/j.actamat.2020.01.026`.

[6] T. Teppernegg, T. Klünsner, P. Angerer, C. Tritremmel, C. Czettl, J. Keckes et al., *International Journal of Refractory Metals and Hard Materials*, 2014, **47**, 80–85, DOI: `10.1016/j.ijrmhm.2014.07.005`.

[7] T. Teppernegg, P. Angerer, T. Klünsner, C. Tritremmel and C. Czettl, *International Journal of Refractory Metals and Hard Materials*, 2015, **52**, 171–175, DOI: `10.1016/j.ijrmhm.2015.06.013`.

[8] G. List, G. Sutter and A. Bouthiche, *International Journal of Machine Tools and Manufacture*, 2012, **54-55**, 1–9, DOI: `10.1016/j.ijmachtools.2011.11.009`.

[9] J. Vetter, *Surface and Coatings Technology*, 1995, **76-77**, 719–724, DOI: `10.1016/0257-8972(95)02499-9`.

[10] U. Schleinkofer, C. Czettl and C. Michotte, in *Comprehensive Hard Materials*, Elsevier, 2014, pp. 453–469, DOI: `10.1016/b978-0-08-096527-7.00016-7`.

[11] P. Panjan, A. Drnovšek, P. Gselman, M. Čekada and M. Panjan, *Coatings*, 2020, **10**, 447, DOI: `10.3390/coatings10050447`.

[12] M. Tkadletz, C. Mitterer, B. Sartory, I. Letofsky-Papst, C. Czettl and C. Michotte, *Surf. Coat. Technol.*, 2014, **257**, 25 years of TiAlN hard coatings in research and industry, 95–101, DOI: `10.1016/j.surfcoat.2014.01.010`.

[13] M. Ohring, *Materials Science of Thin Films - Deposition & Structure*, Academic Press, San Diego, 2nd edn., 2002.

[14] W. D. Sproul, *Surface and Coatings Technology*, 1991, **49**, 284–289, DOI: `10.1016/0257-8972(91)90070-d`.

[15] A. Anders, *Cathodic Arcs*, Springer New York, 2008, DOI: `10.1007/978-0-387-79108-1`.

[16] A. Anders, *Surface and Coatings Technology*, 2014, **257**, 308–325, DOI: `10.1016/j.surfcoat.2014.08.043`.

[17] K. Choy, *Prog. Mater Sci.*, 2003, **48**, 57–170, DOI: `10.1016/S0079-6425(01)00009-3`.

[18] H. O. Pierson, *Handbook of Chemical Vapor Deposition*, Elsevier, 1992, DOI: `10.1016/c2009-0-20448-x`.

[19] H. Gleiter, *Acta Materialia*, 2000, **48**, 1–29, DOI: `10.1016/s1359-6454(99)00285-2`.

[20] I. Petrov, P. B. Barna, L. Hultman and J. E. Greene, *Journal of Vacuum Science & Technology A: Vacuum, Surfaces, and Films*, 2003, **21**, S117–S128, DOI: `10.1116/1.1601610`.

[21] P. H. Mayrhofer, C. Mitterer, L. Hultman and H. Clemens, *Prog. Mater Sci.*, 2006, **51**, 1032–1114, DOI: `10.1016/j.pmatsci.2006.02.002`.

[22] O. Paris, D. Lang, J. Li, P. Schumacher, M. Deluca, R. Daniel et al., *Advanced Engineering Materials*, 2017, **19**, 1600671, DOI: `10.1002/adem.201600671`.

[23] C. Praetzas, T. Teppernegg, J. Mayr, C. Czettl, J. Schäfer and E. Abele, *Procedia CIRP*, 2018, **77**, 118–121, DOI: `10.1016/j.procir.2018.08.240`.

[24] S. S. Kim, J. G. Han and S. Y. Lee, *Thin Solid Films*, 1998, **334**, 133–139, DOI: `10.1016/s0040-6090(98)01131-6`.

[25] E. Macak, W.-D. Münz and J. Rodenburg, *Surface and Coatings Technology*, 2002, **151-152**, 349–354, DOI: `10.1016/s0257-8972(01)01650-4`.

[26] E. B. Macak, W.-D. Münz and J. M. Rodenburg, *Journal of Applied Physics*, 2003, **94**, 2829–2836, DOI: `10.1063/1.1597755`.

[27] R. Novák, I. Kvasnička, D. Nováková and Z. Malá, *Surface and Coatings Technology*, 1999, **114**, 65–69, DOI: `10.1016/s0257-8972(99)00023-7`.

[28] J. Bohlmark, H. Blomqvist, L. Landälv, S. Amerioun and M. Ahlgren, *Materials Science Forum*, 2011, **681**, 145–150, DOI: `10.4028/www.scientific.net/msf.681.145`.

[29] J. E. Krzanowski, S. Veldhuis, P. Aliotta and D. J. Foley, *Journal of Materials Engineering and Performance*, 2012, **22**, 1611–1618, DOI: `10.1007/s11665-012-0449-z`.

[30] M. Meozzi, *Tribology International*, 2006, **39**, 496–505, DOI: `10.1016/j.triboint.2005.03.011`.

[31] J. Valli, *Journal of Vacuum Science & Technology A: Vacuum, Surfaces, and Films*, 1986, **4**, 3007–3014, DOI: `10.1116/1.573616`.

[32] A. Perry, *Thin Solid Films*, 1983, **107**, 167–180, DOI: `10.1016/0040-6090(83)90019-6`.

[33] S. Bull, *Surface and Coatings Technology*, 1991, **50**, 25–32, DOI: `10.1016/0257-8972(91)90188-3`.

[34] S. Bull, *Tribology International*, 1997, **30**, 491–498, DOI: `10.1016/s0301-679x(97)00012-1`.

[35] P. Steinmann, Y. Tardy and H. Hintermann, *Thin Solid Films*, 1987, **154**, 333–349, DOI: `10.1016/0040-6090(87)90377-4`.

[36] N. X. Randall, *Surface and Coatings Technology*, 2019, **380**, 125092, DOI: `10.1016/j.surfcoat.2019.125092`.

[37] K. Holmberg, A. Laukkanen, H. Ronkainen, K. Wallin and S. Varjus, *Wear*, 2003, **254**, 278–291, DOI: `10.1016/s0043-1648(02)00297-1`.

[38] K. Holmberg, A. Laukkanen, H. Ronkainen, K. Wallin, S. Varjus and J. Koskinen, *Surface and Coatings Technology*, 2006, **200**, 3793–3809, DOI: `10.1016/j.surfcoat.2005.03.040`.

[39] K. Holmberg, A. Laukkanen, H. Ronkainen, K. Wallin, S. Varjus and J. Koskinen, *Surface and Coatings Technology*, 2006, **200**, 3810–3823, DOI: `10.1016/j.surfcoat.2005.03.041`.

[40] T. Anderson, *Fracture Mechanics*, CRC Press, 2017, DOI: `10.1201/9781315370293`.

[41] A. A. Griffith, *Philosophical Transactions of the Royal Society of London. Series A, Containing Papers of a Mathematical or Physical Character*, 1921, **221**, 163–198, DOI: `10.1098/rsta.1921.0006`.

[42] A. Riedl, R. Daniel, M. Stefenelli, T. Schöberl, O. Kolednik, C. Mitterer et al., *Scr. Mater.*, 2012, **67**, 708–711, DOI: `10.1016/j.scriptamat.2012.06.034`.

[43] A. Zeilinger, R. Daniel, M. Stefenelli, B. Sartory, L. Chitu, M. Burghammer et al., *J Phys D Appl Phys*, 2015, **48**, 295303, DOI: `10.1088/0022-3727/48/29/295303`.

[44] R. Daniel, M. Meindlhumer, J. Zalesak, B. Sartory, A. Zeilinger, C. Mitterer et al., *Mater. Des.*, 2016, **104**, 227–234, DOI: `10.1016/j.matdes.2016.05.029`.

[45] C. Kainz, N. Schalk, M. Tkadletz, C. Mitterer and C. Czettl, *Thin Solid Films*, 2019, **688**, 137283, DOI: `10.1016/j.tsf.2019.05.002`.

[46] C. Kainz, N. Schalk, M. Tkadletz, C. Mitterer and C. Czettl, *Surface and Coatings Technology*, 2019, **370**, 311–319, DOI: `10.1016/j.surfcoat.2019.04.086`.

[47] C. Kainz, N. Schalk, M. Tkadletz, M. Winkler and C. Czettl, *Surface and Coatings Technology*, 2020, **394**, 125868, DOI: `10.1016/j.surfcoat.2020.125868`.

[48] R. Daniel, M. Meindlhumer, W. Baumegger, J. Todt, J. Zalesak, T. Ziegelwanger et al., *Materials & Design*, 2019, **161**, 80–85, DOI: `10.1016/j.matdes.2018.11.028`.

[49] R. Daniel, M. Meindlhumer, J. Zalesak, W. Baumegger, J. Todt, T. Ziegelwanger et al., *Materials & Design*, 2020, **196**, 109169, DOI: `10.1016/j.matdes.2020.109169`.

[50] R. Hahn, M. Bartosik, R. Soler, C. Kirchlechner, G. Dehm and P. Mayrhofer, *Scripta Materialia*, 2016, **124**, 67–70, DOI: `10.1016/j.scriptamat.2016.06.030`.

[51] J. Buchinger, N. Koutná, Z. Chen, Z. Zhang, P. H. Mayrhofer, D. Holec et al., *Acta Materialia*, 2019, **172**, 18–29, DOI: `10.1016/j.actamat.2019.04.028`.

[52] H. Kindlund, D. Sangiovanni, J. Lu, J. Jensen, V. Chirita, J. Birch et al., *Acta Materialia*, 2014, **77**, 394–400, DOI: `10.1016/j.actamat.2014.06.025`.

[53] F. BARTHELAT, H. TANG, P. ZAVATTIERI, C. LI and H. ESPINOSA, *Journal of the Mechanics and Physics of Solids*, 2007, **55**, 306–337, DOI: `10.1016/j.jmps.2006.07.007`.

[54] F. Barthelat, Z. Yin and M. J. Buehler, *Nature Reviews Materials*, 2016, **1**, DOI: `10.1038/natrevmats.2016.7`.

[55] F. Barthelat and R. Rabiei, *Journal of the Mechanics and Physics of Solids*, 2011, **59**, 829–840, DOI: `10.1016/j.jmps.2011.01.001`.

[56] M. A. Meyers, P.-Y. Chen, A. Y.-M. Lin and Y. Seki, *Progress in Materials Science*, 2008, **53**, 1–206, DOI: `10.1016/j.pmatsci.2007.05.002`.

[57] A. Zeilinger, J. Todt, C. Krywka, M. Müller, W. Ecker, B. Sartory et al., *Scientific Reports*, 2016, **6**, DOI: `10.1038/srep22670`.

[58] B. N. Jaya and V. Jayaram, *International Journal of Fracture*, 2014, **188**, 213–228, DOI: `10.1007/s10704-014-9956-2`.

[59] B. N. Jaya, S. Bhowmick, S. S. Asif, O. L. Warren and V. Jayaram, *Philosophical Magazine*, 2015, **95**, 1945–1966, DOI: `10.1080/14786435.2015.1010623`.

[60] A. K. Mishra, A. Lambai, V. Jayaram and B. N. Jaya, *Theoretical and Applied Fracture Mechanics*, 2020, **105**, 102409, DOI: `10.1016/j.tafmec.2019.102409`.

[61] C. Mitterer, in *Comprehensive Hard Materials*, Elsevier, 2014, pp. 449–467, DOI: `10.1016/b978-0-08-096527-7.00035-0`.

[62] H. Holleck and V. Schier, *Surface and Coatings Technology*, 1995, **76-77**, 328–336, DOI: `10.1016/0257-8972(95)02555-3`.

[63] J. Wagner, C. Mitterer, M. Penoy, C. Michotte, W. Wallgram and M. Kathrein, *International Journal of Refractory Metals and Hard Materials*, 2008, **26**, 120–126, DOI: `10.1016/j.ijrmhm.2007.01.010`.

[64] C. W. Kim and K. H. Kim, *Thin Solid Films*, 1997, **307**, 113–119, DOI: `10.1016/S0040-6090(97)00212-5`.

[65] W.-D. Münz, *J. Vac. Sci. Technol., A*, 1986, **4**, 2717–2725, DOI: `10.1116/1.573713`.

[66] Y. Chim, X. Ding, X. Zeng and S. Zhang, *Thin Solid Films*, 2009, **517**, 4845–4849, DOI: `10.1016/j.tsf.2009.03.038`.

[67] C. Saringer, M. Tkadletz, A. Stark, N. Schell, C. Czettl and N. Schalk, *Surface and Coatings Technology*, 2019, **374**, 617–624, DOI: `10.1016/j.surfcoat.2019.05.072`.

[68] S. Massl, W. Thomma, J. Keckes and R. Pippan, *Acta Mater.*, 2009, **57**, 1768–1776, DOI: `10.1016/j.actamat.2008.12.018`.

[69] S. PalDey and S. Deevi, *Mater. Sci. Eng., A*, 2003, **342**, 58–79, DOI: `10.1016/S0921-5093(02)00259-9`.

[70] J. Almer, U. Lienert, R. L. Peng, C. Schlauer and M. Odén, *Journal of Applied Physics*, 2003, **94**, 697–702, DOI: `10.1063/1.1582351`.

[71] A. Ehrlich, M. Kühn, F. Richter and W. Hoyer, *Surface and Coatings Technology*, 1995, **76-77**, 280–286, DOI: `10.1016/0257-8972(95)02583-9`.

[72] C. Gautier and J. Machet, *Thin Solid Films*, 1997, **295**, 43–52, DOI: `10.1016/s0040-6090(96)09164-x`.

[73] M. Oden, C. Ericsson, G. Hakansson and H. Ljungcrantz, *Surface and Coatings Technology*, 1999, **114**, 39–51, DOI: `10.1016/s0257-8972(99)00019-5`.

[74] J. Almer, M. Oden and G. Hakansson, *Thin Solid Films*, 2001, **385**, 190–197, DOI: `10.1016/s0040-6090(01)00759-3`.

[75] W. Ernst, J. Neidhardt, H. Willmann, B. Sartory, P. Mayrhofer and C. Mitterer, *Thin Solid Films*, 2008, **517**, 568–574, DOI: `10.1016/j.tsf.2008.06.086`.

[76] R. Daniel, K. Martinschitz, J. Keckes and C. Mitterer, *Acta Mater.*, 2010, **58**, 2621–2633, DOI: `10.1016/j.actamat.2009.12.048`.

[77] R. Daniel, D. Holec, M. Bartosik, J. Keckes and C. Mitterer, *Acta Mater.*, 2011, **59**, 6631–6645, DOI: `10.1016/j.actamat.2011.07.018`.

[78] R. Daniel, K. J. Martinschitz, J. Keckes and C. Mitterer, *Journal of Physics D: Applied Physics*, 2009, **42**, 075401, DOI: `10.1088/0022-3727/42/7/075401`.

[79] G. Fontalvo, R. Daniel and C. Mitterer, *Tribology International*, 2010, **43**, 108–112, DOI: `10.1016/j.triboint.2009.05.002`.

[80] M. Stefenelli, R. Daniel, W. Ecker, D. Kiener, J. Todt, A. Zeilinger et al., *Acta Mater.*, 2015, **85**, 24–31, DOI: `10.1016/j.actamat.2014.11.011`.

[81] A. Sugishima, H. Kajioka and Y. Makino, *Surface and Coatings Technology*, 1997, **97**, 590–594, DOI: `10.1016/s0257-8972(97)00402-7`.

[82] A. Reiter, V. Derflinger, B. Hanselmann, T. Bachmann and B. Sartory, *Surface and Coatings Technology*, 2005, **200**, 2114–2122, DOI: `10.1016/j.surfcoat.2005.01.043`.

[83] B. Grossmann, M. Tkadletz, N. Schalk, C. Czettl, M. Pohler and C. Mitterer, *Surface and Coatings Technology*, 2018, **342**, 190–197, DOI: `10.1016/j.surfcoat.2018.02.062`.

[84] M. Pfeiler-Deutschmann, P. H. Mayrhofer, K. Chladil, M. Penoy, C. Michotte, M. Kathrein et al., *Thin Solid Films*, 2015, **581**, 20–24, DOI: `10.1016/j.tsf.2014.10.051`.

[85] T. Weirather, C. Czettl, P. Polcik, M. Kathrein and C. Mitterer, *Surface and Coatings Technology*, 2013, **232**, 303–310, DOI: `10.1016/j.surfcoat.2013.05.022`.

[86] H. Willmann, P. H. Mayrhofer, P. O. Å. Persson, a. E. Reiter, L. Hultman and C. Mitterer, *Scr. Mater.*, 2006, **54**, 1847–1851, DOI: `10.1016/j.scriptamat.2006.02.023`.

[87] H. Willmann, P. H. Mayrhofer, L. Hultman and C. Mitterer, *International Heat Treatment and Surface Engineering*, 2007, **1**, 75–79, DOI: `10.1179/174951507x193657`.

[88] P. Mayrhofer, H. Willmann and A. Reiter, *Surface and Coatings Technology*, 2008, **202**, 4935–4938, DOI: `10.1016/j.surfcoat.2008.04.075`.

[89] P. H. Mayrhofer, H. Willmann, L. Hultman and C. Mitterer, *Journal of Physics D: Applied Physics*, 2008, **41**, 155316, DOI: `10.1088/0022-3727/41/15/155316`.

[90] N. Norrby, L. Rogström, M. Johansson-Jõesaar, N. Schell and M. Odén, *Acta Materialia*, 2014, **73**, 205–214, DOI: `10.1016/j.actamat.2014.04.014`.

[91] L. Rogström, N. Ghafoor, J. Schroeder, N. Schell, J. Birch, M. Ahlgren et al., *Journal of Applied Physics*, 2015, **118**, 035309, DOI: `10.1063/1.4927156`.

[92] Y. Chen, L. Rogström, D. Ostach, N. Ghafoor, M. Johansson-Jõesaar, N. Schell et al., *Journal of Alloys and Compounds*, 2017, **691**, 1024–1032, DOI: `10.1016/j.jallcom.2016.08.299`.

[93] L. Rogström, J. Ullbrand, J. Almer, L. Hultman, B. Jansson and M. Odén, *Thin Solid Films*, 2012, **520**, 5542–5549, DOI: `10.1016/j.tsf.2012.04.059`.

[94] L. Rogström, M. J. Jõesaar, R. Pilemalm, N. Ghafoor, L. Johnson, N. Schell et al., *Journal of Alloys and Compounds*, 2019, **779**, 261–269, DOI: `10.1016/j.jallcom.2018.11.039`.

[95] I. Endler, M. Hähn, M. Herrmann, R. Pitonak, S. Ruppi, M. Schneider et al., *Surf. Coat. Technol.*, 2008, **203**, 530–533, DOI: `10.1016/j.surfcoat.2008.04.098`.

[96] P. Mayrhofer, A. Hörling, L. Karlsson, J. Sjölén, T. Larsson, C. Mitterer et al., *Appl Phys Lett*, 2003, **83**, 2049–2051, DOI: `10.1063/1.1608464`.

[97] R. Zhang and S. Veprek, *Mater. Sci. Eng., A*, 2007, **448**, 111–119, DOI: `10.1016/j.msea.2006.10.012`.

[98] R. Rachbauer, S. Massl, E. Stergar, D. Holec, D. Kiener, J. Keckes et al., *J Appl Phys*, 2011, **110**, 11, DOI: `10.1063/1.3610451`.

[99] P. H. Mayrhofer, D. Music and J. M. Schneider, *J Appl Phys*, 2006, **100**, 5, DOI: `10.1063/1.2360778`.

[100] A. Hörling, L. Hultman, M. Odén, J. Sjölén and L. Karlsson, *Surf. Coat. Technol.*, 2005, **191**, 384–392, DOI: `10.1016/j.surfcoat.2004.04.056`.

[101] L. Chen, J. Paulitsch, Y. Du and P. H. Mayrhofer, *Surf. Coat. Technol.*, 2012, **206**, 2954–2960, DOI: `10.1016/j.surfcoat.2011.12.028`.

[102] A. Joshi and H. Hu, *Surf. Coat. Technol.*, 1995, **76–77, Part 2**, 499–507, DOI: `10.1016/0257-8972(95)02566-9`.

[103] Z. Zhou, P. Tam, P. Shum and K. Li, *Thin Solid Films*, 2009, **517**, 5243–5247, DOI: `10.1016/j.tsf.2009.03.115`.

[104] M. Bartosik, C. Rumeau, R. Hahn, Z. L. Zhang and P. H. Mayrhofer, *Scientific Reports*, 2017, **7**, DOI: `10.1038/s41598-017-16751-1`.

[105] J. Keckes, R. Daniel, C. Mitterer, I. Matko, B. Sartory, A. Köpf et al., *Thin Solid Films*, 2013, **545**, 29–32, DOI: `10.1016/j.tsf.2013.08.001`.

[106] J. Todt, R. Pitonak, A. Köpf, R. Weißenbacher, B. Sartory, M. Burghammer et al., *Surf. Coat. Technol.*, 2014, **258**, 1119–1127, DOI: `10.1016/j.surfcoat.2014.07.022`.

[107] J. Todt, J. Zalesak, R. Daniel, R. Pitonak, A. Köpf, R. Weißenbacher et al., *Surf. Coat. Technol.*, 2016, **291**, 89–93, DOI: `10.1016/j.surfcoat.2016.02.027`.

[108] M. De Graef and M. E. Henry, *Structure of Materials*, Cambridge University Press, 2007.

[109] L. H. Schwartz and J. B. Cohen, *Diffraction from Materials*, Springer, 2nd edn., 1977.

[110] V. Hauk, *Structural and Residual Stress Analysis by Nondestructive Methods*, Elsevier Science B.V., Amsterdam, 2nd edn., 1997.

[111] M. Birkholz, *Thin Film Analysis by X-Ray Scattering*, Wiley, Weinheim, 2005, DOI: `10.1002/3527607595`.

[112] L. Spieß, G. Teichert, R. Schwarzer, H. Behnken and C. Genzel, *Moderne Röntgenbeugung*, Springer Fachmedien Wiesbaden, 2019, DOI: `10.1007/978-3-8348-8232-5`.

[113] *Powder Diffraction File Cards: bcc-Cr 6-0694, bcc-Fe 65-4899., (n.d.)*

[114] *Powder Diffraction File Cards: Al2O3 46-1212, Cr2O3 38-1479., (n.d.)*

[115] M. Stefenelli, J. Todt, A. Riedl, W. Ecker, T. Müller, R. Daniel et al., *J Appl Crystallogr*, 2013, **46**, 1378–1385, DOI: `10.1107/S0021889813019535`.

[116] J. Keckes, M. Bartosik, R. Daniel, C. Mitterer, G. Maier, W. Ecker et al., *Scr. Mater.*, 2012, **67**, 748–751, DOI: `10.1016/j.scriptamat.2012.07.034`.

[117] M. Bartosik, R. Daniel, C. Mitterer, I. Matko, M. Burghammer, P. Mayrhofer et al., *Thin Solid Films*, 2013, **542**, 1–4, DOI: `10.1016/j.tsf.2013.05.102`.

[118] M. Meindlhumer, S. Klima, N. Jäger, A. Stark, H. Hruby, C. Mitterer et al., *Scientific Reports*, 2019, **9**, DOI: `10.1038/s41598-019-54307-7`.

[119] D. P. Gruber, J. Todt, N. Wöhrl, J. Zalesak, M. Tkadletz, A. Kubec et al., *Carbon*, 2019, **144**, 666–674, DOI: `10.1016/j.carbon.2018.12.093`.

[120] N. Jäger, S. Klima, H. Hruby, J. Julin, M. Burghammer, J. Keckes et al., *Acta Materialia*, 2019, **162**, 55–66, DOI: `10.1016/j.actamat.2018.09.031`.

[121] D. P. Gruber, J. Zalesak, J. Todt, M. Tkadletz, B. Sartory, J.-P. Suuronen et al., *Surface and Coatings Technology*, 2020, **399**, 126181, DOI: `10.1016/j.surfcoat.2020.126181`.

[122] W. Ecker, J. Keckes, M. Krobath, J. Zalesak, R. Daniel, M. Rosenthal et al., *Materials & Design*, 2020, **188**, 108478, DOI: `10.1016/j.matdes.2020.108478`.

[123] J. Faber and T. Fawcett, *Acta Crystallographica Section B Structural Science*, 2002, **58**, 325–332, DOI: `10.1107/s0108768102003312`.

[124] S. Gates-Rector and T. Blanton, *Powder Diffraction*, 2019, **34**, 352–360, DOI: `10.1017/s0885715619000812`.

[125] A. Kubec, S. Niese, M. Rosenthal, J. Gluch, M. Burghammer, P. Gawlitza et al., *Journal of Instrumentation*, 2018, **13**, C04011–C04011, DOI: `10.1088/1748-0221/13/04/c04011`.

[126] A. P. Hammersley, *FIT2D: An Introduction and Overview*, ESRF, 1997, `http://www.esrf.eu/computing/scientific/FIT2D/FIT2D_INTRO/fit2d.html`.

[127] J. Kieffer, *J. Phys: Conf. Ser.*, 2013, **425**, 202012, DOI: `10.1088/1742-6596/425/20/202012`.

[128] G. Ashiotis, A. Deschildre, Z. Nawaz, J. P. Wright, D. Karkoulis, F. E. Picca et al., *Journal of Applied Crystallography*, 2015, **48**, 510–519, DOI: `10.1107/s1600576715004306`.

[129] *Powder Diffraction File Cards: fcc-CrN 11-0065, w-AlN 225-1133, WC 25-1047, Co 15-0806., (n.d.)*

[130] L. A. Feigin and D. I. Svergun, *Structure Analysis by Small-Angle X-Ray and Neutron Scattering*, ed. G. W. Taylor, Springer US, 1987, DOI: `10.1007/978-1-4757-6624-0`.

[131] M. Meindlhumer, N. Jäger, S. Spor, M. Rosenthal, J. Keckes, H. Hruby et al., *Scripta Materialia*, 2020, **182**, 11–15, DOI: `10.1016/j.scriptamat.2020.02.031`.

[132] J. Todt, Ph.D. Thesis, Montanuiversität Leoben, 2016.

[133] R. Daniel, J. Keckes, I. Matko, M. Burghammer and C. Mitterer, *Acta Mater.*, 2013, **61**, 6255–6266, DOI: `10.1016/j.actamat.2013.07.009`.

[134] I. C. Noyan and J. B. Cohen, *Residual Stress*, Springer New York, 1987, DOI: `10.1007/978-1-4613-9570-6`.

[135] A. P. Hammersley, S. O. Svensson, M. Hanfland, A. N. Fitch and D. Hausermann, *High Pressure Res.*, 1996, **14**, 235–248, DOI: `10.1080/08957959608201408`.

[136] A. Hammersley, S. Svensson and A. Thompson, *Nucl. Instrum. Methods Phys. Res., Sect. A*, 1994, **346**, 312–321, DOI: `10.1016/0168-9002(94)90720-X`.

[137] A. P. Hammersley, S. O. Svensson, A. Thompson, H. Graafsma, Å. Kvick and J. P. Moy, *Rev. Sci. Instrum.*, 1995, **66**, 2729–2733, DOI: `10.1063/1.1145618`.

[138] W. Oliver and G. Pharr, *J Mater Res*, 1992, **7**, 1564–1580, DOI: `10.1557/JMR.1992.1564`.

[139] R. L. Smith and G. E. Sandly, *Proceedings of the Institution of Mechanical Engineers*, 1922, **102**, 623–641, DOI: `10.1243/pime_proc_1922_102_033_02`.

[140] I. N. Sneddon, *Int. J. Eng. Sci.*, 1965, **3**, 47–57, DOI: `10.1016/0020-7225(65)90019-4`.

[141] W. D. Nix and H. Gao, *J. Mech. Phys. Solids*, 1998, **46**, 411–425, DOI: `10.1016/S0022-5096(97)00086-0`.

[142] K. I. Schiffmann, *Int. J. Mater. Res.*, 2007, **98**, 424–429, DOI: `10.3139/146.101488`.

[143] J. Field and C. Pickles, *Diamond and Related Materials*, 1996, **5**, 625–634, DOI: `10.1016/0925-9635(95)00362-2`.

[144] E. S. Berkovich, *Zavodskaya Laboratoria*, 1950, **13**, 345–347.

[145] J. Zalesak, M. Bartosik, R. Daniel, C. Mitterer, C. Krywka, D. Kiener et al., *Acta Mater.*, 2016, **102**, 212–219, DOI: `10.1016/j.actamat.2015.09.007`.

[146] K. Matoy, H. Schönherr, T. Detzel, T. Schöberl, R. Pippan, C. Motz et al., *Thin Solid Films*, 2009, **518**, 247–256, DOI: `10.1016/j.tsf.2009.07.143`.

[147] K. Matoy, H. Schönherr, T. Detzel and G. Dehm, *Thin Solid Films*, 2010, **518**, 5796–5801, DOI: `10.1016/j.tsf.2010.05.114`.

[148] S. Wurster, C. Motz and R. Pippan, *Philosophical Magazine*, 2012, **92**, 1803–1825, DOI: `10.1080/14786435.2012.658449`.

[149] S. Timoshenko, *Strength of Materials Part, 1: Elementary Theory and Problems*, D. Van Nostrand Company, New York, 1st edn., 1940.

[150] D. Gross and T. Seelig, *Bruchmechanik*, Springer Berlin Heidelberg, 2011, DOI: `10.1007/978-3-642-10196-0`.

[151] H. Tada, P. C. Paris and G. R. Irwin, *The Stress Analysis of Cracks Handbook, Third Edition*, ASME Press, 2000, DOI: `10.1115/1.801535`.

[152] S. Brinckmann, K. Matoy, C. Kirchlechner and G. Dehm, *Acta Materialia*, 2017, **136**, 281–287, DOI: `10.1016/j.actamat.2017.07.014`.

5

List of appended publications

5.1. Papers in scientific journals

Paper A

Nanoscale residual stress and microstructure gradients across the cutting edge area of a TiN coating on WC–Co

M. Meindlhumer, N. Jäger , S. Spor, M. Rosenthal, J.F. Keckes, H. Hruby, C. Mitterer, R. Daniel, J. Keckes, J. Todt

Scripta Materialia 182: 11-15, 2020

doi:10.1016/j.scriptamat.2020.02.031

Paper B

Nanoscale stress distributions and microstructural changes at scratch track cross-sections of a deformed brittle-ductile CrN-Cr bilayer

M. Meindlhumer, J. Zalesak, W. Ecker, M. Rosenthal, H. Hruby, C. Mitterer, R. Daniel, J. Keckes, J. Todt

Materials & Design 195: 19023, 2020

doi:10.1016/j.matdes.2020.109023

Paper C

Evolution of stress fields during crack growth and arrest in a brittle-ductile CrN-Cr clamped-cantilever analysed by X-ray nanodiffraction and modelling

M. Meindlhumer, L. R. Brandt, J. Zalesak, M. Rosenthal, H. Hruby, E. Salvati, C. Mitterer, R. Daniel, J. Todt, J. Keckes, A. M. Korsunsky

Materials & Design, under review

Paper D

Stress-controlled decomposition routes in cubic AlCrN films assessed by in-situ high-temperature high-energy grazing incidence transmission X-ray diffraction

M. Meindlhumer, S. Klima, N. Jäger, A. Stark, H. Hruby, C. Mitterer, J. Keckes, R. Daniel

Scientific Reports 9: 18027, 2019

doi:10.1038/s41598-019-54307-7

Paper E

Biomimetic hard and tough nanoceramic Ti–Al–N film with self-assembled six-level hierarchy

M. Meindlhumer, J. Zalesak, R. Pitonak, J. Todt, B. Sartory, M. Burghammer, A. Stark, N. Schell, R. Daniel, J. F. Keckes, M. Lessiak, A. Köpf, R. Weißenbacher, J. Keckes

Nanoscale 11: 7986-7995, 2019

doi:10.1039/c8nr10339a

A

Nanoscale residual stress and microstructure gradients across the cutting edge area of a TiN coating on WC-Co

M. Meindlhumer[a], N. Jäger[b], S. Spor[a,c], M. Rosenthal[b], J. F. Keckes[d], H. Hruby[c], C. Mitterer[d], R. Daniel[a], J. Keckes[d,e,f], J. Todt[e]

[a]Christian Doppler Laboratory for Advanced Synthesis of Novel Multifunctional Coatings at the Department of Materials Science, Montanuniversität Leoben, Leoben, Austria
[b]European Synchrotron Radiation Facility, Grenoble, France
[c]voestalpine eifeler Vacotec GmbH, Düsseldorf, Germany
[d]Department of Materials Science, Montanuniversität Leoben, Leoben, Austria
[e]Erich Schmid Institute for Materials Science, Austrian Academy of Sciences, Leoben, Austria
[f]Materials Center Leoben GmbH, A-8700 Leoben, Austria

Abstract

The lifetime of coated cutting tools is decisively influenced by residual stress gradients across cutting edges. Here, cross-sectional X-ray nanodiffraction with a beam size of 35×25 nm^2 was used to retrieve gradient properties of a ~2 µm thick TiN coating on WC–Co substrate. The planar regions next to the edge exhibit gradual and constant stress profiles with anisotropic defect build-ups on the flank and rake faces, respectively. Directly at the edge, nonlinear lateral and cross-sectional compressive residual stress gradients up to about -3 GPa were observed. The coating's $\langle 111 \rangle$ fibre texture orientation correlates with the orientation of principal stress components.

Manuscript

Nanocrystalline protective transition metal nitride coatings used in machining industry to enhance the lifetime of cutting tools are severely thermo-mechanically loaded during operation, especially at the tool edge that contacts the workpiece material [1–3]. This imposes strong demands on compositional, microstructural and residual stress design strategies of coatings prepared by plasma-assisted physical vapour deposition (PVD). However, the vast majority of scientific and applied research studies deal with the design, synthesis and properties of coatings on flat substrates, fully neglecting the influence of elemental, stress and microstructure nanoscale near-edge gradients, which evolve as a result of the spatially non-homogeneous process plasma around the substrate edges [4–7]. This striking systematic inconsistency is caused mainly by the unavailability of characterization approaches to assess some of those gradients at the nanoscale.

In previous studies, mostly morphological and chemical near- edge gradients in TiAlCrYN [5], TiAlN/VN [4], TiN [8], CrN [7] and TiAlCrSiN [9] coatings were analysed, indicating the coatings' thickness, roughness and/or Al/Ti ratio dependence on the cutting edge shape (and edge angles), the direction of the incoming ions and/or the accelerating bias voltage magnitude. Macak *et al.* [5] reported 26% thickness increase and 14% Al/Ti ratio decrease in a TiAlCrYN coating on a WC–Co sharp edge with 30° opening angle. Until now, residual stress and microstructure gradients have, however, been characterized only at meso– and micro-scale along edges of TiN [8] , CrN [7] and TiAlCrSiN [9] coatings using conventional X-ray diffraction (XRD) and Raman spectroscopy. Exemplary, in an arc-evaporated TiAlN coating [9] , a stress relaxation from -5.5 to -2.5 GPa was observed from the centre towards the cutting edge using laboratory XRD.

There has been an effort to assess the stress distribution across coated cutting edges using modelling approaches [10, 11]. Gunnars and Alahelisten [12] developed a two-dimensional (2D) finite-element model of residual stress distribution across a diamond coating cutting edge area on WC–Co deposited by chemical vapour deposition, neglecting, however, the growth stress component. The model revealed that (i) the out-of-plane component of the principal stress tensor is orientated along the surface-normal of the edge and (ii) the deviation from the in-plane biaxial stress state scales with the ratio between the coating thickness, the edge radius and the thermal stress. Although the model can be transferred also to other coating-substrate systems, there has not been any theoretical or experimental work published so far, evaluating growth stress evolution at the cutting edge.

In this work, results from cross-sectional X-ray nanodiffraction (CSnanoXRD) characterization of lateral and cross-sectional gradients of residual stresses and crystallographic texture across a TiN coated cutting edge area on a WC–Co substrate are primarily discussed. The aim is to advance the understanding of the stress state and microstructure gradients in PVD coatings deposited onto edge areas and provide nanoscale experimental data for further coating optimisation.

The TiN coating was prepared by cathodic arc evaporation (CAE) in a voestalpine eifeler Vacotec alpha400P deposition system equipped with six powder metallurgical Ti cathodes operated at a cathode current of 90 A, a substrate bias voltage of −100 V, a nitrogen pressure of 4 Pa and a substrate temperature of 480°C. The coating was deposited onto a commercial cemented carbide (WC, 10 wt.% Co) cutting insert with dimensions of $12.65 \times 12.65 \times 4.65\,\mathrm{mm}^3$, a central hole with a diameter of 5.4 mm, an edge opening angle of 76°, and an edge radius of ~10 µm, which was smoothened prior to deposition (*cf.* Suppl. Fig. S.A.1b). The cutting edge was mounted horizontally on the substrate holder with the flank face of the substrates facing the cathodes and moved in two-fold rotation at a cathode-to-substrate distance of ~100 mm (*cf.* Suppl. Fig. S.A.1a). After deposition, a cross-sectional lamella with a thickness of ~40 µm was prepared and characterized at the ID13 beamline of the European Synchrotron Radiation Facility using an X-ray beam with dimensions of $35 \times 25\,\mathrm{nm}^2$ (*cf.* Fig. A.1) [13, 14]. After the alignment of the substrate-coating interface parallel to the incident beam, a total number of 270,541 2D-diffractogramms were recorded in a (y, z) field-of-view of $27.5 \times 24.5\,\mu\mathrm{m}^2$ with a step of 50 nm and analysed using the pyFAI software package [15, 16]. The detector calibration was performed using a NIST corundum powder [13].

After the synchrotron experiment, the cross-section of the edge was prepared by focused ion beam (FIB) milling in a ZEISS LEO 1540XB CrossBeam, first using the gas injection system to deposit a tungsten protection layer in order to inhibit surface damage and using final polishing currents in the range from 500 to 20 pA. Scanning electron microscopy (SEM) was performed in a ZEISS LEO1525 SEM at an acceleration voltage of 3 kV. X-ray spectroscopy analysis (EDS) was performed in the SEM by a Bruker Quantax spectrometer at an accelerating voltage of 10 kV and with a 60 µm aperture and quantified by built-in standards. Complementary laboratory XRD residual stress analysis using the $\sin^2\psi$-method of the sample on the flank and rake face, respectively, was performed using a Rigaku SmartLab 5-circle X-ray diffractometer equipped with Cu-Kα radiation, a parabolic multilayer mirror in the primary beam and a secondary graphite monochromator. Partial laboratory pole figure measurements were performed using Schultz's reflection method using α

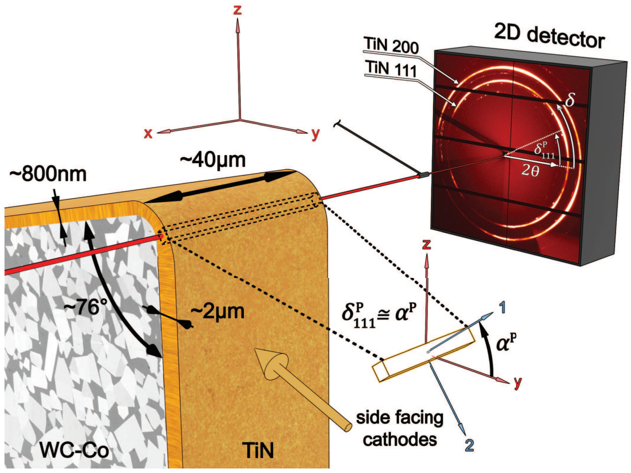

Figure A.1.: Schematic representation of the synchrotron setup. The axes x, y and z indicate the global coordinate system, 1 and 2 display the local orientation of the principal stress tensor for each measurement point, where α^{P} represents the rotation with respect to the global coordinate system. $\delta^{\mathrm{P}}_{111}$ represents the orientation of the azimuthal maximum corresponding to fibre axis of the 111 Debye-Scherrer ring. Additional azimuthal maxima of the 111 Debye-Scherrer ring were found at an inclination of 70.5 ° from the fibre axis consistent with $\langle 111 \rangle$ fibre texture.

and β ranges of 0–80 and 0–360 deg.

In Fig. A.2a, the FIB-prepared cross-section of the investigated cutting edge is shown, which reveals the columnar TiN crystallites growing perpendicular to the curved substrate surface on both flank and rake faces. Even the columnar TiN crystallites that nucleated on the irregularities of the WC–Co rake face surface generated by grinding (*cf.* Figs. A.2c,d) grew perpendicularly to the local substrate surface in the initial growth stages. This behaviour is associated with the ion-assisted competitive growth of the columnar crystallites at biased substrates during CAE [17]. The growth rate and density of the coating strongly depends on the orientation of the cutting edge faces with respect to the evaporation cathodes. The TiN coating on the flank face, orientated parallel to the cathode and thus perpendicular to the incoming ion flux, grew densely to a thickness of 2 µm, whereas at the rake face, a thickness of ~800 nm was reached, accompanied by the formation of nanopores (Figs. A.2a,c,d). The maximum coating thickness of ~2.5 µm was observed at the cutting edge (Fig. A.2a), which can be associated with the highest particle flux density of the non-homogeneous plasma sheath around the WC–Co substrate [5, 7]. The EDS analysis revealed homogeneous distributions of Ti and N elements without lateral or cross-sectional gradients over the cutting edge, documented in

Suppl. Fig. S.A.2.

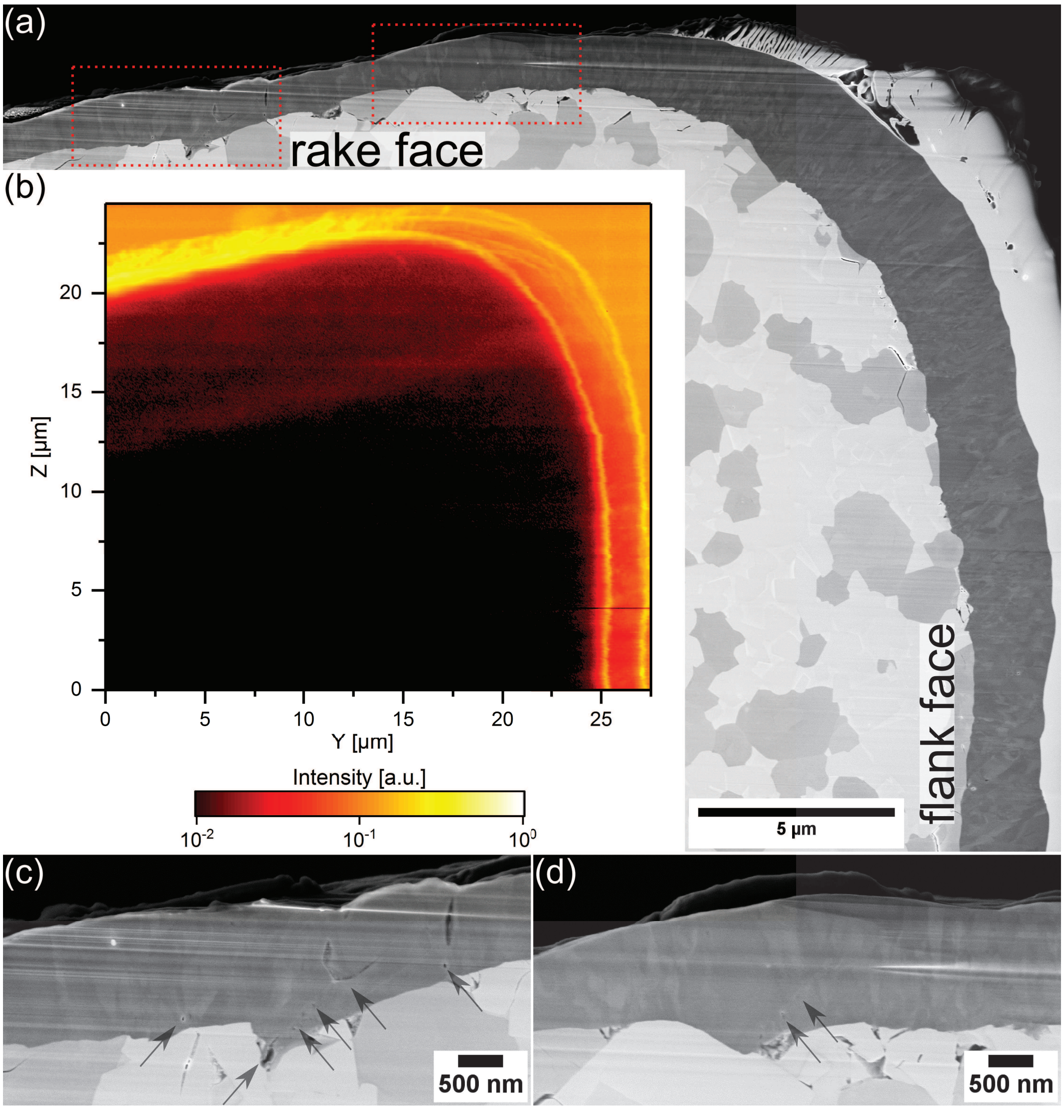

Figure A.2.: FIB-prepared cross-section of the coated cutting edge prepared after the synchrotron experiment (a). SAXS microscopy micrograph of the measured area of the cutting edge (b). The regions of interest (dashed red rectangles) in (a) are shown in (c) and (d) and display the growth perpendicular to the substrate irregularities at the rake face and the arrows indicate the formation of nanopores.

During CSnanoXRD, diffuse X-ray scattering at small diffraction angles around the beam stop (Fig. A.1) typically originates from nanoscale electron density variations associated with alternation of phases, presence of grain boundaries, interfaces, cracks, precipitates and pores [18]. In the present case, the scattered signal on the

2D detector at the diffraction angles of ~0.1–1° (corresponding to the features with sizes of ~55–5.5 nm, respectively) was integrated radially and azimuthally in order to obtain qualitative information on the occurrence of nanoscopic morphological features in the irradiated sample volume. In the small-angle X-ray scattering (SAXS) microscopy image shown in Fig. A.2b, the coating surface and coating/substrate interface can be identified due to their higher scattering contrast. A constant (isotropic) SAXS signal increase from the rake face region as well as localized increase in the SAXS signal intensity along bent lines progressing from the rake face towards the cathode position are observed in Fig. A.2b. A complementary analysis of full width of half maxima (FWHM) of TiN 111 Debye-Scherrer (DS) ring (presented in Suppl. Fig. S.A.3), however, did not reveal any remarkable variation in FWHM, which could be correlated with the SAXS data. Therefore, the increase in the SAXS intensity from the rake face in Fig. A.2b can be interpreted as an increase in the density of nanopores caused by an underdense growth, to which the FWHM is not sensitive and which were detected also by SEM (*cf.* arrowed regions in Figs. A.2c and d). The formation of the SAXS intensity lines (Fig. A.2b) might indicate the formation of planar domains within the coating, which are separated by an interface-like microstructural feature, expressed as an underdense layer in the coating, which originates probably from the nonuniform deposition conditions and changing particle incidence angle during rotation of the substrate during competitive coating growth.

The deposited coating possessed a pronounced $\langle 111 \rangle$ fibre texture, as indicated by exemplary TiN 111 DS rings in Fig. A.1 and the data in Fig. A.3a showing the orientation of the fibre texture axes with respect to the y-axis (*cf.* Fig. A.1). On the flank face and in the corresponding cutting edge area at $z \cong 0 - 18\,\mu\text{m}$, the $\langle 111 \rangle$ fibre texture axes are oriented approximately perpendicular to the substrate surface. However, at the rake face ($y \cong 0 - 17.5\,\mu\text{m}$) and at the cutting edge area ($y \cong 20\,\mu\text{m}$) (Fig. A.3a), $\langle 111 \rangle$ fibre texture are tilted slightly towards the direction of the incoming ions, respectively. These effects can be explained by changes in the initial trajectory of the ions during growth, which is horizontal (parallel to the rake face/deposition flux) and which are diverted from this path by the bias voltage applied to the substrate [19]. The change in the orientation of the $\{111\}$ planes is consistent with the data received from the SAXS micrograph presented in Fig. A.2b and indicates a rather abrupt lateral change in the coating growth mode along the edge with increasing coating thickness.

The residual stress distribution across the cutting edge was evaluated from the directional distortion of the TiN 111 and 200 DS rings, which is caused by the elastic strain present in the coating. For each measurement position (y, z), the ellipticity

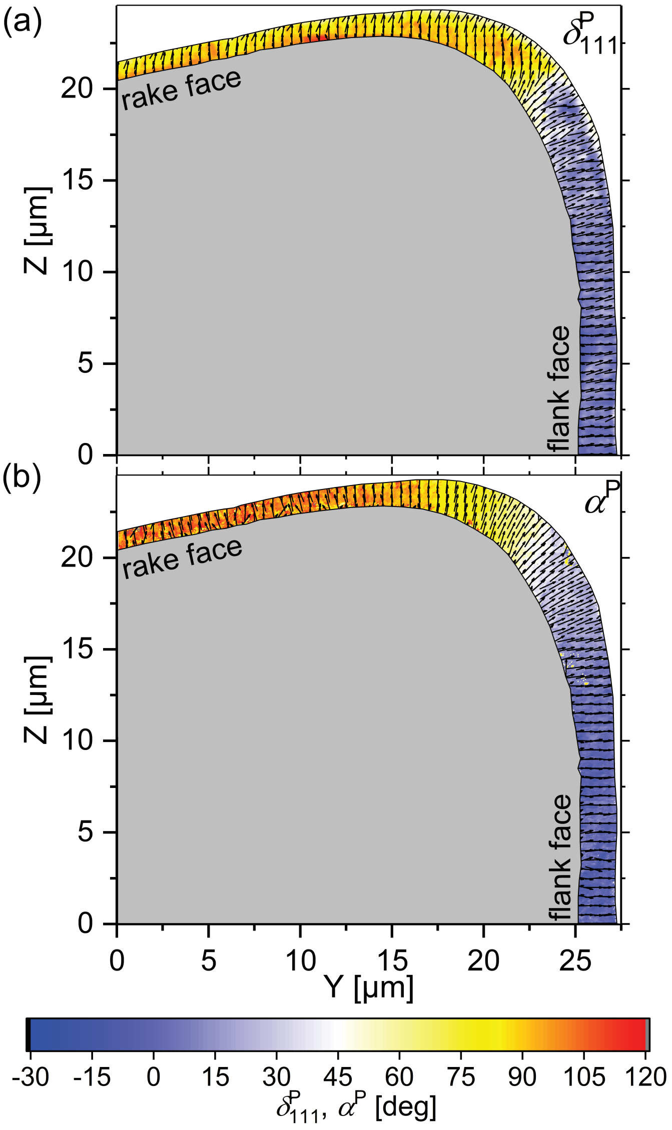

Figure A.3.: 2D contour plot of the orientation $\delta^{\mathrm{P}}_{111}$of the $\langle 111\rangle$ fibre texture (a) and the transformation angle $\alpha^{\mathrm{P}}$of the principal stress tensor (b).

of the DS rings can be expressed as a result of two normal stress components σ_{YY} and σ_{ZZ} and shear stress component stress σ_{YZ} defined in the xyz sample coordinate system (Fig. A.1). Therefore, the azimuthal angle δ dependencies of Bragg's angles θ^{111}_{δ} and θ^{200}_{δ} were used to evaluate lattice parameters $d^{111}_{\delta}$and d^{200}_{δ} using Bragg's law. Then, the unknown stress components $(\sigma_{\mathrm{YY}}, \sigma_{\mathrm{ZZ}}, \sigma_{\mathrm{YZ}})$ at each particular measurements position (y, z) were determined by solving an overdetermined system of linear equations based on XRD Hooke's law [20], applying the experimental lattice parameter values $d_\delta^{111}$and d_δ^{200} , the X-ray elastic constants $S_1^{111} = -0.0601 \times 10^{-5}$, $\frac{1}{2}S_2^{111} = 0.2851 \times 10^{-5}$, $S_1^{200} = -0.0452 \times 10^{-5}$ and $\frac{1}{2}S_2^{200} = 0.2404 \times 10^{-5}\,\mathrm{MPa}^{-1}$ [21, 22] as well as the unstrained lattice parameter a = 0.42372 ± 0.00025 nm, which is slightly below the tabulated lattice parameter of 0.42417 nm [23]. The lattice parameter was derived from the diffraction data by considering the condition of the zero out-of-plane stress component at the surface of the flank face, whereas the uncertainty was determined from the standard deviation of the fitted θ_δ^{111}.

The evaluated $(\sigma_{\mathrm{YY}}, \sigma_{\mathrm{ZZ}}, \sigma_{\mathrm{YZ}})$ stress distributions are presented in Suppl. Fig. S.A.4 and indicate gradual stress magnitude changes in the sample coordinate system. For each (y, z) position, $(\sigma_{\mathrm{YY}}, \sigma_{\mathrm{ZZ}}, \sigma_{\mathrm{YZ}})$ stress values were used to calculate the orientation of the principal stress components (σ_1, σ_2) (Fig. A.1) as well as their orientation by using

$$\tan 2\alpha^{\mathrm{P}} = \frac{2\sigma_{\mathrm{YZ}}}{\sigma_{\mathrm{YY}} - \sigma_{\mathrm{ZZ}}}$$

and

$$\sigma_{1,2} = \frac{\sigma_{\mathrm{YY}} + \sigma_{\mathrm{ZZ}}}{2} \pm \sqrt{\left(\frac{\sigma_{\mathrm{YY}} - \sigma_{\mathrm{ZZ}}}{2}\right)^2 + \sigma_{\mathrm{YZ}}^2}, \tag{A.1}$$

where α^{P} is the transformation angle, indicating the orientation of the stress component σ_1 (cf. Fig. A.1). The α^{P} distribution presented in Fig. A.3b indicates that the orientations of the principal stress components σ_1 and σ_2 (Eq. A.1) correlate with the substrate surface out-of-plane and in-plane directions, respectively. Moreover, the α^{P} distributions in Fig. A.3b together with the data from Fig. A.3a orientation of the principal stress tensors document that the ⟨111⟩ fibre texture axes orientations and the correlate locally.

The evaluated (σ_1, σ_2) data indicate that the out-of-plane stress σ_1 values, lying in the range of $\sim (-250, +250)$ MPa, are negligible up to ~10% of σ_2 , and the principal stresses σ_2 represent dominant residual stress components within the coating in the range of $\sim (0, -2.5)$ GPa (*cf.* Suppl. Fig. S.A.5). However, the absolute values of the principal stresses presented in Suppl. Fig. S.A.5 depend on the actual unstressed lattice parameter at the measurement positions. To compensate this effect of the non-zero out-of-plane principal stress σ_1, the deviatoric contribution of the principal stress tensor $(\sigma_2 - \sigma_1)$, equivalent to the in-plane biaxial residual stress, was evaluated and is presented in Fig. A.4. At the flank face, the data document a gradual increase in compressive stresses from ~—1.2 to ~—2.5 GPa, which can be interpreted by a gradual microstructure evolution during competitive coating growth [24, 25]. Directly within the cutting edge area, the in-plane stresses close to the substrate surface are practically negligible and increase towards the surface up to -3 GPa. Consistent with the position of the SAXS lines in Fig. A.2b, a stress increase can be observed approximately at half of the coating thickness within the cutting edge region. At the rake face, the in-plane stresses are compressive up to ~-3 GPa, no pronounced stress gradients can be observed and the stress values scatter (Fig. A.4), probably as a result of the nanoporous microstructure, as indicated by the SAXS data in Fig. A.2b.

The observed (in-plane) deviatoric stresses ($\sigma_2 - \sigma_1$) in Fig. A.4 can be interpreted as a result of growth stress development during multiple nucleation events and unique coating microstructure growth evolution [26] as well as thermal stress developed during cooling from deposition to room temperature. The thermal stress component [27] was determined as ~1000 MPa, considering thermal expansion coefficients of cemented carbide ($4.5 \times 10^{-6}\,\mathrm{K}^{-1}$ [28]) and TiN ($9.5 \times 10^{-6}\,\mathrm{K}^{-1}$ [29]) and elastic constants from [22]. Therefore, the observed predominantly compressive overall stress in Fig. A.4 indicates that the compressive growth stress developed to a much higher extent than the tensile thermal stress component due to the highly energetic growth conditions during CAE. Furthermore, the compressive stress at the cutting edge evidently decreases towards the coating/substrate interface and increases towards its surface, which is in contrast to the stress distribution at the rake face (Fig. A.4). This is in agreement with the numerical results from [12, 30]. All previously published numerical and experimental residual stress data from cutting edges [9, 12, 30] have, however, not considered the complex microstructure evolution during competitive coating growth resulting in intrinsic growth stress gradients, which were evidenced in this study. The present results document that the complex cutting edge geometry and the predominantly horizontal particle flux result in the formation of a graded microstructure with pronounced lateral and cross-sectional stress gradients and varying density of nanoscopic features reflected by the SAXS signal. The residual stress discontinuity in the vicinity of the cutting edge, at the SAXS line position, might be interpreted by multiple coating re-nucleation during coating growth, which is also supported by the rather constant column width over the coating thickness (*cf.* Fig. A.2a). The nearly negligible stress magnitude at the substrate/coating interface directly at the edge (Fig. A.4) can also be a consequence of a locally enhanced deposition temperature as suggested by [5, 7], together with a strong gradient of residual stress towards the surface, which both could be a consequence of the increased ion flux, as discussed above. Anyway, the gradual

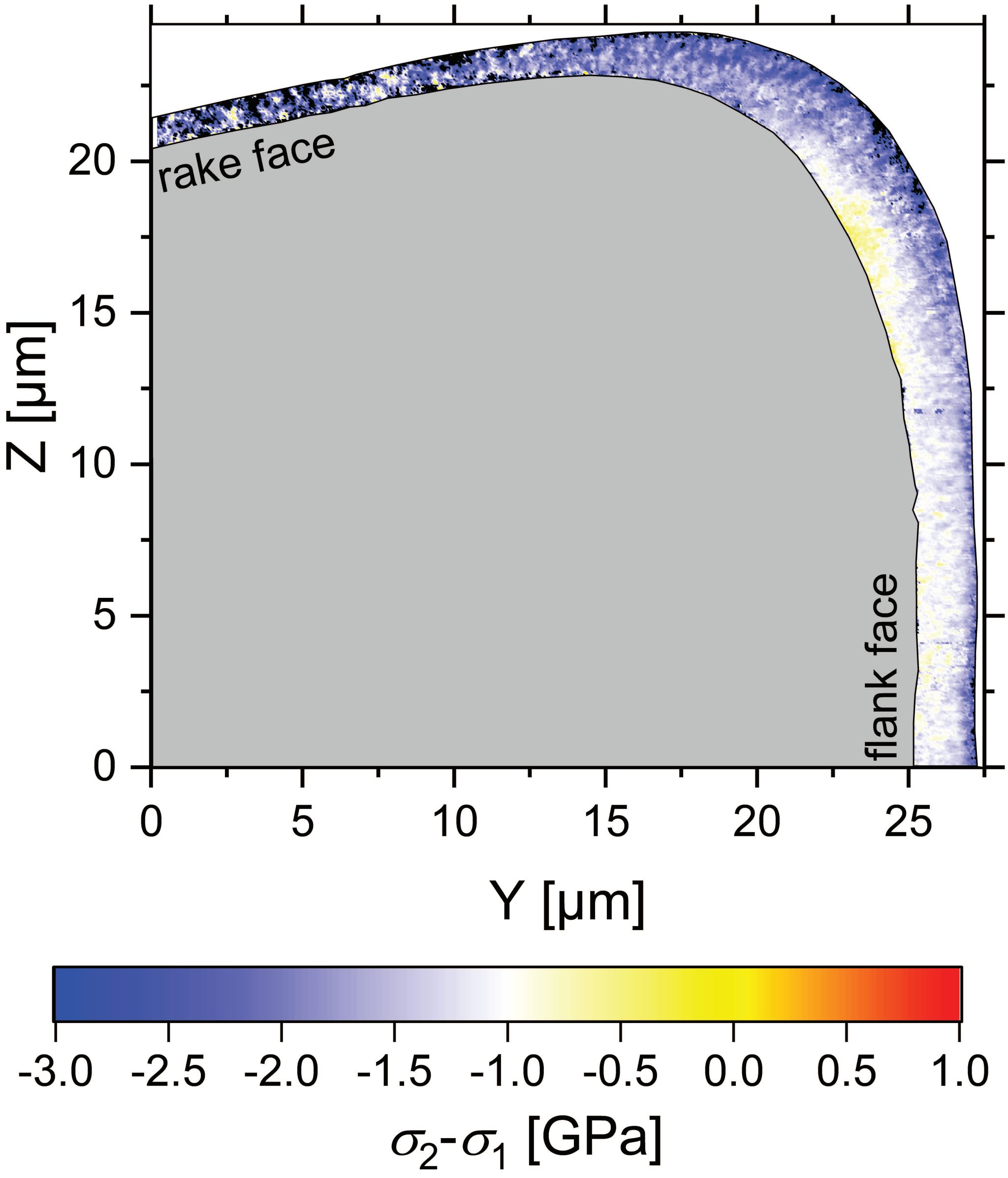

Figure A.4.: 2D contour plot of the maximum deviatoric stress component ($\sigma_2 - \sigma_1$).

compressive stress increase with coating thickness at the cutting edge together with the observed stress discontinuity and the spatial variation of residual stresses at the rake face may represent a reliability issue during operation.

In order to verify the results from CSnanoXRD, laboratory XRD measurements were performed on the TiN 111 and 200 reflections. The pole figures are presented in Supp. Fig. S.A.6c,d and further confirm ⟨111⟩ fibre texture, consistent with the corresponding synchrotron data (Suppl. Fig. S.A.6a,b). The reflection shift revealed average compressive biaxial in-plane stress of -1.7 ± 0.2 and -2.5 ± 0.4 GPa on the flank and rake faces, respectively, which is in good agreement with the data shown in Fig. A.4.

In summary, the unique CSnanoXRD approach revealed a correlation between nanoscale lateral and cross-sectional gradients of microstructure and predominantly compressive residual stresses across the cutting-edge area of TiN coating, in detail, a varying density of nanoscopic features identified by the SAXS microscopy (Fig. A.2b) and possible multiple nucleation regions with stress discontinuities (Figs. A.3a, A.4), whose origin should be further investigated. These unique results allow for further coating optimization to prolong lifetime of coated cutting tools.

Acknowledgments

This work has been financially supported by the Christian Doppler Research Association. The financial support by the Austrian Federal Ministry for Digital and Economic Affairs and the National Foundation for Research, Technology and Development is gratefully acknowledged. Special thanks are devoted to Gabriele Felber for the careful preparation of the synchrotron lamella.

Supplementary material

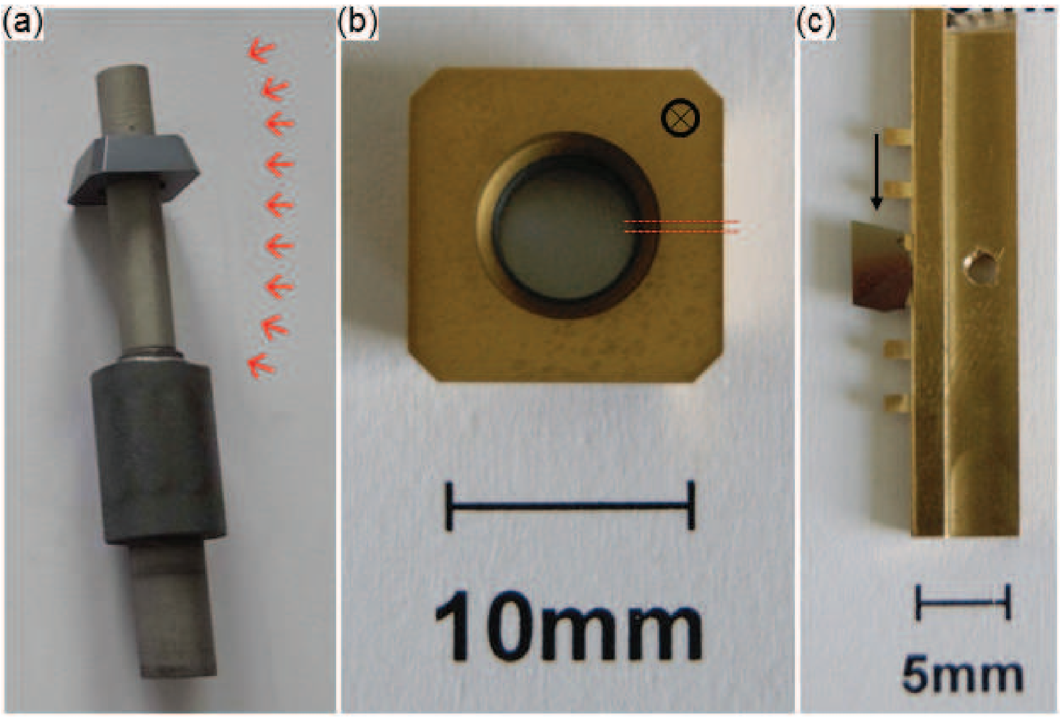

Suppl. Figure A.1. The sample during various stages of preparation. (a) Assembly of the uncoated cutting insert on the substrate holder (the red arrows indicate the direction of the particle flux), (b) the cutting insert after deposition of TiN (the dashed lines indicate the part to be cut for the synchrotron experiment), and (c) the cutting insert prepared for the synchrotron experiment (the arrow indicates the orientation of the upper face, cross-marked in (b)).

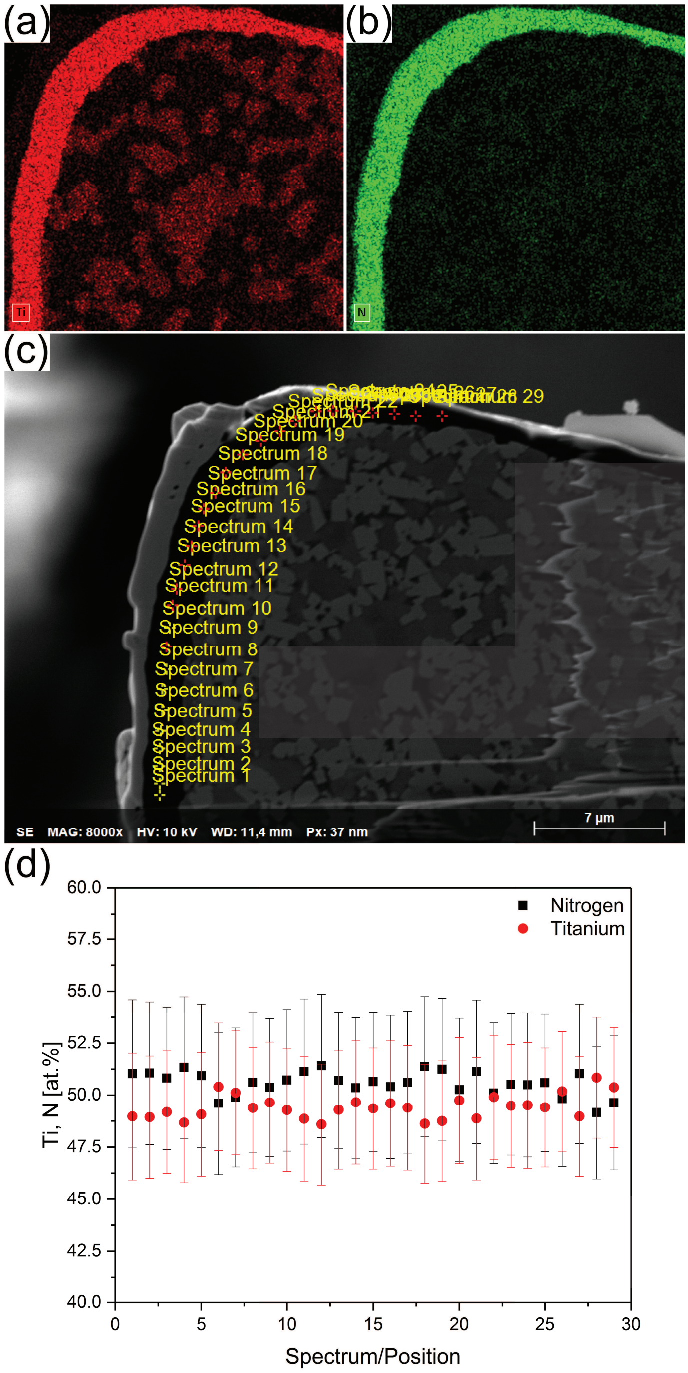

Suppl. Figure A.2. Qualitative elemental distribution of Ti (a) and N (b) around the cutting edge. Measurement positions for quantitative analysis (c) and quantitative analysis of Ti and N around the edge (d). Please note, that the elemental fluctuation detected in (d) is below the average standard deviation of 3.4 and 2.9% for N and Ti for the EDS measurement, respectively.

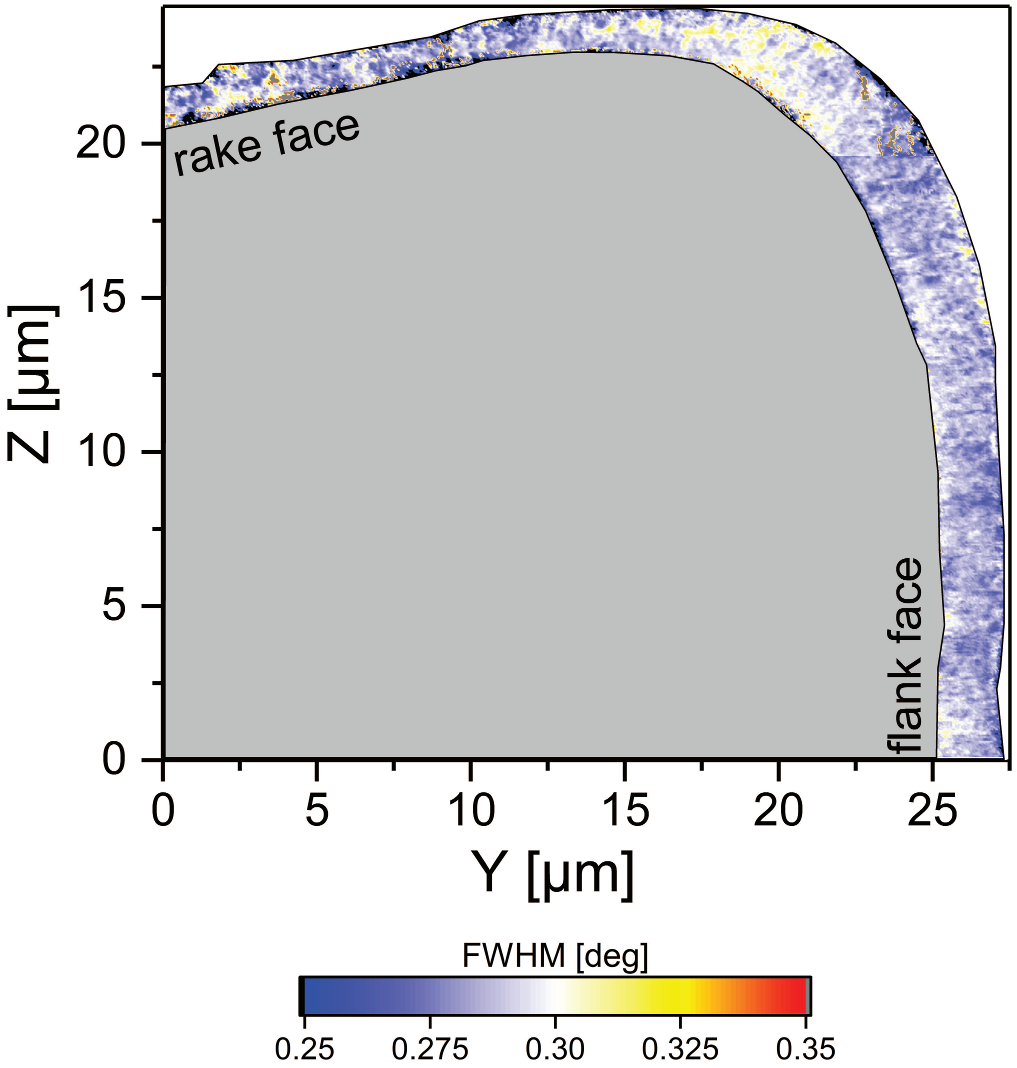

Suppl. Figure A.3. Average full width at half maximum distribution along the investigated field of view.

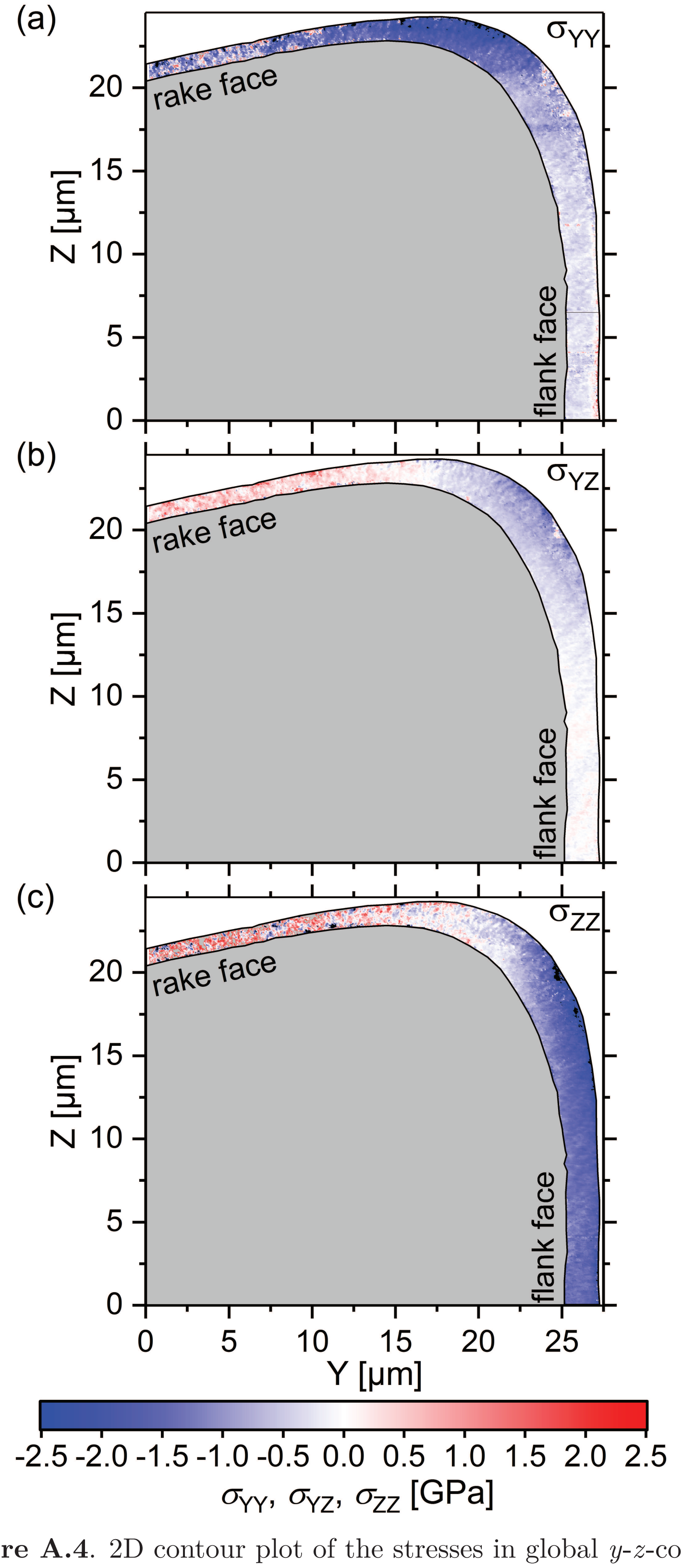

Suppl. Figure A.4. 2D contour plot of the stresses in global *y*-*z*-coordinates. (a) the normal stress σ_{YY} in *y*-direction, (b) the shear stress σ_{YZ} and (c) the normal stress σ_{ZZ} in *z*-direction.

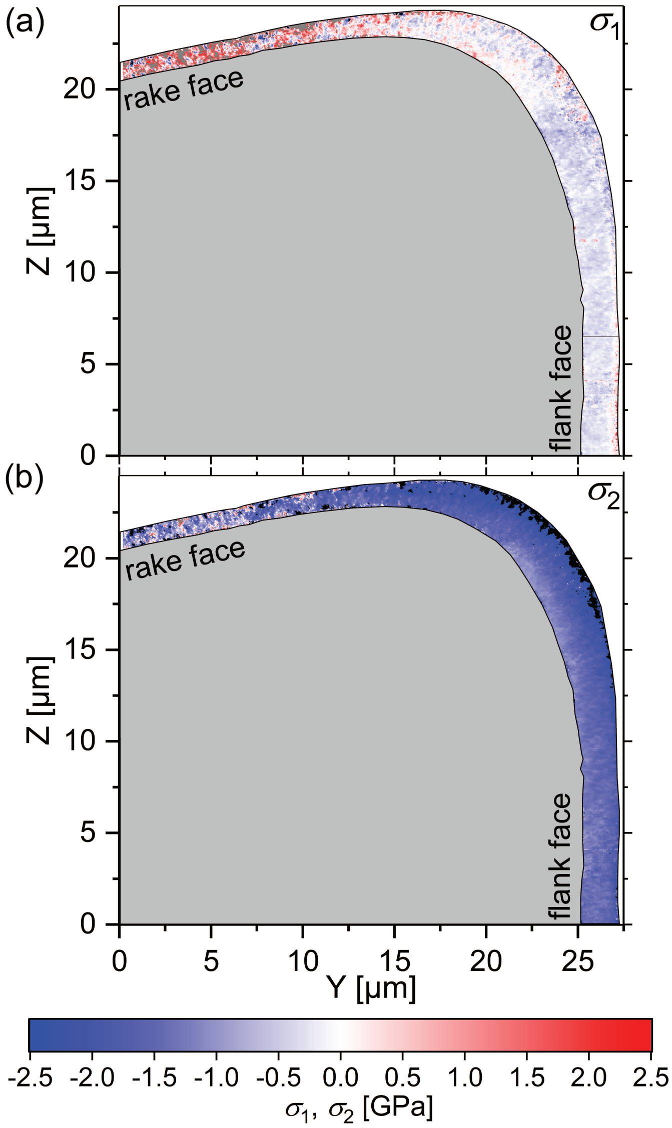

Suppl. Figure A.5. 2D contour plot of the maximum principal stress σ_1 (a) and the minimum principal stress σ_2 (b).

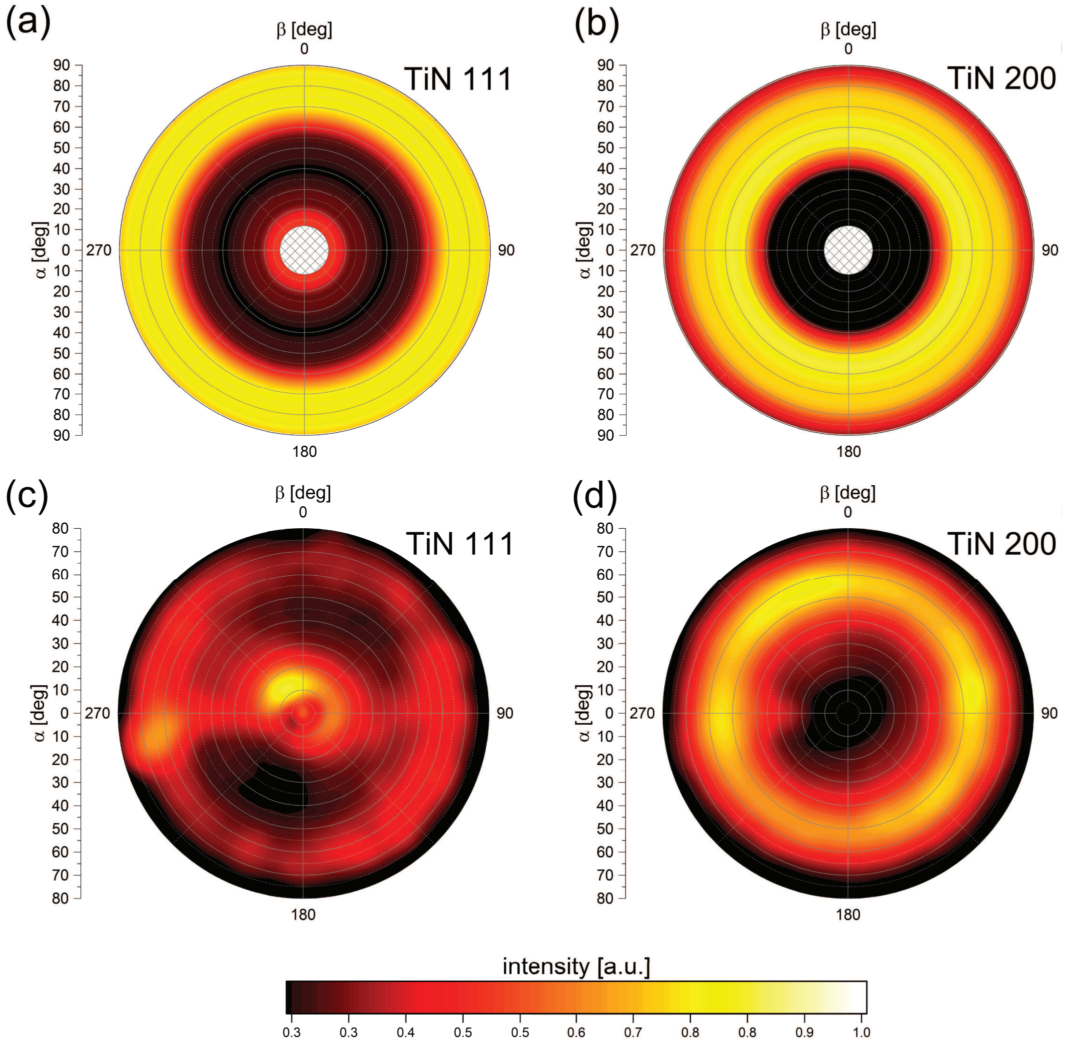

Suppl. Figure A.6. Experimental TiN pole figures processed from exemplary synchrotron data (a,b) and measured in laboratory conditions (c,d), both from the flank face, indicate the ⟨111⟩ fibre-texture of the film.

Bibliography to paper A

[1] T. Teppernegg, T. Klünsner, P. Angerer, C. Tritremmel, C. Czettl, J. Keckes et al., *International Journal of Refractory Metals and Hard Materials*, 2014, **47**, 80–85, DOI: `10.1016/j.ijrmhm.2014.07.005`.

[2] T. Teppernegg, P. Angerer, T. Klünsner, C. Tritremmel and C. Czettl, *International Journal of Refractory Metals and Hard Materials*, 2015, **52**, 171–175, DOI: `10.1016/j.ijrmhm.2015.06.013`.

[3] C. Praetzas, T. Teppernegg, J. Mayr, C. Czettl, J. Schäfer and E. Abele, *Procedia CIRP*, 2018, **77**, 118–121, DOI: `10.1016/j.procir.2018.08.240`.

[4] E. B. Macak, W.-D. Münz and J. M. Rodenburg, *Journal of Applied Physics*, 2003, **94**, 2829–2836, DOI: `10.1063/1.1597755`.

[5] E. Macak, W.-D. Münz and J. Rodenburg, *Surface and Coatings Technology*, 2002, **151-152**, 349–354, DOI: `10.1016/s0257-8972(01)01650-4`.

[6] R. Novák, I. Kvasnička, D. Nováková and Z. Malá, *Surface and Coatings Technology*, 1999, **114**, 65–69, DOI: `10.1016/s0257-8972(99)00023-7`.

[7] S. S. Kim, J. G. Han and S. Y. Lee, *Thin Solid Films*, 1998, **334**, 133–139, DOI: `10.1016/s0040-6090(98)01131-6`.

[8] J. E. Krzanowski, S. Veldhuis, P. Aliotta and D. J. Foley, *Journal of Materials Engineering and Performance*, 2012, **22**, 1611–1618, DOI: `10.1007/s11665-012-0449-z`.

[9] J. Bohlmark, H. Blomqvist, L. Landälv, S. Amerioun and M. Ahlgren, *Materials Science Forum*, 2011, **681**, 145–150, DOI: `10.4028/www.scientific.net/msf.681.145`.

[10] S. Abedini, C. Dong and I. J. Davies, *Surface and Coatings Technology*, 2019, **372**, 148–159, DOI: `10.1016/j.surfcoat.2019.05.026`.

[11] K. Holmberg, H. Ronkainen, A. Laukkanen, K. Wallin, S. Hogmark, S. Jacobson et al., *Wear*, 2009, **267**, 2142–2156, DOI: `10.1016/j.wear.2009.01.004`.

[12] J. Gunnars and A. Alahelisten, *Surface and Coatings Technology*, 1996, **80**, 303–312, DOI: `10.1016/0257-8972(95)02436-0`.

[13] J. Keckes, R. Daniel, J. Todt, J. Zalesak, B. Sartory, S. Braun et al., *Acta Materialia*, 2018, **144**, 862–873, DOI: `10.1016/j.actamat.2017.11.049`.

[14] T. W. Cornelius and O. Thomas, *Progress in Materials Science*, 2018, **94**, 384–434, DOI: `10.1016/j.pmatsci.2018.01.004`.

[15] J. Kieffer, *J. Phys: Conf. Ser.*, 2013, **425**, 202012, DOI: `10.1088/1742-6596/425/20/202012`.

[16] G. Ashiotis, A. Deschildre, Z. Nawaz, J. P. Wright, D. Karkoulis, F. E. Picca et al., *Journal of Applied Crystallography*, 2015, **48**, 510–519, DOI: `10.1107/s1600576715004306`.

[17] A. Anders, *Cathodic Arcs*, Springer New York, 2008, DOI: `10.1007/978-0-387-79108-1`.

[18] L. A. Feigin and D. I. Svergun, *Structure Analysis by Small-Angle X-Ray and Neutron Scattering*, ed. G. W. Taylor, Springer US, 1987, DOI: `10.1007/978-1-4757-6624-0`.

[19] M. Balzer and M. Fenker, *Surface and Coatings Technology*, 2014, **250**, 37–43, DOI: `10.1016/j.surfcoat.2014.02.011`.

[20] A. Zeilinger, J. Todt, C. Krywka, M. Müller, W. Ecker, B. Sartory et al., *Scientific Reports*, 2016, **6**, DOI: `10.1038/srep22670`.

[21] I. C. Noyan and J. B. Cohen, *Residual Stress*, Springer New York, 1987, DOI: `10.1007/978-1-4613-9570-6`.

[22] J. Almer, U. Lienert, R. L. Peng, C. Schlauer and M. Odén, *Journal of Applied Physics*, 2003, **94**, 697–702, DOI: `10.1063/1.1582351`.

[23] *Powder Diffraction File Card TiN 38–1420, n.d.*

[24] R. Daniel, K. Martinschitz, J. Keckes and C. Mitterer, *Acta Mater.*, 2010, **58**, 2621–2633, DOI: `10.1016/j.actamat.2009.12.048`.

[25] R. Daniel, J. Keckes, I. Matko, M. Burghammer and C. Mitterer, *Acta Mater.*, 2013, **61**, 6255–6266, DOI: `10.1016/j.actamat.2013.07.009`.

[26] I. Petrov, P. B. Barna, L. Hultman and J. E. Greene, *Journal of Vacuum Science & Technology A: Vacuum, Surfaces, and Films*, 2003, **21**, S117–S128, DOI: `10.1116/1.1601610`.

[27] R. Daniel, D. Holec, M. Bartosik, J. Keckes and C. Mitterer, *Acta Mater.*, 2011, **59**, 6631–6645, DOI: `10.1016/j.actamat.2011.07.018`.

[28] P. Hidnert, *Journal of Research of the National Bureau of Standards*, 1937, **18**, 47, DOI: `10.6028/jres.018.025`.

[29] M. Bartosik, D. Holec, D. Apel, M. Klaus, C. Genzel, J. Keckes et al., *Scripta Materialia*, 2017, **127**, 182–185, DOI: `10.1016/j.scriptamat.2016.09.022`.

[30] U. Wiklund, J. Gunnars and S. Hogmark, *Wear*, 1999, **232**, 262–269, DOI: `10.1016/s0043-1648(99)00155-6`.

B

Nanoscale stress distributions and microstructural changes at scratch track cross-sections of a deformed brittle-ductile CrN-Cr bilayer

M. Meindlhumer[a], J. Zalesak[b], W. Ecker[c], M. Rosenthal[d], S. Niese[e], P. Gawlitza[f], H. Hruby[g], C. Mitterer[h], R. Daniel[a], Jozef Keckes[b,h]J. Todt[b]

[a]Christian Doppler Laboratory for Advanced Synthesis of Novel Multifunctional Coatings at the Department of Materials Science, Montanuniversität Leoben, Leoben, Austria
[b]Erich Schmid Institute for Materials Science, Austrian Academy of Sciences, Leoben, Austria
[c]Materials Center Leoben Forschung GmbH, Leoben, Austria
[d]ESRF, Grenoble, France
[e]AXO Dresden GmbH, Dresden, Germany
[f]Fraunhofer Institute for Material and Beam Technology IWS, Dresden, Germany
[g]voestalpine eifeler Vacotec GmbH, Düsseldorf, Germany
[h]Department of Materials Science, Montanuniversität Leoben, Leoben, Austria

Abstract

In order to interpret the mechanical response of thin films subjected to scratch tests, it is necessary to elucidate local stress distributions and microstructural changes accompanying deformation across the scratch track area. Here, 50 nm synchrotron cross-sectional X-ray nanodiffraction and electron microscopy are used to characterize nanoscale multiaxial residual stress gradients and irreversible microstructural-morphological changes across a brittle-ductile film consisting of 1.2 and 2 µm thick CrN and Cr sublayers. The experimental results reveal a complex alternation of the original columnar grain microstructure and a formation of pronounced lateral and depth stress gradients, which are complemented by a finite element model. After scratching, steep gradients of in-plane, out-of-plane and shear stress distributions were revealed, ranging from −6 to 1.5 and −1.5 to 1.5 GPa in CrN and Cr, respectively, which are furthermore correlated with microstructural changes and residual curvatures. The scratch test results in intergranular grain sliding and the formation of nanoscopic intragranular defects within CrN, while Cr sublayer's thickness reduction and pile-up formation are accompanied by a bending of columnar crystallites and localized plastic deformation. In summary, the quantitative stress data elucidate the stabilizing role of the Cr sublayer, which suppresses the bilayer's catastrophic fracture during scratch tests.

B.1. Introduction

Scratch testing was developed to investigate the adhesion behaviour of hard ceramic thin films on various types of substrates and is nowadays widely used in research and technology [1, 2]. Subsequent works indicated that a great variety of intrinsic (sample) and extrinsic (method-related) parameters, such as film and substrate mechanical properties, surface roughness, indenter radius (typically 200 µm), applied loads (up to 100 N) and scratching velocity can critically alter the observed scratch behaviour, shifting the failure mode from a film-substrate interface adhesion-dependent regime to a mode where deformation/cohesive strength of the film itself is decisive [3, 4]. Bull *et al.* distinguished between adhesion and deformation/cohesive strength-related film failures using scanning electron microscopy (SEM) analysis and established classification rules for these two types of regimes [5, 6]. Especially in the case of well-adhering films, rather the cohesive strength of the film and its ability to deform plastically is of higher relevance for its resistance against scratching [4, 7, 8]. Further miniaturization of instruments led to the development of the nanoscratch test, where applied loads are in the range of 1–500 mN, using indenter tip radii of 1–20 µm, yielding the possibility to test films by scratching without interference from the substrate [7, 9–11] or even to quantify adhesion [12]. Similar to nanoindentation with a spherical indenter, also in the case of scratch testing, bending of the hard nanoceramic thin film into the plastically deformable substrate may, however, predetermine the indenter's imprinting and/or sliding behaviour [13–16]. In terms of scratch testing, the nanoscratch method has become an important tool for the characterization of nanoscale wear and friction behaviour during single asperity contact [7].

For thin films, special interest was devoted to the experimental scratch analysis of brittle-ductile multilayers. Fontalvo *et al.* [14] analysed the crack behaviour of CrN-Cr bilayered thin films with an overall thickness of 3 µm, where the incremental increase of ductile Cr interlayers thickness led to a reduction of wear by an order of magnitude, despite the fact that the remaining thickness of the hard CrN toplayer was decremented accordingly. As indicated also by an ex-situ analysis of indentation data from the brittle-ductile CrN-Cr model system in Refs. [17, 18], the introduction of thin Cr interlayers has a significant influence on the crack propagation behaviour and on the overall mechanical stability of CrN-Cr multilayers. Ductile Cr interlayers and CrN-Cr interfaces operate as crack blunting and deflection barriers, increase the multilayer's resistance against catastrophic fragmentation and serve as a stabilizing component, preventing also rupture and delamination of the film from the substrate [16, 18–20].

Significant attention has been devoted to the analysis of stress-strain distributions across scratched materials, both experimentally and using theoretical approaches at different length scales. Recent studies of Brinckmann *et al.* on coarse-grained bulk austenitic steel revealed that the complex multi-axial stress distribution introduced during scratching results in the activation of multiple slip systems within the near-surface crystallites, depending on their crystallographic orientation [21, 22]. Pioneering experimental work on the evaluation of stress distributions across scratched surfaces has been reported by Khan *et al.* [23], who investigated scratches in Al alloys by synchrotron X-ray microdiffraction with a spatial resolution of ~50 µm, after scratching using two different types of tools. Consequently, two different types of residual stress distributions were induced, as a result of "ploughing" and "cutting" modes, where the former is more similar to scratching and resulted in residual stress concentrations of ~80% higher compared to the latter [23]. Currently, however, the state-of-the-art experimental studies [24] on the scratch behaviour of nanocrystalline thin films suffer from poor spatial resolution, which does not allow for the determination of complex multiaxial stress-strain concentrations at the sub-micrometre scale.

Finite element modelling (FEM) has been the primary approach of assessing local stress and strain distributions during and after scratch tests on thin films [25–27]. Holmberg *et al.* [26] analysed stress distributions within a TiN film on high-speed-steel (HSS) during scratching with a conventional Rockwell indenter under a load of 20 N using displacement-controlled FEM. They reported principal stress magnitudes up to 3 GPa besides the scratch path and up to -1.75 GPa directly under the indenter tip. The main drawback of state-of-the-art FEM studies is, however, the missing possibility to experimentally verify the modelled stress-strain distributions at the nanoscale.

Since 2012, cross-sectional X-ray nanodiffraction (CSnanoXRD) has been continuously developed and proven to be successful in determining cross-sectional phase, microstructure and stress-strain gradients with a spatial resolution down to $\lesssim 30\,\mathrm{nm}$ [28]. Furthermore, CSnanoXRD is not only capable to resolve the aforementioned gradients, *cf.* for example [29–32], but ex-situ and in-situ studies on thin films subjected to nanoindentation [17, 33, 34] revealed great potential for the quantification of nanoscale multiaxial stress-strain distributions.

In this work, two dimensional (2D) residual stress distributions and microstructural changes are experimentally characterized at cross-sections of a bilayered brittle-ductile nanocrystalline CrN-Cr film on steel substrate by CSnanoXRD and electron microscopy techniques. The observed correlations between the nanoscale multiaxial stress distributions and the microstructural changes at scratch track cross-sections allow for elucidating elasto-plastic deformation mechanisms separately for the brittle and the ductile columnar-grained sublayers, which are further complemented by FEM numerical simulation.

B.2. Experimental

B.2.1. CrN/Cr thin film synthesis

For this study, a bilayer film consisting ofa 1.2 µm thick CrN toplayer and a 2 µm thick Cr sublayer was deposited on an electrolytically polished planar HSS plate with lateral dimensions of $20 \times 20\,\mathrm{mm}$ and a thickness of 2 mm. The film was deposited in a static mode by unbalanced reactive direct current magnetron sputtering using a powder-metallurgically produced Cr target at 350 °C and a total pressure of 1 Pa. Prior to the deposition process, the chamber was evacuated to 10^{-4} Pa, the substrate was then heated to 350°C and Ar plasma etched for 10 min. At first, the Cr sublayer was deposited in a pure Ar atmosphere and an applied substrate bias voltage of $-40\,\mathrm{V}$, whereas the CrN toplayer was grown in an $Ar+N_2$ atmosphere at a N_2 partial pressure of 0.25 Pa and a substrate bias voltage of $-80\,\mathrm{V}$.

B.2.2. Scratch testing

Scratch tracks investigated in this work were produced at constant loads in order to generate relatively homogenous stress fields along the tracks. Therefore, a set of five scratch tests was performed on the surface of the planar CrN/Cr/HSS sample in a Fischer-Cripps Laboratories UMIS nanoindenter equipped with a sphero-conical diamond indenter with a tip radius of 5 µm using constant indenter loads of 100–500 mN, in steps of 100 mN and mutual distance of ~2 mm. The length of the scratches was set to 1 mm, while the indenter tip progressed with 100 µm/s. Surface morphologies of the scratches were then evaluated using SEM. Afterwards, the two scratches produced using indenter loads of and further denoted as *200 mN scratch track* and *400 mN scratch track*, which showed either no significant cracking or multiple cracking of the top CrN toplayer, respectively, were selected for further CSnanoXRD analysis.

B.2.3. Sample preparation

The scratched CrN/Cr/HSS sample was cut perpendicularly to the scratch tracks and then polished to a thickness of ~20 µm mechanically and using a focused ion beam (FIB) workstation in order to produce a cross-sectional synchrotron lamella (Fig. B.1). According to Stefenelli *et al.* [35], changes in the residual stresses due to preparation can be neglected, when maintaining a lamella thickness at least 5 times larger than the film thickness. FIB machining was performed in a ZEISS LEO 1540 CrossBeam Workstation using Ga^+ions with a current of 100 pA. After the CSnanoXRD experiment, a ~500 nm thick tungsten protection layer was deposited onto the surface of the two scratch tracks (200 and 400 mN) using the gas injection system of the FIB workstation to protect the scratch track surface from the Ga^+ion-damage. Afterwards the cross-sections were polished applying decreasing ion currents of 50 and 20 pA in order to reveal cross-sectional morphological features such as cracks, grain reorientation and plastic deformation within the two scratch track areas. Additionally, a FEI Helios NanoLab 660 FIB microscope was used for fabrication of electron-transparent specimens of the scratch track areas. Positions for lift-outs of lamellae were carefully chosen in order to contain the scratch imprints. In order to prepare the lamellae, the FIB was operated at stepwise reduced accelerating voltages from 30 to 2 kV and currents from 20 nA to 50 pA, respectively. The bright field (BF) scanning transmission electron microscope (STEM) micrographs were taken using a JEOL 2200FS operated at an accelerating voltage of 200 kV using a spot size of approx. 0.7 nm. Transmission Kikuchi Diffraction (TKD) was performed in the SEM on a Bruker QUANTAX EBSD analysis system suited for TKD on TEM samples using an accelerating voltage of 30 kV.

B.2.4. CSnanoXRD analysis

CSnanoXRD experiments were performed at the ID13 beamline of The European Synchrotron (ESRF) in Grenoble, France [28]. A pair of multi-layer Laue lenses

(MLLs) [36] working with vertical and horizontal focal sizes of 50 and 35 nm (along z and y directions in Fig. B.1) and a focal depth of ~20 µm were used to focus the X-ray beam with a photon energy of 12.7 keV [28]. Prior to the CSnanoXRD experiment, the interface between the CrN toplayer and Cr sublayer was aligned parallel to the incident X-ray beam direction at two cross-sectional sample y positions (corresponding to the respective 200 and 400 mN scratch track areas) by performing a set of vertical absorption line-scans along the z axis at various sample φ orientations (Fig. B.1) using a passivated, implanted, planar silicon diode detector to measure transmitted X-ray intensities [17, 28]. The two optimal sample orientationswere determined by maximizing the absorption contrast between the CrN toplayer and the Cr-sublayer. Subsequently, 2D absorption scans (presented in Suppl. Fig. S.B.1) were performed to locate the scratch track areas and to determine the centres of the CSnanoXRD mesh scans.

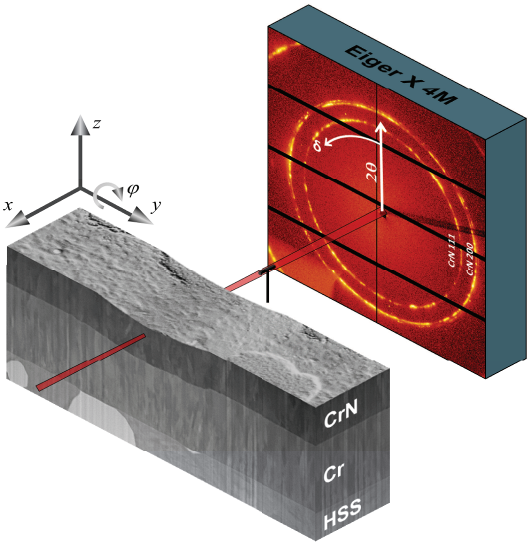

Figure B.1.: A schematic description of the CSnanoXRD experiment. A thin lamella with dimensions of ~0.02 × 5 × 2 mm^3 was scanned in an X-ray beam with dimensions of ~50 × 35 nm^2 along y and z axes using steps of 50 nm. 32,421 and 26,361 2D diffraction patterns were recorded on an Eiger X 4 M CCD detector from (16 × 5) and (13 × 5) µm^2 large scratch tracks' cross-sections, prepared at loads of 200 and 400 mN, respectively.

The two mesh scan areas of (16 × 5) µm^2 and (13 × 5) µm^2 at the positions of the 200 and 400 mN scratches, respectively, were scanned by moving the sample stepwise along the y and z axis direction using 50 nm steps. The 2D diffraction signal was recorded by a Dectris Eiger X 4 M detector at each measurement position using an acquisition time of 50 ms. Altogether, 32,421 and 26,361 2D diffraction patterns were recorded at the two respective scratch track areas. Additionally, line scans with a resolution of 20 nm were performed at presumed points of interest throughout the sample andwere used for detailed texture analysis. The exact detector geometry with respect to the sample was calibrated using a NIST corundum powder. The sample-to-detector distance was evaluated as 129.81 mm. Evaluation of 2D diffraction patterns containing CrN 111 and 200 or CrN 110 Debye-Scherrer (DS) rings (Fig. B.1) was performed using the pyFAI software package [37, 38]. The unstressed lattice constant of $a_0^{\mathrm{CrN}} = 0.416691\,\mathrm{nm}$ was determined from CrN 111 and 200 DS rings collected at the surface of an undeformed CrN film region, considering the stress-free out-of-plane film orientation [39]. For the evaluation of strain from Cr 110 DS rings, a lattice constant of $a_0^{\mathrm{Cr}} = 0.28839\,\mathrm{nm}$ was adopted from literature [40], because no stress-free orientation could be determined due to the absence of a free Cr sublayer surface. The evaluation of in-plane $\sigma_{22}^{\mathrm{m}}(x, y)$, out-of-plane $\sigma_{33}^{\mathrm{m}}(x, y)$ and shear $\sigma_{23}^{\mathrm{m}}(x, y)$ stress distributions in both phases (m) was performed using the approach from Ref. [17] (*cf.* also Supplementary Material). X-ray elastic constants $S_1^{m,hkl}$ and $\frac{1}{2}S_2^{m,hkl}$ of $S_1^{\mathrm{CrN},111} = 9.23 \times 10^{-4}\,\mathrm{GPa}^{-1}$, $\frac{1}{2}S_2^{\mathrm{CrN},111} = 4.446 \times 10^{-3}\,\mathrm{GPa}^{-1}$, $S_1^{\mathrm{CrN},200} = 2.99 \times 10^{-4}\,\mathrm{GPa}^{-1}$, $\frac{1}{2}S_2^{\mathrm{CrN},200} = 2.575 \times 10^{-3}\,\mathrm{GPa}^{-1}$, $S_1^{\mathrm{Cr},110} = 7.49 \times 10^{-4}\,\mathrm{GPa}^{-1}$ and $\frac{1}{2}S_2^{\mathrm{Cr},110} = 4.441 \times 10^{-3}\,\mathrm{GPa}^{-1}$ for CrN and Cr *hkl* reflections were adopted from literature [41, 42].

B.2.5. Simulation

A three-dimensional (3D) FE model was set up by applying the finite element software package Abaqus [43], in order to model and interpret the localized deformation phenomena, which led to the experimentally observed multiaxial stress distributions within a 1 µm thick CrN toplayer followed by the 2 µm thick Cr interlayer and 17 µm of HSS substrate. The width, height and length of the model region were set to 30, 20 and 76 µm, respectively. A half-symmetry condition was applied at the boundary plane containing the scratch path and the normal displacement, as well as the displacements at all other boundary planes except the sample surface were restricted during modelling of the scratch test. In a subsequent relaxation step representing the state during stress measurement, only the rigid body modes of the sample were restricted and the symmetry assumption remained. The interaction between indenter and specimen was defined by means of a penalty-contact with finite sliding formulation and a Coulomb friction coefficient of 0.2. A total number of 92,075 3D hexaeder elements with linear shape functions (C3D8) were used to discretise the sample. The element size was varied from ~100 nm in the contact region to ~4 µm in outer regions. The indenter tip was modelled by 3470 discrete rigid body elements as a quarter sphere with a radius of 5 µm. Isotropic elasto-plastic behaviour was defined for all materials within the simulation. The Young's modulus of CrN was assumed as 490 GPa and the Poisson's ration as 0.21. The flow stress was set to increase piecewise linearly from initially 10 to 20 GPa at 1% and to 25 GPa at 5% plastic strain, initial yield was taken from [44]. For Cr, the Young's modulus was assumed as 300 GPa and the Poisson's ration as 0.3. The yield limit of Cr was assumed to be 2 GPa with multi-linear hardening to 5 GPa and 5.5 GPa at 10% and 100% plastic deformation, respectively [40, 45]. The Young's modulus for HSS was defined as 210 GPa, with an initial flow stress of 2.5 GPa and a flow stress of 3.5 GPa at 5% plastic strain. The Poisson's ration was set to 0.3. The high hydrostatic compression under the indenter tip allowed severe plastic deformation of the involved materials before damage initiation. Therefore, the flow curves are defined up to high plastic strains. An initially equibiaxial residual stress state was defined in the simulation, according to the evaluation of the CSnanoXRD experiment, with −3 GPa for CrN and − 1 GPa for Cr. Variations of the film thickness and an interface peak of residual stress in CrN were neglected in the simulation (experimental data are shown in Suppl. Fig. S.B.2). The simulation consisted of 5 consecutive steps: (i) application of residual stress according to the evaluation of the CSnanoXRD experiment, (ii) application of the indenting/scratching force, (iii) 10 µm of sliding, (iv) withdrawal of the indenter and (v) relaxation due to cutting of the sample lamella. In the case of the 400 mN scratch, the crack formation during scratching was considered, for the sake of simplicity, as a pre-existing single crack with a length and a width of 1 and 15 µm in z and x directions, respectively, located 3 µm from the centre of the scratch path (for details *cf.* Suppl. Fig. S.B.3). It should be noted, that the length of the crack is similar to the thickness of the CrN toplayer.

B.3. Results and Discussion

B.3.1. Cross-sctional scratch track area morphologies

A detailed SEM analysis of the scratch cross-sections is presented in Figs. B.2 and B.5a,c. In general, the CrN-Cr bilayer possessed a typical columnar grain microstructure with V-shaped grains in both sublayers (Figs. B.3a-c, B.5a), and due to heteroepitaxial growth of CrN on Cr, a nucleation layer within the CrN toplayer was not formed (*cf.* Figs. B.3a-c, B.5c), in good agreement with literature [19, 40].

In the groove of the *200 mN scratch track* (Figs. B.2a, B.5a), a slight compression

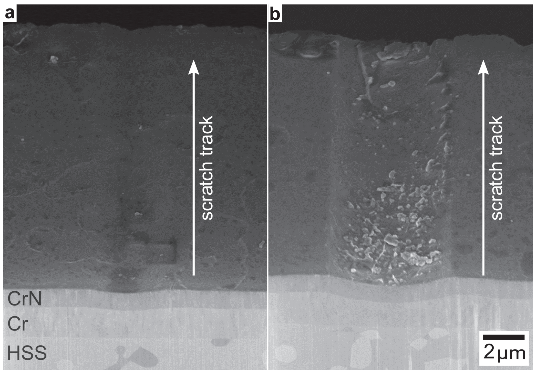

Figure B.2.: SEM micrographs collected at an angle of 45 deg. with respect to the surface of the scratched CrN-Cr bilayer film on a HSS substrate. The scratch prepared using a load of 200 mN (a) left a residual imprint approx. 3 µm wide and 300 nm deep. The scratch prepared with a load of 400 mN (b) left a residual imprint approx. 5 µm wide and 800 nm deep, as measured from the top of the pile-up at the edge to the imprint centre.

of the Cr sublayer in the central area and very small symmetrical pile ups are visible, as indicated by the horizontal dotted line in Fig. B.5a, whereas the thickness of the CrN toplayer appears to remain unchanged. Additionally, under the residual imprint region, there are no surface debris or cross-sectional cracks visible (Fig. B.2a). Furthermore, Fig. B.5a indicates additionally a change in the columnar grain microstructure, namely a bending and/or rotation of the columnar grains within both sublayers. The bending/bulging of Cr grains is observed also within complementary BF-STEM and TDK micrographs in Figs. B.3a and B.4a, respectively.

Additionally, it should be noted that the number of grains within the investigated volume was too small to identify texture qualitatively, which will be discussed later in Sec. B.3.4. In agreement with Ref. [14], pile-up formation and bulging is restricted to the Cr sublayer, whereas in the CrN layer only grain rotation takes place. An entirely different picture would be seen in a single-crystalline brittle material, like SiC, which has no ability of grain rotation or (bulk) plastic deformation, resulting in stress relaxation due to cracking outside the highly deformed zone, as reported in Ref. [46]. Here, the TEM analysis also revealed microscopic intergranular cracks starting from the film surface (Fig.B.3b) and from the CrN-Cr interface (Fig. B.3c) at the edge and in the centre ofthe scratch track, respectively. However, the cracks stop within the CrN toplayer (Fig. B.3b,c). The associated relaxation of tensile stress will further be discussed in detail in Sec. B.3.5. The groove of the 400 mN scratch track shows an imprint depth of ~800 nm measured from the edge of the pile-up to the centre of the groove (Figs. B.2b, B.5c). The presence of microscopic

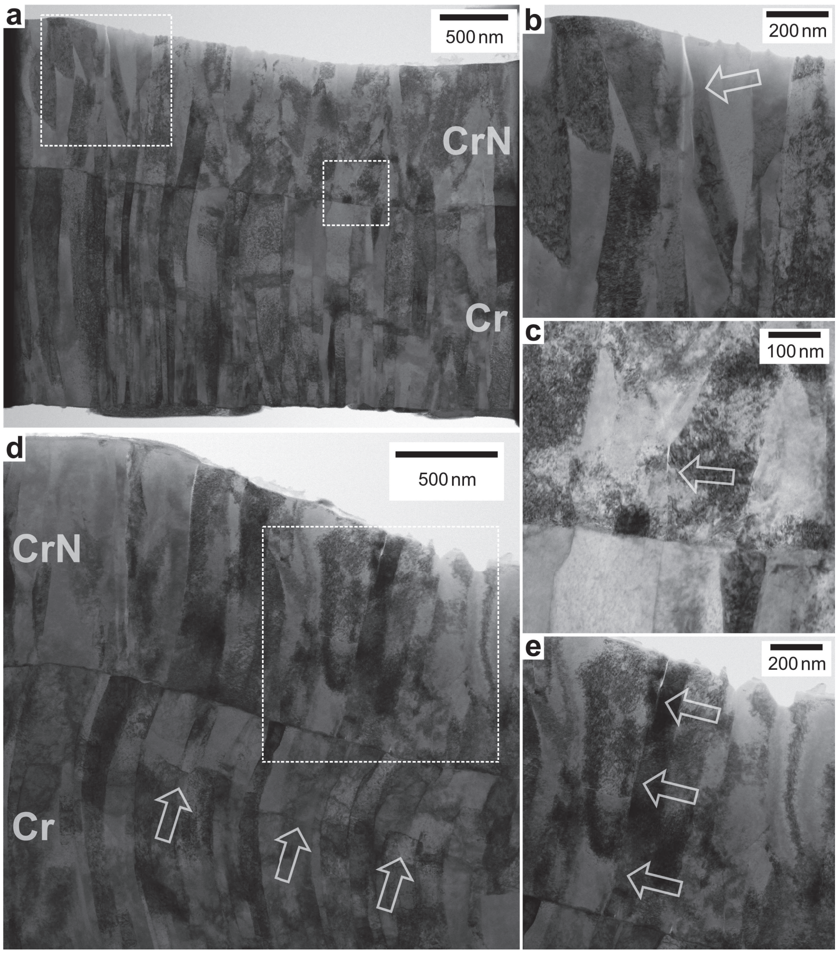

Figure B.3.: BF STEM micrograph of the 200 mN scratch cross-section (a). The dashed regions marked in (a) are magnified in (b) and (c) and show cracks propagating along the columnar grain boundaries from the surface and from the CrN-Cr interface into the brittle CrN toplayer, respectively. STEM micrograph of the 400 mN scratch cross-section (d). The dashed region marked in (d) is magnified in (e) and shows the presence of a cross-sectional intergranular crack within the CrN toplayer, which stops at the CrN-Cr interface. The arrows in (d) indicate the positions of glide planes passing through columnar ductile Cr crystallites, as visible also in Fig. B.4b.

surface debris on the imprint surface in Fig. B.2b indicates a fragmentation of the CrN toplayer and material chipping, which is confirmed also by the cross-sectional intergranular cracks in Fig. B.5c. Additionally, (i) the thickness of the Cr sublayer in the centre of the residual imprint is reduced from 2 to ~1.7 µm, whereas the thickness of CrN toplayer remains again unchanged (Figs. B.2b, B.4, B.5c), (ii) pile-ups are formed in the Cr layer at the edges of the scratch groove (Figs. B.2b,B.5c) and (iii) a rotation and/or a bending of the columnar grains in both materials can be observed in Figs. B.3d, B.4b and B.5c, in agreement with the results from Refs. [15, 16, 18].

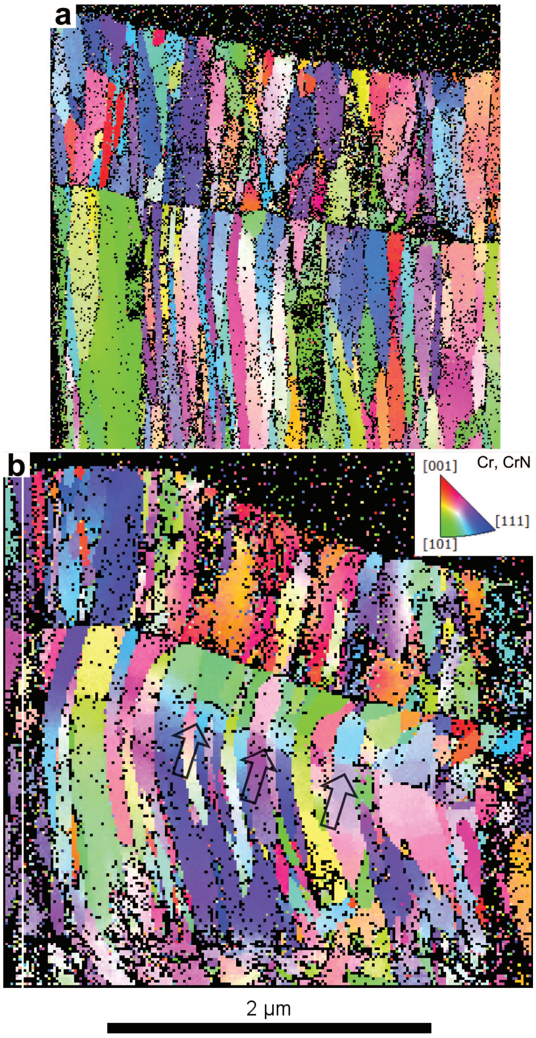

Figure B.4.: TKD maps acquired from the respective TEM lamellae with the 200 mN (a) and 400 mN (b) scratches show orientations of columnar CrN and Cr crystallites with respect to the out-of-plane [001] film orientation. The arrows in (b) indicate scratch-induced changes in the crystallites' orientation caused by plastic deformation of the ductile Cr. The respective glide planes are visible also in Fig. B.3d.

Moreover, BF-STEM and TKD micrographs shown in Figs. B.3d,e and B.4b confirm transgranular gliding of the columnar Cr grains approximately 250 nm beneath the CrN-Cr interface. This gliding is associated with the shearing ofthe columnar grains and the formation of a so-called dislocation trace line, which was also found in Cu during sliding contact at cryogenic temperatures [47–49]. Also, the bulging of Cr grains is more pronounced compared to those within the 200 mN scratch track

(Fig. B.3a). A pronounced bulging of the columnar grains is also found in CrN, as can be seen in Figs. B.3e and B.4b, which differs from the 200 mN scratch case, where only grain rotation was found in the CrN toplayer (Figs. B.3a and B.4a). Remarkably, the intergranular cracks formed during the scratch process penetrated through the entire CrN toplayer and stopped at the CrN-Cr interface (*cf.* Fig. B.3d,e), in agreement with Ref. [18]. The cross-sectional intergranular crack formation in the brittle CrN toplayer is a consequence of the larger curvature caused by the deeper imprint (*cf.* Fig. B.2) resulting in grain boundary sliding (Fig. B.3e). The latter is promoted by the relatively small cohesive energy of the grain boundaries in nanoceramic CrN, as discussed elsewhere [45].

In general, it was observed that columnar grains of the CrN toplayer were oriented normal to the surface of the sliding indenter (towards it) after the scratch test (*cf.* Fig. B.5). Contrary to this, the columnar grains of a monolithic TiN film from Ref. [34] indented with a sharp tip were reoriented parallel to the imprinting indenter facets (away from the imprint surface). While the former is attributed to plastic deformation of the underlying Cr sublayer, which allowed the CrN toplayer to adjust to the sliding indenter, the latter is interpreted mainly by a cleavage-like separation of the grains during the penetration of the layer by the indenter.

B.3.2. Small-angle X-ray scattering microscopy

Generally, diffuse X-ray scattering at relatively small diffraction angles (around the beam stop in Fig. B.1) can be attributed to electron density variation originating from the presence of nanoscopic structural heterogeneities within the X-ray gauge volume. These may include nanoscale alternation of phases, presence of grain boundaries, interfaces, cracks, roughness of surfaces and interfaces, precipitates and pores with sizes of $\sim \lambda/\theta$, where λ represents the X-ray wavelength and θ is the Bragg angle [30, 50]. In the present case, the scattered signal on the 2D detector at the diffraction angles of ~0.1 to ~1 deg. in Fig. B.1 was integrated radially and azimuthally in order to obtain a qualitative information on the occurrence of micro- and nanoscopic morphological and microstructural features within the X-ray beam gauge volume of $(x \times y \times z) = (20,000 \times 35 \times 50)\,\mathrm{nm}^3$. Fig. B.6 shows small-angle X-ray scattering microscopy (SAXSM) micrographs compiled from the CSnanoXRD data collected from the two scratch cross-sections (Fig. B.2).

In the SAXSM micrograph from the 200 mN scratch track (Fig. B.6a), the surface and the film-substrate interface can be clearly resolved due to their higher scattering contrast (Fig. B.6a). Furthermore, the difference in the electron density between

CrN and Cr and probably also in a higher concentration of structural defects within brittle nanoceramic CrN makes it possible to resolve the two sublayers. The latter is supported by findings from Ref. [40], as well as the as-deposited in-plane stress magnitudes $\sigma_{22}^{\mathrm{m}}(y,z)$ presented in Suppl. Fig. S.B.2 and discussed later in Sec. B.3.5. A U-like distribution of significantly scattering intensity is however observed symmetrically within the near-surface CrN toplayer mainly (i) at distances of ~500 nm to ~3 µm from the imprint centre and (ii) close to the CrN-Cr interface in the imprint centre with a symmetrical lateral extent of ~3 µm (Fig. B.6a). The increased SAXS intensity indicates an increased presence of micro- and nanoscopic morphological-microstructural changes or defects within the toplayer, which correlate well with particular $\sigma_{22}^{\mathrm{m}}(y,z)$ concentrations discussed in detail in Sec. B.3.5. At this stage, it can be supposed that the increased SAXS intensity is caused by a mutual sliding of V-shaped grains and formation of nanoscopic intergranular cracks like in Fig. B.3a-c.

In the SAXSM micrograph from the 400 mN scratch track (Fig. B.6b), both sublayers, the surface and the substrate can be again clearly distinguished. Within the scratch track area, a significant rise in the SAXS intensity from the CrN toplayer indicates again higher densities of through-thickness intergranular cracks (*cf.* also Figs. B.3d,e) and of nanoscopic intragranular defects formed as a result of CrN toplayer fragmentation (*cf.* Fig. B.5c), as indirectly confirmed by the texture data in Fig. B.5d, in agreement with the results from Wiecinsky *et al.* [16, 18].

A comparison of the two SAXSM micrographs in Fig. B.6 indicates also different degrees of the compression and pile-up formation of the particular Cr sublayers, both more pronounced in the 400 mN sample (Fig. B.6b). Remarkably, SAXSM micrographs documents that the thickness of the CrN toplayers remains practically unchanged, irrespective of the applied load magnitude. Furthermore, it should be noted, that the plastic deformation of the Cr sublayers (*cf.* Figs. B.3, B.4, B.5) did not obviously lead to changes in SAXS intensities in Fig. B.6, since deformation-induced dislocation movement does not affect the electron density in the investigated volume significantly.

B.3.3. 2D FWHM Analysis

2D diffraction patterns collected in the CSnanoXRD experiments were integrated cake-like using azimuthal integration range of $\Delta\delta = 10\,\mathrm{deg.}$ over the whole DS rings' azimuthal range of $\delta = 0$–$360\,\mathrm{deg.}$ in order to obtain 36 $I(\theta, \delta_i, y, z)$ dependencies. Afterwards CrN 111 and Cr 110 reflections were fitted using Gauss function and 36 FWHM(δ_i, y, z) were evaluated for every measurement position (y, z) as well as detector azimuthal position δ_i and then arithmetically averaged as $\mathrm{FWHM}(y,z) = \frac{1}{36}\sum_{i=1}^{36}\mathrm{FWHM}(\delta_i,y,z)$. Generally, the FWHM evaluated from DS rings is sensitive to the size of coherently diffracting domains, as well as to the presence of structural defects like dislocations, vacancies and other types of micro- and nanoscopic crystal lattice distortions, which can be denoted asmicrostrains of 2nd and 3rd order. Thus, by comparing the FWHM distributions from regions affected by scratch tests with regions of intrinsic defect density (formed during the deposition process, *cf.* Refs. [40, 51]), qualitative conclusions can be drawn on changes in size of coherently diffracting domains and/or microstrains as a result of the scratch process. In contrast to the SAXSM results from Fig. B.6, FWHM data reflect only scratching-induced structural changes within the crystallites and are therefore insensitive to the presence of intergranular cracks and pores in the X-ray gauge volume.

Figs. B.7 shows respective $\mathrm{FWHM}(y,z)$ of CrN 111 and Cr 110 reflections evaluated from the CSnanoXRD data. For the 200 mN scratch track, a relatively homogenous FWHM increase can be observed in CrN toplayer within in the imprint centre with a symmetrical lateral extent of ~2 µm. In the Cr sublayer, the FWHM increase is localized at distances of ~4 µm from the imprint centre. For the 400 mN scratch track, a significantly larger and homogenous increase in FWHM can be again observed within the CrN toplayer, whereas partially localized FWHM increase in Cr interlayer was detected at the positions of ~5 µm from the imprint centre as well as Cr-CrN interface.

The cross-sectional and lateral occurrence of the increased FWHM values in CrN and Cr sublayers (Fig. B.7) correlate well with the changes of out-of-plane residual stress concentrations $\sigma_{33}^{\mathrm{m}}(y,z)$ from Figs. B.8b and B.9b. In the CrN toplayers, the FWHM increase correlates with the build up a high compressive stresses $\sigma_{33}^{\mathrm{CrN}}(y,z)$, up to -2 GPa in the 400 mN scratch track (Figs. B.7b and B.9b). In the Cr sublayer, the FWHM increase correlates with the build up a high tensile stresses $\sigma_{33}^{\mathrm{Cr}}(y,z)$ up to ~2 GPa (Figs. B.7, B.8b and B.9b). Therefore, the FWHM increase in the CrN toplayers (Fig. B.7) can be interpreted by (i) the compaction of the CrN toplayer due to the normal force induced by the sliding indenter, resulting in large out-of-plane compressive stress (*cf.* Sec. B.3.5), (ii) the nanoscopic intragranular fracturing of CrN crystallites mainly due to the friction force oriented along the x-direction, (iii) gradients of 1st order strains within the gauge volume and (iv) the irreversible deformation of the CrN grains, as documented by bulged form of the CrN grains in Fig. B.3e. Especially the gradual FWHM increase towards the surface in the CrN toplayer of the 400 mN scratch track in Fig. B.7b supports the concept of the near-surface fracturing induced by the friction mechanism. In the case of Cr interlayers, the symmetric and localized FWHM increases (Fig. B.7) can be correlated with the bulging of Cr crystallites and their plastic deformation during the imprint formation. Note that in Fig. B.7b, the FWHM increase in the Cr spans the whole width of the measured sample region.

The findings from Fig. B.7 are complementary to the SAXSM-data from the CrN topalyers presented in Fig. B.6. Whereas the localized SAXS intensity increase in both scratch imprints (Fig. B.6) can be correlated with the intergranular cracks and pores formation in CrN mainly due to the changes in $\sigma_{22}^{\mathrm{CrN}}(y,z)$ magnitudes, the FWHM increase across the CrN sublayers documents an increase in the crystal defect density. This is mainly due to the imprint formation, which is accompanied by the CrN grain boundary sliding [caused by the normal force of the indenter (Figs. B.8b and B.9b), which also results in compressive $\sigma_{33}^{\mathrm{CrN}}(y,z)$ in the same region]. Furthermore there is also transgranular cracking (probably due to the friction force), which induces the reduction of the size of coherently diffracting domains and consequently the FWHM increase (*cf.* Fig. B.3e).

B.3.4. Qualitative texture analysis

Qualitative texture analysis was carried out in order to study cross-sectional changes to the Cr and CrN crystallites' orientations due to scratching. For this purpose, azimuthal intensity distributions of CrN 200 and Cr 110 DS rings were evaluated from CSnanoXRD data collected along the dashed vertical lines indicated in Figs. B.5a and c. Due to the small CSnanoXRD probe size, the diffraction statistics were rather limited, but still allowed to evaluate texture changes qualitatively. The logarithmic plots in Figs. B.5b and d show azimuthal DS rings diffraction intensities froma selected azimuthal δ angle range of ± 30 deg., with respect to the $\delta = 0$ deg. diffraction vector orientation, which corresponds approximately to the film normal direction (*cf.* Fig. B.1, Fig. B.5b,d). The distinct vertical intensity lines in Figs. B.5b,d represent diffraction intensities from fibre-textured crystallites with approximately identical orientations with respect to the sample normal. Therefore, the azimuthal positions of the lines can be used to determine the relative orientation of crystallites with respect to the sample surface normal.

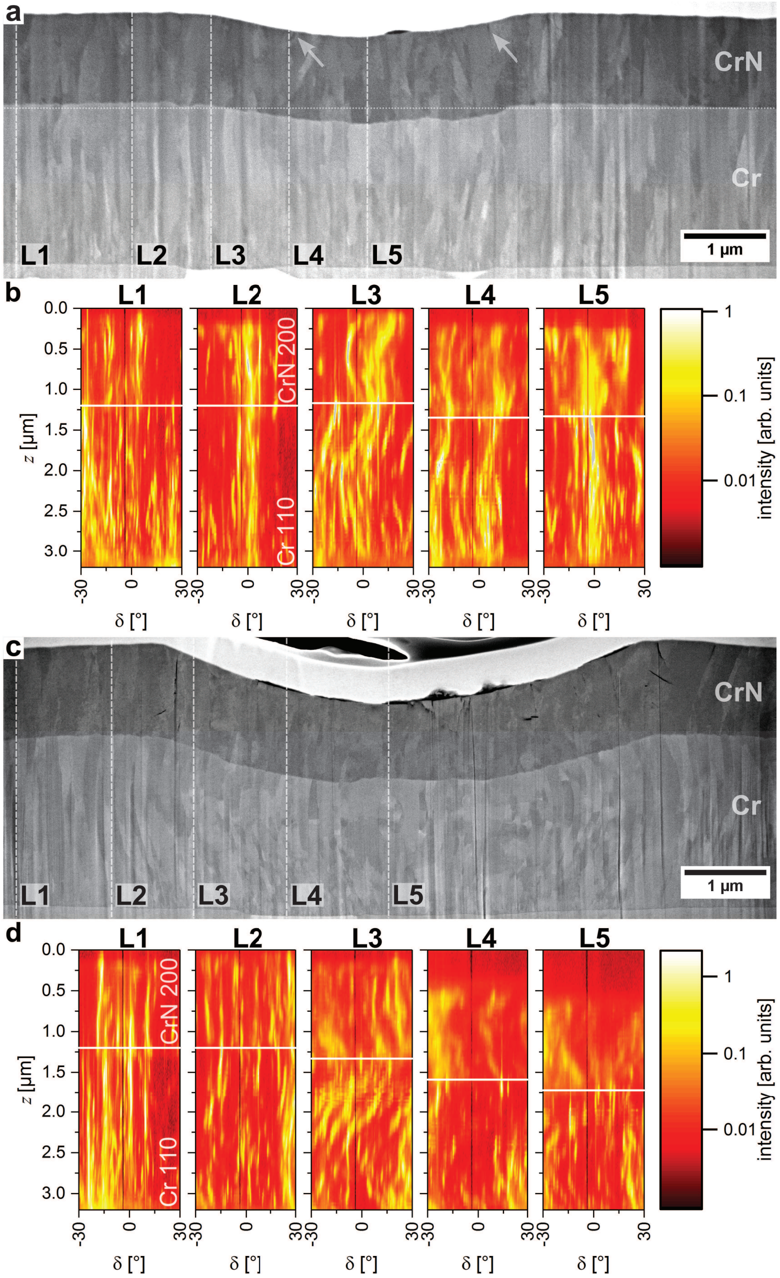

Figure B.5.: SEM micrographs (a) and (c) from FIB-fabricated cross-sections of the 200 and 400 mN scratch tracks, respectively, reveal the columnar grained microstructure and tilting/ bending of the needle-like crystallites up to ∼ 15 and ∼ 25 deg. with respect to the film surface normal direction. In the CrN toplayer, dark regions indicate the presence of cracks, which are seen to propagate in (c), across the whole toplayer at the locations ofthe pile-ups. Respective DS ring azimuthal intensity plots $I(\delta, z)$ in (b) and (d) were evaluated from CSnanoXRD data collected along the dashed lines L1-L5 in (a) and (c), respectively. CrN 200 $I(\delta, z)$ plots from predominantly $\langle 100 \rangle$ fibre textured crystallites show smearing of vertical intensity lines and indicate thus incrementing fragmentation the brittle CrN towards the imprint centres, as supported also by SAXSM data in Fig. B.6. Cr 110 $I(\delta, z)$ plots indicate a $\langle 110 \rangle$ fibre texture, whereas the oscillatory vertical intensity lines document the tilting of the Cr columnar crystallites caused by the plastic deformation present in this layer.

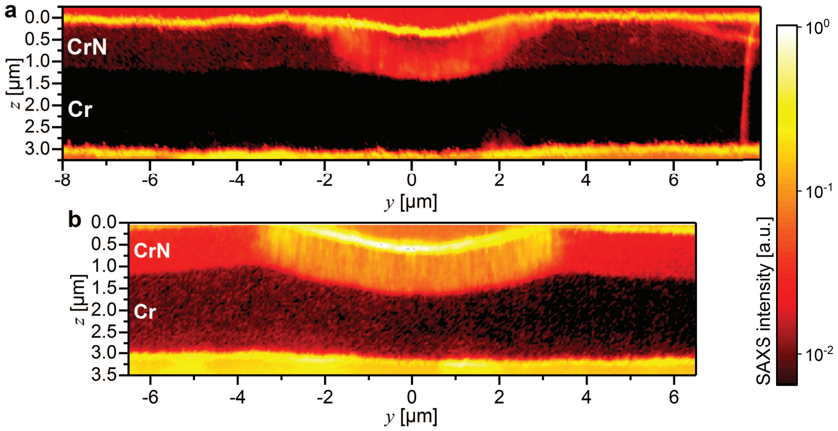

Figure B.6.: Small angle X-ray scattering microscopy (SAXSM) micrographs evaluated from 32,421 and 26,361 2D diffraction patterns collected from the 200 mN (a) and 400 mN (b) scratches, respectively. Their high scattering contrast allows resolving the interfaces and sublayers within the Cr/CrN/HSS sample. The scratch performed with 400 mN induced a significant Cr interlayer thickness reduction and also the formation of symmetrical pile-ups (b). The U-like regions with increased SAXS intensities within the CrN toplayer were attributed to the formation of micro- and nanoscopic intergranular cracks, as documented in Fig. B.3, and also to a reorientation of CrN crystallites, as documented by the texture data in Figs. B.5b,d. In addition, the shape of these high-intensity regions correlates well with the decreased in-plane stress magnitude in Figs. B.8a and B.9a.

The straight vertical intensity lines within plots L1 and L2 of Figs. B.5b and plot L1 of Fig. B.5d indicate the presence of crystallites with orientations unaffected by scratching, where CrN 200 DS ring azimuthal maximum was observed at 0 deg. down to a depth of ~1.2 µm, which allows us to identify a ⟨100⟩ fibre texture. In the deeper regions of the bilayer film, at depths of ~1.2–3.2 µm, the presence of a ⟨110⟩ fibre texture can be deduced in Cr (Fig. B.5b,d), in good agreement with Refs. [19, 20, 40]. The plots L3 and L4 with curved intensity lines in Fig. B.5b indicate a bending of crystallites within both sublayers, in agreement with the SEM micrograph in Fig. B.5a. The plot L5 from the scratch track centre with straight but much broadened intensity lines indicates a fibre texture blunting and weakening of preferred crystallite orientation in both sublayers within the 200 mN scratch track cross-section (Fig. B.5b). Similar, also the plots L2-L5 in Fig. B.5d from the 400 mN scratch track cross-section show intensity lines shifted up to an angle of ~25 deg. counter-clockwise and a steadily increased broadening of the lines towards the scratch track centre, consistent with Ref. [52], indicating a heavy deformation of the grain microstructure, especially in CrN. There is, however, a striking differ-

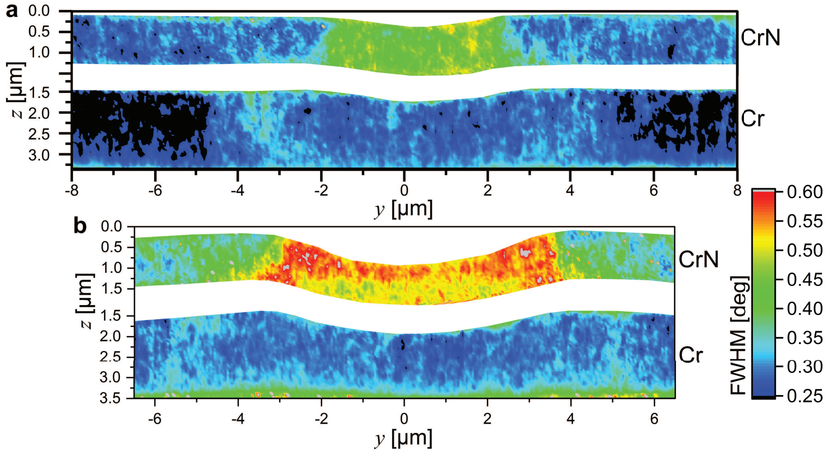

Figure B.7.: FWHM micrographs evaluated from 32,421 and 26,361 2D diffraction patterns collected from the 200 mN (a) and 400 mN (b) scratches, respectively. The CrN 111 FWHM increase is caused by nanoscopic intragranular fracturing of CrN crystallites due to the large out-of-plane compressive stress imposed by the indenter during the scratching. The symmetric and localized Cr 110 FWHM increases can be correlated with a bending of Cr crystallites and their plastic deformation. The cross-sectional occurrence of the increased FWHMs in both materials correlate well with the changes of out-of-plane residual stresses $\sigma_{33}^{m}(y,z)$ from Figs. B.8b and B.9b.

ence between the DS azimuthal distributions obtained from the CrN brittle and Cr ductile sublayers in Figs. B.5b and d. A predominant smearing of the intensity lines collected from the deformed CrN toplayers indicates fracturing of the nanoceramic nitride beneath the scratch track, which results in a large orientation spread and fibre texture blunting. The CrN toplayer fracturing correlates well with the increased SAXS and FWHM intensities in Figs. B.6 and B.7 and also with decreased in-plane $\sigma_{22}^{m}(y,z)$ and increased out-of-plane $\sigma_{33}^{m}(y,z)$ stress magnitudes, respectively, presented in Sec. B.3.5. In the case of Cr sublayers, however, predominantly oscillatory cross-sectional profiles of the intensity lines and less pronounced smearing (Fig. B.5b,d) suggest that the irreversible deformation of the metallic ductile Cr sublayers was accommodated by bending/bulging and plastic deformation of the columnar grains, in agreement with the electron microscopy data from Figs. B.3 and B.4 and partly also with the FWHM data from Fig. B.7.

B.3.5. Stress analysis across scratch track cross-sections

Ex-situ analysis of residual stress distributions was carried out using the methodology described by Ref. [34] and depicted in the Supplementary Material. At first, residual stress gradients $\sigma_{22}^{\mathrm{Cr}}(z)$ and $\sigma_{22}^{\mathrm{CrN}}(z)$ across the Cr and CrN sublayers were determined using Eq. B.4 from a CSnanoXRD line scan collected far off the scratch tracks, where the material was unaffected by the scratch experiment. As indicated in Suppl. Fig. S.B.2, the stress magnitude in the Cr interlayer is nearly constant at ~ -1 GPa, whereas the compressive stresses in CrN increases from -3 GPa at the CrN-Cr interface to -4 GPa at the surface. The compressive stresses in Cr and CrN in the as-deposited film can be attributed to ion-bombardment during film growth and additional thermal stress formed during cooling down from the deposition temperature, as extensively discussed in Refs. [40, 51].

B.3.5.1 Cross-sectional 2D stress distributions for the 200 mN scratch

Cross-sectional residual stress distributions consisting of in-plane $\sigma_{22}^{m}(y,z)$ (a), out-of-plane $\sigma_{33}^{m}(y,z)$, and shear $\sigma_{23}^{m}(y,z)$ magnitudes across the 200 mN scratch track area are presented in Fig. B.8. The results document complex lateral and depth gradients of the stresses, which are a result of the intrinsic stress state developed in the film during deposition (Suppl. Fig. S.B.2) and the scratch-induced residual deformation of the bilayer (Fig. B.8). The latter includes (i) a bending of the CrN toplayer under the indenter tip, similar to the bending of a clamped cantilever, accompanied by a thickness reduction of the Cr sublayer due to plastic flow (Fig. B.2) and (ii) a subsequent partial film curvature relaxation after the indenter tip had translated to further positions on the specimen's surface [26, 53, 54].

This bending-like deformation of the CrN toplayer results (i) in the formation of in-plane tensile stresses at the virtual clamping positions outside the deformed zone and compressive in-plane stresses in the centre of the deformed zone in the CrN near-surface region and (ii) in the formation of alike stress distributions of opposite signs at the CrN-Cr interface. When the fracture stress of CrN is locally exceeded within the tensile stressed zones, nanoscopic cracks are formed within the CrN toplayer (Fig. B.3b,c), which results in a relaxation of tensile stresses and subsequently in the formation of compressive stresses during elastic rebound after the indenter tip has moved away.

Within the CrN toplayer, this results in the observed decrease of the relatively high compressive stresses of ~ -4 GPa (in the as-deposited state) to ~ -1 GPa within (i) the near-surface region at distances of ~500 nm to ~4 µm from the imprint centre and (ii) at the CrN-Cr interface directly under the imprint centre with a symmetric lateral extent of ~3 µm (Fig. B.8a). Furthermore, the preservation of the compressive stress at the surface ofthe imprint centre and the accumulation of even higher compressive stresses up to -6 GPa at the CrN-Cr interface at distances of

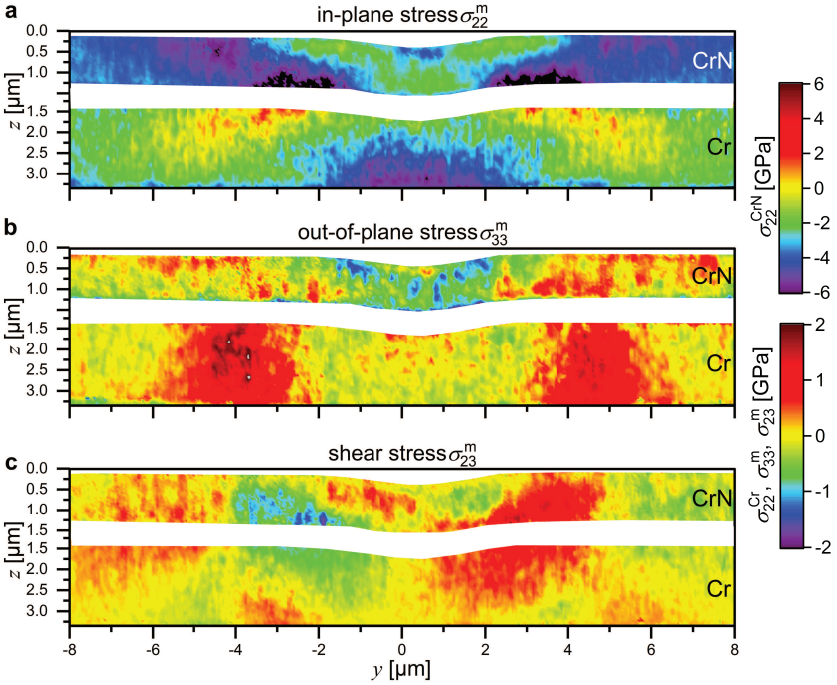

Figure B.8.: Experimental in-plane $\sigma_{22}^{m}(y, z)$ (a), out-of-plane $\sigma_{33}^{m}(y, z)$ (b), and shear $\sigma_{23}^{m}(y, z)$ (c) stress distributions evaluated from the cross-section of the 200 mN scratch track area. Note that $\sigma_{22}^{\mathrm{CrN}}(y, z)$ is displayed with a different stress scale. The data were evaluated from 32,421 2D diffraction patterns.

2 µm to 5 µm left and right of the imprint centre can also be related to this bending-like deformation (Fig. B.8a). Additionally, the compressive stress increase found at distances of 5–7 µm from the centre at the sample surface (outside the virtual clamping positions) is related to the aforementioned elastic rebound after passing of the scratching indenter. The occurrence and the U-shape of the CrN sublayer regions, where the relaxed $\sigma_{22}^{\mathrm{CrN}}(y, z)$ compressive stresses are present in Fig. B.8a, correlate well with the SAXSM data from Fig. B.6a and confirm the assumption that the relaxation was accompanied by intergranular grain boundary sliding and intergranular cracking in CrN (Fig. B.3a-c), which stops within the CrN toplayer (*cf.* Secs. B.3.1 and B.3.2).

Within the Cr sublayer, the in-plane stress distribution $\sigma_{22}^{\mathrm{Cr}}(y, z)$ exhibits relatively high compressive stresses with a magnitude of ~ -1.8 GPa directly at the imprint centre (Fig. B.8a). These originate from the process of (i) the sublayer compression and plastic deformation during loading and (ii) subsequent sublayer curvature relaxation resulting in elastic contraction in the Cr imprint centre, after the indenter tip had moved to further sample position, in agreement with Refs. [26, 53, 54]. Additionally, there are symmetric tensile stress regions $\sigma_{22}^{\mathrm{Cr}}(y,z)$ with up to 800 MPa magnitude located directly next to regions with the highest compressive stress magnitude in CrN (Fig. B.8a). These tensile stress concentrations in the Cr sublayer can be attributed to the bending of the CrN toplayer during the scratch experiment leading to an elongation of the Cr sublayer, whose further relaxation after scratching was however hindered by the deformed CrN toplayer. The corresponding stress fields $\sigma_{22}^{\mathrm{Cr}}(y,z)$ are similar to those resulting from foreign object damage, as reported for a hard steel sphere impacting on a Ti alloy in Refs. [55, 56], indicating similar deformation mechanisms as during high-rate loading of a ductile material. Furthermore, the reduction and increase of in-plane compressive stress $\sigma_{22}^{m}(y,z)$ in CrN and Cr, respectively, directly under the scratch track groove, is in particular agreement to findings from Khan *et al.* [23], where scratching of an Al-alloy also led to formation of tensile and compressive stresses in surface-near and sub-surface regions, respectively, directly under the scratch track groove.

For the $\sigma_{33}^{\mathrm{CrN}}(y,z)$ distributions in Fig. B.8b, minor compressive stresses in the range of ~ -500 MPa were revealed around the residual imprint centre over the CrN toplayer thickness with a lateral extent of ~4 µm. These are a consequence of the deformation-induced compaction of the toplayer by the sliding indenter and the remaining residual deformation. The central region is symmetrically surrounded by tensile stressed areas with a magnitude of ~800 MPa. These tensile stresses revealed besides the scratch track, starting 2 µm away from the centre at the CrN-Cr interface and extending over 4 µm at the Cr-HSS interface, can be attributed to the curvature relaxation after the further movement of the indenter. The same $\sigma_{33}^{\mathrm{Cr}}(y,z)$ stress behaviour is observed in the Cr sublayer, where the tensile stress reaches a maximum of ~1.8 GPa (Fig. B.8b). Generally, the out-of-plane stresses must represent continuity across the CrN-Cr interface, which is not the case within the contact zone of the sliding indenter. This discontinuity is most probably related to a a_0^{CrN} decrease within the process zone, as a consequence of compaction of the (partly) fragmented CrN crystallites (cf. Figs. B.3a-c, B.6a and B.7a), which expresses as a virtual out-of-plane compressive stress.

Compressive out-of-plane stresses directly under the indenter tip are well accounted for during in-situ CSnanoXRD experiments on thin films [33, 34], however, they were not found during prior synchrotron X-ray experiments carried out on scratched Al-Alloys [23], which can be attributed to much higher stress relief through plastic deformation of the Al-alloys during scratching.

The development of the shear stress $\sigma_{23}^{m}(y,z)$ is also dominated by the bending-like deformation and is antisymmetric with respect to the y-axis (Fig. B.8c). The shear stresses are (in this case) a y-axis coordinate-dependent representation of the change of the principal stress orientation, which means positive shear stress in the positive y-axis half represents coordinate-dependent positive (counter-clockwise) rotation of the principal stress tensor, whereas negative shear stress in the negative y-axis half of the stress field represents the opposite, *i.e.* clockwise rotation (Fig. B.8c). Concerning the CrN toplayer, the shear stress distribution reflects the mainly bending-like deformation, whereas in the Cr the distribution of shear stress represents the more complex stress state of $\sigma_{23}^{\mathrm{Cr}}(y,z)$ from Fig. B.8a.

B.3.5.2 Cross-sectional 2D stress distributions for the 400 mN scratch

After scratching the thin film with 400 mN load, the scratch groove exhibits significantly larger curvature compared to that of the 200 mN scratch (Figs. B.2, B.5a,c, B.6). The scratch test resulted in bending of the CrN toplayer, compaction of the Cr interlayer and in the formation of symmetric pile-ups (Figs. B.2b, B.5c, B.6b). Consequently, the $\sigma_{22}^{m}(y,z)$, $\sigma_{33}^{m}(y,z)$ and $\sigma_{23}^{m}(y,z)$ distributions shown in Fig. B.9 exhibit relatively high stress concentrations and reflect crack formation within the sublayers. Fig. B.9a indicates that the bending-like of the CrN toplayer resulted in the relaxation of compressive in-plane stress $\sigma_{22}^{\mathrm{CrN}}(y,z)$ mainly beneath the scratch track groove, as described in detail in Section B.3.5.1. This relaxation can be attributed to the formation of cracks, as visible in Fig. B.3d and B.5c and due to the deformation-induced localized tensile stress build-up, the magnitude of which exceeded the fracture strength of brittle CrN. An additional contribution is given by the friction-induced tension of the film along the x-direction, which also results in tensile stress build-up and cracking [26, 54, 57]. Next to the scratch groove, however, high compressive in-plane stresses $\sigma_{22}^{\mathrm{CrN}}(y,z)$ in CrN up to -6 GPa are revealed. These are a consequence of the symmetric pile-up formation, the CrN toplayer elongation and its subsequent elastic contraction, which was however hindered by the underlying Cr. The nearly complete relaxation of the compressive stresses $\sigma_{22}^{\mathrm{CrN}}(y,z)$ within the U-shaped groove (Fig. B.9a) correlates well with SAXSM (Sec. B.3.2), FWHM (Sec. B.3.3) and texture data (Sec. B.3.4) and supports the suggested assumption of intergranular cracking (Fig. B.3e) and intragranular fragmentation of the brittle CrN (Secs. B.3.3 and B.3.4).

The in-plane stress distribution $\sigma_{22}^{\mathrm{Cr}}(y,z)$ in the Cr-sublayer (Fig. B.9a) is qualitatively similar to that developed after scratching at the load of 200 mN (Fig. B.8a), with a comparatively higher lateral extent of the compressively stressed areas and a remarkable compressive-to-tensile stress gradient across the sublayer. As already discussed above, the compressive stresses $\sigma_{22}^{\mathrm{Cr}}(y,z)$ within the Cr-sublayer next to the HSS interface originate from the elastic contraction of the elongated sublayer after the scratch experiment. Since this elastic contraction was hindered by the CrN toplayer next to the CrN-Cr interface, tensile stresses were formed in the upper regions of the Cr sublayer (Fig. B.9a). The higher stresses in the 400 mN sample are similar to impact test in Refs. [55, 56], where a higher lateral extent of the stress fields and more pronounced pile-up formation due to foreign object damage was found when using a higher impact speed. Again, the reduction and increase of in-plane compressive stress $\sigma_{22}^{m}(y,z)$ in CrN and in Cr, respectively, directly under the residual imprint of the indenter, is in agreement to findings from Khan *et al.* [23], *cf.* Sec. B.3.5.1.

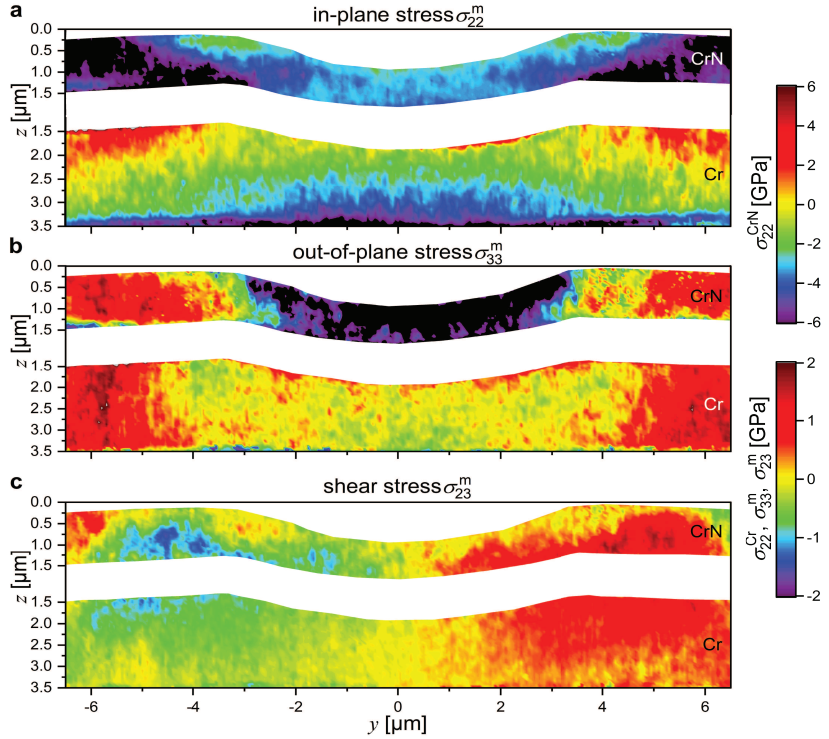

Figure B.9.: Experimental in-plane $\sigma_{22}^{m}(y,z)$ (a), out-of-plane $\sigma_{33}^{m}(y,z)$ (b), and shear $\sigma_{23}^{m}(y,z)$ (c) stress distributions evaluated from the cross-section of the 400 mN scratch track area. Note that $\sigma_{22}^{\mathrm{CrN}}(y,z)$ is displayed with a different stress scale. The data were evaluated from 26,361 2D diffraction patterns.

The out-of-plane stress distribution $\sigma_{33}^{\mathrm{CrN}}(y,z)$ in Fig. B.9b shows high compressive stress magnitudes up to -2 GPa within the scratch groove, which can be correlated with irreversible microstructural changes within the CrN sublayer (*cf.* Sec. B.3.1) and the pronounced surface curvature, which hindered surface relaxation after scratching. Besides the scratch track only minor tensile stresses were revealed in Fig. B.9b. In the Cr-sublayer, qualitatively the same stress distribution $\sigma_{33}^{\mathrm{Cr}}(y,z)$ is visible as for the scratch carried out with 200 mN load, with a higher lateral extent of the stress-free zone in the centre of the scratch track groove. Again, the discontinuity of $\sigma_{33}^{m}(y,z)$ across the CrN-Cr interface found within the contact zone of the sliding indenter could be related to unstressed lattice parameter changes, as explained in Section B.3.5.1 and documented by Figs. B.3e, B.6b and B.7b.

Relatively modest shear stress distributions $\sigma_{33}^{\mathrm{m}}(y,z)$ (Fig. B.9c) revealed in both layers beneath the scratch track (y-positions from −3 to 3 µm) document the uniaxial compaction of the CrN grains after cracking along the columnar grain boundaries and the dominance of in-plane stresses after the plastic deformation in the Cr sublayer. Besides the scratch track, there is a relaxation-induced local rotation of the principal stress axes, which is indicated by the accumulation of interface-near shear stresses with a magnitude up to −1.5 GPa at y-positions from −6 to −4 µm and with a magnitude up to 1.5 GPa at y-positions from 4 to 6 µm (Fig. B.9c).

B.3.6. Finite Element Model

In order to describe the deformation processes during the scratch experiments and to interpret the experimental stress distributions $\sigma_{ij}^{\mathrm{m}}(y,z)$ in CrN and Cr, a 3D FE model was implemented. The calculated stress distributions for the scratch tracks performed with 200 and 400 mN load are displayed in Figs. B.10 and B.11.

B.3.6.1 Modelled stress distributions for the 200 mN scratch track

The calculated stress distributions $\sigma_{ij}^{\mathrm{m}}(y,z)$ across the 200 mN scratch track area are displayed in Fig. B.10. High tensile stress concentrations $\sigma_{22}^{\mathrm{CrN}}(y,z)$ are found symmetrically in the CrN toplayer at lateral distances of 2 to 4 µm at the surface, as well as in the centre of the groove at the Cr/CrN interface with a lateral extent of 2 µm (Fig. B.10a). Additionally, high compressive stress $\sigma_{22}^{\mathrm{CrN}}(y,z)$ with a magnitude of −6 GPa is found at the respectively opposing sides of the CrN layer (Fig. B.10a). Additionally, at distances larger than 5 µm from the imprint centre, compressive stresses $\sigma_{22}^{\mathrm{CrN}}(y,z)$ can be found in the CrN toplayer.

While the magnitude of compressive stress $\sigma_{22}^{\mathrm{CrN}}(y,z)$ found in the experiment is particularly well reflected by the model (*cf.* Figs. B.8a), tensile stress magnitudes found in the model are exaggerated compared to the experimental data. This is a consequence of stress-relief due to nanoscopic crack formation in the tensile stressed zones formed during the experiment (*cf.* Figs. B.3a–c, B.5a, B.6a) and possible grain

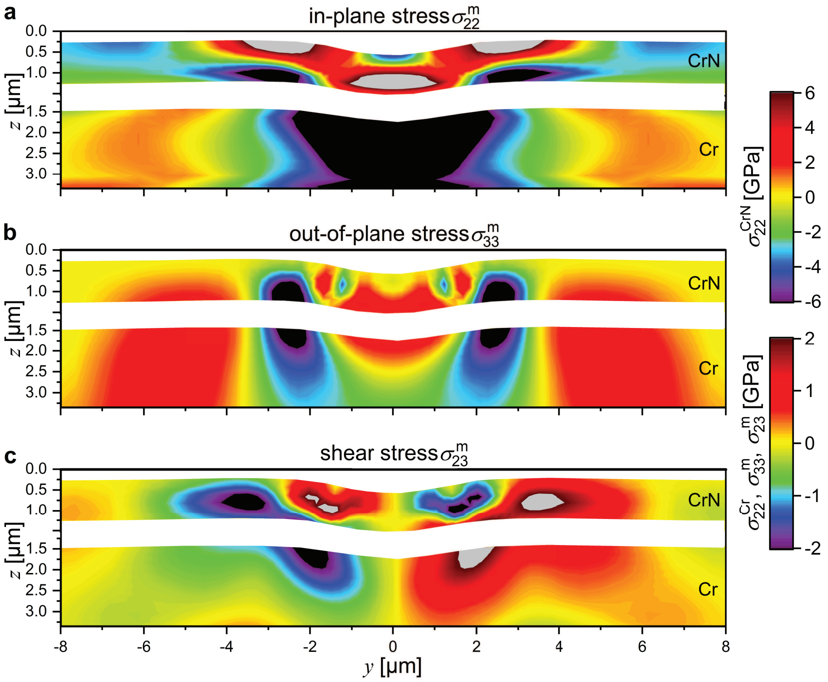

Figure B.10.: FEM calculated in-plane $\sigma_{22}^{m}(y,z)$ (a), out-of-plane $\sigma_{33}^{m}(y,z)$ (b), and shear $\sigma_{23}^{m}(y,z)$ (c) stress distributions evaluated from the cross-section of the 200 mN scratch track area. Note that $\sigma_{22}^{CrN}(y,z)$ is displayed with a different stress scale.

boundary sliding in the centre ofthe scratch track, which are both unaccounted for by the model. In the Cr sublayer, in-plane stress $\sigma_{22}^{Cr}(y,z)$ magnitudes below -2 GPa were found in the imprint centre by the 3D FE model, which were symmetrically surrounded by regions of tensile stress (y outside ±4 µm), in a good agreement with the experimental data.

The symmetric out-of-plane tensile stress concentrations $\sigma_{33}^{CrN}(y,z)$ and $\sigma_{33}^{Cr}(y,z)$ in Fig. B.10b outside the scratch track agree particularly well with the experimental results shown in Fig. B.8b. A highly compressively stressed zone at distances of ~2 to 3 µm from the centre followed by a tensile stressed zone beneath the scratch track is however not validated by the experiment (Fig. B.8b), which again is a consequence of the above-mentioned discrepancies between model and experiment (Fig. B.3a,b). The out-of-plane stresses introduced through the scratch process have to be self-compensating, consequently, the stress-relief found in the experiment due to nanoscopic cracking leads also to a reduction of compressive stresses in the surrounding areas. The shear stress distribution $\sigma_{23}^{CrN}(y,z)$ obtained by the FE model is antisymmetric along the y-axis and reflects the bending-like deformation of the scratched area (Fig. B.10c). The shear stress $\sigma_{23}^{\mathrm{Cr}}(y,z)$ calculated for the Cr sublayer reflects the complex deformation beneath the scratch track groove and, similar to compressive in-plane stresses, fits very well to the experimental findings.

B.3.6.2 Modelled stress distibutions for the 400 mN scratch track

In order to model the stress distributions $\sigma_{ij}^{m}(y,z)$ across the 400 mN scratch track area, cracks were introduced symmetrically at the edges of the groove (Fig. B.11). Adding these two symmetric cracks accomplishes the aim to model the experimental stress distributions as accurately as possible, while still maintaining the necessary computational time at a reasonable level. The observed relatively large differences between the experimental and modelled stress distributions $\sigma_{ij}^{m}(y,z)$ (*cf.* Figs. B.9 and B.11), however, can be explained by the formation of crack patterns and CrN fragmentation, as revealed by electron microscopy in Figs. B.3e and B.5c, as well as in the SAXS micrograph in Fig. B.6b.

The calculated in-plane stress distributions $\sigma_{22}^{\mathrm{m}}(y,z)$ for the CrN and Cr layers are shown in Fig. B.11a. In the CrN toplayer, the stress distributions can be divided into two parts. First, within the residual imprint (y inside ±3 µm), high tensile stress concentrations were revealed by the FE analysis, while besides the groove compressive stress was found. Comparing with the experimental data, the compressive stresses outside the scratch track groove are reproduced by the FE model (*cf.* Figs. B.9a and B.11a), but the modelled high tensile stresses within the residual imprint are not seen in the experimental results. This mismatch between the experimental and calculated data (Figs. B.9a and B.11a) can be interpreted by the above-mentioned computational restrictions and the massive microstructural changes in the CrN layer (*cf.* Figs. B.3c- e, B.4b, B.5c), which resulted in $\sigma_{22}^{\mathrm{CrN}}(y,z)$ stress relaxation within the scratch track area. In the Cr sublayer, high compressive stresses $\sigma_{22}^{\mathrm{Cr}}(y,z)$ are found within the deformed zone, which is surrounded by tensile stressed regions, both in the experimental and the modelled data (Figs. B.9a and B.11a), as a consequence of the compression due to the sliding indenter and the pile-up formation, respectively. Concerning the out-of-plane stress $\sigma_{33}^{m}(y,z)$ (Fig. B.11b) and shear stress $\sigma_{33}^{m}(y,z)$ (Fig. B.11c) distributions, the calculated stresses in the Cr sublayer agree well with the experiment (Fig. B.9b and c), whereas in the CrN toplayer the abovementioned difficulties regarding the FE model have to be considered.

In summary, Figs. B.2, B.3, B.4, B.5, B.6, B.7, B.8 and B.9 document the nanoscopic mechanical and microstructural response of a CrN-Cr bilayer thin film to scratch testing at two different loads. The elastic-plastic 3D-FE model allowed to

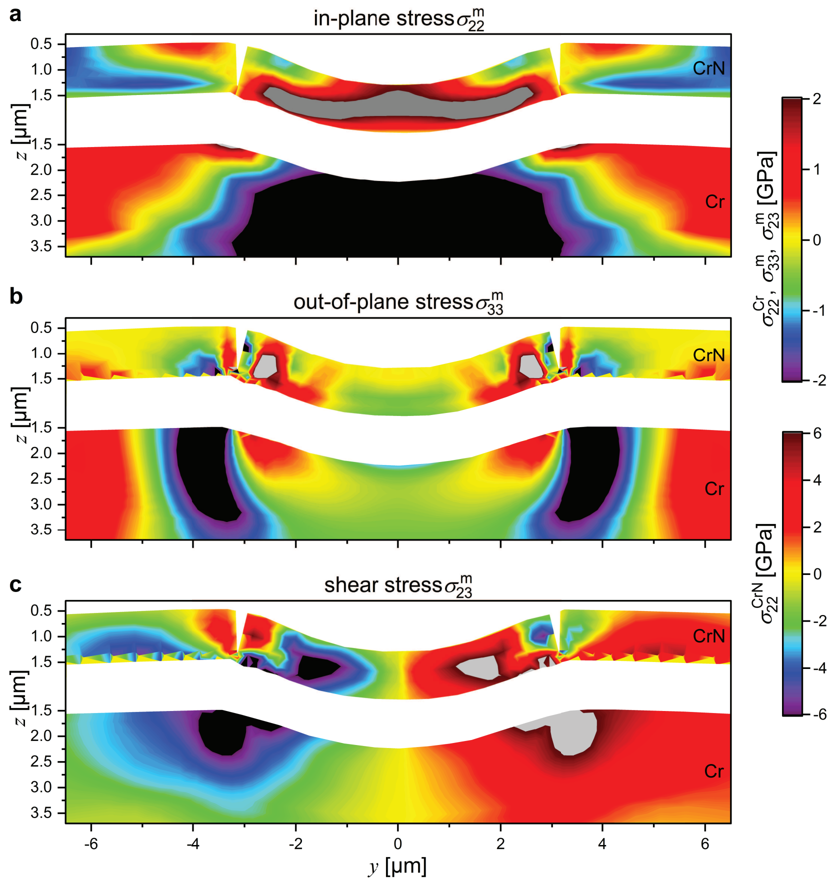

Figure B.11.: FEM calculated in-plane $\sigma_{22}^{\mathrm{m}}(y,z)$ (a), out-of-plane $\sigma_{33}^{\mathrm{m}}(y,z)$ (b), and shear $\sigma_{23}^{\mathrm{m}}(y,z)$ (c) stress distributions evaluated fromthe cross-section of the 200 mN scratch track area. Note that $\sigma_{22}^{\mathrm{CrN}}(y,z)$ is displayed with a different stress scale.

assess the stress distributions in a satisfactory way, especially in the case of the 200 mN scratch (Fig. B.10). In the case of 400 mN scratch, however, it was more challenging to properly model (Fig. B.11) the multiaxial stress distributions from Fig. B.9, because of the complex microstructural changes especially in the CrN toplayer, like the high density of microcracks (Figs. B.3e and B.6b), which altered the mechanical response of the bilayer significantly.

B.4. Discussion of brittle-ductile CrN-Cr bilayer deformation

Mechanical failure of thin films during scratching experiments is influenced by a variety extrinsic and intrinsic factors [3–6, 58]. In the case of nanocrystalline hard films, the particular microstructural and interfacial defects effectively responsible for failure are usually unknown. Similarly, complex stress concentrations around and behind the moving indenter tip, accompanying elastic and plastic deformation, chipping, cracking and delamination have remained unexplored experimentally [24].

Generally, the stress distributions accompanying failure are a superposition of elastic-plastic indentation stresses, frictional stresses and the residual internal stresses present in the film after the deposition [24, 26, 53, 54]. The present work introduces a thorough ex-situ analysis of the residual stress gradients formed after the deposition (Suppl. Fig. S.B.2) and multiaxial residual stress fields developed after the scratch experiment (Figs. B.8, B.9). The experimental data and the FEM calculated stresses (Figs. B.8, B.9, B.10 and B.11) provide an accurate picture of the stress build-up after the two scratch tests, before the onset of critical failure, and also allow us to deduce the stress states under the indenter during the experiments.

According to prior investigation of the mechanical behaviour of CrN-Cr multilayer systems subjected to indentation, CrN can bear very high stress magnitudes up to -10 GPa in compression [17,34]. However, in tension, free-standing FIB-fabricated cantilever beams of magnetron sputtered CrN showed overall brittle fracture upon a (tensile) stress magnitude of ~5.8 GPa [45]. Consequently, it is reasonable to assume that high tensile and compressive stresses with CrN toplayers will be accommodated by the formation of inter- and intragranular cracks within the nanoceramics, respectively. In the case of magnetron sputtered Cr thin films, compressive and tensile stress magnitudes are limited to ~3 GPa due to the onset of plastic deformation at higher stress levels [17, 45].

Following, Figs. B.8a and B.9a document that complementary compressive and tensile in-plane stress build-ups are formed in the regions bordering the CrN-Cr interface, as a result of curvature relaxation after the scratching indenter tip had passed. This implicates that during the indenter loading, tensile stresses were formed at both sides of the CrN-Cr interface as a product of the large curvature (bending-like), whose formation, however, did not result in catastrophic failure of the bilayer. Importantly, the nanoscale stress distributions are correlated with morphological and microstructural changes within the brittle and ductile sublayers (Figs. B.2, B.3, B.4 and B.5). Therefore, it is possible to associate the above-implicated tensile in-plane stress formation in the brittle CrN toplayer with the formation of nanoscopic intergranular cracks (Fig. B.3e) and intragranular defects (Figs. B.6 and B.7) as well as with the development of bilayer curvature. Similarly, the thickness reduction and pile-up formation within the ductile Cr (Fig. B.2) is accompanied by a variety of microstructural changes like columnar grain bending and localized plastic deformation (Figs. B.3, B.4, B.5, B.6 and B.7).

Even though the STEM and SEM micrographs in Figs. B.3e and B.5c document the presence of cross-sectional cracks within the CrN toplayer, the underlying ductile Cr sublayer serves as an effective crack barrier. In other words, even though the fracture strength of CrN was exceeded in multiple places during the scratch test (Figs. B.3, B.5), intergranular fracture along CrN columnar grains was arrested at the ductile Cr sublayer.

Similar to our previous study on the indentation behaviour of multi-layered CrN/Cr films [17], also in the present case the ductile sublayers serve as an important stabilizing component to the bilayer'smechanical integrity during and after scratching. Their ability for thickness reduction, massive plastic deformation, crystallite bending and formation of pile-ups protects the brittle-ductile bilayer from critical failure at loads that would disintegrate a comparable monolithic CrN layer.

B.5. Conclusions

Cross-sectional X-ray nanodiffraction was used to assess multiaxial stress distributions and microstructural changes within a scratch-tested bilayer thin film at a resolution of 50 nm. The experimental results, encompassing also small-angle X-ray scattering micrographs that document nanoscopic microstructural changes, were correlated with electron microscopy analyses and a 3D finite element model. The quantitative results uncover the multiaxial residual stress build-up, which was clearly correlated to the nanoscopic deformation mechanisms within the brittle CrN and ductile Cr layers. While scratch testing results in intergranular grain sliding and intragranular grain fragmentation within the CrN nanoceramic toplayer, without any thickness reduction, the thickness reduction/extension of the ductile Cr interlayer is accompanied by transgranular plastic deformation with unidirectional gliding, formation of piles-up, as well as crystallite bending and rotation. The results confirm the beneficial influence ofcompressive residual stresses and the concept of ductile interlayers to stabilize the brittle components of thin films, especially by revealing the actual stress levels present at different loads in the respective individual layers. Several shortfalls of existing numerical analyses could thus be identified, in particular the failure to address the intergranular crack formation that originates from high tensile stresses in the brittle layer. In short, even though significant damage could be detected in the upper brittle CrN layer at higher scratch loads, the lower ductile Cr layer was able to absorb large amounts of deformation and continued to provide good adhesion, thus maintaining the functionality of the overall structure as a wear-resistant film.

Acknowledgements

This work has been financially supported by the Christian Doppler Research Association. The financial support by the Austrian Federal Ministry of Science, Research and Economy and the National Foundation for Research, Technology and Development is also gratefully acknowledged. The CzechNanoLab project LM2018110 funded by MEYS CR is gratefully acknowledged for the financial support of the measurements/sample fabrication at CEITEC Nano Research Infrastructure. Furthermore, the authors gratefully acknowledge the financial support within the scope of the COMET program in the K2 Center "Integrated Computational Material, Process and Product Engineering (IC-MPPE)" (Project No 859480). This program is supported by the Austrian Federal Ministries for Climate Action, Environment, Energy, Mobility, Innovation and Technology (BMK) and for Digital and Economic Affairs (BMDW), represented by the Austrian research funding association (FFG), and the federal states of Styria, Upper Austria and Tyrol. Special thanks are devoted to Gabriele Felber for the preparation of the synchrotron lamella, Andrea Bachmaier and Stefan Wurster for help with the TKD measurements and Nikolaus Jäger for scratch testing.

Supplementary material

Residual Strain and Stress Data Evaluation

The orientation-dependent lattice strain $\varepsilon_{\delta\theta}^{m,hkl}(y,z)$ for each phase m (CrN or Cr) and DS ring hkl was determined as follows

$$\varepsilon_{\delta\theta}^{m,hkl}(y,z)=\frac{d_{\delta\theta}^{m,hkl}(y,z)-d_0^{m,hkl}}{d_0^{m,hkl}}, \tag{B.1}$$

where θ is the diffraction angle, δ the azimuthal angle on the detector (*cf.* Fig. B.1), $d_{\delta\theta}^{m,hkl}(y,z)$ is the measured lattice spacing and $d_0^{m,hkl}(y,z)=\frac{a_0^m}{\sqrt{h^2+k^2+l^2}}$ is the stress-free lattice spacing for a particular *hkl* reflection. The orientation-dependent lattice strain $\varepsilon_{\delta\theta}^{m,hkl}(y,z)$ measured in the direction of the diffraction vector is a function of unknown triaxial residual strain components $\varepsilon_{ij}^{m,hkl}(y,z)$ defined in the sample coordinate system as follows:

$$\begin{gathered}\varepsilon_{\delta\theta}^{m,hkl}(y,z)=\sin^2\theta\varepsilon_{11}^{m,hkl}(y,z)+\cos 2\theta\sin 2\delta\varepsilon_{22}^{m,hkl}(y,z)+\cos 2\theta\cos 2\delta\varepsilon_{33}^{m,hkl}(y,z)\\ -\sin 2\theta\cos\delta\varepsilon_{13}^{m,hkl}(y,z)+\cos 2\theta\sin 2\delta\varepsilon_{23}^{m,hkl}(y,z)-\sin 2\theta\sin\delta\varepsilon_{12}^{m,hkl},\end{gathered} \tag{B.2}$$

where $i,\ j=1,2$ and 3 correspond to the axes x, y and z in Fig. B.1, respectively. By applying X-ray elastic constants $S_1^{m,hkl}$ and $\frac{1}{2}S_2^{m,hkl}$, the strain components $\varepsilon_{ij}^{m,hkl}(y,z)$ from Eq. B.2 can be substituted by the components of the stress tensor $\sigma_{ij}^{m,hkl}(y,z)$ defined in the sample coordinate system as follows

$$\begin{gathered}\varepsilon_{\delta\theta}^{m,hkl}(y,z)=S_1^{m,hkl}\left[\sigma_{11}^m(y,z)+\sigma_{22}^m(y,z)+\sigma_{33}^m(y,z)\right]\\ +\tfrac{1}{2}S_2^{m,hkl}\Big[\sin^2\theta\sigma_{11}^{m,hkl}(y,z)+\cos^2\theta\sin^2\delta\sigma_{22}^{m,hkl}(y,z)+\cos^2\theta\cos^2\delta\sigma_{33}^{m,hkl}(y,z)\\ -\sin 2\theta\cos\delta\sigma_{13}^{m,hkl}(y,z)+\cos^2\theta\sin 2\delta\sigma_{23}^{m,hkl}(y,z)-\sin 2\theta\sin\delta\sigma_{12}^{m,hkl}\Big].\end{gathered} \tag{B.3}$$

X-ray elastic constants of $S_1^{\mathrm{CrN},111}=9.23\times10^{-4}\,\mathrm{GPa}^{-1}$, $\frac{1}{2}S_2^{\mathrm{CrN},111}=4.446\times10^{-3}\,\mathrm{GPa}^{-1}$, $S_1^{\mathrm{CrN},200}=2.99\times10^{-4}\,\mathrm{GPa}^{-1}$, $\frac{1}{2}S_2^{\mathrm{CrN},200}=2.575\times10^{-3}\,\mathrm{GPa}^{-1}$, $S_1^{\mathrm{Cr},110}=7.49\times10^{-4}\,\mathrm{GPa}^{-1}$ and $\frac{1}{2}S_2^{\mathrm{Cr},110}=4.441\times10^{-3}\,\mathrm{GPa}^{-1}$ for CrN and Cr *hkl* reflections were adopted from literature [41, 42].

At first residual stress depth gradients $\sigma_{ij}^m(z)$ within unaffected bilayer regions were evaluated supposing that the stress state was equibiaxial with non-zero in-plane principal stress components $\sigma_{11}^m(z)=\sigma_{22}^m(z)$, whereas shear stress $\sigma_{ij}^m(z)$ and also out-of-plane $\sigma_{33}^m(z)$ components were neglected for simplicity:

$$\varepsilon_{\delta\theta}^{m,hkl}(y,z) = \sigma_{22}^{m}(y,z)\, 2S_1^{m,hkl} + \sigma_{22}^{m,hkl}(y,z)\, \frac{1}{2}S_2^{m,hkl} \left[\sin^2\theta + \cos^2\theta \sin^2\delta\right]. \quad \text{(B.4)}$$

In this way, in-plane residual stress gradients $\sigma_{22}^{m}(z)$ within both as-deposited sublayers were determined.

In order to evaluate the stress distributions $\sigma_{ij}^{m,hkl}(y,z)$ within the scratch track areas, it was supposed that the in-plane stress component $\sigma_{11}^{m}(y,z)$ along the x-axis did not change significantly during the scratch experiment and therefore $\sigma_{11}^{m}(y,z)$ can be approximated with $\sigma_{22}^{m}(z)$ from Eq. B.4. Moreover, it was supposed that $\sigma_{12}^{m}(y,z)$ and $\sigma_{13}^{m}(y,z)$ can be neglected. Therefore, unknown cross-sectional residual stress distributions $\sigma_{22}^{m}(y,z)$, $\sigma_{33}^{m}(y,z)$ and $\sigma_{23}^{m}(y,z)$ in CrN and Cr sublayers were evaluated by using experimental diffraction vector orientation-dependent X-ray elastic strains $\varepsilon_{\delta\theta}^{m,hkl}(y,z)$ as follows:

$$\begin{aligned} &\varepsilon_{\delta\theta}^{m,hkl}(y,z) = S_1^{m,hkl}\left[\sigma_{11}^{m}(y,z) + \sigma_{22}^{m}(y,z) + \sigma_{33}^{m}(y,z)\right] \\ &+\tfrac{1}{2}S_2^{m,hkl}\Big[\sin^2\theta\sigma_{11}^{m,hkl}(y,z) + \cos^2\theta\sin^2\delta\sigma_{22}^{m,hkl}(y,z) \\ &+\cos^2\theta\cos^2\delta\sigma_{33}^{m,hkl}(y,z) + \cos^2\theta\sin 2\delta\sigma_{23}^{m,hkl}(y,z)\,\Big]. \end{aligned} \quad \text{(B.5)}$$

For every sample measurement point, a system of 36 linear equations (corresponding to 36 δ orientations in each detector image) based on Eq. B.5 was solved according to Ref. [34] and the three unknown stress distributions $\sigma_{22}^{m}(y,z)$, $\sigma_{33}^{m}(y,z)$ and $\sigma_{23}^{m}(y,z)$ were refined for CrN and Cr, whereby $\sigma_{11}^{m}(y,z)$ in Eq. B.5 considered as parameter.

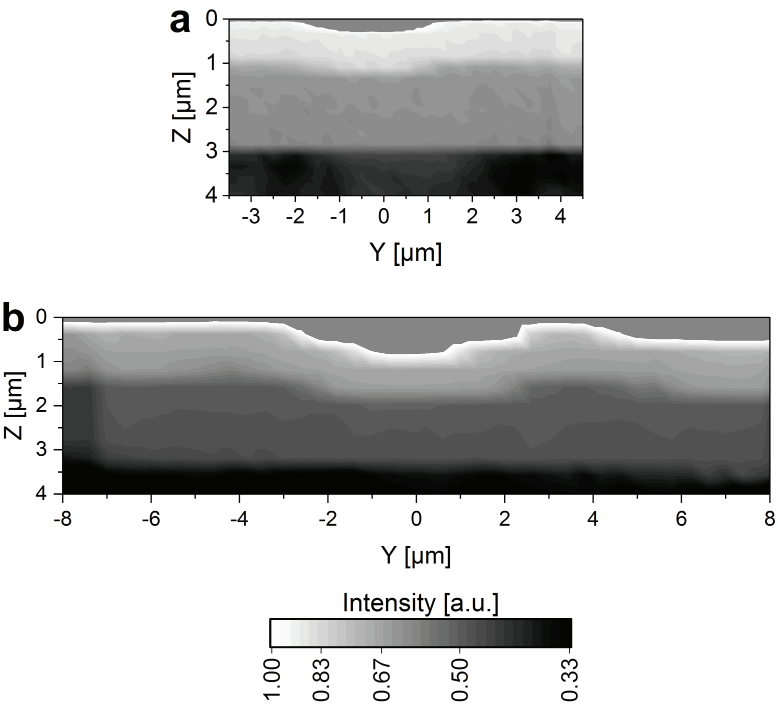

S.B.2 Fig. B.1: Data from the sample absorption scans performed at the cross-sections of the 200 mN (a) and 400 mN (b) scratch track areas collected with 250 and 400 nm sample movement steps, respectively. The brighter upper sub-regions represent X-ray absorption within the less dense CrN toplayers with a thickness of ~1.2 µm.

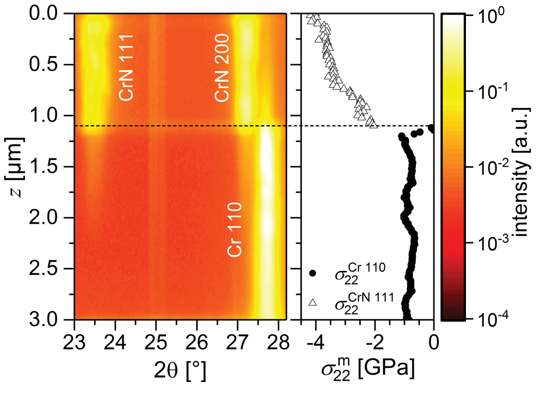

Suppl. Fig. B.2: CSnanoXRD phase diagram with CrN and Cr reflections and the corresponding residual stress gradient $\sigma_{22}^{m}(z)$ across the undeformed CrN-Cr bilayer film.

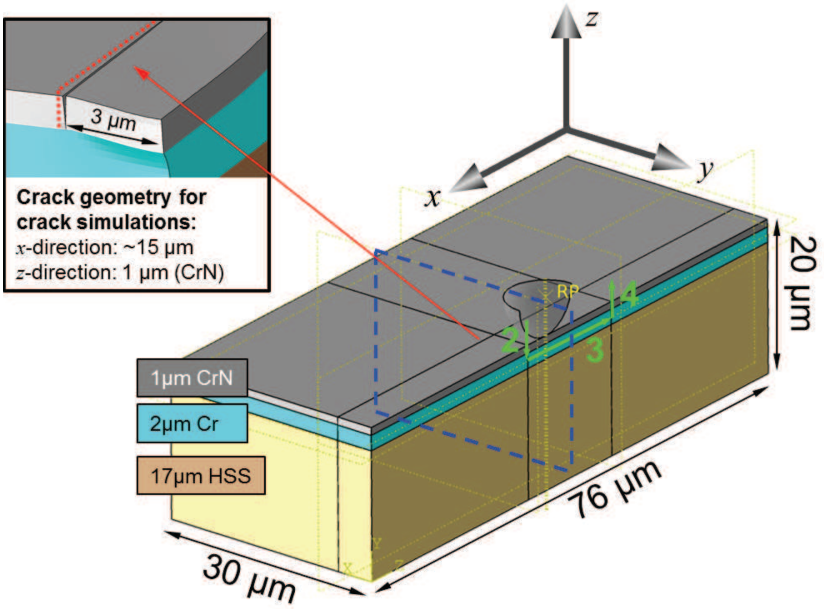

Suppl. Fig. B.3: Schematic sketch of FE-model setup. The numbers 2-4 represent the consecutive steps of applying the indenter load, scratching of the indenter and withdrawal of the indenter, as described in Sec. B.2.5 of the article. The dashed blue line represents the plane, where stress values were extracted for comparison with the experiment.

Bibliography to paper B

[1] A. Perry, *Thin Solid Films*, 1983, **107**, 167–180, DOI: `10.1016/0040-6090(83)90019-6`.

[2] J. Valli, *Journal of Vacuum Science & Technology A: Vacuum, Surfaces, and Films*, 1986, **4**, 3007–3014, DOI: `10.1116/1.573616`.

[3] P. Steinmann, Y. Tardy and H. Hintermann, *Thin Solid Films*, 1987, **154**, 333–349, DOI: `10.1016/0040-6090(87)90377-4`.

[4] H. Ichimura and Y. Ishii, *Surface and Coatings Technology*, 2003, **165**, 1–7, DOI: `10.1016/s0257-8972(02)00718-1`.

[5] S. Bull, *Surface and Coatings Technology*, 1991, **50**, 25–32, DOI: `10.1016/0257-8972(91)90188-3`.

[6] S. Bull, *Tribology International*, 1997, **30**, 491–498, DOI: `10.1016/s0301-679x(97)00012-1`.

[7] B. D. Beake, A. J. Harris and T. W. Liskiewicz, *Tribology - Materials, Surfaces & Interfaces*, 2013, **7**, 87–96, DOI: `10.1179/1751584x13y.0000000037`.

[8] B. Beake, V. Vishnyakov and A. Harris, *Tribology International*, 2011, **44**, 468–475, DOI: `10.1016/j.triboint.2010.12.002`.

[9] B. Bhushan, *Wear*, 2005, **259**, 1507–1531, DOI: `10.1016/j.wear.2005.01.010`.

[10] B. Bhushan, B. Gupta and M. H. Azarian, *Wear*, 1995, **181-183**, 743–758, DOI: `10.1016/0043-1648(95)90191-4`.

[11] X. Li and B. Bhushan, *Materials Characterization*, 2002, **48**, 11–36, DOI: `10.1016/s1044-5803(02)00192-4`.

[12] A. Kleinbichler, M. Pfeifenberger, J. Zechner, S. Wöhlert and M. Cordill, *Materials & Design*, 2018, **155**, 203–211, DOI: `10.1016/j.matdes.2018.05.062`.

[13] M. Larsson, M. Olsson, P. Hedenqvist and S. Hogmark, *Surface Engineering*, 2000, **16**, 436–444, DOI: `10.1179/026708400101517350`.

[14] G. Fontalvo, R. Daniel and C. Mitterer, *Tribology International*, 2010, **43**, 108–112, DOI: `10.1016/j.triboint.2009.05.002`.

[15] J. M. Lackner, W. Waldhauser, B. Major, L. Major and M. Kot, *Thin Solid Films*, 2013, **534**, 417–425, DOI: `10.1016/j.tsf.2013.03.025`.

[16] P. Wiecinski, J. Smolik, H. Garbacz and K. J. Kurzydlowski, *Thin Solid Films*, 2011, **519**, 4069–4073, DOI: `10.1016/j.tsf.2011.01.183`.

[17] M. Stefenelli, R. Daniel, W. Ecker, D. Kiener, J. Todt, A. Zeilinger et al., *Acta Mater.*, 2015, **85**, 24–31, DOI: `10.1016/j.actamat.2014.11.011`.

[18] P. Wieciński, J. Smolik, H. Garbacz and K. Kurzydłowski, *Surf. Coat. Technol.*, 2014, **240**, 23–31, DOI: `10.1016/j.surfcoat.2013.12.006`.

[19] R. Daniel, K. J. Martinschitz, J. Keckes and C. Mitterer, *Journal of Physics D: Applied Physics*, 2009, **42**, 075401, DOI: `10.1088/0022-3727/42/7/075401`.

[20] R. Daniel, M. Meindlhumer, J. Zalesak, B. Sartory, A. Zeilinger, C. Mitterer et al., *Mater. Des.*, 2016, **104**, 227–234, DOI: `10.1016/j.matdes.2016.05.029`.

[21] S. Brinckmann and G. Dehm, *Wear*, 2015, **338-339**, 436–440, DOI: `10.1016/j.wear.2015.05.001`.

[22] S. Brinckmann, C. A. Fink and G. Dehm, *Wear*, 2015, **338-339**, 430–435, DOI: `10.1016/j.wear.2015.04.023`.

[23] M. Khan, M. Fitzpatrick, S. Hainsworth, A. Evans and L. Edwards, *Acta Mater.*, 2011, **59**, 7508–7520, DOI: `10.1016/j.actamat.2011.08.034`.

[24] N. X. Randall, *Surface and Coatings Technology*, 2019, **380**, 125092, DOI: `10.1016/j.surfcoat.2019.125092`.

[25] K. Holmberg, A. Laukkanen, H. Ronkainen, K. Wallin and S. Varjus, *Wear*, 2003, **254**, 278–291, DOI: `10.1016/s0043-1648(02)00297-1`.

[26] K. Holmberg, A. Laukkanen, H. Ronkainen, K. Wallin, S. Varjus and J. Koskinen, *Surface and Coatings Technology*, 2006, **200**, 3793–3809, DOI: `10.1016/j.surfcoat.2005.03.040`.

[27] S. Roy, E. Darque-Ceretti, E. Felder, F. Raynal and I. Bispo, *Thin Solid Films*, 2010, **518**, 3859–3865, DOI: `10.1016/j.tsf.2010.02.004`.

[28] J. Keckes, R. Daniel, J. Todt, J. Zalesak, B. Sartory, S. Braun et al., *Acta Materialia*, 2018, **144**, 862–873, DOI: `10.1016/j.actamat.2017.11.049`.

[29] N. Jäger, S. Klima, H. Hruby, J. Julin, M. Burghammer, J. Keckes et al., *Acta Materialia*, 2019, **162**, 55–66, DOI: `10.1016/j.actamat.2018.09.031`.

[30] M. Meindlhumer, N. Jäger, S. Spor, M. Rosenthal, J. Keckes, H. Hruby et al., *Scripta Materialia*, 2020, **182**, 11–15, DOI: `10.1016/j.scriptamat.2020.02.031`.

[31] M. Meindlhumer, J. Zalesak, R. Pitonak, J. Todt, B. Sartory, M. Burghammer et al., *Nanoscale*, 2019, **11**, 7986–7995, DOI: `10.1039/c8nr10339a`.

[32] D. P. Gruber, J. Todt, N. Wöhrl, J. Zalesak, M. Tkadletz, A. Kubec et al., *Carbon*, 2019, **144**, 666–674, DOI: `10.1016/j.carbon.2018.12.093`.

[33] W. Ecker, J. Keckes, M. Krobath, J. Zalesak, R. Daniel, M. Rosenthal et al., *Materials & Design*, 2020, **188**, 108478, DOI: `10.1016/j.matdes.2020.108478`.

[34] A. Zeilinger, J. Todt, C. Krywka, M. Müller, W. Ecker, B. Sartory et al., *Scientific Reports*, 2016, **6**, DOI: `10.1038/srep22670`.

[35] M. Stefenelli, J. Todt, A. Riedl, W. Ecker, T. Müller, R. Daniel et al., *J Appl Crystallogr*, 2013, **46**, 1378–1385, DOI: `10.1107/S0021889813019535`.

[36] A. Kubec, S. Niese, M. Rosenthal, J. Gluch, M. Burghammer, P. Gawlitza et al., *Journal of Instrumentation*, 2018, **13**, C04011–C04011, DOI: `10.1088/1748-0221/13/04/c04011`.

[37] J. Kieffer, *J. Phys: Conf. Ser.*, 2013, **425**, 202012, DOI: `10.1088/1742-6596/425/20/202012`.

[38] G. Ashiotis, A. Deschildre, Z. Nawaz, J. P. Wright, D. Karkoulis, F. E. Picca et al., *Journal of Applied Crystallography*, 2015, **48**, 510–519, DOI: `10.1107/s1600576715004306`.

[39] M. Bartosik, R. Daniel, C. Mitterer, I. Matko, M. Burghammer, P. Mayrhofer et al., *Thin Solid Films*, 2013, **542**, 1–4, DOI: `10.1016/j.tsf.2013.05.102`.

[40] R. Daniel, K. Martinschitz, J. Keckes and C. Mitterer, *Acta Mater.*, 2010, **58**, 2621–2633, DOI: `10.1016/j.actamat.2009.12.048`.

[41] J. Almer, U. Lienert, R. L. Peng, C. Schlauer and M. Odén, *Journal of Applied Physics*, 2003, **94**, 697–702, DOI: `10.1063/1.1582351`.

[42] J. Pina, A. Dias, M. François and J. Lebrun, *Surface and Coatings Technology*, 1997, **96**, 148–162, DOI: `10.1016/s0257-8972(97)00075-3`.

[43] *Abaqus Unified FEA - SIMULIA(TM) by Dassault Systemes, https://www.3ds.com/products-services/simulia/products/abaqus/ (accessed June 15, 2020)., (n. d.)*

[44] S. Liu, J. Wheeler, J. Michler, X. Zeng and W. Clegg, *Scripta Materialia*, 2016, **117**, 24–27, DOI: `10.1016/j.scriptamat.2016.02.008`.

[45] A. Zeilinger, R. Daniel, M. Stefenelli, B. Sartory, L. Chitu, M. Burghammer et al., *J Phys D Appl Phys*, 2015, **48**, 295303, DOI: `10.1088/0022-3727/48/29/295303`.

[46] P. Wang, P. Ge, W. Bi, T. Liu and Y. Gao, *International Journal of Mechanical Sciences*, 2018, **141**, 1–8, DOI: `10.1016/j.ijmecsci.2018.03.042`.

[47] C. Greiner, Z. Liu, R. Schneider, L. Pastewka and P. Gumbsch, *Scripta Materialia*, 2018, **153**, 63–67, DOI: `10.1016/j.scriptamat.2018.04.048`.

[48] X. Chen, R. Schneider, P. Gumbsch and C. Greiner, *Acta Materialia*, 2018, **161**, 138–149, DOI: `10.1016/j.actamat.2018.09.016`.

[49] C. Haug, F. Ruebeling, A. Kashiwar, P. Gumbsch, C. Kübel and C. Greiner, *Nature Communications*, 2020, **11**, DOI: `10.1038/s41467-020-14640-2`.

[50] L. A. Feigin and D. I. Svergun, *Structure Analysis by Small-Angle X-Ray and Neutron Scattering*, ed. G. W. Taylor, Springer US, 1987, DOI: `10.1007/978-1-4757-6624-0`.

[51] I. Petrov, P. B. Barna, L. Hultman and J. E. Greene, *Journal of Vacuum Science & Technology A: Vacuum, Surfaces, and Films*, 2003, **21**, S117–S128, DOI: `10.1116/1.1601610`.

[52] M. S. Fuller, R. Klassen, N. McIntyre, A. Gerson, S. Ramamurthy, P. King et al., *Journal of Nuclear Materials*, 2008, **374**, 482–487, DOI: `10.1016/j.jnucmat.2007.10.015`.

[53] K. Holmberg, A. Laukkanen, H. Ronkainen, K. Wallin, S. Varjus and J. Koskinen, *Surface and Coatings Technology*, 2006, **200**, 3810–3823, DOI: `10.1016/j.surfcoat.2005.03.041`.

[54] A. Laukkanen, K. Holmberg, J. Koskinen, H. Ronkainen, K. Wallin and S. Varjus, *Surface and Coatings Technology*, 2006, **200**, 3824–3844, DOI: `10.1016/j.surfcoat.2005.03.042`.

[55] B. Boyce, X. Chen, J. Hutchinson and R. Ritchie, *Mechanics of Materials*, 2001, **33**, 441–454, DOI: `10.1016/s0167-6636(01)00064-3`.

[56] B. Boyce, A. Mehta, J. Peters and R. Ritchie, *Journal of Neutron Research*, 2004, **12**, 75–80, DOI: `10.1080/10238160410001734496`.

[57] K. Holmberg, A. Laukkanen, H. Ronkainen and K. Wallin, *Tribology International*, 2005, **38**, 1035–1049, DOI: `10.1016/j.triboint.2005.07.028`.

[58] S. Bull and E. Berasetegui, in *Scratching of Materials and Applications*, Elsevier, 2006, pp. 136–165, DOI: `10.1016/s0167-8922(06)80043-x`.

C

Evolution of stress fields during crack growth and arrest in a brittle-ductile CrN-Cr clamped-cantilever analysed by X-ray nanodiffraction and modelling

M. Meindlhumer[a], L. R. Brandt[b], J. Zalesak[c], M. Rosenthal[d], H. Hruby[e], J. Kopecek[f], E. Salvati[b,g], C. Mitterer[h], R. Daniel[a,h], J. Todt[c,h], J. Keckes[h], A. M. Korsunsky[b,i]

[a]Christian Doppler Laboratory for Advanced Synthesis of Novel Multifunctional Coatings at the Department of Materials Science, Montanuniversität Leoben, Leoben, Austria
[b]MBLEM - University of Oxford, Department of Engineering Science, Parks Road, Oxford OX1 3PJ, United Kingdom
[c]Erich Schmid Institute for Materials Science, Austrian Academy of Sciences, Leoben, Austria
[d]ESRF Grenoble, Grenoble, France
[e]voestalpine eifeler Vacotec GmbH, Düsseldorf, Germany
[f]Institute of Physics, Czech Academy of Science, Praha, Czech Republice
[g]Polytechnic Department of Engineering and Architecture (DPIA), University of Udine, Via delle Scienze 208, Udine, 33100, Italy
[h]Department of Materials Science, Montanuniversität Leoben
[i]Diamond Light Source, Harwell Oxford, OX11 0DE, U.K.

Abstract

In order to understand the fracture resistance of nanocrystalline thin films, it is necessary to assess nanoscopic multiaxial stress fields accompanying crack growth during irreversible deformation. Here, a clamped cantilever with dimensions of $200 \times 23.7 \times 40\,\mu\mathrm{m}^3$ was machined by focused ion beam milling from a thin film composed of four alternating CrN and Cr layers. The cantilever was loaded to 460 mN in two steps and multiaxial strain distributions were determined by *in situ* cross-sectional X-ray nanodiffraction. Characterisation in as-deposited state revealed the depth variation of fibre texture and residual stress across the layers. The *in situ* experiment indicated a strong influence of the residual stresses on the cross-sectional stress fields evolution and crack arrest capability at the CrN-Cr interface. In detail, an effective negative stress intensity of $-5.9 \pm 0.4\,\mathrm{MPa\,m^{1/2}}$ arose as a consequence of the residual stress state. Crack growth in the notched Cr layer occurred at a critical stress intensity of $2.8 \pm 0.5\,\mathrm{MPa\,m^{1/2}}$. The results were complemented by two-dimensional numerical simulation to gain further insight into the elastic-plastic deformation evolution. The quantitative experimental and modelling results elucidate the stepwise nature of fracture advancement across the alternating brittle and ductile layers and their interfaces.

C.1. Introduction

Mechanical integrity of thin films is determined not only by their extraordinary ultimate compressive and tensile strength, but also to a great extent by their ability to resist catastrophic failure due to instable crack propagation from pre-existing defects of various origins [1–3]. The discipline of linear elastic fracture mechanics (LEFM) was developed to quantify the ability of brittle materials to resist crack propagation [4, 5]. Its underlying thermodynamic principle is to link the strain energy release rate due to crack growth with the energy required for the formation of new fracture surfaces. The elasticity solutions for the displacement, strain, and stress fields around the crack tip obtained within this framework contain singularities that violate the assumption of finite material deformability and strength. LEFM deals with this central contradiction by excluding from consideration the so-called process zone (PZ), where material decohesion occurs. Instead, attention is focused on the relevant parameters outside the PZ which are assumed to fully determine the conditions for crack propagation. Key parameters in this consideration are the stress intensity factors (SIF) K_I, K_II and K_III that define the severity of the equivalent conceptual elastic crack tip singularity. Hence, the annular zone surrounding the PZ is sometimes referred to as the K-zone. The sum of squared SIFs with elastic moduli as coefficients allows the strain energy release rate to be evaluated. LEFM is valid for brittle or semi-ductile materials, where plastic deformation is restricted to the relatively small plastic zone surrounding the process zone, itself embedded within the K-zone. It is important to note that even in these (semi-)brittle cases the stress singularity in front of a crack tip leads to plastic deformation and the formation of a plastic zone.

In mainly ductile materials the crack propagation is significantly affected by dislocation emission and plastic deformation, so that the size of the PZ is not small compared to the sample dimensions. Under these conditions of significant ductility, elastic-plastic fracture mechanics (EPFM) needs to be applied instead of LEFM. Hutchinson, Rice and Rosengren demonstrated in their model [6, 7] that at stresses exceeding the yield strength of the elastic-plastic material, hardening controls the stress increase in front of the crack tip. The stress distribution within the plastic and process zones remains of high scientific interest, since the strains and stresses control the plastic deformation and material separation that ultimately leads to catastrophic failure. The experimental assessment of the strains/stresses within the confined volume of the plastic zone is of vital importance to understand the mechanisms of crack growth and failure.

According to the available literature, stress distributions in front of the crack tip have been investigated with neutron or synchrotron X-ray diffraction using gauge volumes of $\sim 2\,\mathrm{mm}$ [8, 9] and down to $\sim 25\,\mu\mathrm{m}$ [10–15], respectively. Some of the reported experimental work has focused on (i) the influence of residual stresses on crack growth in compact tension (CT) samples fabricated from Al alloys, but most works were dedicated to resolving (ii) the influence of overload events on fatigue crack growth in standard sample geometries. In the former case, tensile residual stress in front of the crack tip led to a significant acceleration of (stable) crack growth during unidirectional loading of the sample [8, 9]. However, standard fracture mechanics samples are not suitable for thin film testing due to their restricted thickness. In the field of micromechanical testing several cantilever-based geometries have therefore been proposed and developed [16, 17]. In state-of-the-art experimental setup configurations, cantilevers can be tested *in situ* inside a scanning electron microscope (SEM) that allows following stable crack growth at the sample surface, and evaluating the fracture toughness of the material on the basis of load–deflection and crack length-dependent stiffness data [17]. Digital Image Correlation (DIC) is usually a method of choice to map strain distributions at the sample surface. However, stress distributions within the material remain inaccessible to this technique without the use of additional assumptions (elastic relationship between strains and stresses), or further destructive testing steps [18]. Recent developments of the FIB-DIC technique have demonstrated its capability of mapping residual stresses at micron scale lateral resolution and better than 25 nm in the depth direction [19–21].

On the other hand, cross-sectional X-ray nanodiffraction (CSnanoXRD), described in detail in Refs. [22–25]) coupled with nano-indentation allows for *in situ* characterization of laterally and depth-dependent stress distributions generated in thin films with a spatial resolution down to 200 × 200 nm^2, giving new insights into the deformation behaviour of exemplary nanoceramic TiN [22] and CrN [23], as well as the stress relief caused by cracking. These experiments revealed the key effect of abrupt changes of compressive residual stress parallel to the interfaces between individual layers of similar materials on the formation and growth of cracks. The nucleation of cracks in the top sublayer containing low residual stress is followed by crack re-orientation, extensive crack deflection and crack arrest phenomena observed at the interfaces of monophase sublayers [22, 23] of different residual stresses.

The present study utilised *in situ* CSnanoXRD for the first time to investigate both the residual and loading-induced stresses during stepwise deformation of a CrN-Cr nano-multilayer clamped cantilever. The evolution of a plastic zone originating from a pre-milled notch and crack growth during mechanical loading were monitored, quantified, and correlated with established theoretical approaches. *In situ* experiments revealed the crack arrest effect of the interfaces between brittle CrN and ductile Cr layers, as well as crack tip blunting that could be seen at the highest applied load. The results were correlated with 2D numerical simulations using the eigenstrain-finite element method.

C.2. Experiment and methods

C.2.1. Thin film synthesis

For this study, a multi-layered CrN-Cr film consisting of four layers, each ∼ 5 to 5.5 µm thick, was deposited on an electrolytically polished plate made of high speed steel (HSS) with lateral dimensions of 20 × 20 mm^2 and a thickness of ∼ 5 mm. The film was deposited by unbalanced magnetron sputtering using a powder metallurgically produced Cr target. Prior to the deposition process, the chamber was evacuated to 10^{-4} Pa, the substrate was then heated to 350°C and plasma etched for 10 min. The deposition was also performed at 350°C and a total pressure of 1 Pa was applied. The Cr layers were deposited in a pure Ar atmosphere and an applied bias voltage of −40 V, whereas the CrN layers were grown in an Ar + N_2 atmosphere applying a bias voltage of −80 V. The N_2 partial pressure was adjusted to 0.25 Pa using a capacitive gauge. The resulting overall thickness of the film was ∼ 21.7 µm.

C.2.2. FIB-preparation and investigation of the cantilever

At first, a cross-sectional lamella for the CSnanoXRD experiment with a thickness of $\sim 200\,\mu m$ in beam direction was prepared from the thin film sample by mechanical polishing. In the next step, a Tescan FERA3 FIB using Xe^+-ions at an acceleration voltage of 30 kV and a current of 300 nA was used to further cut the lamella down to a remaining thickness of 45 µm in a region with a length of 200 µm and to remove the substrate under the multilayer in this region. Prior to the cutting operations, a Si-mask was lifted-out using a micromanipulator, which was placed above the actual sample as a sacrificial protection to protect the sample surface from the high Xe^+-ion currents. In order to cut the final geometry $L \times t \times B$ of the clamped cantilever to $200\,\mu m \times 23.7\,\mu m \times 40\,\mu m$, FIB machining was employed in a ZEISS Auriga CrossBeam Workstation by using Ga^+ ions with a current of 13.6 nA. Finally, the notch was cut from the side on the bottom of the cantilever with a current of 500 pA. The cantilever was imaged prior the experiment at an acceleration voltage of 5 kV and an aperture width of 60 µm using the SEM in-lens detector of the workstation. For post mortem imaging after the CSnanoXRD experiment, a $\sim 500\,nm$ thick tungsten protection layer was deposited on the surface of the clamped cantilever using the gas injection system of the FIB workstation to protect the clamped cantilever surface from the Ga^+ ion-damage. Afterwards, the cross-section was fine ion-polished at continuously reduced ion current from 5 nA to 500 pA and imaged with the secondary electron detector using a Ga^+-ion current of 10 pA in order to reveal cross-sectional morphological features such as cracks, grain orientation variations and/or plastic deformation of the clamped cantilever resulting from the bending experiment.

C.2.3. CSnanoXRD experiment

The CSnanoXRD experiments was performed at beamline ID13 of the European Synchrotron (ESRF) in Grenoble, France [24] using the indenter setup developed for *in situ* indentation experiments and described in [23]. The nano-focussing lens (NFL) [25] setup was used to focus the X-ray beam with a photon energy of 14.9 keV to a spot of 150 nm in diameter and a focal depth of $\sim 50\,\mu m$ [24]. Prior to the CSnanoXRD experiment, at first the interfaces between the CrN and Cr layers were aligned parallel to the incident X-ray beam direction at two sample z positions by performing a set of absorption line-scans along the z-axis at various sample orientations around the y-axis (Fig. C.1a) using a point X-ray detector [24, 26]. The optimal sample orientation was determined by maximizing the X-ray absorption contrast between the CrN- and the Cr-layers. Subsequently, two-dimensional (2D) absorption scans (presented in Suppl. Fig. S.C.1) were performed to locate the centre of the clamped cantilever and to determine the centres of the CSnanoXRD mesh scans. The clamped cantilever was incrementally loaded to 150 and 460 mN (*cf.* Fig. C.1b), and four areas of $40 \times 30\,\mu m^2$ were characterized in detail by mesh scanning the sample along the y- and z- direction in 200 nm steps (i) before applying the load, (ii) at 150 mN load, (iii) at 460 mN load and (iv) after unloading. In total, 30351 2D diffractograms were recorded for each step. The 2D diffraction signal was recorded by a Dectris Eiger X 4M detector at each measurement position using an acquisition time of 50 ms. The exact detector geometry with respect to the sample was calibrated using a NIST LaB_6 powder, yielding a sample-to-detector distance of 152.60 mm. The evaluation of the 2D patterns containing CrN 111 and 200 or Cr 110 Debye-Scherrer rings (Fig. C.1) was performed using the pyFAI software package [27, 28].

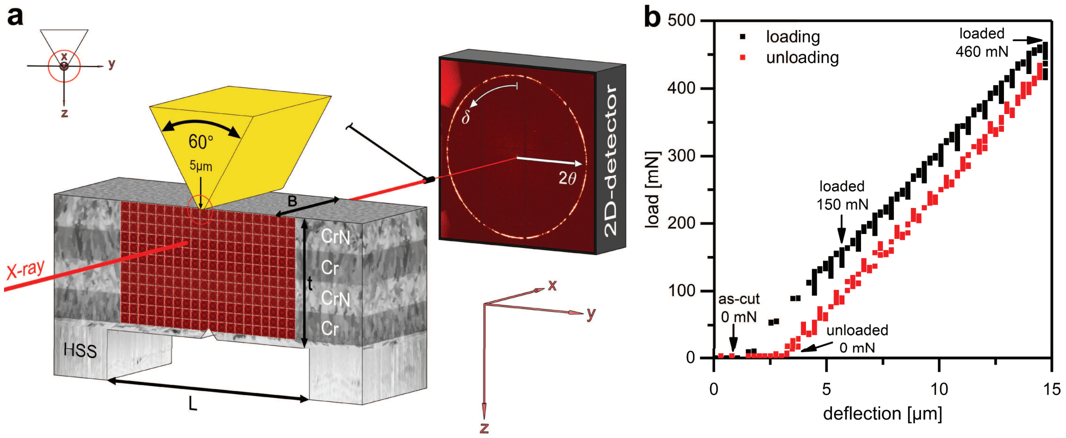

Figure C.1.: (a) Schematic sketch of the *in situ* CSnanoXRD setup. A clamped cantilever cut from the sample lamella with dimensions of $L \times t \times B = 200\,\mu m \times 23.7\,\mu m \times 40\,\mu m$, where L, B and t are the length, width and thickness of the clamped cantilever, respectively, was scanned with an X-ray beam of ~ 150 nm in diameter along y and z axes in steps of 200 nm. During the *in situ* CSnanoXRD experiment 30351 2D diffraction patterns were recorded on an Eiger X 4 M CCD detector from $40 \times 30\,\mu m^2$ large areas at each of the 4 load steps in the centre of the clamped cantilever. A detailed description of the *in situ* CSnanoXRD indentation setup is given in Ref. [23]. (b) Load-deflection curve of the clamped cantilever recorded during the *in situ* synchrotron experiment. The arrow indicates the load of 150 mN. 2D diffraction patterns for structural and stress analysis were recorded during the experiment (i) before loading (0 mN), (ii) at 150 mN, (iii) at 460 mN and (iv) after unloading (0 mN).

C.2.4. CSnanoXRD data analysis

Qualitative texture analysis was carried out by a radial (θ) integration of the CrN 200 and Cr 110 Debye-Scherrer rings providing azimuthal intensity distributions $I^{m,hkl}(\delta, z)$ and the data were plotted as a function of the azimuthal angle δ, which is the angle between the film normal and the projection of the diffraction vector onto the detector (Fig. C.1). The diffuse scattering at relatively small diffraction angles, *i.e.* small-angle X-ray scattering (SAXS), around the beam stop (Fig. C.1) originates primarily from electron density variations, such as alternation of materials, presence of grain boundaries, interfaces, cracks, precipitates and pores with sizes of λ/θ where λ represents the X-ray wavelength and θ is a half of the Bragg angle [29, 30]. In the present case, the signal scattered onto the 2D detector at the diffraction angles of ~ 0.05 to ~ 0.5 degrees was integrated radially (θ) and azimuthally (δ) in order to obtain a qualitative information primarily on the occurrence of the growing crack within the clamped cantilever.

In order to evaluate the stress tensor distributions $\sigma^m_{ij}(y, z)$ with $i, j = x, y, z$, an integration of the diffraction patterns was performed over the azimuthal angle δ in $\Delta\delta$ segments of 10 deg. Thus, 36 radial intensity distributions $I(\theta, \Delta\delta)$ were obtained for each exposure. The positions of CrN 111 and 200 and Cr 110 diffraction peaks $\theta^{m,hkl}\,(\Delta\delta_g)$,$g = [1, 36]$ and, subsequently, the orientation-dependent lattice parameter$d^{m,hkl}_{\delta\theta}(y, z)$, were determined by fitting the X-ray diffraction patterns using a Pseudo-Voigt function in each cake g. The orientation-dependent lattice strain $\varepsilon^{m,hkl}_{\delta\theta}(y, z)$ for each phase m and corresponding Debye-Scherrer ring hkl was determined as follows

$$\varepsilon^{m,hkl}_{\delta\theta}(y, z) = \frac{d^{m,hkl}_{\delta\theta}(y, z) - d^{m,hkl}_0}{d^{m,hkl}_0}, \tag{C.1}$$

where θ is the diffraction angle, δ the azimuthal orientation on the detector (*cf.* Fig. C.1), $d^{m,hkl}_{\delta\theta}(y, z)$ is the lattice parameter obtained at the respective diffraction angle θ and azimuthal orientation δ and $d^{m,hkl}_0(y, z) = \frac{a^m_0}{\sqrt{h^2+k^2+l^2}}$ is the stress-free lattice spacing for a particular hkl reflection.

The unstressed lattice constant of CrN was determined from diffraction data near the surface of an undeformed region of the film, considering the stress-free out-of-plane orientation [31] and found to be $a^{\mathrm{CrN}}_0 = 0.41607$ nm. In the case of Cr, the stress-free lattice parameter $a^{\mathrm{Cr}}_0 = 0.288839$ was adopted from literature [32]. Since the Cr layers are never at a free surface, they are always exposed to inherent stress and hence no location with a stress-free orientation exists for this phase.

The measured orientation-dependent lattice strain $\varepsilon_{\delta\theta}^{m,hkl}(y,z)$ is a function of unknown dependent strain components $\varepsilon_{ij}^{m,hkl}$ with $i,j = x,y,z$ defined in the sample coordinate system as follows

$$\begin{aligned}\varepsilon_{\delta\theta}^{m,hkl}(y,z) = \sin^2\theta\varepsilon_{xx}^{m,hkl}(y,z) + \cos^2\theta\sin^2\delta\varepsilon_{yy}^{m,hkl}(y,z) + \cos^2\theta\cos^2\delta\varepsilon_{zz}^{m,hkl}(y,z)\\ - \sin 2\theta\cos\delta\varepsilon_{xz}^{m,hkl}(y,z) + \cos^2\theta\sin 2\delta\varepsilon_{yz}^{m,hkl}(y,z) - \sin 2\theta\sin\delta\varepsilon_{xy}^{m,hkl},\end{aligned} \tag{C.2}$$

Using X-ray elastic constants $S_1^{m,hkl}$ and $\frac{1}{2}S_2^{m,hkl}$ the strain components $\varepsilon_{ij}^{m,hkl}$ of Eq. C.2 can be replaced by the components of the stress tensor $\sigma_{ij}^{m,hkl}$ defined in the sample coordinate system as follows

$$\begin{aligned}\varepsilon_{\delta\theta}^{m,hkl}(y,z) = S_1^{m,hkl}\left[\sigma_{xx}^{m}(y,z) + \sigma_{yy}^{m}(y,z) + \sigma_{zz}^{m}(y,z)\right]\\ +\tfrac{1}{2}S_2^{m,hkl}\Big[\sin^2\theta\sigma_{xx}^{m,hkl}(y,z) + \cos^2\theta\sin^2\delta\sigma_{yy}^{m,hkl}(y,z) + \cos^2\theta\cos^2\delta\sigma_{zz}^{m,hkl}(y,z)\\ - \sin 2\theta\cos\delta\sigma_{xz}^{m,hkl}(y,z) + \cos^2\theta\sin 2\delta\sigma_{yz}^{m,hkl}(y,z) - \sin 2\theta\sin\delta\sigma_{xy}^{m,hkl}\,\Big].\end{aligned} \tag{C.3}$$

X-ray elastic constants of $S_1^{\mathrm{CrN},111} = 9.23 \times 10^{-4}\,\mathrm{GPa}^{-1}$, $\frac{1}{2}S_2^{\mathrm{CrN},111} = 4.446 \times 10^{-3}\,\mathrm{GPa}^{-1}$, $S_1^{\mathrm{CrN},200} = 2.99 \times 10^{-4}\,\mathrm{GPa}^{-1}$, $\frac{1}{2}S_2^{\mathrm{CrN},200} = 2.575 \times 10^{-3}\,\mathrm{GPa}^{-1}$, $S_1^{\mathrm{Cr},110} = 7.49 \times 10^{-4}\,\mathrm{GPa}^{-1}$ and $\frac{1}{2}S_2^{\mathrm{Cr},110} = 4.441 \times 10^{-3}\,\mathrm{GPa}^{-1}$ for CrN and Cr, respectively, were adopted from literature [33, 34]. Concerning the evaluation of the as-deposited stress gradients within the thin film, the $\sin^2\psi$-method can be adopted as follows

$$\varepsilon_{\delta\theta}^{m,hkl}(y,z) = \sigma_{yy}^{m}(y,z)\,2S_1^{m,hkl} + \sigma_{yy}^{m,hkl}(y,z)\,\frac{1}{2}S_2^{m,hkl}\left[\sin^2\theta + \cos^2\theta\sin^2\delta\right], \tag{C.4}$$

where the shear stresses along the planes parallel to the primary X-ray beam where neglected for simplicity and the in-plane stress state was estimated as equibiaxial $\sigma_{xx}^{m}(y,z) \cong \sigma_{yy}^{m}(y,z)$. Across the loaded cross-section of the clamped cantilever, the stress state was evaluated by least-squares fitting an overdetermined system of 36 linear equations

$$\begin{aligned}\varepsilon_{\delta\theta}^{m,hkl}(y,z) = S_1^{m,hkl}\left[\sigma_{xx}^{m}(y,z) + \sigma_{yy}^{m}(y,z) + \sigma_{zz}^{m}(y,z)\right]\\ +\tfrac{1}{2}S_2^{m,hkl}\Big[\sin^2\theta\sigma_{xx}^{m,hkl}(y,z) + \cos^2\theta\sin^2\delta\sigma_{yy}^{m,hkl}(y,z)\\ + \cos^2\theta\cos^2\delta\sigma_{zz}^{m,hkl}(y,z) + \cos^2\theta\sin 2\delta\sigma_{yz}^{m,hkl}(y,z)\,\Big].\end{aligned} \tag{C.5}$$

based on the measured lattice strain $\varepsilon_{\delta\theta}^{m,hkl}(y,z)$ evaluated for each cake g. It was assumed that the stress components $\sigma_{xj}^{m}(y,z)$ with $j = x,y,z$ did not change significantly during the cantilever loading due to the particular experiment geometry and therefore $\sigma_{xx}^{m}(y,z)$ values from the as-deposited state were considered in Eq. C.5. whereby $\sigma_{xy}^{m}(y,z)$ and $\sigma_{xz}^{m}(y,z)$ values were neglected for simplicity.

C.2.5. 2D-Simulation

In order to gain additional insight into stress and strain accommodation mechanisms within the CrN-Cr multilayer system before and during loading, a finite element (FE) model was created using the COMSOL Multiphysics® package. The cantilever dimensions were selected according to the SEM measurements shown in Fig. C.2. The material properties employed are summarised in Table C.1.

Table C.1.: Material properties of Cr and CrN layers and HSS substrate employed for the FE simulation.

Material	Young's Modulus E [GPa]	Poisson's ratio ν
Cr [32]	279	0.21
CrN [35]	220	0.20
HSS	210	0.29

For all loading steps, the stress distribution within individual layers is a superposition of two main stress sources: (i) residual stress originating from processing, *i.e.* incident particles and thermal mismatch between coating and substrate σ_{res} (*cf.* Sec. C.3.1) and (ii) bending/indentation stresses σ_{ext} arising from the external load applied by the indenter tip (F_{ind}). The residual stress σ_{res} at each point of the multilayer was modelled by prescribing the eigenstrain tensors $\varepsilon^{*}_{E,\mathrm{Cr}}$ and $\varepsilon^{*}_{E,\mathrm{CrN}}$ within the Cr and CrN layers, respectively. These tensors were obtained by iteratively solving the inverse problem of the eigenstrain reconstruction method (ERM) assuming that both the ductile behaviour of Cr interlayers as well as the more rigid behaviour of CrN layers contained either quadratic or constant eigenstrain distribution with respect to the film thickness direction. The eigenstrain component for Cr layers in horizontal direction $\varepsilon^{*}_{11,\mathrm{Cr}}$ was assumed to follow a quadratic function distribution. In contrast, the vertical component $\varepsilon^{*}_{33,\mathrm{Cr}}$ and the out-of-plane component $\varepsilon^{*}_{22,\mathrm{Cr}}$ were modelled as constant. For the CrN layers, all eigenstrain components were chosen to be constant. These assumptions and resulting eigenstrain distributions were validated by comparing the residual stress resulting from the FE modelling with the experimental data from Fig. C.3c. As a result, the following eigenstrain tensors were used for the simulation:

$$\varepsilon^*_{E,\mathrm{Cr}} = \begin{pmatrix} a\left(\varepsilon^*_{11,\mathrm{Cr}}\right)^2 + b\varepsilon^*_{11,\mathrm{Cr}} + c & 0 & 0 \\ 0 & \varepsilon^*_{22,\mathrm{Cr}} & 0 \\ 0 & 0 & \varepsilon^*_{33,\mathrm{Cr}} \end{pmatrix} \tag{C.6}$$

$$\varepsilon^*_{E,\mathrm{CrN}} = \begin{pmatrix} \varepsilon^*_{11,\mathrm{CrN}} & 0 & 0 \\ 0 & \varepsilon^*_{22,\mathrm{CrN}} & 0 \\ 0 & 0 & \varepsilon^*_{33,\mathrm{CrN}} \end{pmatrix} \tag{C.7}$$

For the pre-loaded reference state, a small notch through the HSS substrate was added to the model of the clamped cantilever, as shown in Fig. C.4. Finally, linear elastic material properties and symmetry along the vertical centreline of the cantilever were assumed. Subsequently, the indentation loads F_{ind}= 150 and 460 mN were applied at the centre of the clamped cantilever, keeping the found eigenstrain distribution unchanged to ensure that the residual stress was accounted for during the simulation of the indentation. As the experimental SAXS map data (*cf.* Fig. C.4) clearly indicates the formation of a crack through the Cr layer opposite of the indenter tip after the initial loading, the same crack was considered in the FE model at 460 mN to account for this effect. The simulation results will be discussed in Sec. C.3.3.

C.3. Results

C.3.1. *Ex situ* thin film analysis

C.3.1.1 *Ex situ* microstructural investigations

The as-fabricated clamped cantilever is shown in Fig. C.2a at an inclination of 45 deg. The length and width of the cantilever were ∼ 200 and 40 µm, respectively. The cross-section of the clamped cantilever prepared by FIB at the centre of the sample after the *in situ* CSnanoXRD experiment revealed a dense, columnar-grained microstructure in all 4 layers of the film (Fig. C.2b). The SEM inspection of the sample revealed a remaining portion of the substrate with a thickness of ∼ 2 µm (Fig. C.2b), which was not fully removed by FIB. The notch milled by FIB with a total depth of ∼ 2.7 µm thus resulted in a notch in the Cr sublayer with a depth of ∼ 700 nm. The total thickness of the cantilever was ∼ 23.7 µm. The thickness of individual Cr and CrN layers ranged between 5.2 and 5.5 µm. Furthermore, a quasi-epitaxial relationship between CrN and Cr was revealed by a constant channelling contrast of the individual Cr and CrN grains across the CrN-Cr interface in the FIB-image (Figs. C.2c-e), along with the absence of fine-grained nucleation layers, as observed also elsewhere [32]. No such structural relation was found for the Cr sublayer grown on the HSS substrate (Fig. C.2f). Although a relatively coarse-grained microstructure of the CrN layers would be expected throughout the multilayer [32], the CrN layers were rather fine-grained, which is related to the intense ion bombardment assisting the layer growth. This is in contrast to the coarse-grained Cr layers grown at moderate bias voltage (Fig. C.2b) [32, 36].

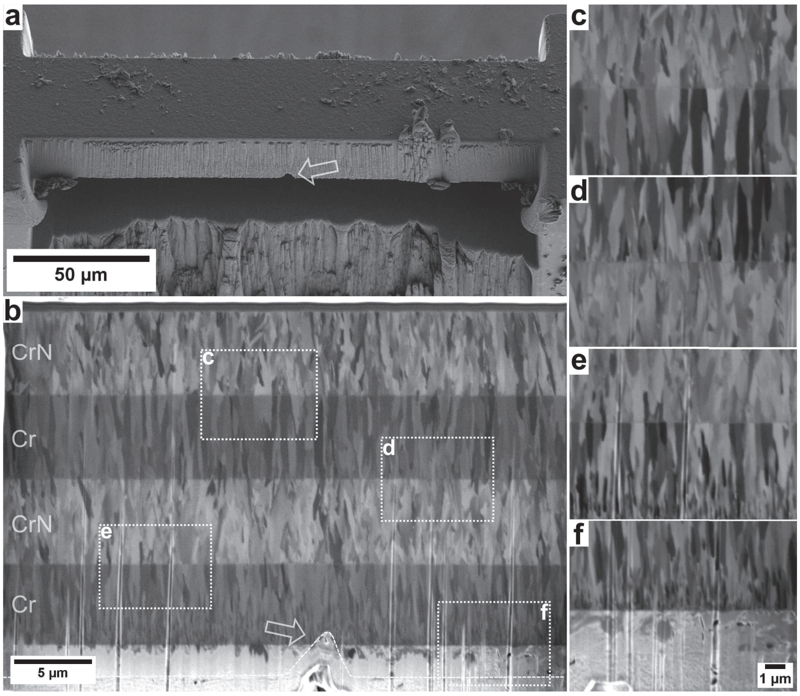

Figure C.2.: (a) SEM micrograph of the as-fabricated clamped cantilever at an inclination of 45 deg and (b) its cross-section prepared after the *in situ* CSnanoXRD synchrotron experiment. SEM cross-sectional micrographs showing in detail individual interfaces marked with the dashed rectangles in (b) from top to bottom between (c) CrN and Cr, (d) Cr and CrN, (e) CrN and Cr and (f) Cr and HSS substrate. The arrows indicate the position of the notch.

C.3.1.2 *Ex situ* CSnanoXRD analysis

Results of the CSnanoXRD analysis performed ex situ on an undeformed region of the sample are shown in Fig. C.3. Fig. C.3a shows averaged diffraction data including Cr 110, CrN 111 and 200 reflections and reflections emanating from the substrate. In addition, weak Cr_2N reflections were detected in the transition zones in the vicinity of the CrN-Cr interfaces (Fig. C.3a). The sharp transition between the individual Cr and CrN sample regions confirms the excellent sample alignment with respect to the incident X-ray beam, also documented by Suppl. Fig. S.C.1. Diffraction data from the non-deformed region were furthermore used for qualitative texture analysis. In the lower Cr sublayer, a $\langle 102\rangle$ fibre texture was detected across the whole layer thickness, as evident by the azimuthal maxima of the 110 Debye-Scherrer ring at azimuthal angles of ± 15, ± 45 and ± 75 deg in Fig. C.3b. The following CrN sublayer is characterized by a $\langle 311\rangle$ fibre texture near the CrN-Cr interface, which gradually changes into a $\langle 111\rangle$ fibre texture. This texture cross-over is evident by a change of the position of the azimuthal maxima of the 200 Debye-Scherrer ring from ± 25 and ± 72 deg to $\sim \pm 55$ deg. The pronounced $\langle 110\rangle$ texture of the top Cr layer completely differs to that of the Cr layer grown on the substrate surface. While the growth of the Cr layer on the HSS substrate is controlled only by fundamental growth mechanisms associated with the minimization of the strain energy at the initial growth stages and kinetic restrictions at greater layer thicknesses resulting in the $\langle 102\rangle$ texture, the growth of the 110-oriented Cr grains on the top of the CrN layer with $\langle 111\rangle$ texture was stimulated by the mutual epitaxial relationship between Cr and CrN grains. It can be expressed as $\{111\}_{\mathrm{CrN}} \parallel \{110\}_{\mathrm{Cr}}$. Epitaxial alignment of the top CrN sublayer along the 110-oriented Cr grains resulted in a subsequent development of the $\langle 311\rangle$ fibre texture of the topmost CrN layer. The gradual texture cross-over from a rather weak $\langle 311\rangle$ fibre texture into a strong $\langle 111\rangle$ fibre texture was driven by the kinetic restrictions associated with a high bias voltage assisting growth of the CrN layer. Moreover, the alignment of $\langle 311\rangle_{\mathrm{CrN}}$ grains of the lower CrN layer on $\langle 102\rangle_{\mathrm{Cr}}$ grains of the lower Cr layer is consistent with the epitaxial relationship $\{100\}_{\mathrm{CrN}} \parallel \{100\}_{\mathrm{Cr}}$, reflected by the intensity maxima at ± 25.3 and ± 26.6 deg off the out-of-plane axis, respectively, which is commonly observed and extensively discussed in literature [32, 37, 38].

Fig. C.3c shows the as-deposited stress state across the undeformed film. Compressive stress in Cr layers ranges between -0.15 and ~ -1.60 GPa and between -2.45 and -3.40 GPa in CrN layers. The compressive stress state in all layers is a result of (i) a dominant high-energy ion bombardment-assisted growth of the film and (ii) compressive stress build-up associated with the mismatch of the coefficients of thermal expansion between the layers and substrate ($\alpha_{\mathrm{HSS}} > \alpha_{\mathrm{Cr}} > \alpha_{\mathrm{CrN}}$) and the subsequent development of compressive thermal stress during cooling of the coated sample from the deposition temperature down to room temperature. The variation of the compressive stress between individual layers is given by different energetic growth conditions (Cr layers were deposited at lower bias voltages than the CrN

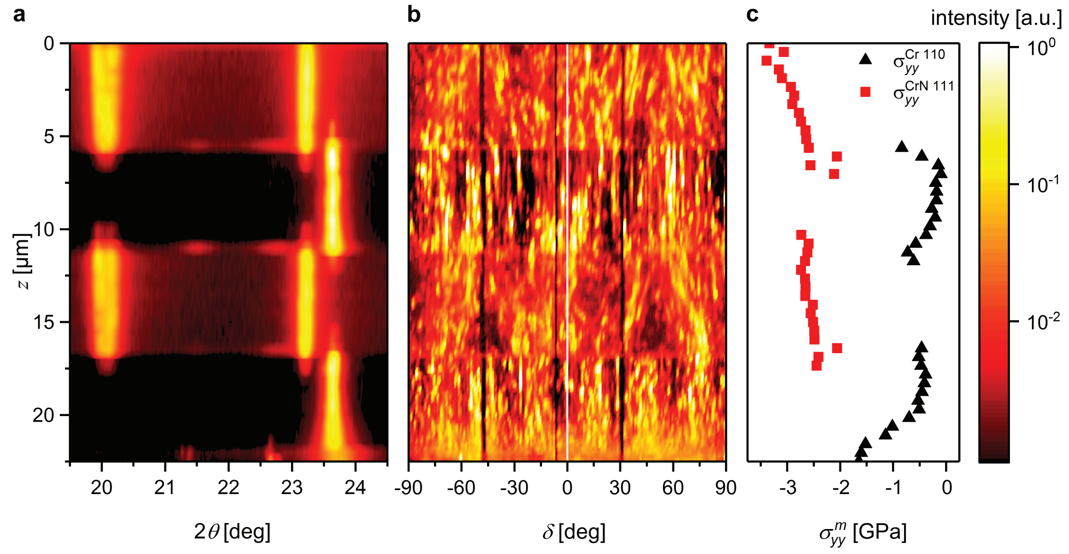

Figure C.3.: Phase plot displaying azimuthally averaged intensities of CrN 111 and 200, as well as Cr 110 Debye-Scherrer rings (a), the azimuthal intensity distributions of CrN 200 and Cr 110 Debye-Scherrer rings (b) and in-plane distribution of average residual stress $\sigma_{yy}^{m}(z)$ in individual CrN and Cr layers (c). $z = 0$ μm corresponds to the film surface, $z = 22.5$ μm corresponds to the film/substrate interface.

layers), the variation of the stress state within individual layers, however, has a different origin. It is predominantly given by the variation of the crystallite size and associated defect density gradients within individual layers [32, 38, 39]. Much higher compressive stress was thus observed in the nucleation layer of the lower Cr sublayer (*cf.* Fig. C.3c), which decreases as the Cr grains increase in size (*cf.* Fig. C.2b). On the other hand, the stress state in the top Cr layer varies to much a lower extent, due to fairly constant Cr grain size throughout the layer, promoted by the local epitaxial growth of Cr on the coarse-grained CrN sublayer [26]. In both CrN layers, residual stress gradually increases over the film thickness, which is associated with multiple re-nucleation events during growth, resulting in repeated reduction of the grain size and increased contribution of the compressive intrinsic stress to the overall stress state (Figs. C.3c). Although the ion bombardment conditions did not change between the two CrN layers, the stress gradient in the top CrN sublayer is more pronounced compared to the lower CrN layer. This can be attributed to microstructural effects, such as crystallite realignment, deformation and splitting, originating form incoming accelerated particles from the plasma discharge [2, 15]. Residual stress gradients emerging from deposition of thin films (Fig. C.3c) have been investigated thoroughly in our earlier reports [32, 39] and are out of the scope of this work.

C.3.2. *In situ* experiment

C.3.2.1 Load-displacement data

Fig. C.1b shows the load-displacement curve recorded during the *in situ* CSnanoXRD experiment. During loading to $\sim 450\,\text{mN}$, only a linear-elastic response was observed, while plastic deformation is not visible. The periodic load drops are related to the stepwise movement of the piezo actuator that is used to load the sample. At loads higher than 450 mN, the change in the slope of the curve indicates a change in stiffness of the cantilever, which is attributed to formation and growth of cracks (Fig. C.1b). The unloading is fully elastic without indications of inelastic changes in the material.

C.3.2.2 Small-angle X-ray scattering microscopy

Fig. C.4 presents small-angle X-ray scattering microscopy (SAXSMs) micrographs compiled from the integrated intensities close to the direct beam, collected at 4 selected load steps (*cf.* Sec. C.2.3) during the *in situ* experiment (before loading, at 150 and 460 mN and after unloading). In the as-fabricated state, the individual Cr and CrN layers can be clearly distinguished due to their different scattering intensity (Fig. C.4a). Furthermore, the CrN-Cr interfaces, the remaining part of the substrate with a thickness of ~2-4.5 µm and the notch, penetrating ~700 nm into the first Cr layer, are clearly visible. At a load of 150 mN, bending of the cantilever was initiated by the indenter, as indicated by translation of the CrN-Cr interfaces from their original positions (Fig. C.4b). An excellent lateral alignment of the indenter and notch indicates symmetrical loading conditions, with a lateral misalignment between indenter tip and notch of only $f \approx 0.8\,\mu\text{m}$, which allows for a precise data interpretation. This alignment is critical for the experiment, because the ratio between mode II stress intensity K_{II} (in-plane shear mode) and mode I stress intensity K_{I} (crack-opening mode) is proportional to the misalignment between the indenter tip and notch over the length of the beam $\frac{f}{L}$ and inversely proportional to the aspect ratio of the cantilever $\frac{L}{t}$ [40, 41].

Consequently, during evaluation of stresses and stress intensities applied to the clamped cantilever, K_{II} can be neglected [40]. The SAXS micrograph recorded at the maximum load of 460 mN (Fig. C.4c) reveals the formation of a crack at the tip of the notch, which is responsible for the change of the slope of the load-displacement curve in Fig. C.1b. After the release of the indenter tip, the interfaces realigned, leaving only slight residual curvature in the region located directly underneath the

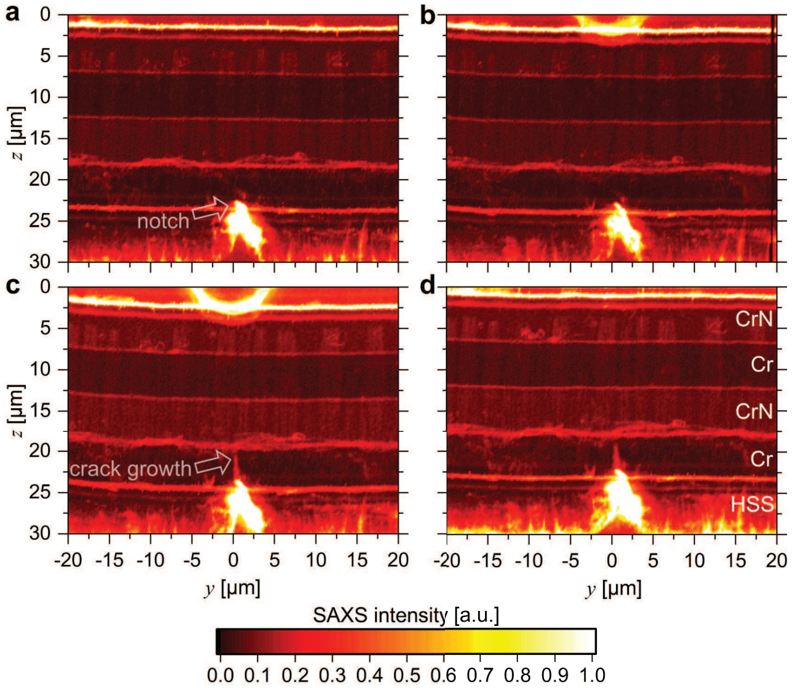

Figure C.4.: SAXSM micrographs of the clamped cantilever (a) in the as-fabricated state, (b) during loading at 150 mN, (c) at a 460 mN load and (d) after unloading.

contact area with the indenter tip (Fig. C.4d).

C.3.2.3 Experimental stress results

The stresses evaluated from the *in situ* experiment according to Sec. C.2.4 are presented here, in the context of linear-elastic (LEFM) and elastic-plastic (EPFM) fracture mechanics.

C.3.2.3.1 Experimental in-plane stresses The in-plane stress distributions $\sigma_{yy}^{m}(y,z)$ at different stages of the *in situ* experiment on the CrN-Cr clamped cantilever are presented over the entire measurement area in Fig. C.5 and in the form of a vertical section at position $y = -20\,\mu\text{m}$ in Fig. C.6. The stress state in the as-fabricated cantilever far away from the notch (y outside $\pm 15\,\mu\text{m}$, Figs. C.5a,C.6a) is almost identical to that determined in the film in its as-deposited state (Fig. C.3c). Slightly increased compressive stress (add. $-500\,\text{MPa}$) in the upper three layers is mainly related to compressive stress introduced by milling the notch and substrate removal (not quantified here).

According to LEFM, the stress $\sigma_{yy}^{\text{elastic}}$ that develops in front of a crack tip intro-

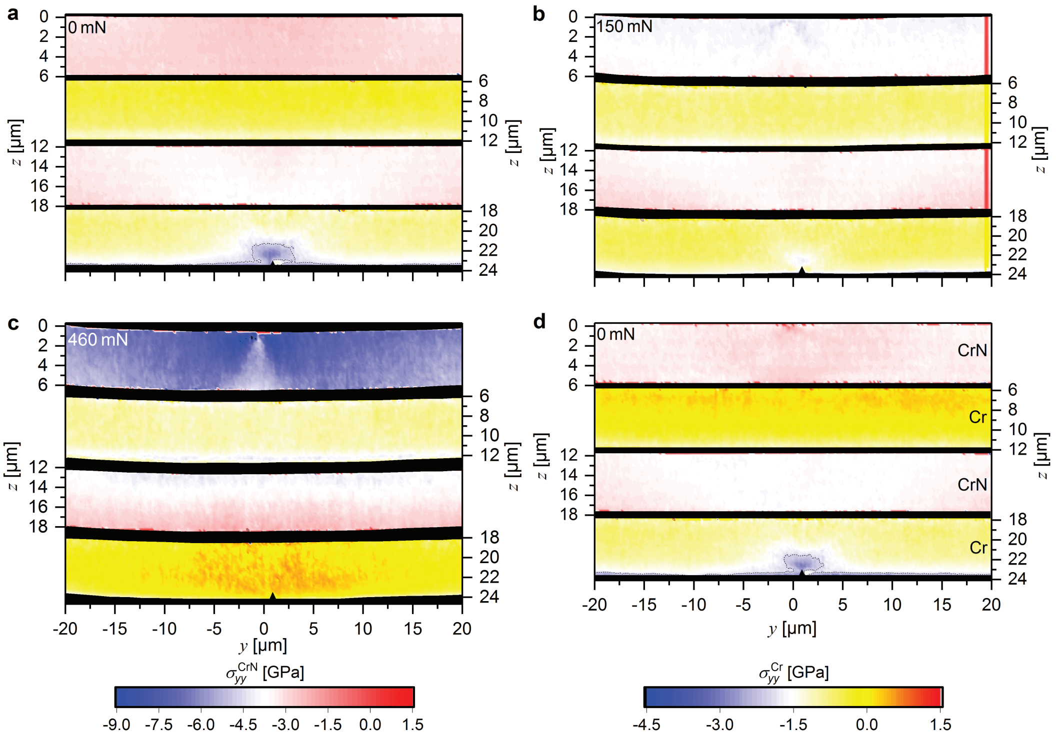

Figure C.5.: In-plane/horizontal stresses $\sigma_{yy}^{m}(y,z)$ in the CrN and Cr layers of the clamped cantilever (a) in the as-fabricated state, (b) during loading at 150 mN, (c) at a 460 mN load and (d) after unloading. The isostress-line in (a) and (d) at -2 GPa shows the different stress concentrations in front of the initial notch before and after loading, respectively. The data at each individual load step were evaluated from 30351 2D diffraction patterns. Note the different stress levels in the colour code for CrN and Cr.

duced in an ideal linear-elastic material is given by the equation

$$\sigma_{yy}^{\text{elastic}} = \frac{K_{\mathrm{I}}}{\sqrt{2\pi r}} \cos\left(\frac{\varphi}{2}\right)\left[1+\sin\left(\frac{\varphi}{2}\right)\sin\left(\frac{3\varphi}{2}\right)\right] \tag{C.8}$$

where K_{I} is the effective stress intensity and r and φ are cylindrical coordinates with the origin located at the crack tip [42]. In the cases of $\varphi = 0$ deg, the equation can be simplified to

$$\sigma_{yy}^{\text{elastic}}(z_r) = \frac{K_{\mathrm{I}}}{\sqrt{2\pi z_r}} \tag{C.9}$$

and at the centre of the plastic zone,

$$\begin{gathered}\sigma_{yy}^{\text{elastic}}\left(y_r, z_r = 0.4\,\mu\text{m}, \varphi = \arctan\tfrac{y_r}{0.4\,\mu\text{m}}\right) = \\ \frac{K_{\mathrm{I}}}{\sqrt{2\pi(y_r^2+(0.4\,\mu\text{m})^2)}} \cos\left(\tfrac{\varphi}{2}\right)\left[1+\sin\left(\tfrac{\varphi}{2}\right)\sin\left(\tfrac{3\varphi}{2}\right)\right]\end{gathered} \tag{C.10}$$

where z_r and y_r are in a relative orthogonal coordinate system with the same origin as r and φ. σ_{yy} in the directions parallel and perpendicular to the crack is shown in Fig. C.7a and C.7b, respectively. Since the residual stress is compressive in all layers, the stress concentration around the notch is also compressive. By applying the experimentally determined stress state to Eqs. C.9 and C.10, an effective stress intensity of $K_{\mathrm{I,eff}} \sim -5.9 \pm 0.4\,\mathrm{MPa\,m}^{1/2}$ (*cf.* Fig. C.7a) was calculated [42, 43]. Although the change of the stress state brought on by introducing the notch is noticeable in all 4 layers (Fig. C.5a), it is most pronounced within a radius of ~4.5-5 µm around the notch, as shown in Fig. C.7b. This can be attributed to the presence of the CrN-Cr interface, which possibly hinders the expansion of the elastic field originating at the crack tip.

Within a distance $z_r \lesssim 800\,\mathrm{nm}$ and $y_r \lesssim \pm 1.4\,\mu\mathrm{m}$ from the crack tip, the stress distributions derived from Eqs. C.8, C.9 and C.10 are no longer corresponding to the experimental data (Fig. C.7a,b). This is a consequence of the stress state at the crack tip exceeding the elastic limit of the Cr layer and resulting in the formation of a plastic zone around the crack tip [42]. An in-plane stress of -2.6 GPa was measured at the intersection between elastic and plastic areas, which exceeds the yield stress for nanocrystalline Cr of $\sim$ 2 GPa [44, 45] and can be related to the significant hydrostatic portion of the stress tensor (*cf.* Sec. C.3.2). The data within the plastic zone have thus to be treated considering the crack-tip-singularity and its effect on a power-law hardening of the material as described by Ramberg and Osgood [46], according to the equation derived by Hutchinson [7] and Rice and Rosengren [6, 7] (HRR) for the stress state within the plastic zone originated at the crack tip

$$\sigma_{rr}(r,\varphi) = C_1(n,\varphi) r^{-\frac{1}{1+n}}, \sigma_{\varphi\varphi}(r,\varphi) = C_1(n,\varphi) r^{-\frac{1}{1+n}}, \tag{C.11}$$

where r and φ are cylindrical coordinates as described above, C_1,C_2 are orientation-dependent variables and n is the power law hardening coefficient ranging from 1 to ∞, where $n = 1$ and $n = \infty$ represent a linear-elastic material and an elastic-ideal plastic material, respectively [46]. Restricting Eq. C.11 to our relative orthogonal coordinate system leads to

$$\sigma_{yy}^{\mathrm{plastic}}(z_r) \equiv \sigma_{\varphi\varphi}(r, \varphi = 0^\circ) = C_1(n, \varphi = 0^\circ) z_r^{-\frac{1}{1+n}}, \tag{C.12}$$

and

$$\sigma_{yy}^{\mathrm{plastic}}(z_r) \equiv \sigma_{\varphi\varphi}(r, \varphi = 0^\circ) = C_1(n, \varphi = 0^\circ) z_r^{-\frac{1}{1+n}}, \tag{C.13}$$

The power law hardening coefficient for Cr in front of the crack tip can be roughly estimated from the observed slope $0.15 \approx \frac{1}{1+n}$ in Fig. C.7a,b and subsequently yields $n \approx 5.7$, which fits well to literature values for Fe deformed by equal-channel angular pressing, for which $n =\sim 4-9$ was determined after considering saturation of the grain size in the nanocrystalline regime [47].

Under elastic loading, the stress state developing inside the cantilever can be described as a sum of stress components originating from (i) the bending of the cantilever beam at a given load, (ii) the stress introduced by the contact with the indenter tip, (iii) the stress developed at the tip of the notch during loading and (iv) the stress associated with the film growth (residual stress) [8, 43], and may thus be very high. In order to better understand axial stress changes due to loading, the stress relative to the residual stress in as-fabricated state at $y = -20\,\mu\text{m}$ is displayed in Fig. C.6c, together with the ideal-elastic loading calculated using the ERM (dashed lines in Fig. C.6c, *cf.* Sec. C.3.3 and Figs. C.6b,C.10). The experimentally assessed relative axial stress magnitudes at the load of 150 mN in the 4 layers correspond very well to magnitudes theoretically calculated ERM (Fig. C.6c). The noticeable deviation between experiment and model in the top CrN layer is highly correlated to the stress introduced by the indenter tip (Fig. C.5b) and in agreement to long-range stress profiles measured during indentation [22, 23]. The axial compressive stress in this layer reached values of $\sim -4.5\,\text{GPa}$ already at a deflection force of 150 mN (Fig. C.6a). The stress field was rather symmetric and the maximum stress was accumulated at an inclination of 30 deg to the surface normal (Fig. C.5b). This stress distribution is determined by the geometry of the indenter tip and the cantilever [22, 23]. On the other hand, the stress near the notch tip, exhibiting values of $\sim -2.5\,\text{GPa}$ in the as-fabricated state, was reduced to $\sim -1.6\,\text{GPa}$ at 150 mN load (Fig. C.7a,d). According to Eq. C.9, this corresponds to an effective stress intensity of $\sim -3.0 \pm 0.5\,\text{MPa}\,\text{m}^{1/2}$. Furthermore, the size of the zone dominated by the elastic field of the crack tip was reduced to $\sim 3\,\mu\text{m}$, which is associated with the bending stress counteracting the initial state. Corresponding to the findings above, the size of the plastic zone and the slope of the stresses within did not change after loading to 150 mN, supporting the conclusion that the stress state accumulated through loading to 150 mN (Figs. C.5b,C.6c,C.7) was elastically superimposed onto the initial stress state before bending (Figs. C.5a,C.6a,c,C.7).

The onset of plastic deformation that is detectable by the change of the slope of the load-displacement curve at a load of 450 mN (Fig. C.1b) was used to calculate fracture toughness of the lower Cr layer, in which initiation and growth of a crack took place (Fig. C.4c). By applying linear-elastic fracture mechanics for the critical

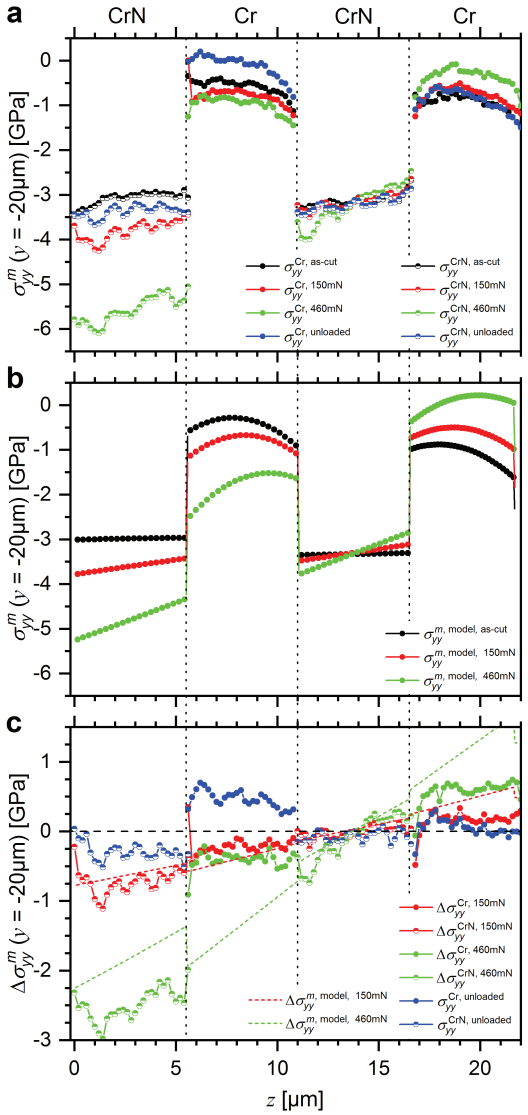

Figure C.6.: In-plane/axial stress magnitudes $\sigma^{m}_{yy}(z)$ far off the notch ($y = -20\,\mu\mathrm{m}$) for (a) CrN and Cr inside the clamped cantilever at selected loads during the *in situ* experiment, (b) in-plane/axial stress magnitudes $\sigma^{m}_{yy}(z)$ far off the notch ($y = -20\,\mu\mathrm{m}$) for CrN and Cr of the clamped cantilever calculated using the ERM, and (c) the difference between the stress at the selected loads and the residual stress in as-fabricated state $\Delta\sigma = \sigma_{yy,i} - \sigma_{yy,\mathrm{as-cut}}$ for the experiment and simulation. The dashed vertical lines show the interfaces between Cr and CrN. $z = 0\,\mu\mathrm{m}$ corresponds to the indented film surface, $z = 22.5\,\mu\mathrm{m}$ corresponds to the film/substrate interface and the position of the notch.

load, a value of 2.8±0.5 MPa m^{½} was obtained, which is in a good agreement with K_{Ic} ≈2.5-2.7 MPa m^{½} determined by bending of microcantilever beams fabricated from Cr thin films having comparable microstructure and residual stress state [3, 45, 48]. The axial stress state at a load of 460 mN is shown in Fig. C.5c and Fig. C.6a. Magnitudes as high as -9 GPa were revealed underneath the indenter tip directly in the contact area (Fig. 5c). Similar values for axial stress have been reported also for other *in situ* and *ex situ* experiments performed on comparable CrN films [23, 26]. The stress field in the CrN top-layer underneath the indenter developed at the load of 460 mN (Fig. C.5c) is similarly shaped to the stress field observed at 150 mN (Fig. C.5b), only the stress values are correspondingly higher. The in-plane stress in the lower Cr interlayer almost fully relaxed due to propagation of the crack through almost the entire Cr layer (Fig. C.4c) and induced extensive stress relief in a large volume including also a part of the CrN layer close to the Cr-CrN interface. The relative stress accumulated after loading to 460 mN is shown in Fig. C.6c together with the elastic stress profile calculated from ERM. Significant differences from ideal elastic loading are revealed by the experimental data, which can be attributed to (i) a loss of stiffness due to crack growth and stress relaxation in the lower Cr sublayer, (ii) high stress concentrations in the top CrN layer as a consequence of indentation and (iii) plastic flow in the top Cr layer as a consequence of compressive stress accumulated through both indentation and bending. Remarkably, directly at the surface of the top CrN layer at $y = \pm 20\,\mu\mathrm{m}$, the increase in compressive stress magnitude is in very good agreement with the results from ERM (Fig. C.6c), which leads us to conclude that the axial stress originated from the indentation are restricted to sub-surface regions [23]. The change of the stress state in both Cr layers from compressive to tensile ($\sim$ 700 MPa in the upper and 200 MPa in the lower Cr sublayer) after unloading (Figs. C.5d,C.6a,c) is associated with the inelastic deformation of the cantilever. For the same reason, the axial stress in the top CrN layer after unloading is more compressive compared to the stress state in its as-fabricated state. Additional compressive residual stress in the centre of the CrN layer is due to plastic deformation near the indenter contact area and also further away in the top Cr sublayer (Fig. C.5d). On the contrary, no inelastic stress changes were observed in the lower CrN layer (Fig. C.5d), which is due to its position close to the neutral fibre of the clamped cantilever. The compressive stress introduced by milling the notch in the lower Cr layer, which was suppressed during bending of the cantilever, re-emerged after loading and exhibits almost the same value of ~ -2.5 GPa (Fig. C.5d). This is related to nearly ideal crack closing and restoration of the material's integrity under compressive load.

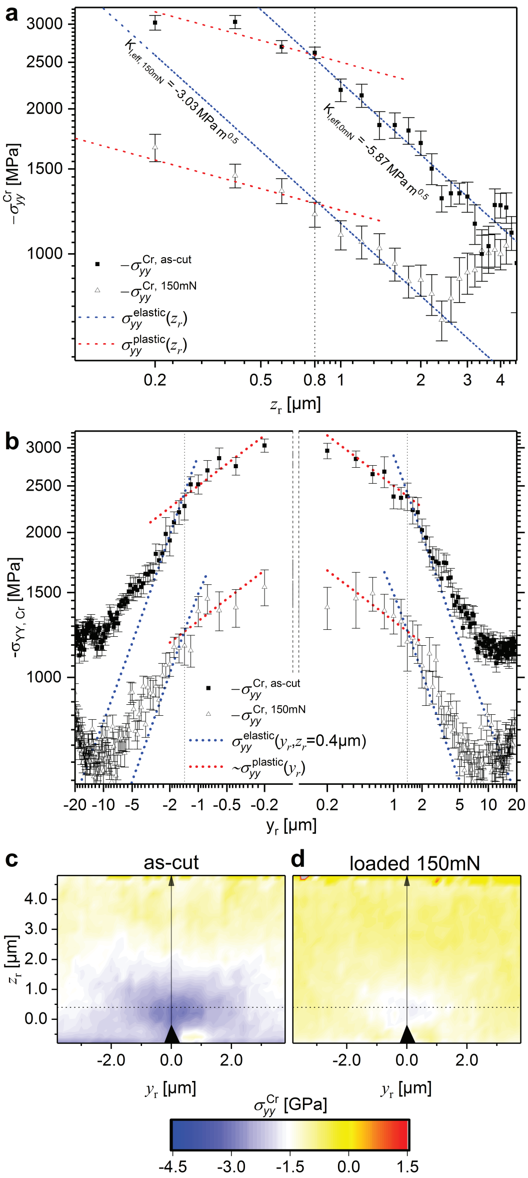

Figure C.7.: In-plane/axial stress $\sigma_{yy}^{\mathrm{Cr}}(y,z)$ developed in front of the notch tip in the Cr/HSS sublayer. Experimental data corresponding to the Cr layer at coordinates (a) $z_\mathrm{r} = [0.2, 4.6]$ µm (b) and $y_\mathrm{r} = [-20, 20]$ µm in the as-fabricated state and at a load of 150 mN. For comparison, power-law-fits for the HRR-dominated plastically deformed zone in front of the notch (red) and the stress-intensity-factor-dominated elastically stressed zone (blue) are also given. The dotted lines at $z_\mathrm{r} = 0.8$ µm and$y_\mathrm{r} = \pm 1.5$ µm in (a) and (b), respectively, indicate the border between elastic and plastc zone. 2D colour plots presented in Fig. C.5 are shown here in detail for the area around the notch tip (c) in the as-fabricated state of the cantilever and (d) at a load of 150 mN. The dotted line in (c) and (d) at $z_\mathrm{r} = 0.4$ µm represent the positions, where the data for (b) were obtained.

C.3.2.3.2 Experimental out-of-plane stresses Concerning the out-of-plane stresses σ^{m}_{zz} in the as-fabricated state displayed in Fig. C.8a, it is evident that the stress distribution is mainly governed by the notch. The out-of-plane stress introduced by a crack tip is given by the equation

$$\sigma^{\text{elastic}}_{zz} = \frac{K_{\text{I}}}{\sqrt{2\pi r}} \cos\left(\frac{\varphi}{2}\right)\left[1 - \sin\left(\frac{\varphi}{2}\right)\sin\left(\frac{3\varphi}{2}\right)\right] \tag{C.14}$$

which is only valid as long as $r \ll a$. In the present case, where $r \approx a$, the solution for the crack tip singularity derived by Sneddon [49] has to be used, which takes the non-singular part, *i.e.* far-field $\sigma_{yy,\infty}$, also into account. This equation can be simplified for the direction parallel to the crack as

$$\sigma^{\text{elastic}}_{zz}(r, \varphi = 0°) \equiv \sigma^{\text{elastic}}_{zz}(z_r) = \frac{K_{\text{I}}}{\sqrt{2\pi r}} - \sigma_{yy,\infty} \tag{C.15}$$

In as-fabricated state, a maximum compressive stress of ~ -1.4 GPa was found at a distance of ~1 µm from the crack tip (*cf.* Fig. C.8a, Suppl. Fig. S.C.3a,b). By comparing this value to $\sigma_{yy}(z_r)$ shown in Fig. C.7, it can be seen that the stress profiles differ by approximately the amount of in-plane residual stress far off the crack tip, which confirms the applicability of Eq. C.15. Comparable deviations of the experimental results from Eq. C.14 were found in [13], where the stress in front of the crack in crack opening (y) and crack-growth (z) direction deviated by a factor of ~ 2.5. Additionally, in contrast to the in-plane/axial stresses, the out-of-plane stress in the cantilever has to fulfil the equilibrium condition at the crack tip, *i.e.* at free surfaces, stress magnitudes parallel to the surface normal have to be 0, which leads to a reduction of the elastic out-of-plane stress magnitudes within the plastic zone. As a load of 150 mN is applied to the clamped cantilever, the stress field originated from the notch is reduced as a consequence of the reduced applied stress intensity (Figs. C.8b, C.7a). Furthermore, the notch-induced stress field is superimposed by the compression field beneath the indenter tip (Fig. C.8b), which resulted in two compressive maxima of ~ -0.75 GPa and ~ -1.25 GPa, induced by the notch and impinging indenter tip, respectively. Corresponding to the in-plane stress magnitudes presented in Fig. C.8a, the size of the elastic zone in front of the crack tip is reduced to ~ 3 µm (Suppl. Fig. S.C.3a,b). Additionally, at the surface of the topmost CrN sublayer, tensile stress of ~ 0.25 GPa form as a consequence of pile-up formation in the indenter imprint region, which is in agreement with results by Zeilinger *et al.* [22] and Ecker *et al.* [23].

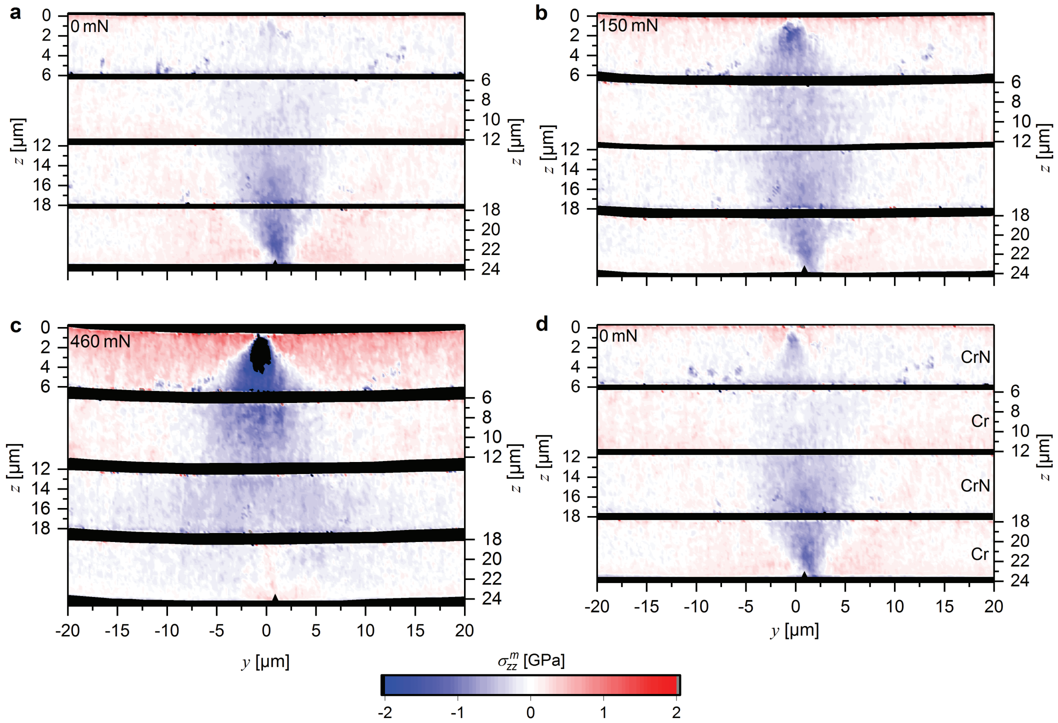

Figure C.8.: Out-of-plane/vertical stresses $\sigma^m_{zz}(y, z)$ in the CrN and Cr layers of the clamped cantilever (a) in the as-fabricated state, (b) during loading at 150 mN, (c) at a 460 mN load and (d) after unloading. The data at each individual load step were evaluated from 30351 2D diffraction patterns.

At the maximum load of 460 mN, the stress field induced by the notch mostly disappeared, whereas the out-of-plane compressive indentation-induced stress reached a maximum in excess of -5 GPa (Fig. C.8c), which is associated with classical Hertzian contact mechanics [22, 23]. At this load, the out-of-plane compressive contact stress penetrated through all layers, and was separated laterally by the stress-free cracked zone in the lowest Cr sublayer as a consequence of crack growth. Furthermore, the tensile stressed zones aside the contact area with the indenter in the topmost CrN layer reached magnitudes of ∼ 1 GPa (Fig. C.8c). After unloading, residual out-of-plane compressive and tensile stress remained around the indentation imprint and additionally, the notch-induced stress field reappeared, which is related to plastic deformation and crack tip blunting in the lower Cr sublayer, as already discussed above (Fig. C.8d).

C.3.2.3.3 Experimental shear stresses The shear stress $\sigma^m_{yz}(y, z)$ evolution during the *in situ* experiment is shown in Fig. C.9. In the as-fabricated state, notch-induced shear stresses are dominant within all layers (Fig. C.9a), reaching a maximum of ±1 GPa symmetrically next to the notch. Furthermore, the formation of shear stresses appears to be independent of the elastic response of the individual layers and is not interrupted by the interfaces (Fig. C.9a). Shear stresses in the crack-tip-area can be described by linear-elastic fracture mechanics as follows

$$\sigma_{yz}^{\text{elastic}} = \frac{K_\mathrm{I}}{\sqrt{2\pi r}} \cos\left(\frac{\varphi}{2}\right) \sin\left(\frac{\varphi}{2}\right) \cos\left(\frac{3\varphi}{2}\right). \tag{C.16}$$

From Eq. C.16 and Fig. C.9, it can be seen that the crack-tip shear stresses are 0 along the z_r axis. Perpendicular to the crack tip (along y_r), Eq. C.16 can be simplified to

$$\left|\sigma_{yz}^{\text{elastic}}\right| = \frac{1}{4}\left|\frac{K_\mathrm{I}}{\sqrt{2\pi y_r}}\right|. \tag{C.17}$$

The shear stresses in as-fabricated state perpendicular to the crack tip are shown in Suppl. Fig. S.C.4a and b, from which follows that the observed shear stresses corresponds to an effective stress intensity of $K_{\mathrm{I,eff}} \sim -5.9 \pm 0.4\,\mathrm{MPa\,m^{1/2}}$, whereas inside the plastic zone, the magnitude decreases.

After loading to 150 mN (Fig. C.9b), an indenter-induced shear stress field is introduced in the topmost CrN sublayer according to Hertzian contact mechanics [22, 23]. This shear stress field reaches a magnitude of ∼ ±0.5 GPa symmetrically off-axis beneath the indenter and appears to be restricted to the topmost CrN sublayer, although a superposition of the shear stress induced by the notch and the shear stress induced by the indenter cannot be excluded. Furthermore, the maximum magnitude of the shear field in front of the crack tip is apparently reduced to ∼ ±0.5 GPa, while its extension is restricted to the lower Cr and CrN layers (Fig. C.9b). In contrast, the magnitude of the shear fields to the sides of the crack tip is increased, having the same sign as the indenter-induced shear stresses (*cf.* Suppl. Fig. S.C.4a,c). Additionally, a shear stress τ_{yz} is induced by the bending load acting as a shear force $Q = \mp\frac{P}{2}$, according to

$$\tau_{yz} = \mp\frac{6P}{Bt}\left(\frac{z}{t} - \left(\frac{z}{t}\right)^2\right) \tag{C.18}$$

where P is the applied load and t and b are the thickness and width of the cantilever, respectively. Hence, a maximum additional shear stress of ∼110 MPa was introduced along the neutral fibre axis at a load of 150 mN, whereas this additional shear stress reached ∼340 MPa at 460 mN. It is obvious that the shear-force induced shear stress counteracted the shear stresses introduced by the notch and the indenter, leading to lower apparent shear stresses in the centre of the clamped cantilever (Fig. C.9b,c). This is especially visible at the transition from the lower Cr to the lower CrN sublayer at 150 mN load (Fig. C.9b), where the change from positive to negative shear stresses is drawn closer to the symmetry axis, compared to the as-fabricated state (Fig C.9a). After loading to 460 mN, the notch-induced shear stresses disappeared as a consequence of crack growth, whereas the shear stress induced by the indenter tip perpetrated in this case through all layers, reaching maxima of about ±2 GPa, symmetrically in the topmost CrN sublayer (Fig. C.9c). After unloading, again a superposition of indenter tip- and notch-related stress distributions were observed, indicating inelastic deformation in the topmost CrN sublayer and crack tip blunting in the lowest CrN sublayer, respectively (Fig C.9d).

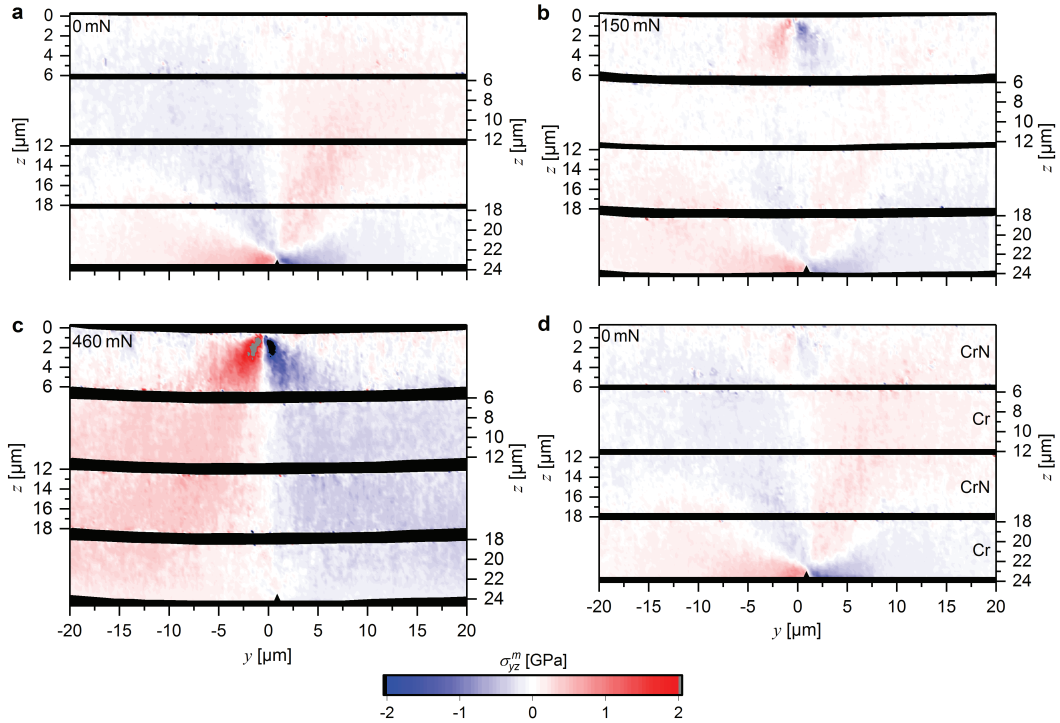

Figure C.9.: Shear stresses $\sigma_{yz}^{m}(y,z)$ in the CrN and Cr layers of the clamped cantilever (a) in the as-fabricated state, (b) during loading at 150 mN, (c) at a 460 mN load and (d) after unloading. The data at each individual load step were evaluated from 30351 2D diffraction patterns.

C.3.2.3.4 Experimental equivalent von-Mises stresses and experimentally found plastic zone Equivalent von-Mises stresses were calculated from the experimental data in the area surrounding the notch for plane stress and plane strain state, respectively, using the following equations

$$\sigma_{\mathrm{vM,plane\,stress}} = \sqrt{\sigma_{yy}^2 + \sigma_{zz}^2 - \sigma_{yy}\sigma_{zz} + 3\sigma_{yz}^2} \tag{C.19}$$

and

$$\begin{aligned}\sigma_{\mathrm{vM,plane\,stress}} = &\sqrt{\left(\sigma_{yy}^2 + \sigma_{zz}^2\right)\left(\nu^2 - \nu + 1\right)} \\ &\overline{-\sigma_{yy}\sigma_{zz} + 3\sigma_{yz}^2}\end{aligned} \tag{C.20}$$

where ν is the Poisson ratio defined for Cr in Table C.1. The von-Mises stress state is shown for plane stress and plane strain conditions in Suppl. Fig. S.C.5 and S.C.6, respectively. It can be seen from both Suppl. Figs. that the experimentally determined von-Mises yield stress ranges from 2.0 to 2.3 GPa. Additionally, perpendicular to the crack tip, the plastic zone is apparently elongated to $\sim$ 3.5 µm and is larger compared to that shown in Fig. C.7, where the size of the plastic zone was determined to be 1.4 µm along the axial (y_r) direction. By replacing σ_{yy}, σ_{zz} and σ_{yz} in Eqs.C.19 and C.20 with their counterparts from Eqs. C.8, C.14 and C.15 under the assumption of a linear-elastic/ideal plastic material, quadratic equations in $\frac{1}{\sqrt{r_p}}$ were constructed as follows

$$\begin{aligned}0 = &\left(\tfrac{1}{\sqrt{r_p}}\right)^2 \left(\tfrac{K_{\mathrm{I}}\cos\left(\frac{\varphi}{2}\right)}{\sqrt{2\pi}}\right)^2 \left(1 + 3\sin^2\left(\tfrac{\varphi}{2}\right)\right) + \\ &\left(\tfrac{1}{\sqrt{r_p}}\right)\sigma_{yy,\infty}\left(3\sin\left(\tfrac{\varphi}{2}\right)\sin\left(\tfrac{3\varphi}{2}\right) - 1\right) \\ &+\sigma_{yy,\infty}^2 - \sigma_f^2\end{aligned} \tag{C.21}$$

for plane stress and

$$\begin{aligned}0 = &\left(\tfrac{1}{\sqrt{r_p}}\right)^2 \left(\tfrac{K_{\mathrm{I}}\cos\left(\frac{\varphi}{2}\right)}{\sqrt{2\pi}}\right)^2 \left(\left(1 - 2\nu^2\right) + 3\sin^2\left(\tfrac{\varphi}{2}\right)\right) + \\ &\left(\tfrac{1}{\sqrt{r_p}}\right)\sigma_{yy,\infty}\left(3\sin\left(\tfrac{\varphi}{2}\right)\sin\left(\tfrac{3\varphi}{2}\right) - \left(1 - 2\nu^2\right)^2\right) \\ &+\sigma_{yy,\infty}^2\left(1 + \nu^2 - \nu\right) - \sigma_f^2\end{aligned} \tag{C.22}$$

for plane strain condition, respectively, where $\sigma_{yy,\infty}$ is the stress far off the notch (assumed as constant) and σ_f is the flow stress of Cr. The solutions for plane stress and plane strain conditions are shown in Suppl. Figs. S.C.5c and S.C.6c for values of $\sigma_{yy,\infty} = -1.2$ GPa and $\sigma_f = 2.15$ GPa. While the former was obtained from Fig. C.3, the latter is a value from literature [44]. The calculated plastic zone in Suppl. Figs. S.C.5c and S.C.6c shows that (i) the size of the plastic zone is less dependent on plane stress and plane strain condition and (ii) that the extension of the plastic zone is significantly larger along the y-axis, contrary to the solutions presented in Ref. [4]. Both results are a consequence of the comparatively higher deviatoric component of the stress tensor in front of the crack tip, caused mostly by the far-field induced reduction of σ_{zz} at distances of $r \approx a$.

C.3.3. Simulated stress results

After solving the eigenstrain problem using FEM, the in-plane/axial stress $\sigma^{m}_{yy}(y,z)$ components were obtained (Figs. C.6b and C.10). A comparison between Figs. C.5 and C.10 shows excellent agreement between the experimental and simulated experiment for the as-fabricated state ($F_{ind} = 0\,\mathrm{mN}$) and the first loading step ($F_{ind} = 150\,\mathrm{mN}$). Before loading, the stress distribution is governed by the residual stress induced by the deposition process and the presence of the notch that acts as a stress raiser (Fig. C.10a). Additional contributions of compressive residual stress were evaluated at the edges of clamping positions, which originate from the boundary conditions. The excellent agreement with experimental data at the edge of the experimentally investigated volume can be seen in Fig. C.6. After applying the first loading step, stress concentrations around corners are reduced and intensified at the top surface and the bottom of the clamped cantilever, respectively. Overall, the bending deformation results in additional stress contributions, which are (i) in-plane tensile stress at the clamping positions and compressive in-plane stress in the centre in the top half of the clamped cantilever and (ii) in similar stress distributions of opposite signs formed at the lower half of the clamped cantilever. As a consequence, the stress at the notch tip is significantly reduced, while the stress magnitudes within the experimentally observed regions of the Cr layers still vary between −1.5 GPa and −0.4 GPa and the compressive stress within the CrN layers varies between −4.5 GPa and −2.5 GPa. The calculated stress magnitudes agree particularly well with experimental in-plane stresses $\sigma^{m}_{yy}(y,z)$ (*cf.* Fig. C.5b), which validates the correct assumption of elastic deformation during loading up to 150 mN.

While the experimentally determined stress distributions (Fig. C.5 well agree with the calculated data (Fig. C.10) for 150 mN load, they differ for the load of 460 mN. This is likely caused by a combination of two effects: (i) the onset of plastic deformation within both Cr and CrN was not taken into account by the linear-elastic FEM model and (ii) the crack growth through the bottom Cr layer led to a relief and consequent re-distribution of the axial component of stress. High stress concentrations around the crack tip, as well as at the penetration point of indenter and at the corner joining the cantilever with the rest of the multilayer become apparent during this final loading steps, ranging from 5 GPa tension up to −10 GPa in compression. These values exceed the elastic limits of nanocrystalline Cr and it is therefore not surprising to see lower stress values in the experimental data. In summary, the high accuracy of the FE model confirms the experimental data in the elastic load range and further highlights highly stressed regions at even higher loads, which makes it very easy to identify, by considering the elastic limits of both layer components and the substrate, inelastically deformed and potentially damaged material regions, when comparing simulation and experiment.

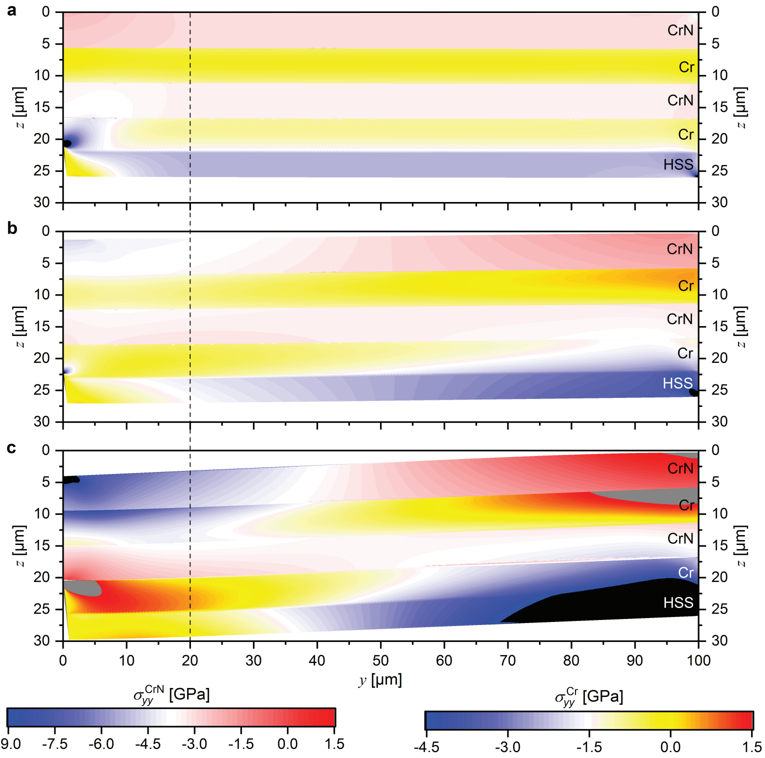

Figure C.10.: In-plane/axial stress $\sigma_{yy}^{m}(y,z)$ magnitudes calculated using the ERM for CrN and Cr inside the clamped cantilever in its (a) as-fabricated state, and at loads of (b) 150 mN and (c) 460 mN. The dashed line indicates the edge of the stress fields assessed by the experiment. Note the different stress values in the colour code for CrN and Cr.

C.4. Discussion

C.4.1. *In situ* synchrotron setup and measurement conditions

In previous *ex situ* and *in situ* X-ray diffraction studies, focussed on the determination of stresses in front of a crack tip during fatigue experiments and overload fatigue events, beam sizes (gauge volumes) between 25 and 60 µm have been applied to compact tension samples [11, 13–15]. In these studies, normal stresses in the sample volume and total strain at the surface in front of the crack tip have been investigated using synchrotron X-ray diffraction and DIC, respectively, while the actual crack tip has been tracked at the sample surface using optical microscopy. In only one other study, residual strain and crack closure have been measured *ex situ* after an overload event by a combination of X-ray diffraction and X-ray tomography in the sample volume [10], allowing for separation of plasticity-induced closure and residual stress contributions to fatigue crack retardation following an overload [50]. In contrast, the *in situ* CSnanoXRD setup at the nanofocus beamline (ID13, ESRF) presented in [23] and utilized in this study allowed, for the first time, to determine the stress distributions in the crack-tip area and within the plastic zone with nanoscale resolution for a thin film material (*cf.* Figs. C.5, C.6, C.7, C.8, C.9). Our work thus represents the first successful attempt to map the full 2D stress tensor perpendicular to the incident X-ray beam including also shear stresses (*cf.* Figs. C.5, C.6, C.7, C.8, C.9) and simultaneously visualizing the crack and its growth within the investigated volume (*cf.* Fig. C.4). In a first step, validity of the fracture experiment is asserted by the condition

$$a, (t-a), B \geq 2.5 \left(\frac{K_{\mathrm{Ic}}}{\sigma_f}\right)^2, (22) \tag{C.23}$$

where the cantilever width B, the ligament size $t-a$ and the notch depth a have to be large compared to the process (plastic) zone, which is fulfilled in the present case. Additionally, concerning the formation of a plastic zone in front of the crack tip/notch, the influence of Ga^{+}-ions from FIB preparation of the sample can be neglected, since the ions penetrate into a depth of only $\sim$ 50 nm below the specimen surface, and influence only an insignificant fraction of the measured plastic zone [51, 52]. However, as seen in Eqs. C.2 and C.3, a drawback of the transmission geometry used in the CSnanoXRD setup is that for low-angle *hkl*-Debye Scherrer rings, there is only a very low sensitivity for the normal stress parallel to the beam direction. The stresses retrieved from the experimental diffraction data can, however, be well compared to theoretical considerations of the Griffith model [5] or the HRR stress field [5–7] (*cf.* Eq. C.11). Furthermore, the direct evaluation of K_{I} using the stresses in front of the crack tip is independent of geometry factors that are otherwise necessary to evaluate the stress intensity and the fracture toughness. The stress distribution perpendicular to the X-ray beam around the crack tip in mode I loading is independent of the presence of plane stress or plane strain conditions, *i.e.* only the stress component parallel to the beam would differ. On the one hand, the inability to distinguish between these two stress states means that the measurement is exact, but on the other hand, the material properties, especially the plastic behaviour of ductile phases, have to be guessed to a certain degree (*cf.* Sec. C.3.2.3.4). In the following sections, the effects observed during the *in situ* synchrotron experiment will be discussed with regards to the experimental limitations.

C.4.2. Stress state around the crack tip in as-fabricated state

Since most studies interested in the residual stress in front of the crack tip have encountered crack propagation during cyclic loading after an overload event[11, 13–15], a comparison to our findings can be made especially regarding the stress fields found directly after unloading from an overload event. The overload induces plastic deformation, which relieves (tensile) stresses and in turn generates a compressive residual stress field after unloading. This compressive residual stress field can be assumed to be similar to a residual stress originating from the physical vapor deposition (PVD) process used for the synthesis of thin films. In fact, the σ_{yy} distribution found after unloading from an overload event in Ref. [13] is similar to the one observed in Fig. C.5. However, the residual stresses introduced by an overload event are highly localized and non-uniform compared to the laterally uniform residual stresses induced by the PVD process. Secondly, the stress distribution is closely related to the LEFM and EPFM models [4], as shown in Sec. C.3.2, despite the opposite sign of the stress distributions. Additionally, significant differences between the magnitudes of applied stresses in crack-opening (y) and crack-growth (z) directions were also found in [13, 14, 53], which is comparable to our findings in Figs. C.5a and C.8a.

In as-fabricated state, the lower Cr sublayer is highly compressively stressed as a consequence of the deposition process. Therefore also the effective stress intensity $K_{\mathrm{I,eff,0\,mN}}$ is negative. Furthermore, the magnitude of the stress intensity due to the residual stresses in as-fabricated state K_{res} ($= K_{\mathrm{I,eff,0\,mN}}$) exceeds the fracture toughness of Cr $K_{\mathrm{Ic,Cr}}$ $\approx$2.5-2.7 MPa m$^{1/2}$ [3, 45] by a factor of 2, which is only possible due to its negative sign. The opposite example can be seen in Ref. [8], where a tensile residual stress present in the material before loading leads to a localized (tensile) stress increase at the crack tip and subsequently significant acceleration of (stable) crack growth.

In our case, a pronounced plastic zone is formed in front of the crack tip, which demonstrates the potential of a crack retardation by compressive residual stress. Consequently, a natural defect, such as droplets, formed within the thin film during processing, would have been enclosed by a plastic zone immediately during thin film growth, due to compressive residual stress as present here for the Cr layer. Furthermore, the evaluation of σ_{yy} in front of the crack tip shows that the approach of LEFM accompanied by small-scale yielding is appropriate, since the stresses at $z_r > 0.8\,\mu\mathrm{m}$ are characterized by K_I and at smaller distances z_r =0.2-0.8 µm by the HRR solution [4]. The von-Mises yield stress, presented in Suppl. Figs. S.C.5 and S.C.6 at the intersection between elastic and plastic zone, is in good agreement with the results obtained from micro-pillar compression of ultra-fine grained Cr [44]. Additionally, the shift of the experimentally determined plastic zone in the positive z-direction (compared to the one calculated in Sec. C.3.2) can be related to the hardening parameter n, as shown in Ref. [4]. In general, the stress state across the clamped cantilever complies very well with theoretical considerations [4, 6, 7, 49] and experimental results [13], and is also supported, regarding the elastic response, by the 2D FE model (Fig. C.10).

C.4.3. Loading, crack growth, crack tip blunting and crack closing

The comparison of the experimental and calculated results validated that LEFM can be applied to study deformation of the clamped cantilever consisted of Cr and CrN layers. Based on that finding, the applied stress intensity can be added linearly to the effective stress intensity $K_{\mathrm{I,eff,0\,mN}}$ evaluated from the data in as-fabricated state, *cf.* Ref. [43]. Additionally, according to LEFM, the applied stress intensity is proportional to the applied stress, which is furthermore proportional to the applied indenter load [4]. However, attributing the stresses to their origin during and after loading is rather difficult due to the overlap of (i) crack tip, (ii) indenter, (iii) bending and (iv) residual stress contributions to the overall stress state (*cf.* Figs. C.5, C.6, C.7, C.8, C.9). In the case of elastic loading, these contributions to the overall measured stress state are accumulated linearly [43], as can be seen when the clamped cantilever is loaded to 150 mN (Fig. C.6). During loading to 150 mN, an additional stress intensity K_app of 2.9 MPa m$^{1/2}$ thus applied to the crack tip, which resulted in an effective stress intensity of $K_{\mathrm{I,eff,150\,mN}} = -3.0\,\mathrm{MPa\,m^{1/2}}$. As already discussed above, the effective stress intensity in front of the crack tip in Cr can be quantified to be negative at 0 and 150 mN load, while the loading can be considered as purely elastic. The reasonability of applying LEFM (and small scale yielding) to analyse fracture behaviour of magnetron sputtered Cr even on a microscale has been validated also in previous studies [3, 45].

Unfortunately, no 2D stress pattern was recorded at loads between $\sim$ 300 and 400 mN, which could have resolved the influence of the plastic zone formed in compression on the stresses in tension. However, the influence of the plastic zone formed in front of the crack tip may be minor, since cracks in thin films are supposed to propagate along grain boundaries of low cohesive energy, as seen for example also in Ref. [48], where intergranular fracture of ultra-fine-grained Cr has been observed during microbending tests. This is furthermore supported by the fact that the fracture toughness calculated from the load-displacement curve and the experimental stress data (under the assumption of LEFM) is comparable to literature values [3, 45, 48].

When the stress intensity overcomes the fracture toughness of the Cr sublayer, unstable crack starts to grow, which is stopped at the adjacent Cr-CrN interface (Fig. C.4c). It results in a loss of geometric stiffness and hence in a rise of applied stresses (while keeping the load constant). Presumably, the applied load then surpasses the elastic limit of the top Cr layer and plastic deformation again reduces the magnitudes of applied stress (Fig. C.5c), while the CrN layers still remain loaded elastically (except for the regions surrounding the indenter contact area, Figs. C.5c, C.8c, C.9c). Additionally, no influence of the crack is visible in the lower CrN layer, indicating that the crack tip has blunted while approaching the still compressively stressed CrN, which is a major difference between the experiment and the linear-elastic 2D FE model (*cf.* Figs. C.5, C.10). During further loading, the clamped cantilever would then behave like an unnotched specimen with a discontinuous bottom layer. After unloading, stress fields from the notch reappear (Fig. C.5d), uninfluenced by the presence of the crack, which also can be seen in the SAXS micrograph (Fig. C.4d). This indicates nearly ideal closing of the crack and restoration of the materials integrity under compressive load.

C.5. Conclusions

CSnanoXRD was utilized to investigate *in situ* the nanoscale stress fields in a notched clamped cantilever with a lateral resolution of 200 nm × 200 nm. The experimentally determined stresses were correlated with small-angle X-ray scattering and electron microscopy and interpreted in light of a 2D elastic finite element model. The compressive stress distribution originating from the deposition process influenced the fracture behaviour tremendously, resulting in the immediate formation of a (compressive) plastic zone of considerable size in front of the crack tip in Cr layer. During loading, fracture in the lower Cr layer was retarded by a factor of 3, since the initial (unloaded) stress intensity was double the negative critical value. This demonstrates the beneficial influence of the compressive residual stress and the concept of structural heterogeneity to mechanically stabilize thin films, as demonstrated by the crack stopping ability of heterogeneous interfaces. In summary, it was possible for the first time, to retrieve quantitative information on the nanoscale stress state within the plastic zone during a fracture experiment in nanocrystalline thin films and to manifest the potential of the microstructural design in toughening of hard yet brittle nanostructured materials.

Acknowledgments

The work has been financially supported by Christian Doppler Research Association. The financial support by the Austrian Federal Ministry of Science, Research and Economy and the National Foundation for Research, Technology and Development is also gratefully acknowledged. Special thanks are devoted to J. F. Keckes for help with the artwork and G. Felber for the mechanical preparation of the synchrotron lamella. Special thanks are also devoted to M. Alfreider for the fruitful discussion about fracture mechanics.

Supplementary material

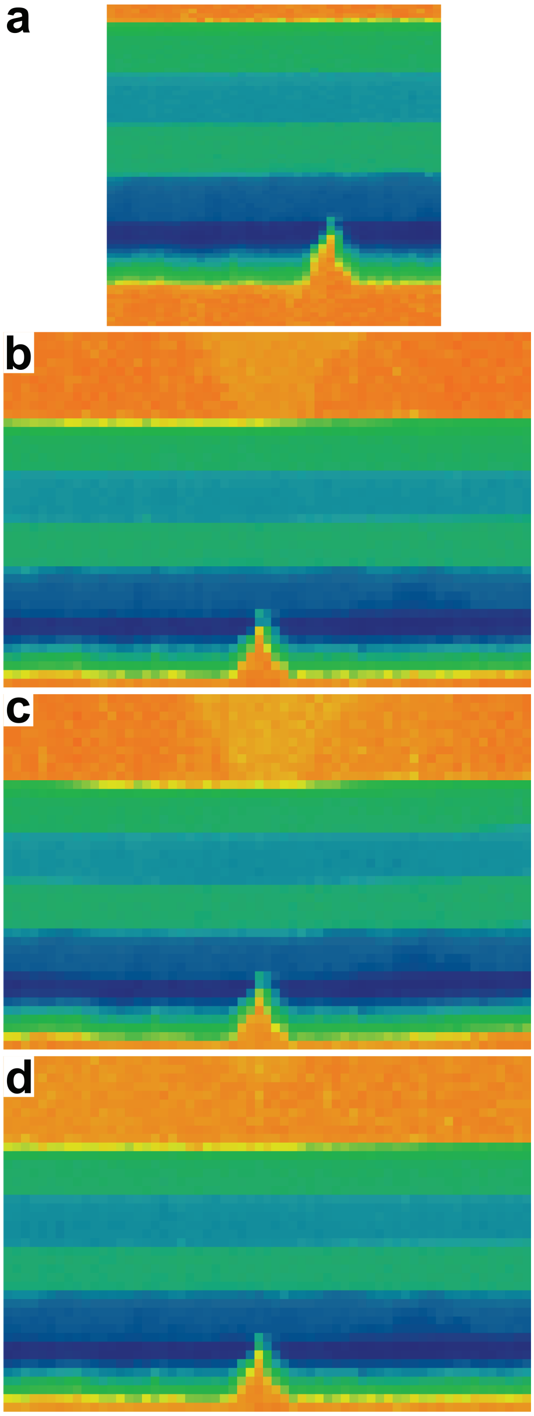

Suppl. Fig. C.1. X-ray absorption micrographs of the clamped cantilever in as-fabricated (a), during loading at 150 mN (b) at 460 mN (c) and after unloading (d). Note that pixel size for (a) is 500 nm × 500 nm, whereas for the others the resolution is 1 µm × 1 µm.

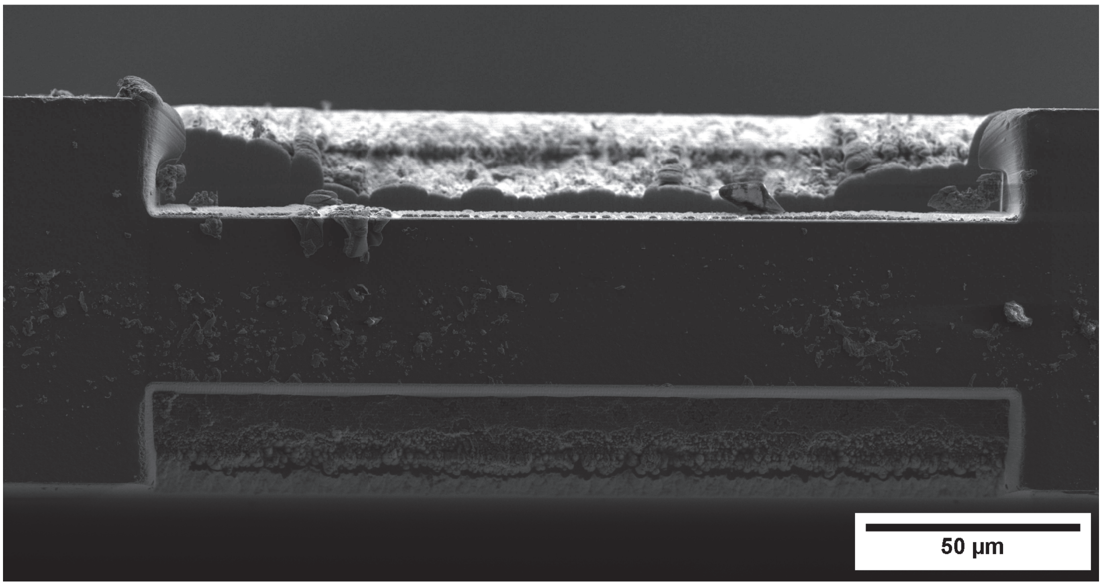

Suppl. Fig. C.2. Top-view SEM micrograph of the clamped cantilever. L and B were measured as 200 and 40 µm, respectively.

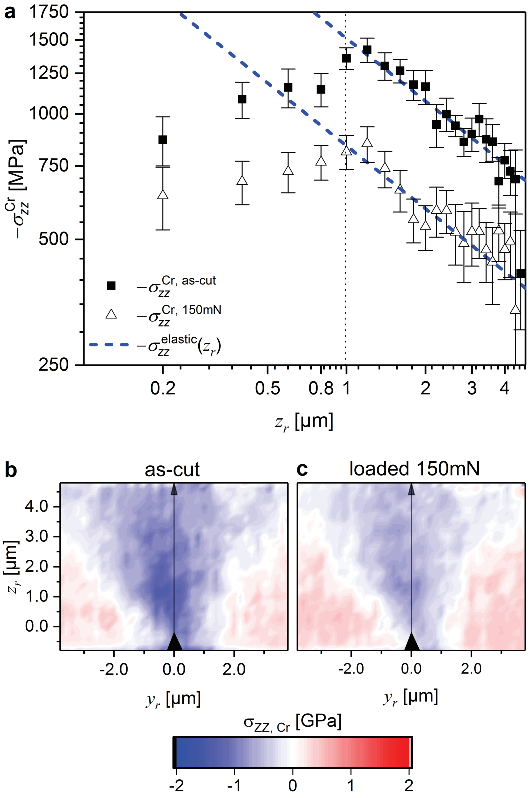

Suppl. Fig. C.3. Out-of-plane stress in the lowest Cr sublayer in front of the notch. Experimental stress values in Cr in the as-fabricated state and at a load of 150 mN are shown for coordinates of $z_\mathrm{r} = [0.2, 4.6]$ µm, along with the fit for a stress-intensity-factor-dominated elastically stressed zone (blue) (a). Details of the area around the notch are presented in the 2D colour plots for the as-fabricated state (b) and at a load of 150 mN (c).

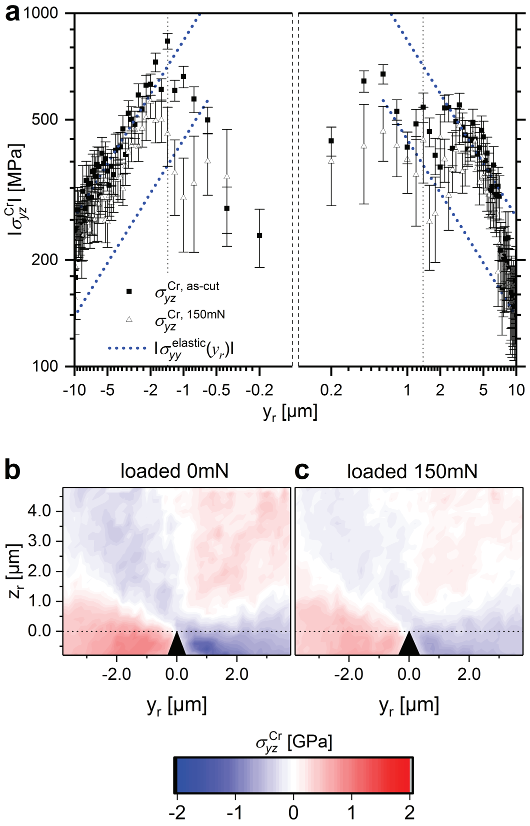

Suppl. Fig. C.4. Shear stress in the lowest Cr sublayer perpendicular to the notch. Experimental stress values in Cr in the as-fabricated state and at a load of150 mN are shown for coordinates of $y_{\mathrm{r}} = [-10, 10]\,\mu\mathrm{m}$, along with the fit for a stress-intensity-factor-dominated elastically stressed zone (blue) (a). Details of the area around the notch are presented in the 2D colour plots for the as-fabricated state (b) and at a load of 150 mN (c).

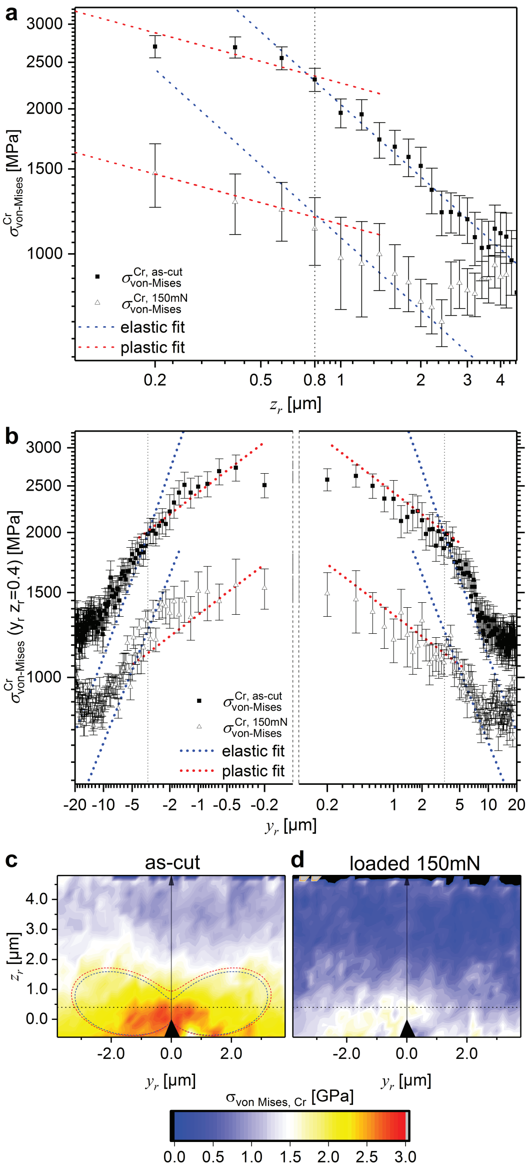

Suppl. Fig. C.5. Von-Mises equivalent stress concerning the plane stress condition in the lowest Cr sublayer in front of the notch. Experimental stress values in Cr in the as-fabricated state and at a load of 150 mN are shown for coordinates of $z_r = [0.2, 4.6]$ µm (a) and $y_r = [-20, 20]$ µm (b), along with power-law-fits for the HRR-dominated plastically deformed zone in front of the notch (red) and the stress-intensity-factor-dominated elastically stressed zone (blue). Details of the area around the notch are presented in the 2D colour plots for the as-fabricated state (c) and at a load of 150 mN (d). In (c), the theoretical extent of the plastic zone under plain stress (red) and plane strain (blue) is also indicated.

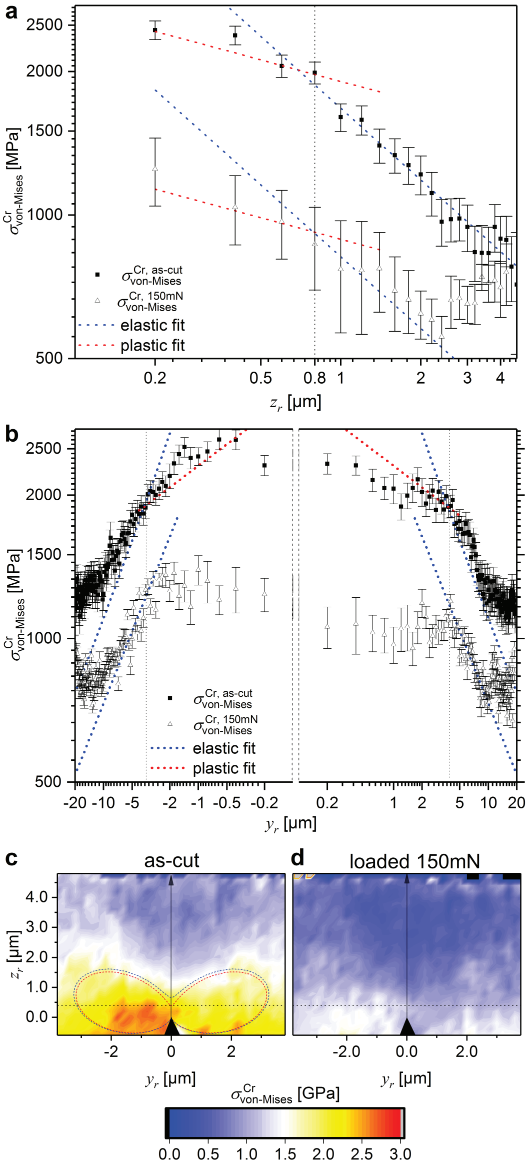

Suppl. Fig. C.6. Von-Mises equivalent stress concerning the plane strain condition of the lowest Cr sublayer in front of the notch. Experimental stress values in Cr in as-fabricated state and at a load of 150 mN are shown for coordinates of $z_r = [0.2, 4.6]$ µm (a) and $y_r = [-20, 20]$ µm (b) together with power-law-fits for the HRR-dominated plastically deformed zone in front of the notch (red) and the stress-intensity-factor-dominated elastically stressed zone (blue). Details of the area around the notch are presented in the 2D colour plots for the as-fabricated state (c) and at a load of 150 mN (d). In (c), the theoretical extent of the plastic zone under plain stress (red) and plane strain (blue) is also indicated.

Bibliography to paper C

[1] P. Panjan, A. Drnovšek, P. Gselman, M. Čekada and M. Panjan, *Coatings*, 2020, **10**, 447, DOI: `10.3390/coatings10050447`.

[2] S. Liu, J. Wheeler, J. Michler, X. Zeng and W. Clegg, *Scripta Materialia*, 2016, **117**, 24–27, DOI: `10.1016/j.scriptamat.2016.02.008`.

[3] R. Daniel, M. Meindlhumer, J. Zalesak, B. Sartory, A. Zeilinger, C. Mitterer et al., *Mater. Des.*, 2016, **104**, 227–234, DOI: `10.1016/j.matdes.2016.05.029`.

[4] T. Anderson, *Fracture Mechanics*, CRC Press, 2017, DOI: `10.1201/9781315370293`.

[5] A. A. Griffith, *Philosophical Transactions of the Royal Society of London. Series A, Containing Papers of a Mathematical or Physical Character*, 1921, **221**, 163–198, DOI: `10.1098/rsta.1921.0006`.

[6] J. R. Rice and G. F. Rosengren, *PLANE STRAIN DEFORMATION NEAR A CRACK TIP IN A POWER LAW HARDENING MATERIAL*, tech. rep., 1967, DOI: `10.21236/ad0659300`.

[7] J. Hutchinson, *Journal of the Mechanics and Physics of Solids*, 1968, **16**, 337–342, DOI: `10.1016/0022-5096(68)90021-5`.

[8] H. Coules, G. Horne, K. A. Venkata and T. Pirling, *Materials & Design*, 2018, **143**, 131–140, DOI: `10.1016/j.matdes.2018.01.064`.

[9] H. E. Coules and G. Horne, *Procedia Structural Integrity*, 2019, **17**, 934–941, DOI: `10.1016/j.prostr.2019.08.124`.

[10] A. Steuwer, L. Edwards, S. Pratihar, S. Ganguly, M. Peel, M. Fitzpatrick et al., *Nuclear Instruments and Methods in Physics Research Section B: Beam Interactions with Materials and Atoms*, 2006, **246**, 217–225, DOI: `10.1016/j.nimb.2005.12.063`.

[11] A. Steuwer, M. Rahman, A. Shterenlikht, M. Fitzpatrick, L. Edwards and P. Withers, *Acta Materialia*, 2010, **58**, 4039–4052, DOI: `10.1016/j.actamat.2010.03.013`.

[12] P. J. Withers, *Philosophical Transactions of the Royal Society A: Mathematical, Physical and Engineering Sciences*, 2015, **373**, 20130157, DOI: `10.1098/rsta.2013.0157`.

[13] P. Lopez-Crespo, M. Mostafavi, A. Steuwer, J. F. Kelleher, T. Buslaps and P. J. Withers, *Fatigue & Fracture of Engineering Materials & Structures*, 2016, **39**, 1040–1048, DOI: `10.1111/ffe.12463`.

[14] P. Lopez-Crespo, J. Peralta, J. Kelleher and P. Withers, *International Journal of Fatigue*, 2019, **127**, 500–508, DOI: `10.1016/j.ijfatigue.2019.06.029`.

[15] W. Zhang, C. Simpson, T. Leitner, X. Zhang, R. Pippan and P. Withers, *Acta Materialia*, 2020, **184**, 225–240, DOI: `10.1016/j.actamat.2019.11.024`.

[16] J. Ast, M. Ghidelli, K. Durst, M. Göken, M. Sebastiani and A. Korsunsky, *Materials & Design*, 2019, **173**, 107762, DOI: `10.1016/j.matdes.2019.107762`.

[17] M. Alfreider, D. Kozic, O. Kolednik and D. Kiener, *Materials & Design*, 2018, **148**, 177–187, DOI: `10.1016/j.matdes.2018.03.051`.

[18] A. M. Korsunsky, M. Sebastiani and E. Bemporad, *Materials Letters*, 2009, **63**, 1961–1963, DOI: `10.1016/j.matlet.2009.06.020`.

[19] M. Sebastiani, E. Rossi, M. Z. Mughal, A. Benedetto, P. Jacquet, E. Salvati et al., *Nanomaterials*, 2020, **10**, 853, DOI: `10.3390/nano10050853`.

[20] E. Salvati, L. Romano-Brandt, M. Mughal, M. Sebastiani and A. Korsunsky, *Journal of the Mechanics and Physics of Solids*, 2019, **125**, 488–501, DOI: `10.1016/j.jmps.2019.01.007`.

[21] A. J. Lunt and A. M. Korsunsky, *Surface and Coatings Technology*, 2015, **283**, 373–388, DOI: `10.1016/j.surfcoat.2015.10.049`.

[22] A. Zeilinger, J. Todt, C. Krywka, M. Müller, W. Ecker, B. Sartory et al., *Scientific Reports*, 2016, **6**, DOI: `10.1038/srep22670`.

[23] W. Ecker, J. Keckes, M. Krobath, J. Zalesak, R. Daniel, M. Rosenthal et al., *Materials & Design*, 2020, **188**, 108478, DOI: `10.1016/j.matdes.2020.108478`.

[24] J. Keckes, R. Daniel, J. Todt, J. Zalesak, B. Sartory, S. Braun et al., *Acta Materialia*, 2018, **144**, 862–873, DOI: `10.1016/j.actamat.2017.11.049`.

[25] J. Keckes, M. Bartosik, R. Daniel, C. Mitterer, G. Maier, W. Ecker et al., *Scr. Mater.*, 2012, **67**, 748–751, DOI: `10.1016/j.scriptamat.2012.07.034`.

[26] M. Stefenelli, R. Daniel, W. Ecker, D. Kiener, J. Todt, A. Zeilinger et al., *Acta Mater.*, 2015, **85**, 24–31, DOI: `10.1016/j.actamat.2014.11.011`.

[27] J. Kieffer, *J. Phys: Conf. Ser.*, 2013, **425**, 202012, DOI: `10.1088/1742-6596/425/20/202012`.

[28] G. Ashiotis, A. Deschildre, Z. Nawaz, J. P. Wright, D. Karkoulis, F. E. Picca et al., *Journal of Applied Crystallography*, 2015, **48**, 510–519, DOI: `10.1107/s1600576715004306`.

[29] L. A. Feigin and D. I. Svergun, *Structure Analysis by Small-Angle X-Ray and Neutron Scattering*, ed. G. W. Taylor, Springer US, 1987, DOI: `10.1007/978-1-4757-6624-0`.

[30] M. Meindlhumer, N. Jäger, S. Spor, M. Rosenthal, J. Keckes, H. Hruby et al., *Scripta Materialia*, 2020, **182**, 11–15, DOI: `10.1016/j.scriptamat.2020.02.031`.

[31] M. Bartosik, R. Daniel, C. Mitterer, I. Matko, M. Burghammer, P. Mayrhofer et al., *Thin Solid Films*, 2013, **542**, 1–4, DOI: `10.1016/j.tsf.2013.05.102`.

[32] R. Daniel, K. Martinschitz, J. Keckes and C. Mitterer, *Acta Mater.*, 2010, **58**, 2621–2633, DOI: `10.1016/j.actamat.2009.12.048`.

[33] J. Almer, U. Lienert, R. L. Peng, C. Schlauer and M. Odén, *Journal of Applied Physics*, 2003, **94**, 697–702, DOI: `10.1063/1.1582351`.

[34] J. Pina, A. Dias, M. François and J. Lebrun, *Surface and Coatings Technology*, 1997, **96**, 148–162, DOI: `10.1016/s0257-8972(97)00075-3`.

[35] A. Riedl, R. Daniel, M. Stefenelli, T. Schöberl, O. Kolednik, C. Mitterer et al., *Scr. Mater.*, 2012, **67**, 708–711, DOI: `10.1016/j.scriptamat.2012.06.034`.

[36] I. Petrov, P. B. Barna, L. Hultman and J. E. Greene, *Journal of Vacuum Science & Technology A: Vacuum, Surfaces, and Films*, 2003, **21**, S117–S128, DOI: `10.1116/1.1601610`.

[37] R. Daniel, E. Jäger, J. Todt, B. Sartory, C. Mitterer and J. Keckes, *Journal of Applied Physics*, 2014, **115**, 203507, DOI: `10.1063/1.4879243`.

[38] R. Daniel, J. Keckes, I. Matko, M. Burghammer and C. Mitterer, *Acta Mater.*, 2013, **61**, 6255–6266, DOI: `10.1016/j.actamat.2013.07.009`.

[39] R. Daniel, D. Holec, M. Bartosik, J. Keckes and C. Mitterer, *Acta Mater.*, 2011, **59**, 6631–6645, DOI: `10.1016/j.actamat.2011.07.018`.

[40] B. N. Jaya and V. Jayaram, *International Journal of Fracture*, 2014, **188**, 213–228, DOI: `10.1007/s10704-014-9956-2`.

[41] B. N. Jaya, S. Bhowmick, S. S. Asif, O. L. Warren and V. Jayaram, *Philosophical Magazine*, 2015, **95**, 1945–1966, DOI: `10.1080/14786435.2015.1010623`.

[42] D. Gross and T. Seelig, *Bruchmechanik*, Springer Berlin Heidelberg, 2011, DOI: `10.1007/978-3-642-10196-0`.

[43] P. J. Withers, *Reports on Progress in Physics*, 2007, **70**, 2211–2264, DOI: `10.1088/0034-4885/70/12/r04`.

[44] R. Fritz, V. Maier-Kiener, D. Lutz and D. Kiener, *Materials Science and Engineering: A*, 2016, **674**, 626–633, DOI: `10.1016/j.msea.2016.08.015`.

[45] A. Zeilinger, R. Daniel, M. Stefenelli, B. Sartory, L. Chitu, M. Burghammer et al., *J Phys D Appl Phys*, 2015, **48**, 295303, DOI: `10.1088/0022-3727/48/29/295303`.

[46] W. Ramberg and W. R. Osgood, *Natl. Advis. Com. Aeronaut. Technical*, 1943.

[47] J. A. M. Bolaños, O. F. H. Cobos and J. M. C. Marrero, *IOP Conference Series: Materials Science and Engineering*, 2014, **63**, 012143, DOI: `10.1088/1757-899x/63/1/012143`.

[48] I. Issa, A. Hohenwarter, R. Fritz and D. Kiener, *Journal of Materials Research*, 2019, **34**, 2370–2383, DOI: `10.1557/jmr.2019.140`.

[49] I. N. Sneddon, *Proceedings of the Royal Society of London. Series A. Mathematical and Physical Sciences*, 1946, **187**, 229–260, DOI: `10.1098/rspa.1946.0077`.

[50] E. Salvati, H. Zhang, K. S. Fong, X. Song and A. M. Korsunsky, *Journal of the Mechanics and Physics of Solids*, 2017, **98**, 222–235, DOI: `10.1016/j.jmps.2016.10.001`.

[51] J. P. Best, J. Zechner, I. Shorubalko, J. V. Oboňa, J. Wehrs, M. Morstein et al., *Scripta Materialia*, 2016, **112**, 71–74, DOI: `10.1016/j.scriptamat.2015.09.014`.

[52] D. Kiener, C. Motz, M. Rester, M. Jenko and G. Dehm, *Materials Science and Engineering: A*, 2007, **459**, 262–272, DOI: `10.1016/j.msea.2007.01.046`.

[53] P. LOPEZ-CRESPO, P. J. WITHERS, F. YUSOF, H. DAI, A. STEUWER, J. F. KELLEHER et al., *Fatigue & Fracture of Engineering Materials & Structures*, 2012, **36**, 75–84, DOI: `10.1111/j.1460-2695.2012.01670.x`.

D

Stress-controlled decomposition routes in cubic AlCrN films assessed by in-situ high-temperature high-energy grazing incidence transmission X-ray diffraction

M. Meindlhumer[a], S.Klima[a], N. Jäger[b], A. Stark[b], H. Hruby[c], C. Mitterer[d], J. Keckes[d], R. Daniel[a]

[a]Christian Doppler Laboratory for Advanced Synthesis of Novel Multifunctional Coatings at the Department of Materials Science, Montanuniversität Leoben, Leoben, Austria
[b]Helmholtz-Zentrum Geesthacht, Centre for Materials and Coastal Research, Geesthacht, Germany
[c]voestalpine eifeler Vacotec GmbH, Düsseldorf, Germany
[d]Department of Materials Science, Montanuniversität Leoben, Leoben, Austria

Abstract

The dependence of decomposition routes on intrinsic microstructure and stress in nanocrystalline transition metal nitrides is not yet fully understood. In this contribution, three $Al_{0.7}Cr_{0.3}N$ thin films with residual stress magnitudes of -3510, -4660 and -5930 MPa in the as-deposited state were *in-situ* characterized in the range of 25-1100°C using *in-situ* synchrotron high-temperature high-energy grazing-incidence-transmission X-ray diffraction and temperature evolutions of phases, coefficients of thermal expansion, structural defects, texture as well as residual, thermal and intrinsic stresses were evaluated. The multi-parameter experimental data indicate a complex intrinsic stress and phase changes governed by a microstructure recovery and phase transformations taking place above the deposition temperature. Though the decomposition temperatures of metastable cubic $Al_{0.7}Cr_{0.3}N$ phase in the range of 698-914°C are inversely proportional to the magnitudes of deposition temperatures, the decomposition process itself starts at the same stress level of ~ -4300 MPa

in all three films. This phenomenon indicates that the particular compressive stress level functions as an energy threshold at which the diffusion driven formation of hexagonal Al(Cr)N phase is initiated, provided sufficient temperature is applied. In summary, the unique synchrotron experimental setup indicated that residual stresses play a decisive role in the decomposition routes of nanocrystalline transition metal nitrides.

D.1. Introduction

Protective nanocrystalline thin films prepared by physical vapour deposition are characterized by complex temperature-dependent microstructure/strain evolution and multistage decomposition routes, which control their physical and functional properties. Typical materials are transition metal nitride hard films based on $Ti_xAl_{1\text{-}x}N$ and $Cr_xAl_{1\text{-}x}N$, which have been extensively studied in the past due to their beneficial functional properties [1]. A special interest has been devoted, in particular, to AlCrN because of its ability to form a metastable solid solution by replacing Cr over a wide concentration range with Al in the cubic (c) B1 structure, resulting in enhancement of mechanical properties, wear and especially oxidation resistance compared to TiAlN [2]. However, when the solubility limit of AlN in CrN is exceeded, stable wurtzite (w) B4 Al(Cr)N is formed [3, 4]. w-Al(Cr)N forms in several steps also when c-AlCrN solid solution is annealed at temperatures above ~800°C. Firstly, w-Al(Cr)N precipitates are formed at the grain boundaries (GBs), followed by the formation of h-$Cr(Al)N_{0.5}$-phase as a consequence of nitrogen loss with a subsequent two-step decomposition of CrN into Cr_2N and Cr [5–8]. The determination of the onset temperature of the phase decomposition ($T_{\mathrm{o,d}}$) over a wide Al composition range, as well as its correlation to the film microstructure and stress, is crucial because the formation of the stable w-Al(Cr)N phase results in a reduction of hardness, wear and oxidation resistance [9–13]. In the case of AlCrN-based thin films, however, the complex interplay between temperature-dependent characteristics and properties such as the onset of phase transformation, coefficients of thermal expansion (CTEs), gradients of residual stresses, defect density, hardness, toughness and elastic modulus in different atmospheres is however not yet fully understood [5, 6, 8, 14–16]. Here, especially the role of microstructure and residual stresses has not been evaluated thoroughly.

In the case of transition metal nitride hard thin films, *in-situ* synchrotron XRD has been used to study temperature-dependent phenomena and physical parameters like phase evolution, lattice parameters and/or in-plane strains (i) in powders of

TiAlN and TiCrAlN films and (ii) in thin slices of TiAlN and TiZrAlN films in transmission diffraction geometry [17–21]. The former experiments concentrated mostly on the understanding of complex decomposition routes and related lattice parameter/strain changes.

The motivation of this work is to further extend the possibilities of *in-situ* XRD characterization, which will be used to obtain a complex picture of the multistage decomposition routes and also microstructure/strain changes in AlCrN-based thin films during thermal cycling. We use a newly developed *in-situ* high-temperature high-energy grazing incidence transmission synchrotron X-ray diffraction (HT-HE-GIT-XRD) [22] to simultaneously characterize temperature evolution of (i) phases, (ii) residual stresses, (iii) thermal strains, (iv) CTEs, (v) domain sizes and (vi) texture up to 1100°C. Primarily, the onset temperature of the decomposition of metastable c-AlCrN into stable c-Cr(Al)N and w-Al(Cr)N phases has been investigated as a function of the as-deposited residual stress state and microstructure, intentionally predefined by the applied deposition conditions. The multi-parameter temperature-dependent structure-property correlations indicate a decisive role of residual stress magnitude in the decomposition routes of metastable c-AlCrN.

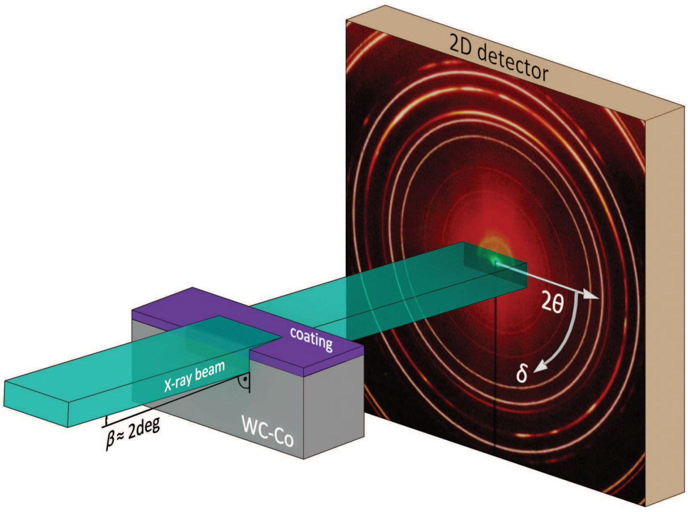

Figure D.1.: Schematic representation of the *in-situ* high-temperature high-energy grazing incidence transmission X-ray diffraction method.

D.2. Results

D.2.1. *In-Situ* Phase Analysis

Thermal stability of the metastable AlCrN thin films was investigated in the temperature range between room temperature (RT) and 1100°C by analysing Debye-Scherrer rings for the detector azimuthal angles δ in the range of 0 to -180 deg by a sectoral integration of the patterns, as the rest of the data, corresponding to the δ complementary angles, comprised mostly diffraction signal from the WC-Co substrate (*cf.* Fig D.1).

Along the text, mainly experimental data from the film B are presented and interpreted in Figs. D.2 and D.3, whereby the results from other two films can be found in the supplementary data. The phase plots displayed in Fig. D.2b and in Suppl. Figs. S.D.1b and S.D.3b represent temperature-dependent evolutions of diffraction intensities in the 2θ range of 2.9 to 5.4 deg. For every Bragg's angle θ (and annealing temperature T), the particular intensity was obtained by integrating the diffraction signal from the detector in the azimuthal angle range δ from -180 to 0 deg. The temperature and phase evolution during one temperature cycle are presented in Figs. D.2a,b together with the tabulated reflection positions of w-AlN, c-CrN, Cr_2N and substrate WC and c-Co phases adapted from the JCPDF database [23]. The featured 111 and 200 reflections indicate that the $Al_{0.7}Cr_{0.3}N$ thin film deposited at $T_{S,B} = 400°C$ was at RT in metastable state and possessed the face-centred cubic B1 (c) structure. In addition to the reflections emanating from the film, also WC 100 and 101, as well as c-Co 111 and 200 reflections corresponding to the cemented carbide substrate are visible (Fig. D.2b). With the temperature increase, all diffraction peaks shift to smaller diffraction angles, as a consequence of thermal expansion of the film and substrate phases and changes in thin film stress state. At temperatures above ~830°C, the metastable c-$Al_{0.7}Cr_{0.3}N$ phase started to decompose into c-Cr(Al)N and w-AlCrN phases, as indicated by the presence of the 100 diffraction peak (at $2\theta = 3.026$ deg) from the w-AlCrN phase detected above that critical temperature. This process corresponds to the formation of Al(Cr)N precipitates at the GBs with wurtzite crystallographic structure, as extensively discussed elsewhere [5, 6]. For the films A, B and C, the different onset temperatures of the phase decomposition were determined as 698-748°C, 834-851°C and 880-914°C (Fig. D.5c), respectively. The uncertainty of ~20-50°C originates from the nonzero detector exposure time and the relatively large heating rate.

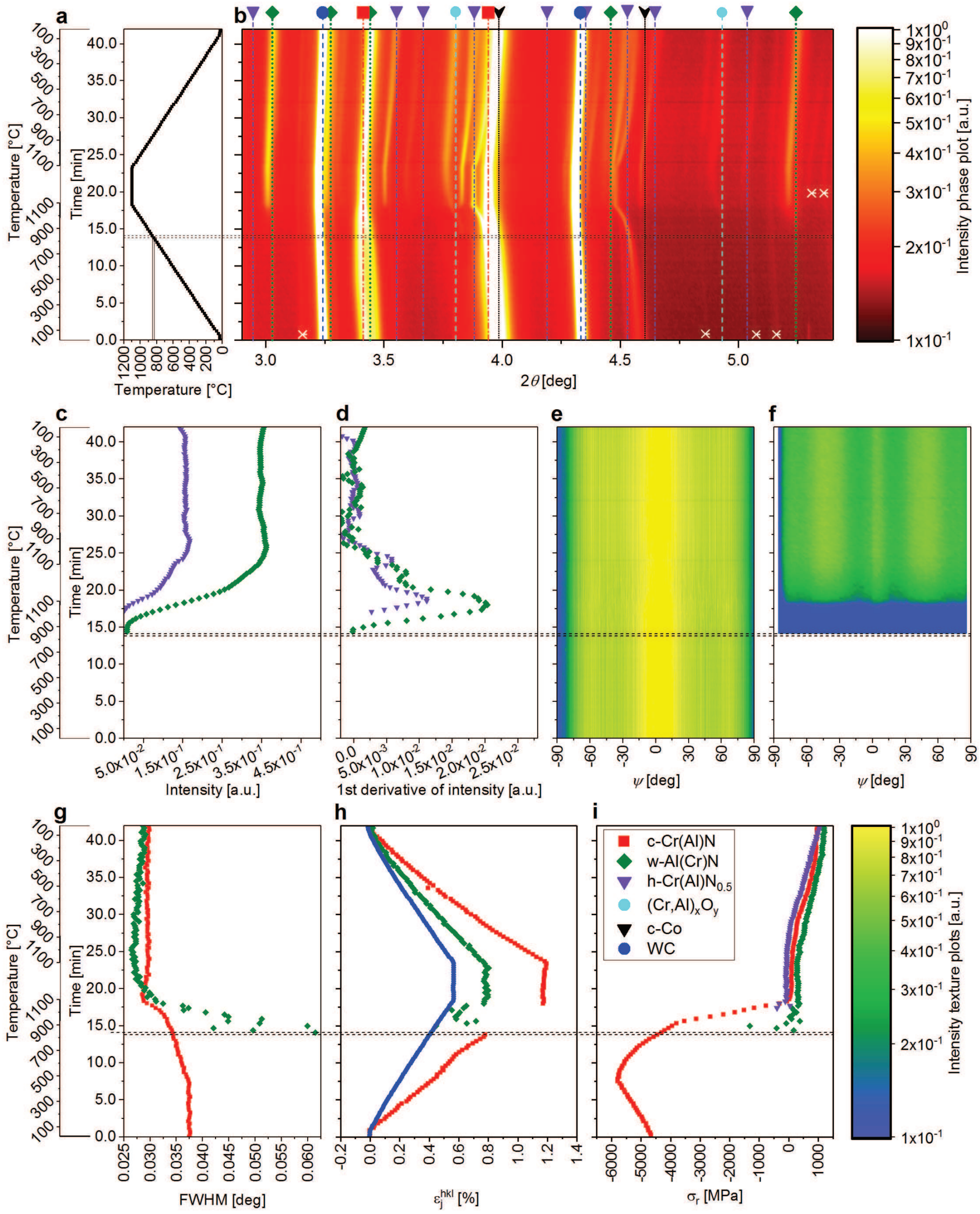

Figure D.2.: The applied temperature cycle (a) and the experimental data of the AlCrN film B, phase plot with indicated diffraction angles for tabulated particular phases, where the white crosses indicate additional diffraction peaks representing 2^{nd} order diffraction due to the presence of the second harmonic's wavelength in the primary beam (b), evolution of intensity (c) and the 1^{st} derivative of the intensity (d) of w-Al(Cr)N 100 (green) and h-Cr_2N 100 (violet) reflections, the texture plot for c-Cr(Al)N 111 reflection indicating ⟨111⟩ fibre texture (e), texture plot for w-Al(Cr)N 100 reflection indicating overlapping ⟨100⟩ and ⟨110⟩ fibre texture (f), evolution of FWHM of c-Cr(Al)N 111 (red) and w-Al(Cr)N 100 (green) reflections (g), thermal expansion of c-Cr(Al)N (red, evaluated from the 200 reflection), w-Al(Cr)N (green, 100 reflection) and WC substrate (blue) (h) and residual stress evaluated from the c-Cr(Al)N 200 (red), w-Al(Cr)N 100 (green) and h-Cr2N 100 (violet) reflections (i).

The w-Al(Cr)N 100 diffraction peak was selected to semi-quantitatively assess the progress of the decomposition process of the metastable cubic AlCrN phase and the formation of the w-AlCrN polytype. The variation in the intensity of the w-Al(Cr)N 100 reflection and its first derivative are depicted in Figs. D.2c and d, respectively. Since the decomposition of the metastable c-AlCrN is a diffusion-controlled process, its end can be identified by the decrease in the first derivative of the w-Al(Cr)N 100 reflection intensity to zero ($\partial I_{\mathrm{w-AlCrN\,100}}(T)/\partial T \rightarrow 0$) (Fig. D.2d).

After the onset of the decomposition of c-AlCrN to c-Cr(Al)N and w-Al(Cr)N, non-stoichiometric $(\mathrm{Cr}, \mathrm{Al})_x\mathrm{O}_y$ is formed as a consequence of residual oxygen presence in the dilatometer chamber. The $(\mathrm{Cr}, \mathrm{Al})_x\mathrm{O}_y$ stoichiometry changes throughout further heating and the holding segment are indicated by the changes of the 2θ-positions of the respective reflections in Fig. D.2b. The formation of $(\mathrm{Cr}, \mathrm{Al})_x\mathrm{O}_y$ is a in agreement with the literature data, where previous results stated reduced oxidation resistance of c-Cr(Al)N and w-Al(Cr)N phases after decomposition [9, 10].

In Fig. D.2b, the onset of the decomposition of CrN into $\mathrm{Cr_2N}$ can be also identified by the appearance of the $\mathrm{Cr_2N}$ reflections from several $\mathrm{Cr_2N}$ crystalline polytypes at the temperature of ~1080°C, in agreement with literature values [6, 7, 24]. No further crystallographic changes were found during cooling down to RT.

D.2.2. *In-Situ* Qualitative Texture Analysis

Qualitative texture analysis was carried out by a radial (θ) integration of Debye-Scherrer rings providing azimuthal intensity distributions $I_{hkl}(\delta, T)$ and the data were plotted as a function of the ψ angle as $I_{hkl}(\psi, T)$, where ψ represents the angle between the film normal and the diffraction vector. Due to the high energy of photons resulting in negligibly diffraction angles (*cf.* Fig. D.2b), the transformation between the azimuthal angle δ and the tilt angle ψ can be generally expressed as

$$\cos\psi = \sin\delta\cos\theta \cong \sin\delta \tag{D.1}$$

and further

$$\psi = \delta + 90 \tag{D.2}$$

as shown by Keckes *et al.* [25].

A qualitative texture analysis was carried out for the c-AlCrN 111 and w-AlCrN 100 reflections. Therefore, the azimuthal intensity distributions $I_{\mathrm{hkl}}(\psi, T)$ are dis-

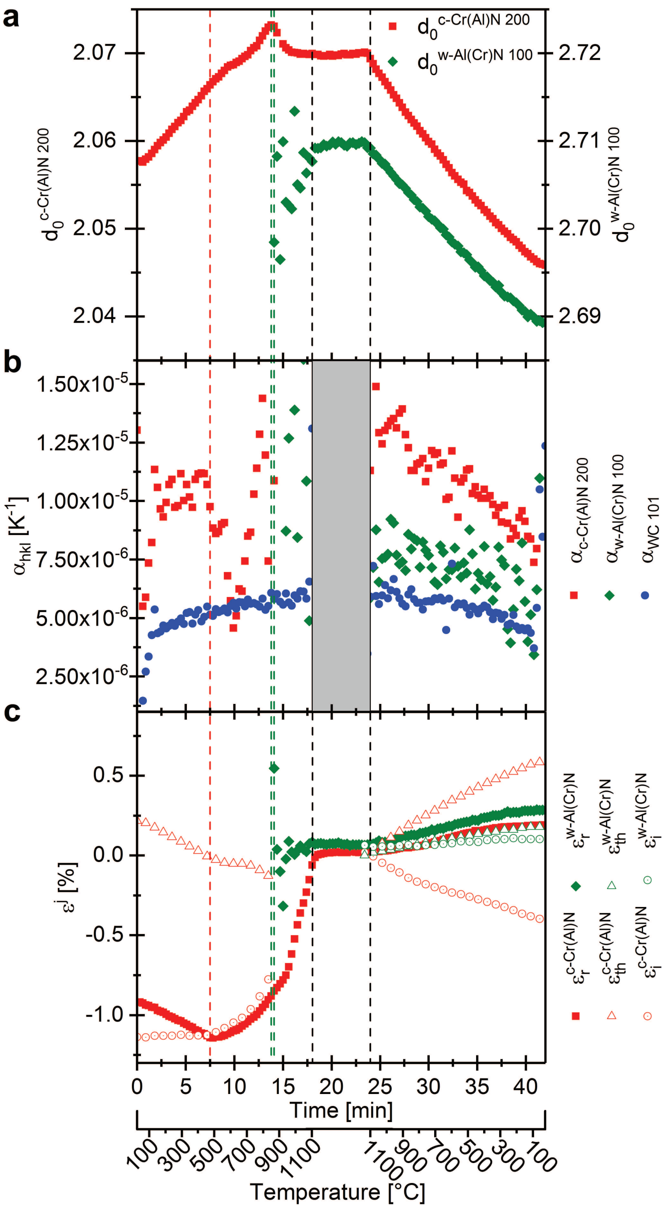

Figure D.3.: Experimental assessment for film B deposited at 400°C: the development of the unstrained lattice parameter $d_0(T)$ of c-Cr(Al)N and w-Al(Cr)N phase over the temperature (a), the thermal expansion coefficient calculated for the individual reflections (b) and the evolution of thermal, intrinsic and residual strain over the temperature cycle for c-Cr(Al)N (red) and w-Al(Cr)N (green), respectively (c). The vertical red dashed line represents the deposition temperature, the green dashed line the onset of the phase decomposition and the vertical black segmented lines the beginning and the end of the holding segment.

played in Figs. D.2e,f for c-Cr(Al)N 111 and w-Al(Cr)N 100 Debye-Scherrer rings, respectively. The diffraction intensities recorded at $\psi = 0$ and ± 90 degrees correspond to the out-of-plane and in-plane orientations of the diffraction vectors, respectively. The plots in Figs. D.2e,f allow to draw conclusions about the preferred orientation of the fibre-textured phases. It revealed the $\langle 111 \rangle$ fibre texture of the cubic c-Cr(Al)N phase, as the maximum intensity of the c-Cr(Al)N 111 reflection was found approximately at the diffraction vector orientation which is parallel to the film normal and corresponds to $\psi \cong 0$ deg (*cf.* exemplary data for the film B in Fig. D.2e and Supplementary Figs. S.D.1e, S.D.1e). Texture analysis carried out for the w-Al(Cr)N 100 reflection revealed azimuthal maxima at $\psi \cong 0, \pm 60$ deg and $\psi \cong \pm 30$ deg corresponding to $\langle 100 \rangle$ and $\langle 110 \rangle$ fibre textures, respectively (Fig. D.2f, and Supplementary Figs. S.D.1f, S.D.3f for A and C samples). This indicates that the densely packed $\{002\}$ planes of the wurtzite phase were oriented actually parallel to the columnar GBs of the c-Cr(Al)N phase [26]. The temperature dependencies of $I_{\mathrm{hkl}}(\psi, T)$ for the c-Cr(Al)N 111 and w-Al(Cr)N 100 reflections in Figs. D.2e,f indicate that the textures of the particular phases did not change significantly during the thermal cycles.

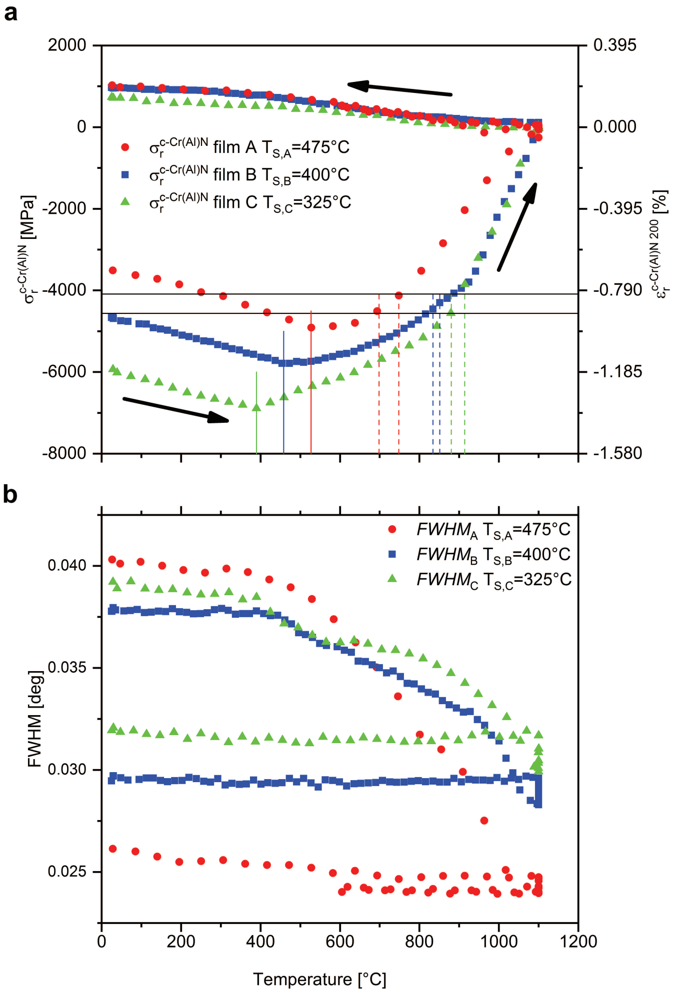

Figure D.4.: Residual stress evolutions over the heating cycles for films A, B and C deposited at 475°C, 400°C and 325°C, respectively (a). Full vertical lines indicate the end of the thermoelastic regime, dashed lines indicate the onset of phase decomposition and horizontal lines show the mean values of stress magnitude for the three onsets of phase decomposition in the individual coatings. FWHM of c-AlCrN evolution up to 1100°C for coatings A, B and C deposited at 475°C, 400°C and 325°C, respectively (b).

D.2.3. Full Width at Half Maximum Analysis

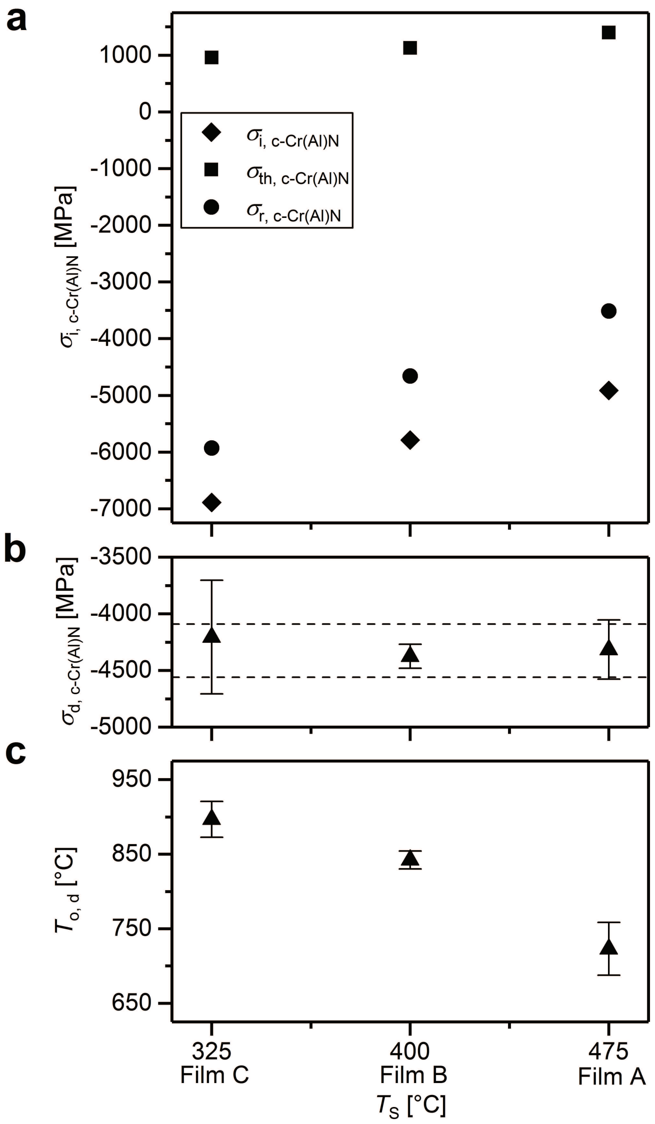

Figure D.5.: Correlations between applied deposition temperature T_S and (i) the intrinsic stress $\sigma_{i,c-CrN}$, (ii) the thermal stress $\sigma_{th,c-CrN}$, (iii) the resulting residual stress $\sigma_{r,c-CrN}$ in the as-deposited state (a), (iv) the decomposition onset stress $\sigma_{d,c-CrN}$ (b) and (v) the onset temperature of phase decomposition (c) $T_{o,d}$ for films A ($T_S = 475$°C), B ($T_S = 400$°C) and C ($T_S = 325$°C).

Generally, the full width at half maximum (FWHM) of X-ray diffraction peaks correlates with the size of coherently diffracting domains as well as with the density of structural defects such as dislocations and lattice distortions, represented by strains of 2nd and 3rd order. Since the AlCrN crystallites of all thin films exhibited columnar grain morphology, which overall did not change during the thermal treatment, it can be assumed that the FWHM changes over the temperature cycle are sensitive primarily to the variation of structural defect density in the nanocrystals [25, 27–29]. In order to evaluate FWHM, c-Cr(Al)N 111 and w-Al(Cr)N 100 diffraction peaks were fitted using the Pseudo-Voigt function for the diffraction vector out-of-plane orientation. The results in Fig. D.2g indicate that the defect density in c-CrAlN remains constant up to the deposition temperature of 400°C, below which no relaxation processes took place. Above ~400°C, a relaxation of structural defects [30] is reflected by a continuous decrease in the FWHM. A further decrease of the FWHM of c-CrAlN above the onset temperature of the phase decomposition between ~850 and ~1100°C (Fig. D.2g) indicates a gradual defect recovery accompanied by microstrain development as the w-Al(Cr)N phase is formed in the film. On the contrary, a slight increase in the FWHM was detected during the subsequent temperature holding segment, which is attributed to the ongoing phase decomposition and a possible reduction of the size of the coherently diffracting domains due to the emerging of the w-Al(Cr)N and h-Cr(Al)$N_{0.5}$ phase fractions. The corresponding FWHM of w-Al(Cr)N 100 reflection was relatively large at the beginning of the phase decomposition (Fig. D.2g). In the next heating steps and during the holding segment, the FWHM continuously decreases, which reflects the ongoing phase transformation accompanied by the w-Al(Cr)N phase crystallite growth. On the contrary, no significant change in the FWHM was detected during the cooling segment of the temperature cycle.

The temperature dependent behaviour of FWHM was similar for all films, as shown in Fig. D.4b. The differences in the magnitudes and temperature dependencies of the FWHM, which correlate with the phase microstructural evolution during thermal cycling, can be attributed to the specific as-deposited states in terms of microstructure and residual stress.

D.2.4. Unstrained Lattice Parameter Analysis

The changes in the temperature-dependent unstressed lattice parameters $d_0^{hkl}(T)$ of the particular phases were evaluated using Bragg's law according to

$$d_0^{hkl}(\delta^*) = \frac{\lambda}{2\sin\theta^{hkl}(\delta^*)}, \tag{D.3}$$

where λ is the X-ray wavelength and $\theta(\delta^*)$ is the diffraction angle of the selected Debye-Scherrer ring at the ring azimuthal orientation δ^*. The diffraction signal collected at the ring position δ^* represents the diffraction on $\{hkl\}$ crystallographic planes, which are, due to the equibiaxial in-plane stress state, not strained. This azimuthal angle δ^* can be determined as follows [29, 31]

$$\sin \delta^* = \sqrt{\frac{1 - \nu^{hkl}}{1 + \nu^{hkl}}} \tag{D.4}$$

Here, ν^{hkl} is the Poisson's ratio of the investigated Debye-Scherrer ring *hkl* of the phase of interest. Poisson's ratios ν^{200} and ν^{100} of 0.132 and 0.253, calculated from the X-ray elastic constants using the Hill-type grain interaction model [32], were used to determine the stress-free lattice parameters $d_0^{hkl}(\delta^*)$ of the c-AlCrN and w-Al(Cr)N phases, respectively [33, 34]. The unstrained sample orientations of $\delta_\mathrm{c}^* =\sim -61$ and $\delta_\mathrm{w}^* =\sim -51$ deg were found for c-Cr(Al)N 200 and w-Al(Cr)N 100 rings, respectively. The WC 101 Debye-Scherrer rings were found to be unaffected by the presence of residual stress in the film. Using Eqs. (D.3) and (D.4), lattice spacing of WC at RT was evaluated from the WC 101 reflection as 1.88126 Å, which is ~0.1% smaller than the tabulated lattice parameter [23] of 1.88266 Å, which can be attributed to the limits in the detector calibration accuracy. For the cubic AlCrN phase, two different lattice parameters d_0^{200} of 2.05838 Å for the as-deposited state and 2.04584 Å for the annealed state were obtained. In the case of the w-Al(Cr)N phase, a lattice parameter d_0^{100} of 2.68915 Å after the thermal cycle was determined, which is close to the tabulated lattice parameter [23] of 2.69542 Å. Temperature dependencies of unstressed lattice parameter $d_0^{200}(T)$ of the c-Cr(Al)N phase and $d_0^{100}(T)$ of the w-Al(Cr)N are presented in Fig. D.3a. The scattering of the lattice parameter $d_0^{100}(T)$ was caused by the small measurable volume of the w-Al(Cr)N crystallites at early stages of the decomposition. The relative changes in the lattice parameters $d_0^{hkl}(T)$ of the particular (j) phases with respect to RT $\frac{d_0^{hkl}(T)}{d_{0,\mathrm{RT}}^{hkl}}$ were used to quantify the thermal expansion $\varepsilon_j^{hkl}(T)$ as follows

$$\varepsilon_j^{hkl}(T) = \frac{d_0^{hkl}(T) - d_{0,\mathrm{RT}}^{hkl}}{d_{0,\mathrm{RT}}^{hkl}} \tag{D.5}$$

In Fig. D.2h, the different slopes of the $\varepsilon_j^{hkl}(T)$ dependencies for c-Cr(Al)N, w-Al(Cr)N and WC phases indicate differences in the CTEs. In the case of WC the thermal expansion of $\varepsilon_\mathrm{WC}^{101}(T) \sim 0.6\%$ at 1100°C is in good agreement to values of 0.2% after heating to 400°C reported by Hidnert [35]. The variation of the lattice parameter during heat treatment is a consequence of (i) thermal expansion of the particular crystal lattices, (ii) defect annihilation and lattice recovery, (iii) phase decomposition and diffusion of Al out of the cubic Cr(Al)N phase and (iv) nitrogen loss and subsequent formation of Cr_2N at elevated temperatures, both accompanied by the massive formation of point defects within the cubic phase.

D.2.5. Experimental Thermal Expansion Coefficients and Thermal Strains

The evaluated $d_0^{hkl}(T)$ dependencies were used to determine (i) the CTEs α_{hkl} of the film and substrate phases and, subsequently, (ii) the experimental in-plane thermal strain ε_{th}^{j} formed within individual phases (j) during temperature changes (Eqs. (D.5), (D.6)). CTEs were determined as follows

$$\alpha_{hkl}(T) = \frac{1}{d_0^{hkl}(T)} \frac{\partial d_0^{hkl}(T)}{\partial T} \cong \frac{\partial \varepsilon_j^{hkl}(T)}{\partial T}, \tag{D.6}$$

where the $d_0^{hkl}(T)$ is the unstrained lattice parameter. The *hkl* subscript was used in α_{hkl} to denote the Debye-Scherer ring, which was used to evaluate the particular CTE for the individual phase. The CTEs determined for the c-Cr(Al)N and w-Al(Cr)N phases of the film B over both the heating and cooling segments are shown in Fig. D.3b and represent actually the first derivation of the $d(T)$ dependencies from Fig. D.3a with respect to the temperature T. The relatively large scattering of the CTEs experimental data is caused by the small intensity of the diffraction signal as well as small lattice parameter changes in the range of ~1%. The microstructural processes responsible for the non-linear temperature evolution of CTEs will be extensively discussed in Sec. D.3. Quantitatively, both phases showed a typical development of their CTEs within the investigated temperature region, as Bartosik *et al.* showed for powdered AlCrN films [36]. For the WC substrate, values of the CTE in the range of $\sim 4 \times 10^{-6}\text{K}^{-1}$ at RT to $\sim 6 \times 10^{-6}\text{K}^{-1}$ at 1100°C were determined, in agreement with Hidnert [35]. Subsequently, experimental values of $\alpha_{hkl}(T)$ from the substrate and the film were used to quantify changes in experimental in-plane thermal strains $\Delta\varepsilon_{\text{th}}^{j}(T)$ developed in the film during the particular heating and cooling segments [37] as follows

$$\Delta\varepsilon_{\text{th}}^{j}(T) = \int (\alpha_{\text{S}}(T) - \alpha_{hkl}(T))dT, \tag{D.7}$$

where α_{hkl} and α_{S} are the experimental CTEs of the film and the substrate, respectively. Since the thermal strain $\varepsilon_{\text{th}}^{j}(T)$ in the c-Cr(Al)N phase is assumed to be zero at the deposition temperature T_{S} (see the arguments in Sec. D.2.6 *In-situ* Residual Strain and Stress Evolution), *i.e.*

$$\varepsilon_{\mathrm{th}}^{\mathrm{c}}(T_S) = 0 \tag{D.8}$$

the determination of the accumulated in-plane thermal strain up to ~800°C is rather straightforward and the results are shown in Fig. D.3c. In order to evaluate the strain development during cooling down, an assumption was considered that in-plane residual strain is negligible during the holding segment at 1100°C in both phases (Fig. D.2i, D.4a), which implies that in-plane thermal and intrinsic strains could also be neglected:

$$\varepsilon_{\mathrm{i}}^{\mathrm{hkl}}(1100°\mathrm{C}) = \varepsilon_{\mathrm{th}}^{\mathrm{hkl}}(1100°\mathrm{C}) \cong 0 \tag{D.9}$$

The formalism from Eq. (D.7) could thus be used to evaluate the temperature dependencies of $\Delta\varepsilon_{\mathrm{th}}^{j}(T)$ from the data of Fig. D.3b for both c-Cr(Al)N and w-Al(Cr)N phases, which are presented together with in-plane residual strains in Fig. D.3c.

D.2.6. *In-situ* Residual Strain and Stress Evolution

In order to evaluate residual in-plane strain ε_r^{hkl} and stress σ_{r}, an azimuthal integration of the diffraction patterns was performed over the azimuthal angle δ range from 0 to -180 deg in $\Delta\delta$ segments of 5 deg. Thus, 36 radial intensity distributions $I(\theta, \Delta\delta, T)$ were obtained for each exposure. The positions of c-Cr(Al)N 200, w-Al(Cr)N 100 and WC 101 diffraction peaks $\theta^{hkl}(\Delta\delta_i, T)$ were determined by fitting the XRD patterns using a Pseudo-Voigt function. The equibiaxial in-plane stress σ_{r} can be determined according to

$$\frac{\partial d^{hkl}(\Delta\delta, T)}{\partial \sin^2\delta} = \sigma_r(T) \times \frac{1}{2}s_2^{hkl} \times d_0, \tag{D.10}$$

where $d^{hkl}(\Delta\delta, T)$ is the lattice parameter evaluated for a particular $\Delta\delta_i$ segment, $\frac{1}{2}s_2^{hkl}$ is the X-ray elastic constant and d_0 is the unstrained lattice parameter. Since the temperature dependence of $\frac{1}{2}s_2^{hkl}$ was neglected due to the missing high-temperature $\frac{1}{2}s_2^{hkl}$ values, in-plane stresses are presented together with the evaluated in-plane residual strains in Fig. D.4a. The residual biaxial in-plane X-ray elastic strain ε_r^{hkl} can be calculated using the same approach as follows

$$\frac{\partial d^{hkl}(\Delta\delta, T)}{\partial \sin^2\delta} = \varepsilon_r^{hkl}(T)\frac{1+\nu^{hkl}}{1-\nu^{hkl}} \times d_0, \tag{D.11}$$

but with the advantage, that all parameters are known except of the Poisson's ratio ν^{hkl} of the thin film, which was adopted from literature.

The elastic constants [33] $\frac{1}{2}s_2^{200}$ of $0.2575\times10^{-5}\text{MPa}^{-1}$ and ν^{200} of 0.132 were used for the c-AlCrN 200 reflection. The elastic strain in the wurtzite Al(Cr)N phase was determined by analysing the w-Al(Cr)N 100 reflection and by taking into account elastic constants [34] $\frac{1}{2}s_2^{100}$ of $0.4052 \times 10^{-5}\text{MPa}^{-1}$ and ν^{100} of 0.253. For h-Cr_2N elastic constants [24] $\frac{1}{2}s_2^{100}$ of $0.3713\times10^{-5}\text{MPa}^{-1}$ and ν^{100} of 0.293 were used. All X-ray elastic constants were calculated using the Hill-type grain interaction model [32]. Since $\varepsilon_r^{hkl}(T)$ values are *hkl* dependent, equibiaxial reflection-independent elastic strains $\varepsilon_r^{j}(T)$ can be calculated for the individual phases (j) using

$$\varepsilon_r^{j}(T) = \frac{\frac{E^{hkl}}{1-\nu^{hkl}}}{\frac{E}{1-\nu}}\varepsilon_r^{hkl}(T), \tag{D.12}$$

where E is the Young's modulus and ν is the Poisson's ratio of the phase.

Fig. D.2i presents the evolution of the residual stress in the c-AlCrN and w-AlCrN phases. In Fig. D.4a, the experimental data are shown as a function of the applied temperature for all films A, B and C, deposited at temperatures 475, 400 and 325°C, respectively. By heating the sample from RT to the deposition temperature T_S, the contribution of the thermal stress to σ_r decreases and σ_r at T_S thus corresponds exclusively to the intrinsic stress. The compressive stress state in the film B at RT (Figs. D.2i, D.4a) was −4660 MPa and increased with the annealing temperature to −5790 MPa at 400°C (corresponding to the deposition temperature).

Table D.1.: onset temperatures and onset stresses of phase decomposition for the films A, B and C.

	onset temperature of phase decomposition $T_\mathrm{o,d}$ [°C]			**onset stress of phase decomposition $\sigma_\mathrm{o,d}$ [MPa]**		
	A	**B**	**C**	**A**	**B**	**C**
lower limit	697	834	880	−4500	−4450	−4560
upper limit	748	851	914	−4130	−4300	−3850

Magnitudes of residual stresses at RT, intrinsic and thermal stresses for all films are summarized in Fig. 5a. Remarkably, the mean onset residual stress of the phase decomposition in all three films was found between -4090 and -4500 MPa, as shown in Figs. D.4a, D.5b and Table D.1, irrespective of the onset temperature of phase decomposition derived from Fig. D.5c (*cf.* also Sec. D.3). Furthermore, although all three films were prepared with significantly different residual stresses, after the temperature cycle, the RT stresses in A, B and C films are with values of 1030, 970 and 740 MPa, respectively, comparable. This behaviour can be interpreted by the full stress relaxation at 1100°C.

D.2.7. Experimental In-Plane Intrinsic Strains

The residual equibiaxial in-plane stress σ_{r} in thin films prepared by physical vapour deposition originates from two dominant stress contributions, namely from intrinsic stress σ_{i}, developed during ion-assisted film growth, and thermal stress σ_{th}, developed during the cooling of the coated sample from the deposition temperature to RT as a consequence of the CTEs mismatch of the film and substrate [28]. Therefore, σ_{r} can be generally expressed as the sum of both of these stress components:

$$\sigma_{\mathrm{r}} = \sigma_{\mathbf{i}} + \sigma_{\mathrm{th}}. \tag{D.13}$$

Usually, only σ_{r} values can be determined using XRD and wafer curvature experiments. Here, we want to demonstrate that using our new multi-parameter approach, experimental temperature dependences of all three stress components from Eq. (D.13) can be evaluated. Due to the unique diffraction setup used in this study, the diffraction data from film and substrate could be simultaneously detected as a function of temperature and then used to evaluate equibiaxial residual strains in the film $\varepsilon_{\mathrm{r}}^{j}$ (Sec. *In-situ* Residual Strain and Stress Evolution). Furthermore, by comparing the experimental CTEs of the thin film and the substrate, also equibiaxial experimental thermal strains $\varepsilon_{\mathrm{th}}^{j}(T)$ could be determined (Sec. Experimental Thermal Expansion Coefficients and Thermal Strains). Having both $\varepsilon_{\mathrm{r}}^{j}$ and $\varepsilon_{\mathrm{th}}^{j}$ components, $\varepsilon_{\mathrm{r}}^{j}$ can be generally expressed as

$$\varepsilon_{\mathrm{r}}^{j} = \varepsilon_{\mathrm{i}}^{j} + \varepsilon_{\mathrm{th}}^{j}, \tag{D.14}$$

where $\varepsilon_{\mathrm{i}}^{j}$ represents the unknown intrinsic strain. The intrinsic strain values can thus be calculated using Eqs. (D.7), (D.8), (D.11), (D.12) and (D.14). The temperature evolution of experimental residual, thermal and intrinsic strain $\varepsilon_{\mathrm{i}}^{j}(T)$ for the c-Cr(Al)N and w-Al(Cr)N phases are shown in Fig. D.3c. The $\varepsilon_{\mathrm{i}}^{j}(T)$ data indicate that intrinsic strains start to change above the deposition temperature due the microstructure recovery and the subsequent phase transformation.

D.2.8. Complementary Analyses

Structural and chemical analysis performed by SEM on the film cross sections shows that the films possess (i) similar columnar grain-like microstructure in the

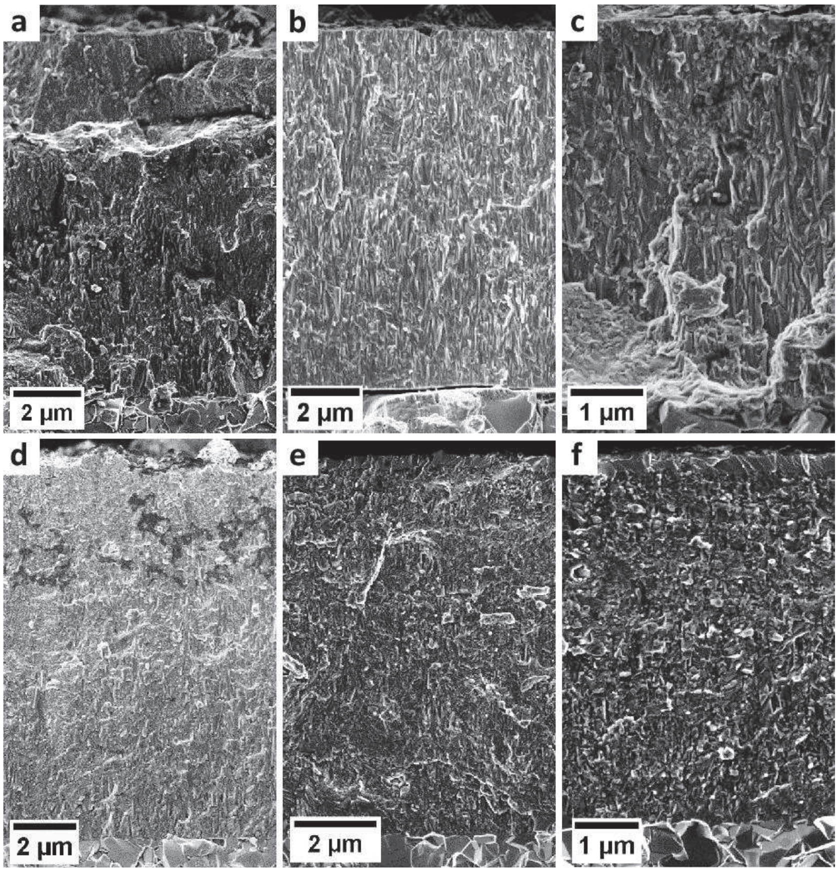

Figure D.6.: SEM micrographs of cross-sections of films A, B and C in as-deposited (a–c) and annealed (d–f) states, respectively.

as-deposited state irrespective of the deposition temperature (see Figs. D.6a-c) and (ii) the same elemental composition within the detection limits of EDS (Table D.2).

Table D.2.: Al and Cr content and Al/Cr ratio measured by EDS for thin films A, B and C.

	A	**B**	**C**
Al [%]	63.5 ± 1.0	63.5 ± 1.0	63.3 ± 1.0
Cr[%]	36.5 ± 1.0	36.5 ± 1.0	36.7 ± 1.0
Al/Cr ratio	1.74	1.74	1.72

After annealing, the cross-sectional microstructure changed to globular-like with many subgrains formed as a consequence of the decomposition of metastable c-AlCrN phase (Sec. D.3). Table D.3 summarizes indentation hardness and modulus of all three AlCrN films investigated in this study.

Table D.3.: hardness and indentation modulus for films A, B and C, in as-deposited and annealed state.

	as-deposited			**annealed**		
	A	**B**	**C**	**A**	**B**	**C**
H [GPa]	32.9±3.5	32.9±3.8	35.6±2.7	28.8±2.7	26.5±2.0	28.7±2.3
E_i [GPa]	449±28	470±32	484±41	411±28	425±30	316±19

It can be seen that both hardness and elastic modulus of the films in their as-deposited state increased with decreasing substrate temperature but are well comparable and much lower after annealing, which is associated with the changes of the crystal structure, morphology and residual stress state, as demonstrated by the results in Figs. D.2, D.3, D.4, D.5 and D.6.

D.3. Discussion

The methodological novelty of this work resides in introducing the HT-HE-GIT XRD method, which was used to study the temperature dependent behaviour of $Al_{0.7}Cr_{0.3}N$ films and WC-Co substrates and revealed the remarkable dependence of the film phase transformation temperature on the magnitude of the residual stress. Compared to other laboratory and synchrotron approaches reported in the literature, there is a twofold methodological advantage of the HT-HE-GIT XRD approach, namely (i) the collected 2D diffraction data provides a variety of experimental characteristics on phase composition, microstructure and strain evolution in film and substrate crystalline phases and (ii) the temperature-dependent values of CTEs from all film and substrate phases are evaluated experimentally and compared in order to quantify in-plane residual, thermal and intrinsic strains/stresses, which can be correlated with the actual film microstructure and phase evolution. Up to now, thin film lamellas of TiAlN [19], ZrAlN [20] and TiZrAlN [21] were investigated in terms of phase and/or residual stress evolution at high temperatures. But, due to the reduced thickness of thin film lamellas, the residual stress state of the film on the lamella is expected to be different compared to the residual stress state of the film on a bulk substrate [29]. On the contrary, in the present approach, all thin film properties were measured on the bulk substrate, with little sample preparation effort. Furthermore, a minor disadvantage of the presented method is, that the film has to be positioned carefully with respect to the primary beam to optimize the film/substrate intensity ratio (*cf.* Methods' section) compared to probing a thin film lamella, where shading due to the substrate represents a minor complication. Additionally, (semi-)quantitative phase analysis during decomposition [17, 18] and the evaluation of thin film CTEs [36] was in the past exclusively performed on thin film powders.

Therefore, the robust approach of HT-HE-GIT XRD available currently at the HEMS beamline of the Petra III light source in Hamburg provides temperature-dependent multi-parameter results and insights on the processes in the substrate and in the film simultaneously and allows to follow the evolution of phases, texture, CTEs, FWHMs (reflecting defects densities and grain sizes) and stresses variations, both in films and substrates, in real time. Till now, the decomposition paths of the metastable CrAlN system has been mostly studied *in-situ* by differential scanning calorimetry combined with *ex-situ* structural analysis such as XRD or TEM or *ex-situ* by X-ray diffraction analysis of powders [5–7].

In contrast, the HT-HE-GIT XRD method is well suitable to study the HT behaviour of metastable systems such as AlCrN, undergoing multiple-step phase decomposition. Although there are numerous reports on the decomposition paths of the AlCrN system [5–7], the application of the HT-HE-GIT XRD method allows to get new insights especially into the stress development of individual phases, crystallographic relations between the precipitates and decomposed matrix and furthermore into the variation of thermal strains and thermal expansion of individual phases, all as a function of temperature by using a single setup in reasonable time.

The decomposition of the c-CrAlN system as a consequence of segregation of Al towards the GBs and subsequent formation of more thermodynamically stable Al-rich w-Al(Cr)N phases coexisting with Cr-rich c-Cr(Al)N proceeds in several steps, which can be described as follows:

$$\begin{gathered} c-CrAlN{\rightarrow}c-Cr(Al)N+w-AlCrN{\rightarrow}c-CrN \\ +c-Cr(Al)N+w-Al(Cr)N{\rightarrow}h-Cr_2N \\ +c-Cr(Al)N+wAl(Cr)N\,(lately\,Cr_2N{\rightarrow}Cr) \end{gathered}$$

This complete decomposition pathway observed during *in-situ* HT-HE-GIT XRD confirms in principal what is known from literature [5, 6] but is furthermore complemented by new important findings summarized hereafter.

During heating to T_S, the lattice parameter d^*continuously increases, which reflects the expansion of the crystal lattice. Since the CTE is a temperature-dependent physical quantity (see its non-linear increase with temperature in Fig. D.3b), also the variation of the lattice parameter is not linear (Fig. D.3a). On the contrary, as lattice defects generated during ion-assisted film growth and contributing to lattice distortion become mobile at temperatures higher than T_S, the lattice parameter is reduced above ~500 °C and thus partially compensated for the increase of the lattice as a consequence of the lattice thermal expansion (visible as a decreased slope of the $d(T)$ curve between 500 and 900°C in Fig. D.3a). The complementary FWHM analysis, which reflects the contribution of both the finite size of coherently diffracting domains and defect density, allows to identify the diffusion-induced defect recovery processes and crystallite size variations occurring during heating and cooling (Figs. D.2g and D.4b). No defect recovery of the c-CrAlN lattice or grain growth taking place at temperatures below T_S corresponds to insufficient energy delivered to the system below T_S to activate diffusion-driven relaxation and growth processes [28]. The analysis of lattice strain and its individual components revealed a continuous linear change of thermal strain ε^c_{th} from tension to compression between RT and 900°C as a consequence of a CTE mismatch of the film and substrate depicted in Fig. D.3b, while the compressive intrinsic strain component $\varepsilon^c_i$was constant to T_S followed by a gradual relaxation between T_S and the onset temperature of phase decomposition (Fig. D.2c). The defect recovery above T_S is in good agreement with the development of the FWHM in this temperature range shown in Fig. D.4b and is also reflected by the variation of the compressive residual strain ε^c_r in Fig. 3c and residual stress evaluated in Figs. D.2i and D.4a, consisting of both intrinsic and thermal components.

Above $\sim$ 700–900°C, the ongoing relaxation of defects results in the formation of the w-Al(Cr)N phase at the GBs in all three investigated $Al_{0.7}Cr_{0.3}N$ films, which is revealed in the phase plot in Fig. D.2b by the appearance of the w-Al(Cr)N reflection and by a decrease of the lattice parameter d^* (Fig. D.3a), corresponding to the detriment of Al in the crystal lattice in the initial stage of the decomposition of c-AlCrN.

The segregated Al acts at the GBs as a nucleation site for the formation of w-Al(Cr)N crystalline nuclei, serving for further growth of the high Al-containing wurtzite phase. This interpretation was suggested by large FWHMs of the w-Al(Cr)N reflections with small intensity (Fig. D.2c,d). Moreover, the c-Cr(Al)N crystallites obviously grew in the temperature range of 900–1100°C, as indicated by a fast decrease of the FWHM shown in Figs. D.2g and D.4b. The strength of the HT-HE-GIT XRD approach is also in the ability to reveal the nucleation and growth rate of the w-Al(Cr)N precipitates, which reached their maximum between 1000 and 1100°C, as demonstrated by an increase of the first derivative of the peak intensity (Fig. D.2d) and a decrease of the FWHM of the w-Al(Cr)N 100 reflection (Fig. D.2g). Further decrease in the compressive strain above 1000°C is associated with an interplay of several strain-reducing mechanisms associated with the ongoing decomposition of c-Cr(Al)N and CrN and phase softening. Moreover, the nitrogen loss and formation of the Cr_2N phase associated with an increase of number of N vacancies results in a shrinkage of the crystal lattices (Figs. D.2b and D.3a), also accompanied by a reduction of the compressive strain. The capability of the HT-HE-GIT XRD method to detect the variations in $\varepsilon_{\mathrm{i}}^{j}$, $\varepsilon_{\mathrm{th}}^{j}$ and $\varepsilon_{\mathrm{r}}^{j}$ nearly in the entire temperature range of the annealing experiment makes the method unique, especially because other parameters simultaneously detected during the experiment allow for interpretation of the origin of these variations and to reveal the ongoing processes. The onset temperature of decomposition of Cr_2N at ~1080°C (Fig. D.2b–d and Supplementary Figs. D.4b–d and D.4b–d) is in good agreement with literature values [5, 6, 38] of 1015–1140 °C.

During the holding segment at 1100°C, the intensity increase of the w-Al(Cr)N and h-Cr_2N reflections indicates further development of both phases (Fig. D.2c), their volume increases at continuously decreasing rate (Fig. D.1d). This indicates slowed-down diffusion of Al towards GBs of c-Cr(Al)N and nitrogen loss during the holding segment, which is furthermore corroborated by the almost constant lattice parameter d^* of c-Cr(Al)N (Fig. D.3a). A decrease in the FWHM of the w-Al(Cr)N crystallites indicates their continuous growth during the holding segment (Fig. D.2g). The orientation of the c-Cr(Al)N and w-Al(Cr)N crystallites remains, however, unchanged (Fig. D.2e,f).

During cooling from 1100 to 900°C, the energy delivered to the system is obviously still sufficient for diffusion-driven structural variations, which are indicated by a further increase of the intensity of the w-Al(Cr)N and h-Cr_2N reflections (Fig. D.2c), even though at lower rates (Fig. D.2d), revealing a decaying development of both phases. Since the film microstructure consists of three phases at this stage of the annealing experiment (c-Cr(Al) N, w-Al(Cr)N and h-Cr_2N), which all differ in their CTEs, the thermal tensile strain continuously increase during cooling (note also different CTE of the WC-Co substrate). Remarkably, the residual stress of all phases exhibited rather the same values (Fig. D.2i).

The HT-HE-XRD method allows identifying the role of deposition temperature on the development of film microstructure, individual stress components and stability of the c-CrAlN phase, which obviously differ with the increasing energy delivered to the system during the deposition process. While the microstructural changes with T_{S} were almost negligible, as demonstrated by almost identical SEM micrographs

(Fig. D.6) and FWHM values (Fig. D.4b) of the films in the as-deposited state, their residual compressive stress state decreased with increasing temperature (Fig. D.4a). Also the onset of defect recovery, indicating their thermal stability, is obviously proportional to the deposition temperature. This is evident from Fig. D.4a by a deviation of σ_{r} from its thermo-elastic behaviour slightly above the varied T_{S}. While the tensile thermal stress σ_{th} in the deposited state of the films increases with, and as a consequence of the deposition temperature, the compressive intrinsic stress σ_{i} decreased due to enhanced adatom mobility resulting in subsequent defect recovery occurring already during film growth (Fig. D.5a). The development of the compressive residual stress to a different extent at various T_{S} results also in an increasing magnitude of the total stress recovery after the annealing experiment (Fig. D.4a) indicating an obvious correlation between the residual stress state and the driving force for stress recovery during annealing. The deposition temperature also affects the thermal stability of intrinsic defects in the film microstructure. In agreement with other studies [30], defect recovery was in all three cases detected above T_{S}, which has to be exceeded to promote the diffusion processes and thus determines the defect stability. The residual stress state after the annealing was almost identical for all films (Fig. D.4a). The difference of the FWHM of the films after the annealing experiment clearly showed that the c-Cr(Al)N crystallites grew much more than those of the films deposited at lower T_{S} (see smaller FWHM of the film A than that of B and C in Fig. D.4b).

Since the elemental and phase composition of the films A, B and C (Table D.2), their microstructure in terms of the crystallite size and texture (Fig. D.2e and Supplementary Figs. D.4e and D.4e) as well as the FWHM were almost identical (the film texture moreover did not change during annealing), another effect controlling the thermal stability of the c-CrAlN phase needs to be considered. Whereas the onset temperature of phase decomposition was ranging between 698 and 914°C from films A to C, respectively, the onset stress of phase decomposition was relatively constant between the magnitudes of -4560 and -3850 MPa (Table D.1). Remarkably, the onset temperature of the phase decomposition lies within this range of about 600 MPa regardless of the thermomechanical history of the thin films.

The important role of the compressive residual stress magnitude on the decomposition of the metastable c-CrAlN solid solution may be related to the suppressed Al diffusion towards GBs. Also theoretical calculations are supporting the stabilization of the cubic structure at high compressive stresses estimated to -11.5 GPa to -16 GPa to stabilize the unstable c-AlN phase [39]. An analogy to this effect may be found in the stabilization of the cubic c-$\mathrm{Cr}_{1-x}\mathrm{Al}_x\mathrm{N}$ with respect to its composition.

Theoretical calculations found that without compressive stresses, the cubic phase can be at 0 K stabilized up to $x = 0.69$, whereas in the presence of a hydrostatic compressive stress state of 4 GPa, the cubic phase can be stabilized up to $x = 0.80$ [40].

D.4. Conclusions

In-situ high-temperature high-energy grazing incidence X-ray diffraction was used to analyse the (i) phases, (ii) texture, (iii) domain size, (iv) coefficients of thermal expansion and subsequently thermal strains, (v) residual and (vi) intrinsic stresses of three $Al_{0.7}Cr_{0.3}N$ thin films on a cemented carbide bulk substrate. By using this novel approach, it was possible to comprehensively characterize the thermal stability of these thin films. The results revealed (i) a strain/stress controlled phase decomposition, where the decomposition onset temperature is predominantly dependent on the as-deposited in-plane residual stress magnitude, (ii) similar $\langle 111 \rangle$ fibre texture in the cubic phase and a combination of $\langle 100 \rangle$ and $\langle 110 \rangle$ in the hexagonal phase for all three investigated thin films and (iii) the measurement of CTE during heating and cooling for the substrate as well as the cubic and the hexagonal phase. The results demonstrate that the residual stress state plays a dominant role in enhancing the thermal stability of the metastable solid solution of c-AlCrN. Finally, it was shown, that the newly developed *in-situ* approach leads to a better understanding of the structural changes in metastable thin films at high thermal loads and can be applied as an powerful tool for further thin film design.

Methods

Thin film synthesis

The $Al_{0.7}Cr_{0.3}N$ thin films were prepared by cathodic arc evaporation in a voestalpine eifeler-Vacotec alpha400P deposition system equipped with six $Al_{70}Cr_{30}$ cathodes operated at a cathode current of 100 A, substrate bias voltage $U_B = -100\,\mathrm{V}$ and nitrogen pressure $p_{N2} = 4\,\mathrm{Pa}$. The deposition temperature varied from $T_{S,A} = 475°C$, $T_{S,B} = 400°C$ to $T_{S,C} = 325°C$ for films denoted as A, B and C, respectively. The mirror-polished cemented carbide (WC, 6 wt.% Co) substrates of a dimension of $10 \times 5 \times 5\,\mathrm{mm}^3$ were mounted on the sample holder in one-fold-rotation at a cathode-to-substrate distance of $\sim$ 100 mm and plasma cleaned prior deposition. Films A and B had a thickness of $\sim$ 11 µm, while the film C had a reduced thickness of ∼ 6 µm, as only 3 cathodes were used at the same deposition time in order to reduce the deposition temperature to 325°C.

Laboratory characterization

Cross-sectional characterization of the films was performed in a Zeiss LEO 1525 scanning electron microscope (SEM) with 3 kV accelerating voltage and an aperture of 20 µm. In order to reveal the elemental composition of the films, energy-dispersive X-ray spectroscopy analysis (EDS) was performed in SEM and quantified by built-in standards (Zeiss LEO 1525, Bruker Quantax, with 20 kV accelerating voltage and 60 µm aperture). Indentation modulus and hardness of the films were determined by means of nanoindentation (UMIS, Fischer-Cripps Laboratory Ltd.).

In-Situ high-temperature synchrotron characterization

The in-situ HE-HT-GIT-XRD experiments were performed at the P07B beamline of the PETRA III synchrotron source in Hamburg (D) in transmission geometry, using a pencil X-ray beam with a size of 400 × 100 µm^2 and an energy of 87.1 keV. The samples were mounted into a DIL 805 dilatometer (TA Instruments) with the surface aligned with respect to the primary beam at an incidence angle β of ∼ 2 deg (Fig. D.1). The incidence angle of ∼ 2 deg was set to probe as much film volume as possible in transmission, whilst maintaining the intensity of substrate reflections at a minimum. The exact incidence angle and the position of the sample surface with respect to the primary beam are dependent on the individual sample and have to be repeatedly adjusted to an optimum before starting the *in-situ* HT-HE-GIT XRD experiment.

The thermal cycle included heating to 1100°C at a rate of 1 K/s followed by a holding segment of 300 s at the maximum temperature (both in vacuum at $p_{\text{total}} < 10^{-2}$ mbar) and subsequent cooling to RT at a rate of ~1 K/s, controlled by the Ar flow through the dilatometer chamber. Two dimensional (2D) X-ray diffraction patterns were recorded continuously using a Perkin-Elmer detector with a pixel size of 200 × 200 µm^2 and an exposure time of ∼ 25 s per frame (Fig. D.1). The temperature for each diffraction pattern exposure was recorded with a Type S thermocouple welded to the sample surface with a resolution of ∼ 0.5°C. The detector calibration was performed using a LaB$_6$-powder and the Fit2D software package [41]. The sample-to-detector distance, the detector tilt and the rotation angle of the tilt plane of 1949.4 mm, 0.0895 deg and 69.453 deg were evaluated, respectively. The beam centre on the detector was evaluated from the lower left corner 1031.246

and 978.412 pixels in horizontal and vertical direction. The 2D data evaluation was performed using the pyFAI software package [42].

Acknowledments

The work has been financially supported by Christian Doppler Research Association. The financial support by the Austrian Federal Ministry of Science, Research and Economy and the National Foundation for Research, Technology and Development is also gratefully acknowledged. A part of this work was supported by Österreichische Forschungsförderungsgesellschaft mbH (FFG), Project No. 864828, “Tough_TiAlN”. Special thanks to J. Todt, J. F. Keckes and S. C. Bodner for the extensive discussion, help with the artwork and assistance during the measurements, respectively. The high-temperature end-station was equipped through financial support by the German Federal Ministry of Education and Research (BMBF projects 05KS7FK3 and 05K10FK3) which is also greatly acknowledged. The P07 team is gratefully thanked for provision of the access to the high-temperature end station.

Supplementary material

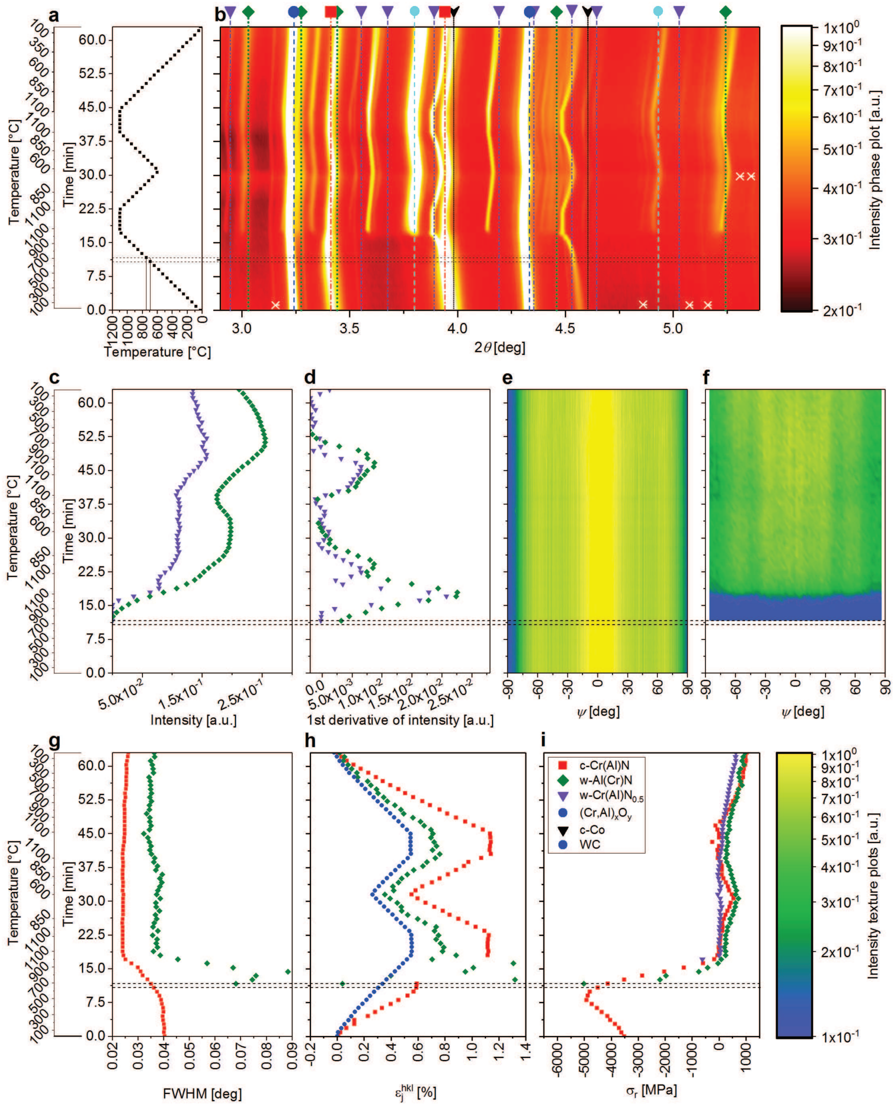

Suppl. Fig. D.1: the applied temperature cycle (a) and the experimental data of the AlCrN film A, phase plot with indicated diffraction angles for tabulated particular phases, where the white crosses indicate additional diffraction peaks representing 2nd order diffraction due to the presence of the second harmonic's wavelength in the primary beam (b), evolution of intensity (c) and the 1st derivative of the intensity (d) of w-Al(Cr)N 100 (green) and h-Cr$_2$N 100 (violet) reflections, the texture plot for c-Cr(Al)N 111 reflection indicating ⟨111⟩ fibre texture (e), texture plot for w-Al(Cr)N 100 reflection indicating overlapping ⟨100⟩ and ⟨110⟩ fibre texture (f), evolution of FWHM of c-Cr(Al)N 111 (red) and w-Al(Cr)N 100 (green) reflections (g), thermal expansion of c-Cr(Al)N (red, evaluated from the 200 reflection), w-Al(Cr)N (green, 100 reflection) and WC substrate (blue) (h) and residual stress evaluated from the c-Cr(Al)N 200 (red), w-Al(Cr)N 100 (green) and h-Cr$_2$N 100 (violet) reflections (i).

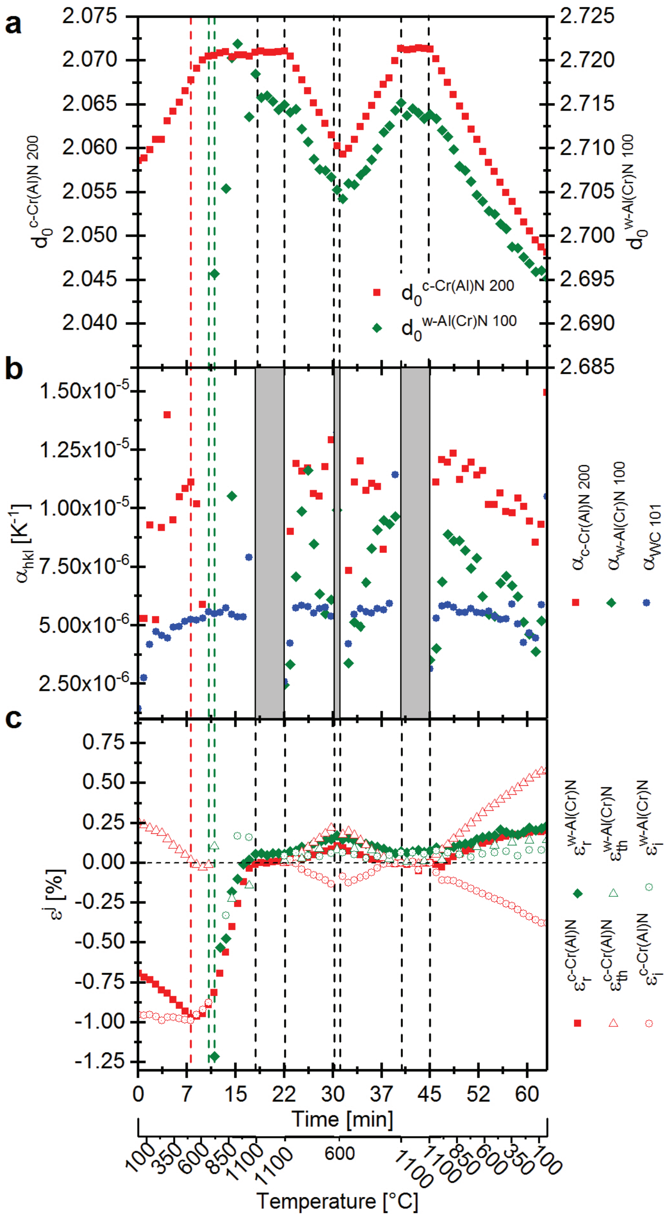

Suppl. Fig. D.2: Experimental assessment for film A deposited at 475°C: the development of the unstrained lattice parameter $d_0(T)$ of c-Cr(Al)N and w-Al(Cr)N phase over the temperature (a), the thermal expansion coefficient calculated for the individual reflections (b) and the evolution of thermal, intrinsic and residual strain over the temperature cycle for c-Cr(Al)N (red) and w-Al(Cr)N (green), respectively (c). The vertical red dashed line represents the deposition temperature, the green dashed line the onset of the phase decomposition and the vertical black segmented lines the beginning and the end of the holding segment.

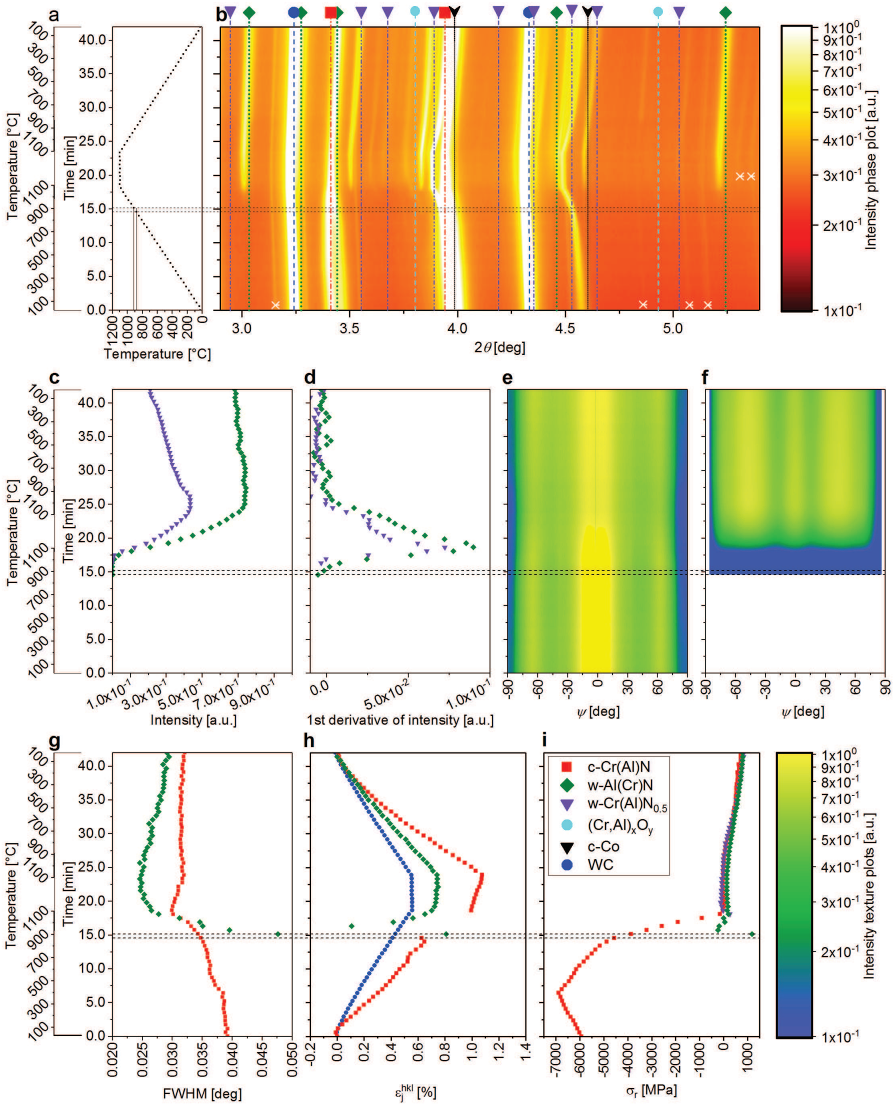

Suppl. Fig. D.3: the applied temperature cycle (a) and the experimental data of the AlCrN film C, phase plot with indicated diffraction angles for tabulated particular phases, where the white crosses indicate additional diffraction peaks representing 2nd order diffraction due to the presence of the second harmonic's wavelength in the primary beam (b), evolution of intensity (c) and the 1st derivative of the intensity (d) of w-Al(Cr)N 100 (green) and h-Cr_2N 100 (violet) reflections, the texture plot for c-Cr(Al)N 111 reflection indicating ⟨111⟩ fibre texture (e), texture plot for w-Al(Cr)N 100 reflection indicating overlapping ⟨100⟩ and ⟨110⟩ fibre texture (f), evolution of FWHM of c-Cr(Al)N 111 (red) and w-Al(Cr)N 100 (green) reflections (g), thermal expansion of c-Cr(Al)N (red, evaluated from the 200 reflection), w-Al(Cr)N (green, 100 reflection) and WC substrate (blue) (h) and residual stress evaluated from the c-Cr(Al)N 200 (red), w-Al(Cr)N 100 (green) and h-Cr_2N 100 (violet) reflections (i).

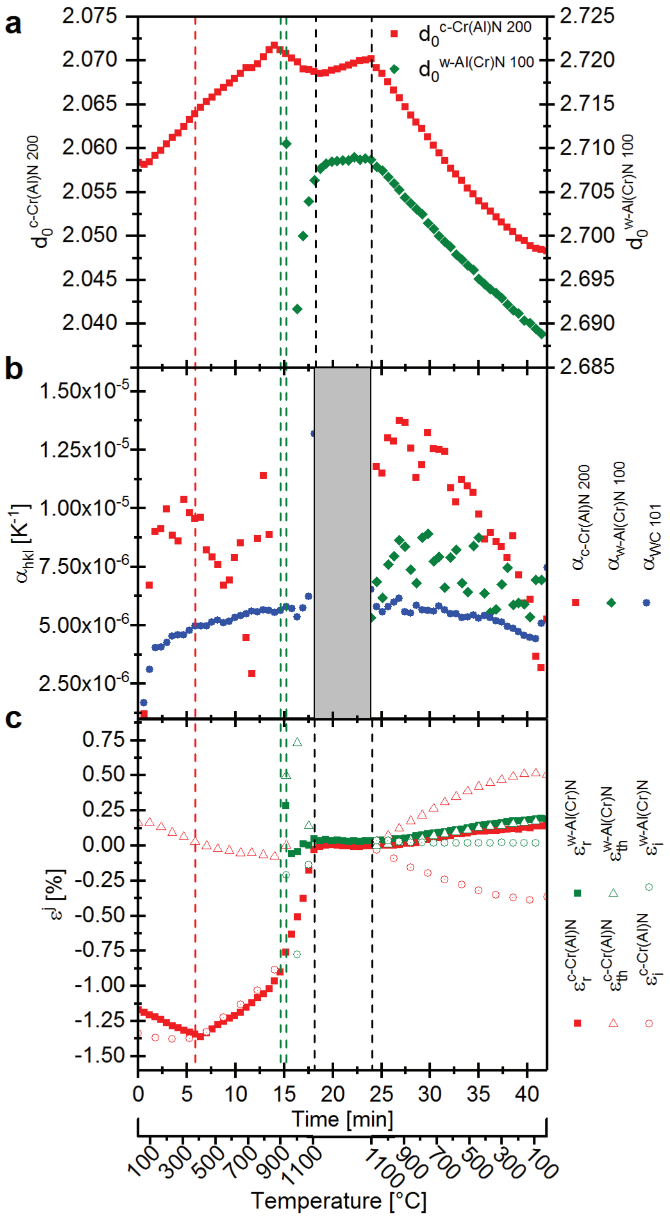

Suppl. Fig. D.4: Experimental assessment for film C deposited at 475°C: the development of the unstrained lattice parameter $d_0(T)$ of c-Cr(Al)N and w-Al(Cr)N phase over the temperature (a), the thermal expansion coefficient calculated for the individual reflections (b) and the evolution of thermal, intrinsic and residual strain over the temperature cycle for c-Cr(Al)N (red) and w-Al(Cr)N (green), respectively (c). The vertical red dashed line represents the deposition temperature, the green dashed line the onset of the phase decomposition and the vertical black segmented lines the beginning and the end of the holding segment.

Bibliography to paper D

[1] J. Vetter, *Surface and Coatings Technology*, 1995, **76-77**, 719–724, DOI: `10.1016/0257-8972(95)02499-9`.

[2] M. Kawate, A. K. Hashimoto and T. Suzuki, *Surface and Coatings Technology*, 2003, **165**, 163–167, DOI: `10.1016/s0257-8972(02)00473-5`.

[3] A. Reiter, V. Derflinger, B. Hanselmann, T. Bachmann and B. Sartory, *Surface and Coatings Technology*, 2005, **200**, 2114–2122, DOI: `10.1016/j.surfcoat.2005.01.043`.

[4] M. Kawate, A. Kimura and T. Suzuki, *Journal of Vacuum Science & Technology A: Vacuum, Surfaces, and Films*, 2002, **20**, 569–571, DOI: `10.1116/1.1448510`.

[5] H. Willmann, P. H. Mayrhofer, L. Hultman and C. Mitterer, *International Heat Treatment and Surface Engineering*, 2007, **1**, 75–79, DOI: `10.1179/174951507x193657`.

[6] H. Willmann, P. H. Mayrhofer, P. O. Å. Persson, a. E. Reiter, L. Hultman and C. Mitterer, *Scr. Mater.*, 2006, **54**, 1847–1851, DOI: `10.1016/j.scriptamat.2006.02.023`.

[7] P. H. Mayrhofer, H. Willmann, L. Hultman and C. Mitterer, *Journal of Physics D: Applied Physics*, 2008, **41**, 155316, DOI: `10.1088/0022-3727/41/15/155316`.

[8] C. Sabitzer, J. Paulitsch, S. Kolozsvári, R. Rachbauer and P. Mayrhofer, *Thin Solid Films*, 2016, **610**, 26–34, DOI: `10.1016/j.tsf.2016.05.011`.

[9] B. Grossmann, M. Tkadletz, N. Schalk, C. Czettl, M. Pohler and C. Mitterer, *Surface and Coatings Technology*, 2018, **342**, 190–197, DOI: `10.1016/j.surfcoat.2018.02.062`.

[10] M. Pfeiler-Deutschmann, P. H. Mayrhofer, K. Chladil, M. Penoy, C. Michotte, M. Kathrein et al., *Thin Solid Films*, 2015, **581**, 20–24, DOI: `10.1016/j.tsf.2014.10.051`.

[11] T. Weirather, C. Czettl, P. Polcik, M. Kathrein and C. Mitterer, *Surface and Coatings Technology*, 2013, **232**, 303–310, DOI: `10.1016/j.surfcoat.2013.05.022`.

[12] W. Tillmann, D. Kokalj, D. Stangier, M. Paulus, C. Sternemann and M. Tolan, *Surface and Coatings Technology*, 2017, **328**, 172–181, DOI: `10.1016/j.surfcoat.2017.08.046`.

[13] W. Tillmann, D. Kokalj, D. Stangier, M. Paulus, C. Sternemann and M. Tolan, *Applied Surface Science*, 2018, **427**, 511–521, DOI: `10.1016/j.apsusc.2017.09.029`.

[14] N. Jäger, S. Klima, H. Hruby, J. Julin, M. Burghammer, J. Keckes et al., *Acta Materialia*, 2019, **162**, 55–66, DOI: `10.1016/j.actamat.2018.09.031`.

[15] E. Mohammadpour, Z.-T. Jiang, M. Altarawneh, N. Mondinos, M. M. Rahman, H. N. Lim et al., *RSC Advances*, 2017, **7**, 22094–22104, DOI: `10.1039/c7ra00342k`.

[16] K. Bobzin, N. Bagcivan, M. Ewering, R. Brugnara and S. Theiß, *Surface and Coatings Technology*, 2011, **205**, 2887–2892, DOI: `10.1016/j.surfcoat.2010.10.056`.

[17] N. Norrby, L. Rogström, M. Johansson-Jõesaar, N. Schell and M. Odén, *Acta Materialia*, 2014, **73**, 205–214, DOI: `10.1016/j.actamat.2014.04.014`.

[18] Y. Chen, L. Rogström, D. Ostach, N. Ghafoor, M. Johansson-Jõesaar, N. Schell et al., *Journal of Alloys and Compounds*, 2017, **691**, 1024–1032, DOI: `10.1016/j.jallcom.2016.08.299`.

[19] L. Rogström, J. Ullbrand, J. Almer, L. Hultman, B. Jansson and M. Odén, *Thin Solid Films*, 2012, **520**, 5542–5549, DOI: `10.1016/j.tsf.2012.04.059`.

[20] L. Rogström, N. Ghafoor, J. Schroeder, N. Schell, J. Birch, M. Ahlgren et al., *Journal of Applied Physics*, 2015, **118**, 035309, DOI: `10.1063/1.4927156`.

[21] L. Rogström, M. J. Jõesaar, R. Pilemalm, N. Ghafoor, L. Johnson, N. Schell et al., *Journal of Alloys and Compounds*, 2019, **779**, 261–269, DOI: `10.1016/j.jallcom.2018.11.039`.

[22] M. Meindlhumer, J. Zalesak, R. Pitonak, J. Todt, B. Sartory, M. Burghammer et al., *Nanoscale*, 2019, **11**, 7986–7995, DOI: `10.1039/c8nr10339a`.

[23] *Powder Diffraction File Cards: fcc-CrN 11-0065, w-AlN 225-1133, WC 25-1047, Co 15-0806., (n.d.)*

[24] M. Yan and H. Chen, *Computational Materials Science*, 2014, **88**, 81–85, DOI: `10.1016/j.commatsci.2014.02.035`.

[25] J. Keckes, R. Daniel, J. Todt, J. Zalesak, B. Sartory, S. Braun et al., *Acta Materialia*, 2018, **144**, 862–873, DOI: `10.1016/j.actamat.2017.11.049`.

[26] M. Bartosik, R. Daniel, C. Mitterer and J. Keckes, *Surface and Coatings Technology*, 2010, **205**, 1320–1323, DOI: `10.1016/j.surfcoat.2010.08.089`.

[27] J. Keckes, M. Bartosik, R. Daniel, C. Mitterer, G. Maier, W. Ecker et al., *Scr. Mater.*, 2012, **67**, 748–751, DOI: `10.1016/j.scriptamat.2012.07.034`.

[28] R. Daniel, K. Martinschitz, J. Keckes and C. Mitterer, *Acta Mater.*, 2010, **58**, 2621–2633, DOI: `10.1016/j.actamat.2009.12.048`.

[29] M. Stefenelli, J. Todt, A. Riedl, W. Ecker, T. Müller, R. Daniel et al., *J Appl Crystallogr*, 2013, **46**, 1378–1385, DOI: `10.1107/S0021889813019535`.

[30] H. Köstenbauer, G. A. Fontalvo, M. Kapp, J. Keckes and C. Mitterer, *Surface and Coatings Technology*, 2007, **201**, 4777–4780, DOI: `10.1016/j.surfcoat.2006.10.017`.

[31] M. Bartosik, R. Daniel, C. Mitterer, I. Matko, M. Burghammer, P. Mayrhofer et al., *Thin Solid Films*, 2013, **542**, 1–4, DOI: `10.1016/j.tsf.2013.05.102`.

[32] I. C. Noyan and J. B. Cohen, *Residual Stress*, Springer New York, 1987, DOI: `10.1007/978-1-4613-9570-6`.

[33] J. Almer, U. Lienert, R. L. Peng, C. Schlauer and M. Odén, *Journal of Applied Physics*, 2003, **94**, 697–702, DOI: `10.1063/1.1582351`.

[34] K. Kim, W. R. L. Lambrecht and B. Segall, *Physical Review B*, 1996, **53**, 16310–16326, DOI: `10.1103/physrevb.53.16310`.

[35] P. Hidnert, *Journal of Research of the National Bureau of Standards*, 1937, **18**, 47, DOI: `10.6028/jres.018.025`.

[36] M. Bartosik, D. Holec, D. Apel, M. Klaus, C. Genzel, J. Keckes et al., *Scripta Materialia*, 2017, **127**, 182–185, DOI: `10.1016/j.scriptamat.2016.09.022`.

[37] J. Keckes, *Journal of Applied Crystallography*, 2005, **38**, 311–318, DOI: `10.1107/s0021889805001044`.

[38] P. Mayrhofer, H. Willmann and A. Reiter, *Surface and Coatings Technology*, 2008, **202**, 4935–4938, DOI: `10.1016/j.surfcoat.2008.04.075`.

[39] N. E. Christensen and I. Gorczyca, *Physical Review B*, 1993, **47**, 4307–4314, DOI: `10.1103/physrevb.47.4307`.

[40] D. Holec, F. Rovere, P. H. Mayrhofer and P. B. Barna, *Scripta Materialia*, 2010, **62**, 349–352, DOI: `10.1016/j.scriptamat.2009.10.040`.

[41] A. P. Hammersley, S. O. Svensson, M. Hanfland, A. N. Fitch and D. Hausermann, *High Pressure Res.*, 1996, **14**, 235–248, DOI: `10.1080/08957959608201408`.

[42] J. Kieffer, *J. Phys: Conf. Ser.*, 2013, **425**, 202012, DOI: `10.1088/1742-6596/425/20/202012`.

E

Biomimetic hard and tough nanoceramic Ti–Al–N film with self-assembled six-level hierarchy

M. Meindlhumer[a,b], J. Zalesak[a,b], R. Pitonak[c], J. Todt[a], B. Sartory[d], M. Burghammer[e], A. Stark[f], N. Schell[f], R. Daniel[b], J. F. Keckes[a], M. Lessiak[c], A. Köpf[c], R. Weißenbacher[c], Jozef Keckes[a]

[a]Department of Materials Physics, Montanuniversität Leoben and Erich Schmid Institute for Materials Science, Austrian Academy of Sciences, 8700 Leoben, Austria
[b]Department of Physical Metallurgy and Materials Testing, Montanuniversität Leoben, 8700 Leoben, Austria
[c]Boehlerit GmbH & Co KG, A-8605 Kapfenberg, Austria
[d]Materials Center Leoben Forschung GmbH, 8700 Leoben, Austria
[e]ESRF, 38043 Grenoble, France
[f]Helmholtz Zentrum Geesthacht, Centre for Materials and Coastal Research, Geesthacht, Germany

Abstract

Nature uses self-assembly of a fairly limited selection of components to build hard and tough protective tissues like nacre and enamel. The resulting hierarchical micro/nanostructures provide decisive toughening mechanisms while preserving strength. However, to mimic microstructural and mechanical characteristics of natural materials in application-relevant synthetic nanostructures has proven to be difficult. Here, we demonstrate a biomimetic synthesis strategy, based on chemical vapour deposition technology, employed to fabricate a protective high-temperature resistant nanostructured ceramic TiAlN thin film with six levels of hierarchy. By using just two variants of gaseous precursors and through bottom-up self-assembly, an irregularly arranged hard and tough multilayer stack was formed, consisting of hard sublayers with herringbone micrograins, separated by tough interlayers with spherical nanograins, respectively composed of lamellar nanostructures of alternating coherent/incoherent, hard/tough, single-/poly-crystalline platelets. Micro- and nanomechanical testing, performed *in situ* in scanning and transmission electron microscopes, manifests intrinsic toughening mechanisms mediated by five types of interfaces resulting in intergranular, transgranular and cleavage fracture modes with zigzag-like crack patterns at multiple length-scales. The hierarchical 2.7 µm thick film self-assembled during ~ 15 minutes of deposition time shows hardness, fracture stress and toughness of ~ 31 GPa, ~ 7.9 GPa and $\sim 4.7\,\mathrm{MPa\,m^{0.5}}$, respectively, as well as phase/microstructural thermal stability up to $\sim 950/900$°C. The film's microstructural and mechanical characteristics represent a milestone in the production of protective and wear-resistant thin films.

E.1. Introduction

In order to increase resistance to fracture and preserve strength, nature has developed unique strategies to synthesize hard and tough tissues like nacre, bone and enamel [1, 2]. These lightweight biomaterials are formed at ambient temperatures through bottom-up self-assembly strategies from a fairly limited selection of chemical components [3–6]. A unique aspect of practically all protective and wear-resistant biological tissues is a hierarchical architecture [7–9] and the adoption of multiscale interfaces between alternating phases, which are responsible for an entire set of extrinsic and intrinsic toughening mechanisms [10–15], each of which is acting on a particular length scale. Even though the common biomimetic motifs for the design of lightweight, strong and tough materials have been derived [13–17], the fabrication of synthetic nanostructures that mimic the structural and mechanical characteristics of their natural counterparts, is a very challenging task and has succeeded only in a limited number of cases [18–23], mainly at the laboratory scale [24, 25]. Also in the field of protective and high-temperature resistant thin films, large-scale manufacturing technology has been practically unable to provide application-relevant hard and tough protective nanomaterials with a large number of hierarchical levels and multiscale interfaces, despite decades of research [24, 26].

Here we demonstrate that, by means of a common industrial-scale chemical vapour deposition (CVD) [27] process, it is possible to produce a truly biomimetic protective TiAlN thin film with six-level hierarchy, which is simultaneously hard, tough and high-temperature resistant. Most importantly, the thin film's nanostructure is the result of fast bottom-up self-assembly from two sets of gaseous precursors at well-selected process parameters of temperature and pressure. We characterize the correlation between the thin film's hierarchical nanostructure and crack propagation behaviour at the micro- and nanoscale as well as the thermal stability of its cubic phase and nanostructure and discuss the obtained quantitative results.

E.2. Results

E.2.1. Self-assembly of hierarchical microstructure

As an assembly approach, we used CVD [27]. The fabrication of various monolithic protective thin films with columnar and/or nanocomposite grain microstructures using this approach has already been reported [28–32]. Our aim was to further explore the self-assembly reactions taking place under intentionally varied process conditions and to synthesize a novel thin film with maximal levels of hierarchy and a number of multi-scale interfaces. We were inspired by biological microstructures, especially by nacre, and wanted to implement various micro- and nanostructural obstacles for potential cracks to overcome, as well as alternating hard and tough phases at various hierarchical levels to explore toughening mechanisms [2, 11, 16, 32]. The critical factors during the self-assembly process were the partial pressures of precursor gases, the deposition temperature and the total pressure in the chamber. The variation of the first parameter controlled the local thin film composition and the two others predefined the shapes and sizes of the polycrystalline grains, as well as their internal nanostructure. By the interplay of all three parameters during the ∼ 15-minute deposition process applying just two sets of gaseous precursors, we created a novel hierarchical thin film with six levels of hierarchy (*cf.* Sec. Methods).

We used scanning and transmission electron microscopy (SEM and TEM) to analyse the thin film's cross-sectional architecture (Fig. E.1), which is schematically described in Fig. E.2. In Fig. S.E.1, S.E.2 and S.E.3 of the supplementary material, microscopy images are shown in full resolution. The 2.7 µm thick film's cross-section comprises 9 thick hard sublayers and 9 thin tough interlayers, exhibiting a thickness ratio of ∼ 10/1, and a soft oxidation resistant hexagonal (h) AlN top layer (Fig. E.1a). To achieve the formation of the observed nacre-like cross-sectional morphology, the respective partial pressures of $AlCl_3$ and $TiCl_4$ precursor gases were optimized to 0.368 and 0.022 kPa for the thin tough interlayers and 0.404 and 0.09 kPa for the thick hard sublayers (*cf.* Sec. Methods). The hierarchical film was grown onto a WC-Co cemented carbide substrate coated with a TiN adhesion layer, at a deposition temperature of ∼ 810°C (Fig. E.1a). Since the thin film was formed in a process of kinetically controlled oscillating reactions [30, 33], the topology of the interfaces between sublayers is irregular (Fig. E.1a and b) and possesses many kinks, lowering the probability of interface failure by crack propagation in the thin film's in-plane direction.

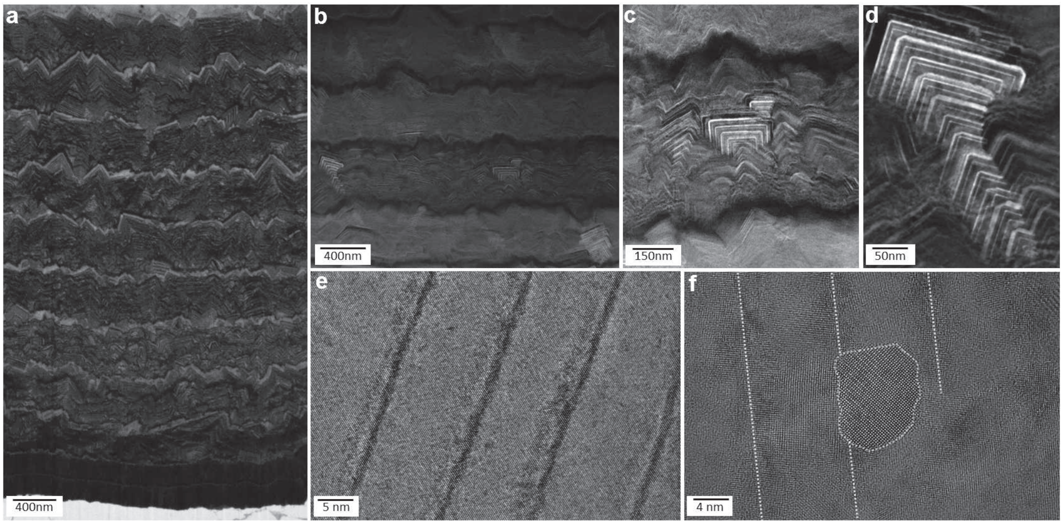

Figure E.1.: SEM and TEM micrographs of the hierarchical TiAlN film's cross-sectional nanostructure. (a) 2.7 µm thick film self-assembled on WC-Co substrates with a TiN bonding layer, consisting of nine hard (dark) and soft/tough (bright) sublayers. (b) The (bright) hard sublayers are composed of herringbone and cube micrograins, whose in-plane orientation is random. (c–e) These micrograins consist of nanolamellar packets based on alternating coherent c-Ti(Al)N and c-Al(Ti)N platelets. (f) Nanograins within tough interlayers are composed of incoherent c-Ti(Al)N and h-Al(Ti)N platelets, which themselves consist of globular nanocrystals with hexagonal structure. The dashed lines indicate approximately the location of the thin c-Ti(Al)N platelets and a grain boundary of a globular h-Al(Ti)N nanocrystal satisfying diffraction conditions (*cf.* Supplementary material).

The individual hard and tough sublayers exhibit a complex internal nanostructure with four and five hierarchical sublevels, respectively (Fig. E.2). Within each hard sublayer, there is a $\sim$ 100 nm thin nucleation region with randomly oriented nanocrystals, which further develops into a region of herringbone or cube-shaped micrograins of $\sim$ 250 nm in size (cf. Fig. E.1c,d and E.2). The thickness of the hard sublayers was set to $\sim$ 250 nm in order to avoid the formation of fully columnar grain morphology involving grain boundaries of low cohesive energy, which would develop at larger thicknesses due to competitive grain growth [34]. The micrograins possess a lamellar nanostructure whose period is however not regular and varies slightly across the individual grains (Fig. E.1d). The nanolamellae consist of alternating cubic (c) TiN and AlN platelets including some traces of the respective

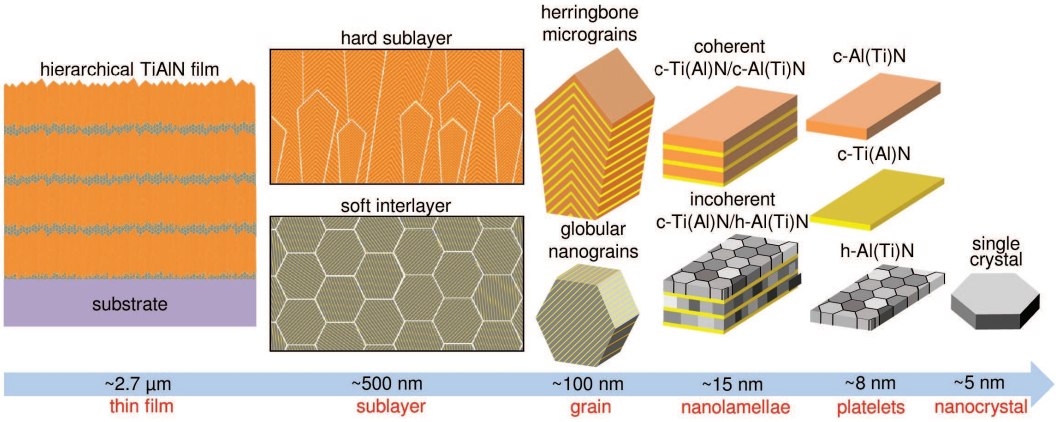

Figure E.2.: A schematic description of the six levels of hierarchy – from microscopic film to nano-crystal. The film consists of alternating hard and tough sublayers with thicknesses of ~ 500 and ~ 50 nm. The hard sublayers are composed of herringbone columnar micrograins. The internal nanostructure of the micrograins is composed of c-Ti(Al)N/c-Al(Ti)N nanolamellar stacks with coherent interfaces between platelets. The soft/tough nanocomposite interlayers consist of spherical nanograins composed of c-Ti(Al)N/h-Al(Ti)N nanolamellae with incoherent interfaces between the individual platelets. The h-Al(Ti)N platelets further consist of globular nanocrystals.

other metal species, which we will therefore term c-Ti(Al)N and c-Al(Ti)N platelets (Fig. E.1e), respectively. The spontaneous formation of a nanolamellar structure is a result of alternating growth of the individual platelets, whose cubic crystal structures and lattice parameters are mutually stabilized into perfectly coherent heteroepitaxial superlattices by self-adjusting the respective thickness and composition of each platelet. Similar planar cubic AlN/TiN superlattices have also been prepared by magnetron sputtering, using a tedious process of alternating deposition from Al and Ti targets [35]. In our process, the precise control of the nitrogen content during the kinetically controlled oscillating reactions at the growing thin film surface plays apparently the key role in the lamellae self-assembly process, as suggested in our previous report on a monolithic epitaxial TiAlN thin film deposited onto Al_2O_3 (0001) [30]. The polycrystalline tough interlayers consist of globular nanograins with sizes of ~ 50 nm, possessing an incoherent lamellar nanostructure consisting of c-Ti(Al)N and h-Al(Ti)N platelets (Fig. E.1f and E.2), which are also formed as a result of oscillating surface reactions. The individual h-Al(Ti)N platelets are polycrystalline, composed of ~ 5 nm large single crystals with random in-plane orientation. In fact, both hard and tough sublayers significantly differ in terms of their phase composition, microstructure and mechanical properties. In descending order of hierarchy, the tough interlayers consist of nanometer-sized globular grains, nanolamellae, platelets and nanocrystals, whereas all platelets in the hard sublayer are composed of single crystals, which, in contrast to the tough sublayer, results in only five hierarchical levels of this particular constituent (Fig. E.2). This difference stems from the pressure ratio of the applied precursor gases, which influences the crystallographic structure of the nanocrystals organized in the platelets, and thereby also their ability to stabilize the respective cubic polytype of the TiAlN solid solution in neighbouring platelets during the self-assembly process. Crystallographically, the hard sublayers consist of only cubic phases which are significantly harder and more brittle compared to the ductile and soft hexagonal phase present in thin tough interlayers. Energy-dispersive X-ray and electron energy loss spectroscopies revealed a very complex non-stochiometric composition of the self-assembled nanostructure, which fluctuates at the sub-nm scale. Within the thin c-Ti(Al)N platelets of the hard sublayers (Fig. E.1e), the Al metallic fraction is $\sim$ 0.4–0.7 and, in the thick c-Al(Ti)N platelets, the metallic fraction of Ti is below $\sim$ 0.05. Within the globular nanograins of tough interlayers (Fig. E.1), the thin c-Ti(Al)N platelets possess a metallic fraction of Ti in range of $\sim$ 0.95–1.0 and the thick h-Al(Ti)N platelets exhibit a composition close to pure AlN [30].

E.2.2. Micro- and nanomechanics

In order to evaluate mechanical properties of the hierarchical thin film, we performed nanoindentation tests and *in situ* micro- and nanocantilever bending experiments in SEM and TEM [36]. The cantilevers were fabricated using focused ion beam (FIB) milling. In addition to the hierarchical thin film, we synthesized also two reference monolithic thin films using constant $AlCl_3$ and $TiCl_4$ precursor partial gas pressures of 0.404 and 0.0909 kPa as well as 0.368 and 0.022 kPa, which we further term hard and soft thin films, respectively (*cf.* Suppl. Fig. S.E.4).

All three thin films were mechanically tested in order to evaluate the role of the hierarchical architecture on overall mechanical properties and crack propagation behaviour. The hardness of the hierarchical thin film lies between that of the soft and hard monolithic thin films, as this property is mainly given by the intrinsic strength and stiffness of individual con- stituents (*cf.* Table E.1). Bending experiments on unnotched and notched (Fig. 3a) microcantilevers in SEM (*cf.* Video S1 of supplementary material) were used to determine the respective Young's modulus E, fracture stress σ_F and fracture toughness K_{IC} of each thin film (Table E.1) [37, 38].

Table E.1.: Mechanical properties of the reference soft and hard films and of the hierarchical film

Thin film type	Young's modulus E [GPa]	Hardness [GPa]	Fracture stress σ_F[GPa]	Fracture toughness K_{IC} [MPa m$^{0.5}$]
Soft film	224 ± 4	26 ± 1	4.9 ± 0.5	3.1 ± 0.2
Hard film	383 ± 19	36 ± 1	5.7 ± 0.5	4.7 ± 1.0
Hierarchical film	355 ± 7	31 ± 4	7.9 ± 0.2	4.7 ± 0.4

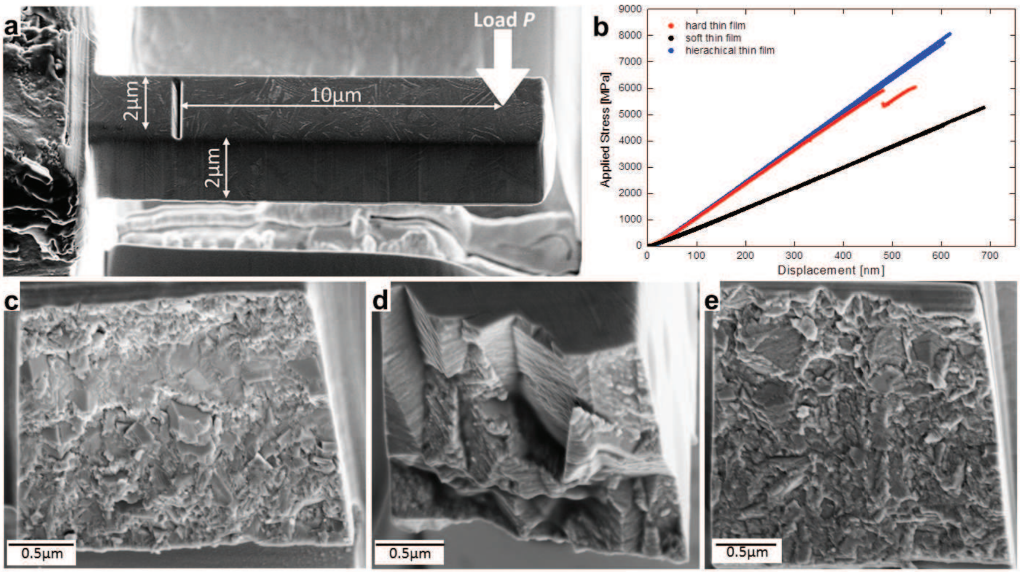

Figure E.3.: Results from mechanical tests on micro-cantilevers in SEM. (a) An example of a notched cantilever used for toughness characterization. (b) Experimental load-deflection curves from two cantilevers each, fabricated from the hierarchical thin film and from two reference soft and hard thin films. (c–e) Fracture surfaces of reference soft (c), hard (d) films and of the hierarchical films (e).

Representative load-deflection curves recorded for six unnotched microcantilevers (two for each thin film type) presented in Fig. E.3b indicate dominant linear-elastic response without plastic deformation, as expected for brittle ceramic materials. The evaluated elastic moduli, which are proportional to the slope of the stress-displacement curves in Fig. E.3b, approximately follow the rule of mixture and are, similar to hardness, determined by the volume fraction of either elastic or stiff constituents. The evaluated fracture stress and fracture toughness values clearly demonstrate the importance of thin film architecture for the fracture behaviour. Although the fracture toughness of the hierarchical and hard thin films is comparable and significantly higher than that of the soft thin film (Table E.1), there is a significant difference in fracture stress. The resistance of the thin films to fracture evidently depends on their architecture, as the fracture stress is by far highest for the hierarchical thin film, reaching a value of 7.9 GPa.

In order to understand this effect, fracture surface (FS) morphologies of the tested microcantilevers were analysed in the SEM. FSs obtained from the soft thin film (Fig. E.3c) indicate relatively smooth brittle fracture with a significant fraction of cleaved grains (transgranular fracture, TGF), whereas FSs from the hard thin film (Fig. E.3d) show mainly intergranular fracture (IGF) along the boundaries of the large columnar herringbone grains (Fig. E.1c). The specific arrangement of the herringbone grains resulted in an increased FS area due to multiple crack deflection events, resulting in a high fracture toughness value (Table E.1). Remarkably, FSs of the hierarchical thin film (Fig. E.3e) again show relatively smooth brittle fracture with only few micro- and nanoscopic protruding features, very similar to the FSs of the soft thin film, albeit with less TGF.

At the microscopic scale, there are two dominant competing effects which lead to excellent fracture toughness in our films, namely, (i) crack growth and deflection at the grain boundaries of the herringbone crystallites (Fig. E.3d) and (ii) crack arrest and deflection at the microscopic interfaces between hard and tough sublayers (Fig. 1a). The fracture stress enhancement in the hierarchical film is caused by the presence of the multi-layered morphology (Fig. E.1a), which limits the size of herringbone crystallites (Fig. E.3c) and restrains the crack length (Fig. E.3e). The equal fracture toughness of the hierarchical film, compared to the hard film, is however a result of the balance between the less pronounced crack deflection at morphologically smaller herringbone crystallites and multiple crack arrests as well as deflections at the interfaces between tough and hard sublayers, which also results in significantly different fracture surface morphologies (*cf.* Fig. E.3d and e).

In order to obtain more insights into the fracture behaviour of our hierarchical thin film at the nanoscale, we fabricated nanocantilevers from various regions of the hierarchical thin film (Fig. E.4a, inset), loaded them in TEM using a pico-indentation device and observed the crack propagation *in situ*, while load-deflection data were simultaneously recorded (*cf.* Suppl. Fig. S.E.5). In Fig. E.4a, load-deflection curves from three representative nanocantilevers are shown. Depending on their internal nanostructure, the cantilevers exhibited distinctly different fracture behaviour. The load-deflection curve of a cantilever fabricated (mainly) from a tough interlayer indicates relatively low elastic modulus and fracture stress values, which is in line with the behaviour of the monolithic soft thin film (*cf.* Fig. E.3b).

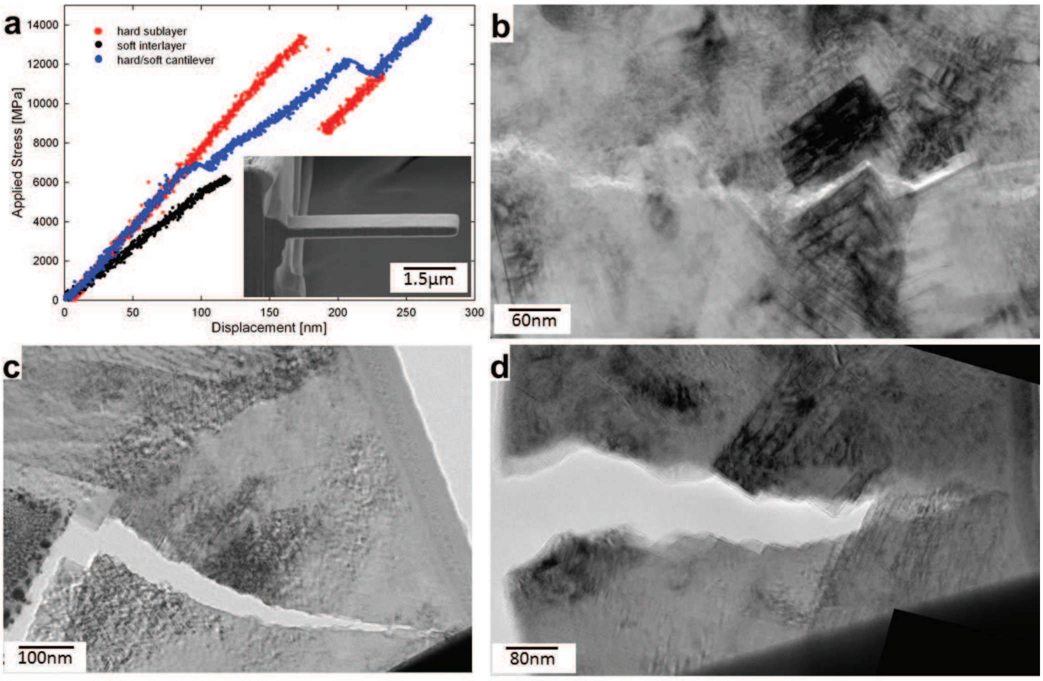

Figure E.4.: Nanomechanical behaviour of the hierarchical thin film. (a) Load-deflection curves from nanocantilevers machined using FIB from soft, hard and soft–hard hierarchical film regions, respectively, and the corresponding cantilever geometry (inset). (b–d) Representative zigzag-like crack patterns showing cleavage (b), transgranular (c) and intergranular/mixed (d) fracture.

On the other hand, the cantilever fabricated from the thin film region consisting of both hard and tough sublayers (containing a significant portion of herringbone crystallites) broke in a stepwise fashion, which is reflected in the jagged load-deflection curve (Fig. E.4a). This behaviour is caused by intermittent crack extension, as there are multiple crack deflection and crack arrest events during the cantilever's fracture. A similar behaviour can be observed in the case of the hard sublayer, however, to a lower extent, which can be explained by the lower level of hierarchy with respect to the specimen containing both hard and soft sublayers. Different fracture mechanisms, occurring during bending of the individual pre-selected regions of the thin films, were revealed by a detailed analysis of the FSs and by studying *in situ* fracture processes in TEM (*cf.* Videos S2–S6 of the supplementary material). Besides protruding herringbone nano- and micrograins, also mixed IGF, TGF and cleavage fracture (CF) modes occur at various levels of the thin film's hierarchical architecture. IGF takes place along the grain boundaries of the herringbone micrograins and between globular nanograins (Fig. E.4d) in hard and tough sublayers, respectively. TGF is found in soft globular nanograins and is equivalent to a combination of IGF between h-Al(Ti)N nanocrystals, CF along the nanolamellar interfaces and CF across c-Ti(Al)N lamellae (Fig. E.4c). Additionally, we observed that IGF along the grain boundaries of herringbone crystallites was drawn into and interrupted at the tough interlayers, an effect which is known as the shielding/anti-shielding effect and which is typical for nacre-like microstructures [14, 38]. CF was further observed mainly along {100} planes of the cubic phases, coinciding with the interfaces of c-Ti(Al)N/c-Al(Ti)N nanolamellae inside the herringbone micrograins (Fig. E.4b). Finally, CF infrequently also progressed perpendicular to these interfaces (Fig. E.4c), similar to TGF in soft globular nanograins. These latter modes of CF are associated with a high energy release rate, due to the necessity of breaking the strong chemical bonds along coherent interfaces or across single-crystalline cubic platelets, which significantly contribute to an increase of the overall macroscopic fracture toughness. A TEM micrograph in Supplementary Fig. S.E.5 and *in situ* TEM videos of supplementary material further document the crack propagation behaviour through different regions of the hierarchical thin film, as discussed above.

Based on the SEM and TEM observations, we suggest that the remarkably high fracture stress of the hierarchical nanostructured ceramic thin film (Table E.1) originates mainly from (i) the high volume fraction of hard cubic phases and (ii) the shielding/anti-shielding effects across multiple length scales associated with the multiscale alternation of hard/soft phases within the hard/tough thin film sublayers, within micrograins and nanograins as well as hard/tough c-Ti(Al)N/h-Al(Ti)N nano- lamellae (*cf.* Fig. E.2) [14, 38]. On the other hand, the high fracture toughness of the complex hierarchical structure is evidently given by a combination of all the described toughening mechanisms and most decisively supported by the latter one [11, 14, 39]. In general, the extraordinary fracture resistance originates from an interplay of various intrinsic toughening mechanisms at multiple length scales and multiple crack deflection events associated with the complex hierarchical nanostructure, despite the brittle nature of the individual ceramic platelets [10, 11, 40]. The importance of the hierarchical nanostructure in the fracture toughness behaviour is also indirectly supported by the quantitative K_{IC} data recently reported from a conventional monolithic TiAlN thin film, which was prepared using magnetron sputtering and which exhibited smaller K_{IC} values even after age hardening [41].

E.2.3. High-temperature stability

In addition to mechanical properties, we also investigated thermal stability of our hierarchical nanostructures. Thermal stability up to peak temperatures of ~ 1000°C, reached within ms, is a general requirement in the contact region between coated cutting tool and work piece in the metal cutting industry. Grazing incidence laboratory and cross-sectional synchrotron X-ray diffraction (XRD) analyses validated the phase compositions of the soft, hard and hierarchical thin films as summarized in Fig. E.2 (*cf.* also Suppl. Fig. S.E.6). XRD analysis of the hard film with the prevailing c-TiAlN phase was performed in order to investigate the thermal stability of the metastable cubic TiAlN phase and the corresponding nanolamellar microstructure. The film was exposed to temperatures up to ~ 1100°C at a heating rate of $1\,\mathrm{Ks}^{-1}$ during *in situ* high-energy high-temperature grazing-incidence transmission synchrotron XRD with photon energy of 87.1 keV. As shown in Fig. E.5 and Suppl. Fig. S.E.7, the heating results in the shift of c-TiAlN 111 and 200 reflections (along with a substrate 200 reflection) to smaller diffraction angles due to the crystal lattice expansion up to ~ 950°C. Above this temperature, an onset of cubic phase decomposition and accompanying thin film softening is manifested by an increase in the intensity of the h-TiAlN 100 reflection (Fig. E.5e). Additionally, the small-angle X-ray scattering (SAXS) signal (Fig. E.5) from the nanolamellae's 2$^{\mathrm{nd}}$ order reflection indicates that the cubic nanolamellae start to lose their ordered microstructure above a critical temperature of ~ 900°C as indicated by the SAXS reflection shift to small diffraction angles in Fig. E.5f. In comparable conventional TiAlN thin films prepared by magnetron sputtering, the phase decomposition starts usually already at temperatures above ~ 800°C [41–44]. In Suppl. Fig. S.E.7, corresponding two dimensional X-ray diffraction patterns are presented. We suggest that the high temperature stability of our hierarchical nanostructure in terms of both phase composition and microstructure can be understood in light of their mutually stabilizing interplay. It is supposed that the interfaces between the nanolamellae lower the diffusion rates needed for the formation of the stable soft hexagonal phase, which is observed in polycrystalline TiAlN thin films prepared by magnetron sputtering already from ~ 800°C [41].

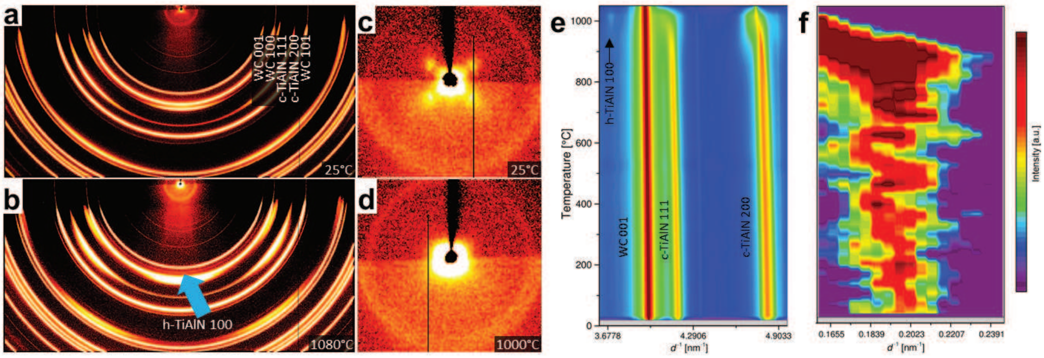

Figure E.5.: Thermal stability of the monolithic hard film studied by XRD. (a, b) Debye–Scherrer rings from the film show the presence of hexagonal phase at 1080°C, as indicated by the arrow. (c, d) Four small-angle X-ray scattering (SAXS) maxima from the herringbone crystallites in (c) disappear at high temperatures. (e) The evolution of 111 and 200 reflections during heating indicates thermal stability of the c-TiAlN phase up to ~ 950°C and (f) SAXS data show the evolution of the nanolamellae's 2^{nd} order peak (*cf.* (a), (c)) and the stability of the nanolamellar nanostructure up to ~ 900°C (*cf.* Suppl. Fig. SE.3)

E.3. Discussion and Conclusions

In the field of hard thin films, and especially of transition metal nitrides, during the last decades research focused primarily on the understanding of the impact of deposition conditions, multi-layered microstructures, structural defects and various alloying constituents on the thin films' overall functional behaviour [26, 45–47]. First-principle calculations were extensively used to predict improved mechanical properties like hardness and toughness in alloyed thin films, but failed to yield significantly improved functionality [26, 47]. The biomimetic self-assembly approach presented here demonstrates that the application of a hierarchically nanostructured thin film architecture can serve as a very effective concept for the enhancement of toughness, while preserving hardness and thermal stability [11]. By using only a simple time-dependent variation of the composition of reactant gases, it is possible to deposit protective bionic thin films with a sequence of nanostructured hierarchical hard/tough sublayers, whereupon synergistic properties can be realized, which are not found in the monolithic structures.

The self-assembly mechanism responsible for the formation of the nanolamellar microstructure in CVD TiAlN films is still in dispute [29, 31, 48]. Recent reports suggested that the nanolamellae formation could be a result of a phase separation at the deposition temperature *via* surface diffusion or kinetically-controlled oscillating reactions at the film surface [30, 49, 50]. The regular morphology of the herringbone crystallites with well-developed $\{100\}$ interfaces between platelets (Fig. E.2) as well as the geometrical and compositional matching at nanolamellar boundaries reported by Zalesak *et al.* [30] in monolithic epitaxial TiAlN films suggest, however, that the nanolamellae's self-assembly is most likely a consequence of kinetically controlled oscillatory reactions at the growing film's surface described already by Bartsch *et al.* [33] In other words, the nanolamellae are formed as a result of a sequential epitaxial overgrowth of $\{100\}$ facets by individual Al- and Ti-rich sublayers [30]. Depending on the ratio of $AlCl_3$ and $TiCl_4$ precursor gases, however, hard and tough nanostructures are formed with respective coherent c-Ti(Al)N/c-Al(Ti)N and incoherent c-Ti(Al)N/h-Al(Ti)N nanolamellae.

Our six-hierarchy level film self-assembled during ~ 15 minutes of deposition time shows simultaneously high hardness, fracture stress and toughness of ~ 31 and ~ 7.9 GPa and $\sim 4.7\,\mathrm{MPa\,m^{0.5}}$, respectively, as well as excellent phase/microstructural stability at high temperatures up to $\sim 950/900$°C. The experimental jagged load-deflection curves [10, 11, 40] from Fig. E.4a clearly demonstrate that the thin film's six-level structural hierarchy induces multiscale crack deflections events (Fig. E.4b–d), which result in fracture stress enhancement. The additional level of hierarchy obtained by combining the hard and soft sublayers significantly increases the fracture stress to values 40 and 60% beyond that of the individual constituents, respectively, while fracture toughness remains at least as good as that of the better-performing constituent sublayer. Additional strengthening and toughening mechanisms, induced by this structural enhancement, are responsible for this superior functional performance [11].

Biomineralized materials like nacre, bone and enamel represent a typical example of many-level hierarchical materials with a remarkable combination of high fracture toughness and strength up to $\sim 7\,\mathrm{MPa\,m^{0.5}}$ and several hundred MPa, respectively [32, 51–54]. Similarly, biomimetic artificial nacres, bones and teeth were reported with amazing microstructures and mechanical properties[18–25] like fracture toughness of $30\,\mathrm{MPa\,m^{0.5}}$ and yield strengths of 200 MPa in the case of nacre-like poly(methyl methacrylate)-alumina materials [39, 55]. Since all biomineralized and also most of the biomimetic microstructures include proteins or polymers, however, their application is usually limited to a restricted temperature range [24]. Moreover, most of the reported nacre-like microstructures were produced only at the laboratory scale and/or during laborious long-term assembly [18–20, 55]. In comparison, our hierarchical film can be used at temperatures up to ~ 900°C and the self-assembly process takes just several minutes.

Also in the field of protective thin films, there have been numerous reports on synthetic microstructures with alternating phases and relatively high toughness, which were produced mainly by magnetron sputtering from two or more targets [56–60]. Our biomimetic film (Fig. E.1) introduces however a novel approach based on multiple hierarchy levels and fast and economic self-assembly in an industrial scale deposition system.

In order to synthesize the hierarchical film with the remark- able hierarchical microstructure from Fig. E.1, however, the relatively high deposition temperature of ∼ 810°C is needed, which may restrict or limit the use of some substrates (like high speed steel). Therefore, further effort is needed to decrease the temperature of the self-assembly process.

Finally, the employed CVD recipe attracts especially by its high deposition rate of ∼ 10 µm per hour, simplicity and the ability to produce an applicable industrial material. Therefore, we suggest that further exploration of CVD processes featuring self-assembly reactions holds much promise for incorporation of truly hierarchical biomimetic design into novel application-relevant materials.

Methods

Thin film synthesis

Hierarchical as well as hard and soft monolithic thin films studied in this work were grown with a thickness of ∼ 2.7, ∼ 4 and ∼ 3.8 µm in a commercial Bernex MT-CVD-300 medium temperature reactor at a temperature of ∼ 810°C, resulting in a deposition rate of ∼ 10 µm per hour. The partial pressures of precursors $AlCl_3$, $TiCl_4$, NH_3, HCl, N_2 as process gases and H_2 as the carrier gas were 0.404, 0.09, 0.331, 0.110, 1.653, 22.413 kPa for the thick hard sublayers and 0.368, 0.022, 0.332, 0.113, 1.66, 22.505 kPa for thin tough interlayers, respectively, at a total pressure of 25 kPa. These two sets of parameters were used to prepare also the respective hard and soft monolithic films.

Electron microscopy characterization

Zeiss AURIGA CrossBeam and Tescan GAIA3 workstations were used to collect scanning electron microscopy (SEM) micrographs from thin film cross-sections prepared using focused ion beam (FIB) milling. The micro- and nanocantilever fabrication was performed by FIB using an acceleration voltage of 30 kV and currents in the range from 20 nA to 50 pA. Special care was taken to avoid sample damage by Ga ions by using low FIB cutting currents as well as Pt protective layers. High-resolution transmission electron microscopy (TEM) analysis, energy-dispersive X-ray and electron energy loss spectroscopies were performed using a Cs-corrected JEOL JEM-2100F system operated at 200 kV. Conventional TEM was performed using a Philips CM12 system operated at 120 kV.

Bending experiments on microcantilevers of $2 \times 2 \times 10\,\mu m^3$ in size were performed in a SEM (LEO 982, Zeiss) equipped with an indentation system (PicoIndenter 85, Hysitron). Bending tests on nanocantilevers with a cross-section of $\sim 1 \times 0.3\,\mu m^2/\sim 1 \times 0.5\,\mu m^2$ and a length of $\sim 3.5\,\mu m$ were performed using a Hysitron PI-95 TEM Pico-indenter in a JEOL JEM-2100F microscope operated in conventional (CTEM) mode.

Hardness characterization

Nanoindentation measurements were carried out using a UMIS II (UltraMicro Indentation System) Nanoindenter from Fischer-Cripps Laboratories, equipped with a Berkovich tip and data were evaluated using the Oliver–Pharr method. This particular setup was chosen due to the samples' high surface roughness, necessitating higher indentation forces and indentation depths.

Synchrotron analysis

In situ high-energy high-temperature grazing incidence trans- mission X-ray diffraction HE-HT-GIT-XRD in the temperature range of 25–1100°C was performed at the German Synchrotron (DESY) at PETRA III, (beamline P07B side hutch) in transmission geometry with a pencil beam with a size of 400 µm × 100 µm, an incidence angle of 1 degree and a photon energy of 87.1 keV. The samples were mounted on the sample stage of a dilatometer Bähr DIL 805 and heated with a heating rate of $1\,Ks^{-1}$ in high vacuum. Cross-sectional X-ray nanodiffraction experiments were performed at the ID13 beamline of ESRF in Grenoble (F) using an X-ray beam of 100 nm in diameter and an energy of 12.7 keV.

Acknowledgements

This work was supported by Österreichische Forschungsförderungsgesellschaft mbH (FFG), Project No. 864828, "Tough_TiAlN". Financial support by the Austrian Federal Government (in particular from Bundesministerium für Verkehr, Innovation und Technologie and Bundesministerium für Wissenschaft, Forschung und

Wirtschaft) represented by Österreichische Forschungsförderungsgesellschaft mbH and the Styrian and the Tyrolean Provincial Government, represented by Steirische Wirtschaftsförderungsgesellschaft mbH and Standortagentur Tirol, within the framework of the COMET Funding Programme is gratefully acknowledged. A part of this work was carried out with the support of CEITEC Nano Research Infrastructure (ID LM2015041, MEYS CR, 2016–2019), CEITEC Brno University of Technology.

Supplementary material

For supplementary videos see DOI: 10.1039/c8nr10339a.

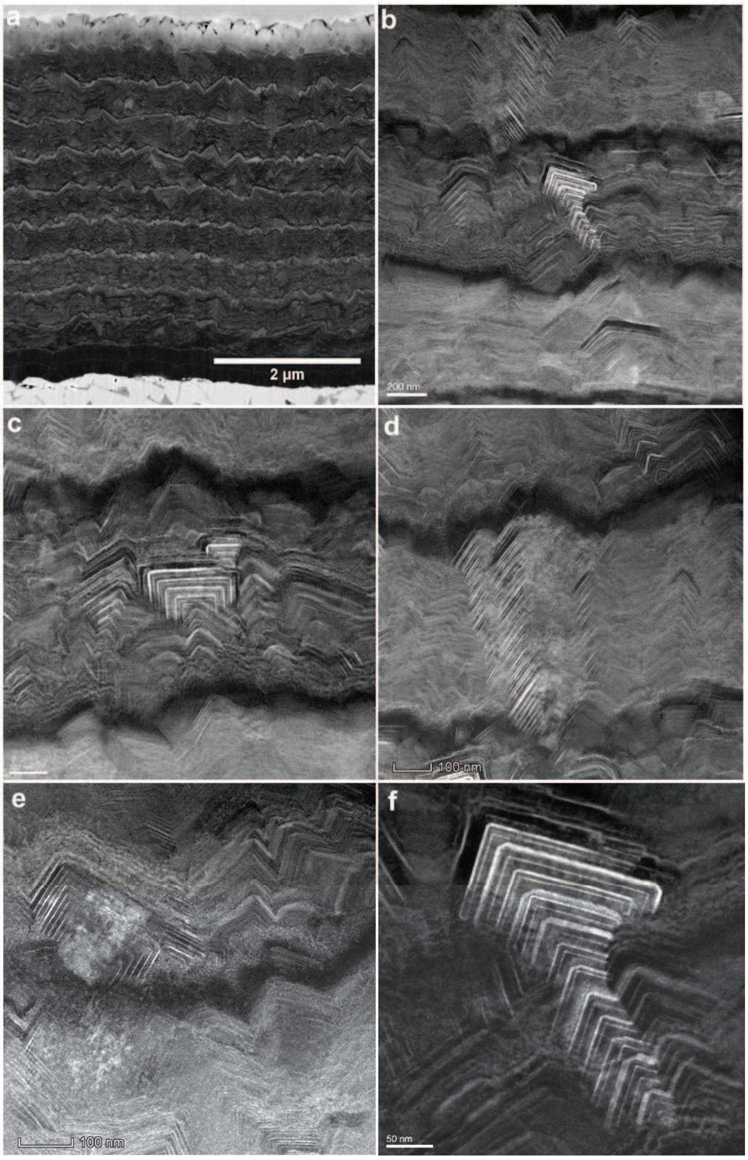

Suppl. Fig. E.1 | Cross-sectional microstructure of the hierarchical film. (a), SEM micrographs of the film's cross-section with 9 hard sublayers and 9 tough interlayers deposited onto a WC-Co substrate coated with a TiN bonding layer and finalized by an AlN top oxidation resistant layer. (b-f), TEM cross-sectional micrographs showing cube and herringbone crystallites in the thick hard sublayers.

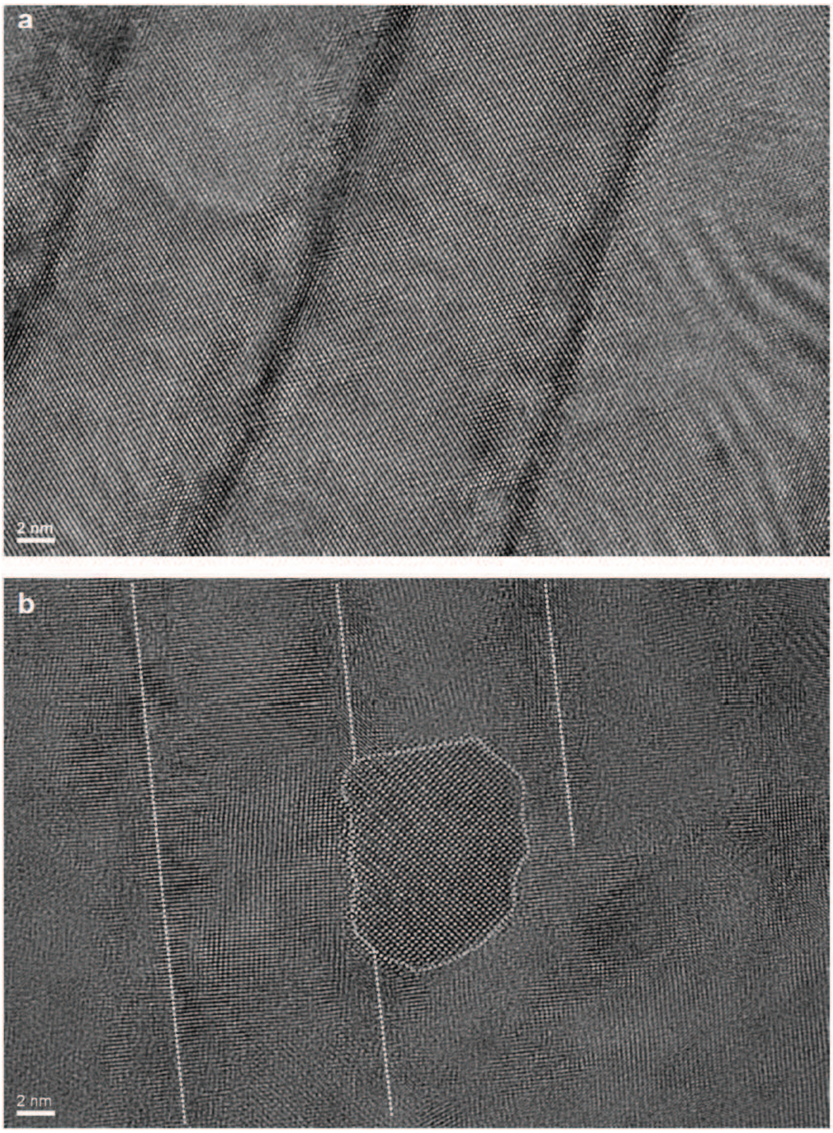

Suppl. Fig. E.2 | Atomistic microstructure of micro- and nanocrystals in hard and tough sublayers of the hierarchical film. (a) HR-TEM micrograph showing coherent nanolamellae with thin c-Ti(Al)N and thick c-Al(Ti)N platelets in the hard sublayers. (b) HR-TEM micrograph showing incoherent and partly irregular nanolamellar microstructure of a tough interlayer with thin c-Ti(Al)N platelets (indicated approximately by dotted lines) and thick h-Al(Ti)N platelets of random orientation along with a globular h-Al(Ti)N nanocrystal with its $(\bar{1}2\bar{1}0)$ lattice planes satisfying diffraction condition.

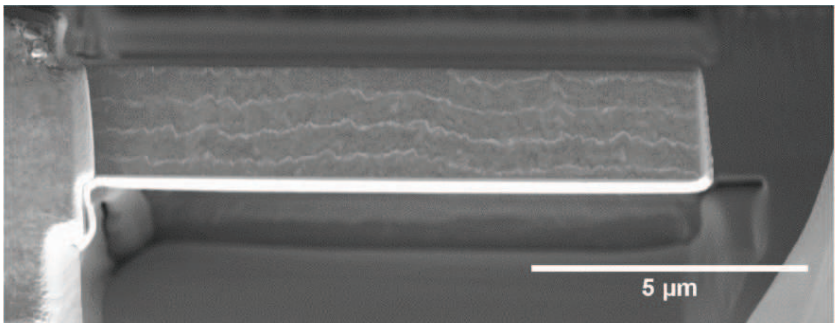

Suppl. Fig. E.3 | Cross-sectional microstructure of a microcantilever machined from the hierarchical film. The SEM micrograph shows an irregularly arranged multilayer stack consisting of hard sublayers separated by thin (bright) tough interlayers. The wavy cross-sectional morphology is a result of complex self-organization phenomena and is favorable for the film's fracture properties.

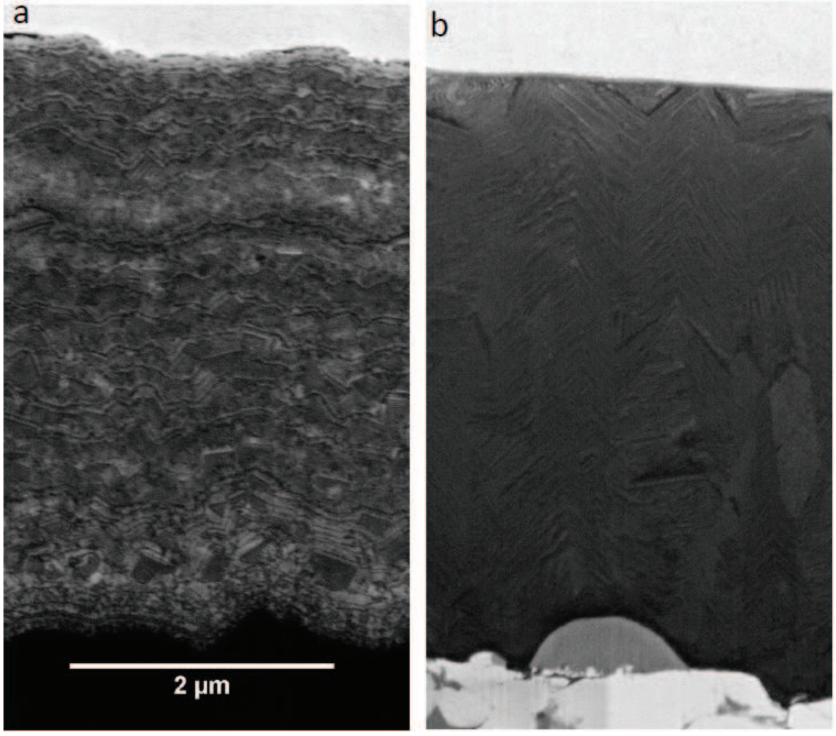

Suppl. Fig. E.4 | Cross-sectional microstructure of the reference films. SEM micrographs indicate nanocrystalline (a) and coarse-grained (b) microstructures of the soft and hard reference films, respectively.

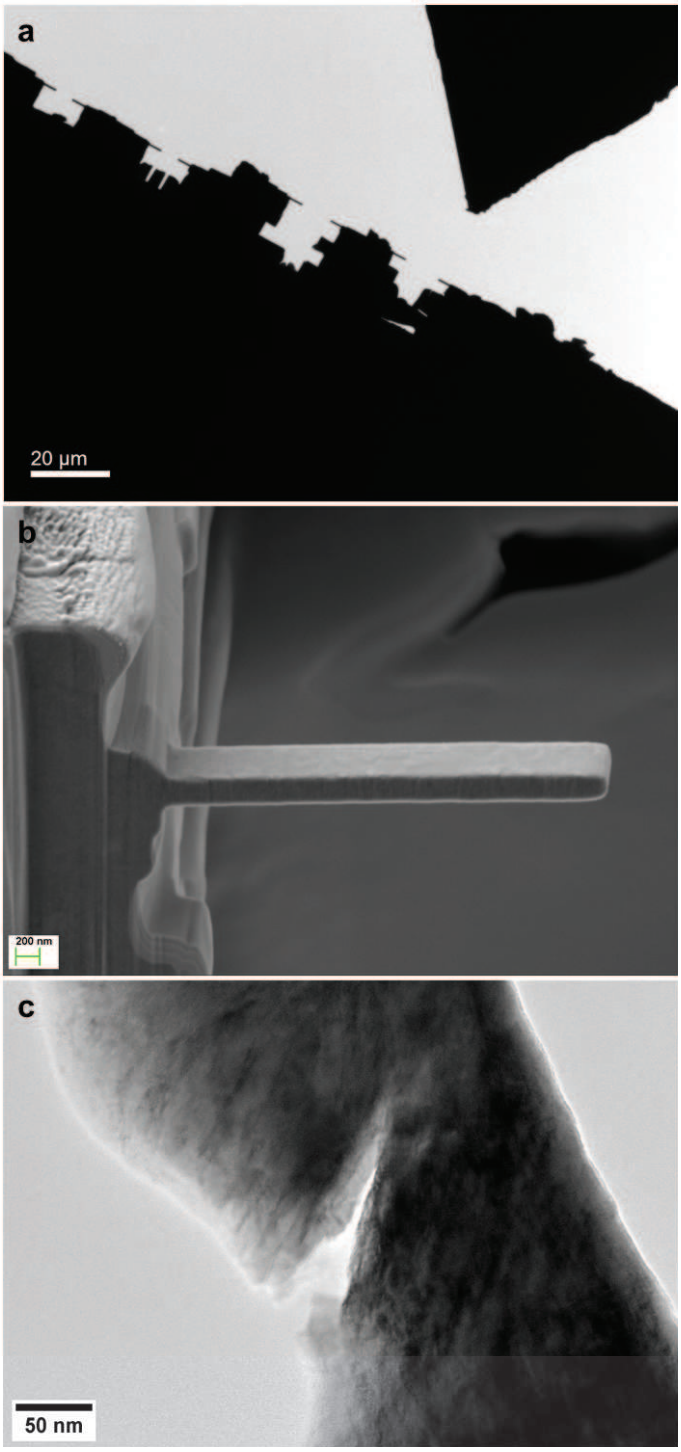

Suppl. Fig. E.5 | Loading experiments on nanocantilevers in TEM. (a) A diamond tip approaching the nanocantilevers. (b) A detailed view of a nanocantilever. (c) Zigzag-like crack propagation across a nanocantilever machined from the hierarchical film.

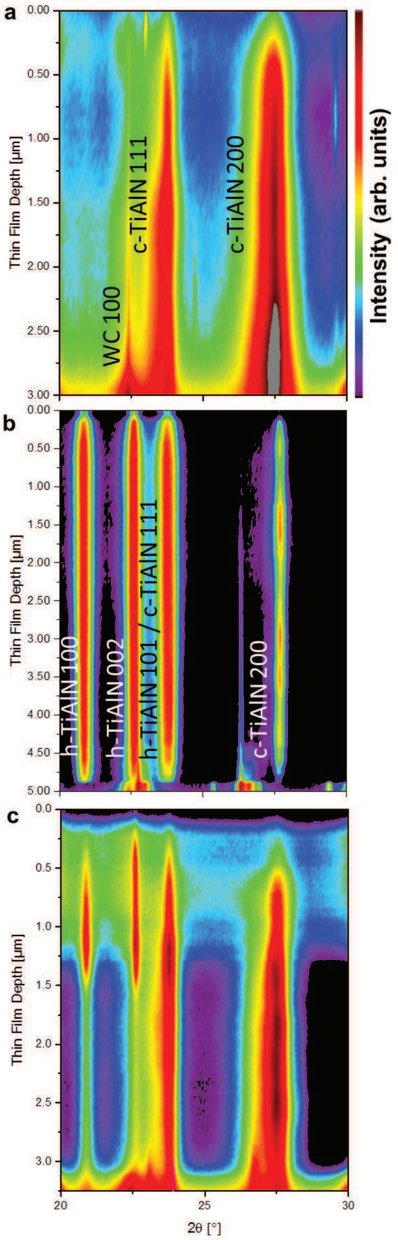

Suppl. Fig. E.6 | Results from cross-sectional X-ray nanodiffraction analysis (CSnanoXRD) performed on hard, soft and hierarchical films using a synchrotron X-ray beam with a diameter of 100nm and a photon energy of 12.7keV. (a) Monolithic hard film consists of cubic TiAlN phases (and also some traces of hexagonal TiAlN phase with concentration <∼ 5%). (b) Monolithic soft film consists of hexagonal and cubic TiAlN phases. (c) Hierarchical film consists of hard and tough sublayers with cubic and hexagonal TiAlN phases. Due to the wavy morphology of the hierarchical film (*cf.* Supplementary Figure S.E.3), it was not possible to resolve the individual sublayers of the film using CSnanoXRD.

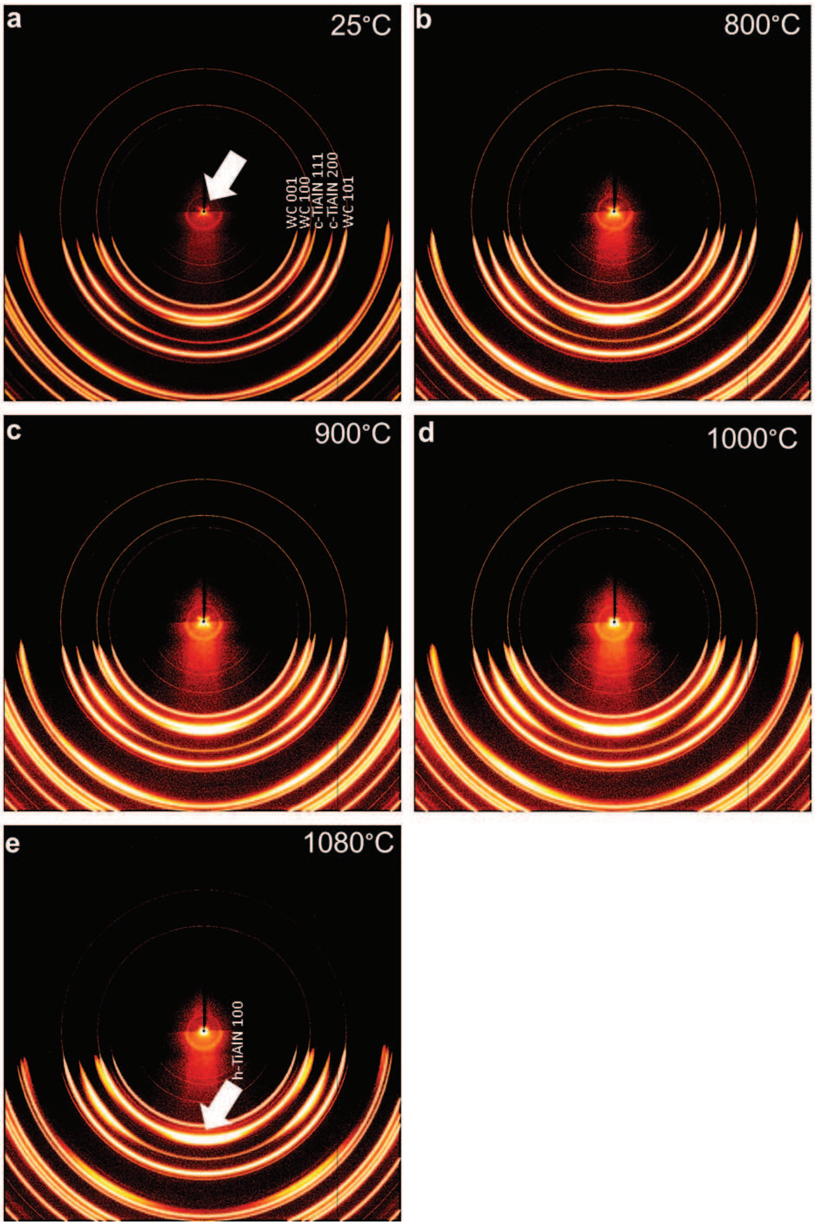

Suppl. Fig. E.7 | Results from high-energy high-temperature transmission X-ray diffraction experiment on the hard film on WC-Co substrate demonstrate the film's thermal stability. (a) Wide angle X-ray diffraction patterns collected at temperatures of 25, 800, 900, 1000 and 1080°C. In patterns (a-c) only the presence of WC and c-TiAlN diffraction peaks is observed, whereas in (b) the occurrence of h-TiAlN 100 reflection is visible. The arrow in (a) indicates the small-angle scattering signal from the film's lamellar nanostructure, which disappears in (d) and (e).

Bibliography to paper E

[1] J. W. Dunlop and P. Fratzl, *Annual Review of Materials Research*, 2010, **40**, 1–24, DOI: `10.1146/annurev-matsci-070909-104421`.

[2] M. A. Meyers, P.-Y. Chen, A. Y.-M. Lin and Y. Seki, *Progress in Materials Science*, 2008, **53**, 1–206, DOI: `10.1016/j.pmatsci.2007.05.002`.

[3] P. Fratzl, H. S. Gupta, E. P. Paschalis and P. Roschger, *J. Mater. Chem.*, 2004, **14**, 2115–2123, DOI: `10.1039/b402005g`.

[4] M. Suzuki, K. Saruwatari, T. Kogure, Y. Yamamoto, T. Nishimura, T. Kato et al., *Science*, 2009, **325**, 1388–1390, DOI: `10.1126/science.1173793`.

[5] M. J. Harrington, A. Masic, N. Holten-Andersen, J. H. Waite and P. Fratzl, *Science*, 2010, **328**, 216–220, DOI: `10.1126/science.1181044`.

[6] N. Kroger, *Science*, 2009, **325**, 1351–1352, DOI: `10.1126/science.1177055`.

[7] Z. Liu, M. A. Meyers, Z. Zhang and R. O. Ritchie, *Progress in Materials Science*, 2017, **88**, 467–498, DOI: `10.1016/j.pmatsci.2017.04.013`.

[8] P. Fratzl and R. Weinkamer, *Progress in Materials Science*, 2007, **52**, 1263–1334, DOI: `10.1016/j.pmatsci.2007.06.001`.

[9] J. Sun and B. Bhushan, *RSC Advances*, 2012, **2**, 7617, DOI: `10.1039/c2ra20218b`.

[10] W. J. Clegg, K. Kendall, N. M. Alford, T. W. Button and J. D. Birchall, *Nature*, 1990, **347**, 455–457, DOI: `10.1038/347455a0`.

[11] R. O. Ritchie, *Nature Materials*, 2011, **10**, 817–822, DOI: `10.1038/nmat3115`.

[12] B. J. F. Bruet, J. Song, M. C. Boyce and C. Ortiz, *Nature Materials*, 2008, **7**, 748–756, DOI: `10.1038/nmat2231`.

[13] H. Gao, *International Journal of Fracture*, 2006, **138**, 101–137, DOI: `10.1007/s10704-006-7156-4`.

[14] O. Kolednik, J. Predan, F. D. Fischer and P. Fratzl, *Advanced Functional Materials*, 2011, **21**, 3634–3641, DOI: `10.1002/adfm.201100443`.

[15] B. L. Smith, T. E. Schäffer, M. Viani, J. B. Thompson, N. A. Frederick, J. Kindt et al., *Nature*, 1999, **399**, 761–763, DOI: `10.1038/21607`.

[16] H. Gao, B. Ji, I. L. Jager, E. Arzt and P. Fratzl, *Proceedings of the National Academy of Sciences*, 2003, **100**, 5597–5600, DOI: `10.1073/pnas.0631609100`.

[17] P. Fratzl, O. Kolednik, F. D. Fischer and M. N. Dean, *Chemical Society Reviews*, 2016, **45**, 252–267, DOI: `10.1039/c5cs00598a`.

[18] Z. Tang, N. A. Kotov, S. Magonov and B. Ozturk, *Nature Materials*, 2003, **2**, 413–418, DOI: `10.1038/nmat906`.

[19] S. Elsharkawy, M. Al-Jawad, M. F. Pantano, E. Tejeda-Montes, K. Mehta, H. Jamal et al., *Nature Communications*, 2018, **9**, DOI: `10.1038/s41467-018-04319-0`.

[20] B. Yeom, T. Sain, N. Lacevic, D. Bukharina, S.-H. Cha, A. M. Waas et al., *Nature*, 2017, **543**, 95–98, DOI: `10.1038/nature21410`.

[21] L.-B. Mao, H.-L. Gao, H.-B. Yao, L. Liu, H. Colfen, G. Liu et al., *Science*, 2016, **354**, 107–110, DOI: `10.1126/science.aaf8991`.

[22] H.-L. Gao, S.-M. Chen, L.-B. Mao, Z.-Q. Song, H.-B. Yao, H. Cölfen et al., *Nature Communications*, 2017, **8**, DOI: `10.1038/s41467-017-00392-z`.

[23] X.-F. Pan, H.-L. Gao, Y. Lu, C.-Y. Wu, Y.-D. Wu, X.-Y. Wang et al., *Nature Communications*, 2018, **9**, DOI: `10.1038/s41467-018-05355-6`.

[24] U. G. K. Wegst, H. Bai, E. Saiz, A. P. Tomsia and R. O. Ritchie, *Nature Materials*, 2014, **14**, 23–36, DOI: `10.1038/nmat4089`.

[25] X. Wang, S. Xu, S. Zhou, W. Xu, M. Leary, P. Choong et al., *Biomaterials*, 2016, **83**, 127–141, DOI: `10.1016/j.biomaterials.2016.01.012`.

[26] P. H. Mayrhofer, R. Rachbauer, D. Holec, F. Rovere and J. M. Schneider, in *Comprehensive Materials Processing*, 2014, vol. 4, ch. 14, pp. 355–388.

[27] K. Choy, *Prog. Mater Sci.*, 2003, **48**, 57–170, DOI: `10.1016/S0079-6425(01)00009-3`.

[28] J. Todt, R. Pitonak, A. Köpf, R. Weißenbacher, B. Sartory, M. Burghammer et al., *Surf. Coat. Technol.*, 2014, **258**, 1119–1127, DOI: `10.1016/j.surfcoat.2014.07.022`.

[29] J. Todt, J. Zalesak, R. Daniel, R. Pitonak, A. Köpf, R. Weißenbacher et al., *Surf. Coat. Technol.*, 2016, **291**, 89–93, DOI: `10.1016/j.surfcoat.2016.02.027`.

[30] J. Zalesak, D. Holec, I. Matko, M. Petrenec, B. Sartory, N. Koutná et al., *Acta Materialia*, 2017, **131**, 391–399, DOI: `10.1016/j.actamat.2017.04.009`.

[31] A. Paseuth, K. Yamagata, A. Miura, M. Higuchi and K. Tadanaga, *Journal of the American Ceramic Society*, 2016, **100**, ed. M. Cinibulk, 343–353, DOI: `10.1111/jace.14549`.

[32] R. Z. Wang, Z. Suo, A. G. Evans, N. Yao and I. A. Aksay, *Journal of Materials Research*, 2001, **16**, 2485–2493, DOI: `10.1557/jmr.2001.0340`.

[33] K. Bartsch, A. Leonhardt and E. Wolf, *Surf. Coat. Technol.*, 1992, **54**, 193–197, DOI: `10.1016/S0257-8972(09)90049-4`.

[34] I. Petrov, P. B. Barna, L. Hultman and J. E. Greene, *Journal of Vacuum Science & Technology A: Vacuum, Surfaces, and Films*, 2003, **21**, S117–S128, DOI: `10.1116/1.1601610`.

[35] A. Madan, I. W. Kim, S. C. Cheng, P. Yashar, V. P. Dravid and S. A. Barnett, *Phys Rev Lett*, 1997, **78**, 1743–1746, DOI: `10.1103/PhysRevLett.78.1743`.

[36] G. Dehm, B. Jaya, R. Raghavan and C. Kirchlechner, *Acta Materialia*, 2018, **142**, 248–282, DOI: `10.1016/j.actamat.2017.06.019`.

[37] K. Matoy, H. Schönherr, T. Detzel, T. Schöberl, R. Pippan, C. Motz et al., *Thin Solid Films*, 2009, **518**, 247–256, DOI: `10.1016/j.tsf.2009.07.143`.

[38] B. Bruet, H. Qi, M. Boyce, R. Panas, K. Tai, L. Frick et al., *Journal of Materials Research*, 2005, **20**, 2400–2419, DOI: `10.1557/jmr.2005.0273`.

[39] E. Munch, M. E. Launey, D. H. Alsem, E. Saiz, A. P. Tomsia and R. O. Ritchie, *Science*, 2008, **322**, 1516–1520, DOI: `10.1126/science.1164865`.

[40] D. Sen and M. J. Buehler, *Scientific Reports*, 2011, **1**, DOI: `10.1038/srep00035`.

[41] M. Bartosik, C. Rumeau, R. Hahn, Z. L. Zhang and P. H. Mayrhofer, *Scientific Reports*, 2017, **7**, DOI: `10.1038/s41598-017-16751-1`.

[42] S. PalDey and S. Deevi, *Mater. Sci. Eng., A*, 2003, **342**, 58–79, DOI: `10.1016/S0921-5093(02)00259-9`.

[43] P. Mayrhofer, A. Hörling, L. Karlsson, J. Sjölén, T. Larsson, C. Mitterer et al., *Appl Phys Lett*, 2003, **83**, 2049–2051, DOI: `10.1063/1.1608464`.

[44] M. Bartosik, R. Daniel, Z. Zhang, M. Deluca, W. Ecker, M. Stefenelli et al., *Surf. Coat. Technol.*, 2012, **206**, 4502–4510, DOI: `10.1016/j.surfcoat.2012.02.035`.

[45] G. Greczynski, J. Lu, J. Jensen, I. Petrov, J. Greene, S. Bolz et al., *Thin Solid Films*, 2014, **556**, 87–98, DOI: `10.1016/j.tsf.2014.01.017`.

[46] H. Kindlund, D. G. Sangiovanni, L. Martinez-de-Olcoz, J. Lu, J. Jensen, J. Birch et al., *APL Materials*, 2013, **1**, 042104, DOI: `10.1063/1.4822440`.

[47] P. H. Mayrhofer, C. Mitterer, L. Hultman and H. Clemens, *Prog. Mater Sci.*, 2006, **51**, 1032–1114, DOI: `10.1016/j.pmatsci.2006.02.002`.

[48] J. Keckes, R. Daniel, C. Mitterer, I. Matko, B. Sartory, A. Köpf et al., *Thin Solid Films*, 2013, **545**, 29–32, DOI: `10.1016/j.tsf.2013.08.001`.

[49] F. Uny, S. Achache, S. Lamri, J. Ghanbaja, E. Fischer, M. Pons et al., *Surface and Coatings Technology*, 2019, **358**, 923–933, DOI: `10.1016/j.surfcoat.2018.12.014`.

[50] F. Pacher, P. H. Mayrhofer and D. Holec, *Surface and Coatings Technology*, 2017, **326**, 37–44, DOI: `10.1016/j.surfcoat.2017.07.012`.

[51] F. Barthelat, C.-M. Li, C. Comi and H. D. Espinosa, *Journal of Materials Research*, 2006, **21**, 1977–1986, DOI: `10.1557/jmr.2006.0239`.

[52] L. H. He and M. V. Swain, *Journal of the Mechanical Behavior of Biomedical Materials*, 2008, **1**, 18–29, DOI: `10.1016/j.jmbbm.2007.05.001`.

[53] K. J. Koester, J. W. Ager and R. O. Ritchie, *Nature Materials*, 2008, **7**, 672–677, DOI: `10.1038/nmat2221`.

[54] S. Bechtle, S. F. Ang and G. A. Schneider, *Biomaterials*, 2010, **31**, 6378–6385, DOI: `10.1016/j.biomaterials.2010.05.044`.

[55] S. Deville, *Science*, 2006, **311**, 515–518, DOI: `10.1126/science.1120937`.

[56] J. M. Lackner, W. Waldhauser, B. Major, L. Major and M. Kot, *Thin Solid Films*, 2013, **534**, 417–425, DOI: `10.1016/j.tsf.2013.03.025`.

[57] J. Xu, X. Zhao, P. Munroe and Z. Xie, *Scientific Reports*, 2014, **4**, DOI: `10.1038/srep04239`.

[58] M. Schlögl, C. Kirchlechner, J. Paulitsch, J. Keckes and P. Mayrhofer, *Scr. Mater.*, 2013, **68**, 917–920, DOI: `10.1016/j.scriptamat.2013.01.039`.

[59] P. Wo, X. Zhao, P. Munroe, Z. Zhou, K. Li, D. Habibi et al., *Acta Materialia*, 2013, **61**, 193–204, DOI: `10.1016/j.actamat.2012.09.049`.

[60] R. Hahn, M. Bartosik, R. Soler, C. Kirchlechner, G. Dehm and P. Mayrhofer, *Scripta Materialia*, 2016, **124**, 67–70, DOI: `10.1016/j.scriptamat.2016.06.030`.

List of co-authored publications

Multi-scale interface design of strong and damage resistant hierarchical nanostructured materials
R. Daniel, M. Meindlhumer, J. Zalesak, W. Baumegger, J. Todt, T. Ziegelwanger, J. F. Keckes, C. Mitterer, J. Keckes
Mateials & Design 196: 109169, 2020
doi:10.1016/j.matdes.2020.109169

Nanoindentation and microbending analyses of glassy and crystalline Zr(Hf)Cu thin-film alloys
S. Haviar, T. Kozáka, M. Meindlhumer, M. Zítek, K. Opatovác, L. Kučerová, J. Keckes, P. Zeman
Surface & Coatings Technology 399, 126139, 2020
doi:10.1016/j.surfcoat.2020.126139

Microstructural evolution and thermal stability of AlCr(Si)N hard coatings revealed by in-situ high-temperature high-energy grazing incidence transmission X-ray diffraction
N. Jäger, M. Meindlhumer, S. Spor, H.Hruby, J. Julin, A. Stark, F. Nahif, J. Keckes, C. Mitterer, R. Daniel
Acta Materialia 186, 545-554, 2020
doi:10.1016/j.actamat.2020.01.026

Anisotropy of fracture toughness in nanostructured ceramics controlled by grain boundary design
R. Daniel, M. Meindlhumer, W. Baumegger, J. Todt, J. Zalesak, T. Ziegelwanger, C. Mitterer, J. Keckes
Materials and Design, 161, 80-85, 2019
doi:10.1016/j.matdes.2018.11.028

Grain boundary design of thin films: Using tilted brittle interfaces for multiple crack deflection toughening
R. Daniel, M. Meindlhumer, W. Baumegger, J. Zalesak, B. Sartory, M. Burghammer, C. Mitterer, J. Keckes
Acta Materialia, 122, 130-137, 2017
doi:10.1016/j.actamat.2016.09.027

Fracture toughness enhancement of brittle nanostructured materials by spatial heterogeneity: A micromechanical proof for CrN/Cr and TiN/SiOx multilayers
R. Daniel, M. Meindlhumer, J. Zalesak, B. Sartory, A. Zeilinger, C. Mitterer, J. Keckes
Materials and Design, 104, 227-234, 2016
doi:10.1016/j.matdes.2016.05.029

In-situ Observation of Cross-Sectional Microstructural Changes and Stress Distributions in Fracturing TiN Thin Film during Nanoindentation
A. Zeilinger, J. Todt, C. Krywka, M. Müller, W. Ecker, B. Sartory, M. Meindlhumer, M. Stefenelli, R. Daniel, C. Mitterer, J. Keckes
Scientific Reports 6, 22670, 2016
doi:10.1038/srep22670